

THESE DE DOCTORAT DE L'UNIVERSITE PARIS 6

Spécialité
Astronomie et Astrophysique

Présentée par
Mr Johann KOLB

Pour obtenir le grade de
DOCTEUR de l'UNIVERSITÉ PARIS 6

Sujet de la thèse :

Calibration and test tools for MCAO systems: Application
to the ESO Demonstrator MAD

Outils d'étalonnage et de test pour les systèmes d'OAMC :
Application au démonstrateur MAD de l'ESO

Soutenue le 12 Décembre 2005

Devant le jury composé de :

Mme Laurence REZEAU	Présidente
Mr Michel TALLON	Rapporteur
Mr Roberto RAGAZZONI	Rapporteur
Mr Benoît MOSSER	Examineur
Mr Gérard ROUSSET	Directeur de thèse
Mr Enrico MARCHETTI	Superviseur

Title: Calibration and test tools for MCAO systems: Application to the ESO Demonstrator MAD

Summary :

Multi Conjugate Adaptive Optics (MCAO) is a recent technique which aim is to correct in real-time for the effect of the atmospheric turbulence on astronomical images, over a rather large Field of View. The MCAO Demonstrator (MAD) is a prototype currently under development in the laboratories of the European Southern Observatory (ESO). Its calibration and test are two important phases occurring before the system is mounted on a telescope.

The objective of the work described in this thesis was to develop new calibration strategies and test tools for MCAO, and to validate them on MAD. First, a new kind of telescope and turbulence simulator MAPS (Multi-Atmospheric Phase screens and Stars) has been produced, and is now intensively used to evaluate the performances of MAD in the laboratory under realistic turbulence conditions. It has been designed, integrated, tested and fully characterized in the framework of this PhD thesis.

In the second part is described an innovative way of correcting for the on-axis and field-dependant Non-Common Path Aberrations (NCPA) present in the optical path of an MCAO instrument. The theoretical aspects are described, the practical implementation is discussed and results obtained on MAD are presented.

Finally, in the third part is proposed a method simplifying the heavy process of Interaction Matrix (IM) calibration for an MCAO system, and simulations demonstrate the validity of the method before it is applied to MAD.

The experience acquired during the calibration and test of MAD will be a baseline for the next generation of AO instruments on current observatories and future Extremely Large Telescopes (ELT).

Keywords: MULTI CONJUGATE ADAPTIVE OPTICS, PHASE DIVERSITY, NON-COMMON PATH ABERRATIONS, INTERACTION MATRIX CALIBRATION, ATMOSPHERIC TURBULENCE, PHASE SCREEN

Titre : Outils d'étalonnage et de test pour les systèmes d'OAMC : Application au démonstrateur MAD de l'ESO

Résumé :

L'Optique Adaptative Multi Conjuguée (OAMC) est une technique récente qui a pour but de corriger en temps réel les effets de la turbulence atmosphérique sur les images astronomiques, et ceci sur un champ relativement étendu. Le démonstrateur MAD est un prototype actuellement en développement dans les laboratoires de l'ESO. Son étalonnage et test sont deux phases importantes qui se dérouleront avant que le système ne soit installé sur le télescope.

L'objectif du travail décrit dans cette thèse fut de développer de nouvelles stratégies de calibration et outils de test pour l'OAMC, et de les valider sur MAD. Tout d'abord, un nouveau genre de simulateur de télescope et de turbulence MAPS a été réalisé, et est actuellement utilisé intensivement pour évaluer les performances de MAD en laboratoire sous des conditions de turbulence réalistes. Il a été conçu, intégré et testé au cours de cette thèse.

Dans la seconde partie est décrite une méthode innovante pour corriger les aberrations non communes sur axe et dans le champ d'un système d'OAMC. Les aspects théoriques y sont décrits, la mise en œuvre pratique discutée, et les résultats obtenus sur MAD sont présentés.

Finalement, dans la troisième partie est proposée une méthode simplifiant les lourds processus d'étalonnage des matrices d'interaction en OAMC, et des simulation démontrent la validité de la méthode avant qu'elle ne soit appliquée à MAD.

L'expérience acquise durant les étalonnages et tests de MAD serviront de base pour la prochaine génération d'instruments d'OA sur les observatoires actuels ou sur de futurs très grands télescopes.

Mot Clés: OPTIQUE ADAPTATIVE MULTI-CONJUGUEE, DIVERSITE DE PHASE, ABERRATIONS NON COMMUNES, ETALONNAGE DE MATRICE D'INTERACTION, TURBULENCE ATMOSPHERIQUE, ECRAN DE PHASE

Acknowledgements

My first thanks go naturally to my thesis advisor Gérard Rousset and to my supervisor at ESO Enrico Marchetti, who made me benefit from their great experience during those three years. The day to day collaboration with Enrico has been extremely enriching, and although we were far apart, the meetings with Gérard were always fruitful and leading to new and unexpected ideas.

Thanks also to Benoit Mosser and Alain Abergel for giving me the chance of following their “DESS”. Those 6 months spent in Meudon put me in the tracks I am following now.

Of course I cannot forget all the members of the AO group at ESO, past and present, for the good working mood they create, their support and their precious advices.

Thanks to Michel Tallon and Roberto Ragazzoni for accepting the functions of reporter, and to Laurence Rezeau for accepting to be the president of the jury.

Thanks to my parents and all my family for their support through all those years spent away from them.

Finally I would like to thank the friends I met in Munich for all the great moments we spent together: Raphaël, Romuald, Rudolf, Nicolas, Frédéric and the others.

To all, thanks a lot.

This work has been partially funded by the European Research and Training Network “Adaptive Optics for Extremely Large Telescopes” with Contract HPRN-CT-2000-00147.

Table of contents

Acknowledgements.....	5
Table of contents	7
Acronyms	11
Summary in French / Résumé en français	13
Introduction	13
L'Optique Adaptative	13
L'Optique Adaptative Multi Conjuguée (OAMC)	14
Le Démonstrateur d'OAMC	15
MAPS, un générateur de turbulence pour OAMC.....	16
Présentation	16
Conception	16
Ecrans de phase.....	17
Correction des aberrations statiques.....	18
Présentation	18
Correction des aberrations grâce à une matrice d'interaction	19
Correction des aberrations de champ.....	21
Application au contrôle de l'optique active de OWL.....	22
Interpolation de Matrices d'interaction	23
Problématique.....	23
Simulations en boucle ouverte.....	23
Simulations en boucle fermée.....	24
Conclusion et perspectives	25
1. Introduction	29
2. From classical AO to MAD.....	31
2.1. Adaptive Optics.....	31
2.1.1. Principle	31
2.1.2. Limitation	32
2.1.3. Application	33
2.2. Multi Conjugate Adaptive Optics (MCAO).....	34
2.3. The MCAO Demonstrator.....	36
2.3.1. General overview	36
2.3.2. Opto-mechanical layout	36
2.3.3. Wave Front Sensors	38
2.3.4. Deformable Mirrors	40
2.4. Useful notions.....	42
2.4.1. The Zernike polynomials.....	42
2.4.2. Atmosphere models.....	43
2.4.3. SHWFS	44
2.4.4. Calibration of a single-AO system.....	45
2.4.5. Strehl Ratio computation.....	47
3. MAPS, a turbulence generator for MCAO	50
3.1. Former systems / need for MAPS	50
3.2. MAPS concept.....	52

3.3.	Opto-mechanics	53
3.3.1.	MAPS design	53
3.3.2.	Alignment	54
3.3.3.	Optical quality testing	56
3.3.4.	Side effects.....	58
3.3.5.	Light source system.....	59
3.4.	Phase Screens	63
3.4.1.	General Assumptions	63
3.4.2.	Designing the Phase maps	63
3.4.3.	Testing the phase maps.....	66
3.4.4.	Optical specifications	72
3.4.5.	Prototyping with SMOS	74
3.4.6.	Prototyping with SILIOS.....	77
3.4.7.	Final screens testing.....	82
3.5.	Conclusion / Discussion	88
4.	Correction of the static aberrations	91
4.1.	Presentation of the problem	91
4.2.	Phase diversity	92
4.3.	NACO	95
4.4.	MAD	96
4.5.	Correction of the static aberrations using a calibration matrix.....	98
4.5.1.	Correction of the NCPA in NACO	98
4.5.2.	Improvement / Analogy with AO calibration	99
4.5.3.	Building of the IM	99
4.5.4.	Critical parameters for recording a good IM: aberrations subtraction	100
4.5.5.	Critical parameters for recording a good IM: amplitude of the modes to apply	101
4.5.6.	Critical parameters for recording a good IM: Number of Zernike polynomials produced by the DM.....	102
4.5.7.	Correction.....	103
4.5.8.	Iterations	104
4.6.	Application to MAD	105
4.6.1.	Dummy mirrors.....	106
4.6.2.	Best criterion for the image quality	107
4.6.3.	Ghosts of the ITC.....	108
4.6.4.	Building of the IM	109
4.6.5.	Correction.....	110
4.6.6.	MAD + visible camera	111
4.6.7.	Discussion.....	113
4.7.	Improvements: close loop corrections	114
4.7.1.	Description	114
4.7.2.	Experiment on BOA	116
4.7.3.	MAD + ITC	125
4.8.	Aberrations correction in the Field of View	126
4.8.1.	Idea.....	126
4.8.2.	Theoretical background about tomography	127

4.8.3.	Application to the correction of static aberrations, practical implementation.....	128
4.8.4.	Simulations.....	130
4.8.5.	Application to MAD.....	134
4.9.	Application to the Active optics of OWL.....	138
4.9.1.	Introduction	138
4.9.2.	Simulation tool	139
4.9.3.	Results	140
4.10.	Discussion	144
5.	Interaction Matrix interpolation	145
5.1.	Problematic.....	145
5.2.	SCAO open loop simulations.....	147
5.2.1.	Simulation tools	147
5.2.2.	Simulations outline	150
5.2.3.	Interpolation methods	152
5.2.4.	Size and geometry of the grid.....	154
5.2.5.	Simulation results	155
5.3.	MCAO closed loop simulations	157
5.3.1.	Outline	158
5.3.2.	Calibration.....	158
5.3.3.	Correction.....	160
5.3.4.	Results	161
5.4.	Discussion	162
6.	Conclusion and perspectives.....	164
7.	Bibliography	167
8.	Appendices	174
8.1.	The shape of the Zernike polynomials	174
8.2.	SPIE paper “MAPS, a turbulence simulator for MCAO”	176
8.3.	SPIE paper “Calibration of the static aberrations in an MCAO system” 189	
8.4.	Example test report from SILIOS.....	201
8.5.	The Infrared cameras of MAD.....	202

Acronyms

ADC	Atmospheric Dispersion Compensator
ADONIS	ADaptive Optics Near Infrared System
AM	Active Mirror
AO	Adaptive Optics
a.u.	arbitrary units
BOA	Banc d'Optique Adaptative
CAMCAO	CAmera for MCAO
CAOS	Code for Adaptive Optics Systems
CFHT	Canada-France-Hawaii Telescope
CM	Control Matrix
COME-ON	Cge Observatoire de paris-MEudon ONera
CONICA	COudé Near Infrared Camera
CRIRES	CRyogenic high-resolution IR Echelle Spectrograph
DIMM	Differential Image Motion Monitor
DM	Deformable Mirror
DOTA	Département d'Optique Théorique et Appliquée
ELT	Extremely Large Telescope
ESO	European Southern Observatory
FoV	Field of View
FWHM	Full-Width at Half Maximum
GALACSI	Ground Atmospheric Layer Adaptive Corrector for Spectroscopic Imaging
GLAO	Ground Layer Adaptive Optics
GRAAL	GRound layer Adaptive optics Assisted with Lasers
GS	Guide Star
HAWK-I	High Acuity Wide field K-band Imager
IF	Influence Function
IM	Interaction Matrix
IP	Internal Product
IR	InfraRed
IRACE	InfraRed Array Control Electronics
ITC	Infrared Test Camera
LO	Layer-Oriented
MACAO	Multi-Application Curvature Adaptive Optics
MAD	McAo Demonstrator
MAP	Maximum A Posteriori
MAPS	Multi-Atmospheric Phase screens and Stars
MCAO	Multi Conjugate Adaptive Optics
MUSE	Multi Unit Spectroscopic Explorer
NACO	NAos-CONica
NAOS	Nasmyth Adaptive Optics System
NCPA	Non-Common Path Aberration
NGS	Natural Guide Star

ONERA	Office National d'Etudes et de Recherches Aérospatiales
OTF	Optical Transfer Function
OWL	Overwhelmingly Large telescope
PS	Phase Screen
PSF	Point Spread Function
PTV	Peak To Valley
PUEO	Probing the Universe by Enhanced Optics
RTC	Real-Time Computer
SCAO	Single Conjugate Adaptive Optics
SHU	Shack-Hartmann Unit
SHWFS	Shack-Hartmann Wave Front Sensor
SINFONI	Spectrograph for INtegral Field Observations in the Near Ir
SNR	Signal to Noise Ratio
SO	Star-Oriented
SR	Strehl Ratio
SVD	Singular Values Decomposition
TBD	To Be Defined
TG	Turbulence Generator
TSVD	Truncated SVD
VLT	Very Large Telescope
VLTI	VLT Interferometer
WFS	Wave Front Sensor
Φ D	Phase Diversity

Summary in French / Résumé en français

Introduction

L'Optique Adaptative

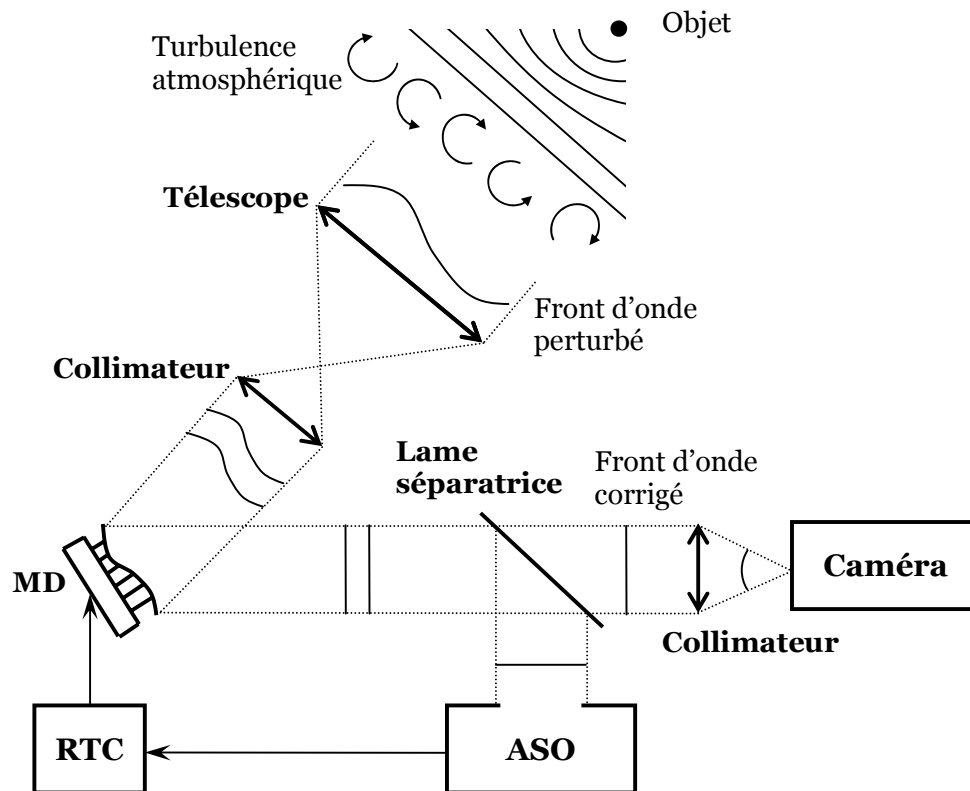
Depuis plus d'un siècle, les progrès technologiques ont permis de construire des télescopes de plus en plus grands, jusqu'à atteindre des diamètres de 8 à 10 mètres dans les dernières années. Le pouvoir de concentration de la lumière a augmenté avec la surface du télescope, et avec l'aide de la qualité des optiques et des revêtements, les astronomes ont eu accès aux objets les plus faibles du ciel nocturne.

Cependant, un autre avantage qu'on l'on pourrait attendre de ces grands diamètres est un accroissement de la résolution, mais malheureusement celle-ci est limitée dans le visible à la résolution d'un télescope de quelques dizaines de centimètres seulement. La raison en est la turbulence dans l'atmosphère terrestre qui, dans les derniers kilomètres avant qu'il n'atteigne le sol, perturbe le front d'onde venant d'un objet astronomique, après qu'il aie traversé inchangé parfois des milliards d'années-lumière.

Depuis que cet effet est connu, des méthodes ont été proposées pour restaurer a posteriori la haute résolution angulaire de l'objet. L'optique Adaptative (OA) est une autre solution qui consiste à mesurer et corriger en temps réel les aberrations dans le front d'onde incident. La plupart des grands télescopes sont maintenant équipés d'instruments d'OA, qui leur permettent d'attendre la limite de diffraction permise par leur diamètre.

La prochaine génération de systèmes d'OA est en cours de conception. Leurs buts sont l'amélioration des performances de la correction (OA extrême) et/ou l'extension de la taille du champ corrigé (OA Multi Conjuguée), normalement limité par le phénomène d'anisoplanétisme, tout en s'accommodant des contraintes liées à l'utilisation de grand télescopes, en particulier la limitation du temps nocturne utilisé pour l'étalonnage et les tests de l'instrument.

D'une part, des améliorations peuvent être apportées grâce à une meilleure conception de l'instrument, une optimisation des algorithmes de reconstruction, la prédiction des performances par simulations... et d'autre part des problèmes purement pratiques (aberrations statiques, erreurs de calibration ...) ne peuvent être abordés qu'une fois l'instrument construit.



Description générale d'un système d'imagerie équipé d'Optique Adaptative. L'Analyseur de Surface d'Onde (ASO) mesure le résidu des perturbations, et l'ordinateur en temps réel (« Real-Time Computer » = RTC) le converti en tensions à appliquer au Miroir Déformable pour avoir une image corrigée de la turbulence sur la caméra d'imagerie.

L'Optique Adaptative Multi Conjuguée (OAMC)

L'OAMC est une généralisation de l'OA classique, dont la limitation principale vient du fait que le seul MD du système est conjugué avec un plan pupille, et donc ne peut corriger la turbulence qui est produite en altitude de l'atmosphère et qui est responsable du phénomène d'anisoplanétisme. Dans ce cas, la minimisation de phase est faite dans la pupille pour une direction, et appliquée à tout le champ, ce qui résulte en une dégradation des performances en fonction de la position angulaire dans le champ.

Le concept de l'OAMC est d'analyser et de corriger la turbulence dans son volume. Cela implique :

- Plusieurs étoiles guide (et donc plusieurs ASO) permettant de mesurer la phase dans plusieurs directions du champ
- Un algorithme de reconstruction qui déduit la phase dans le volume de l'atmosphère
- Plusieurs Miroirs Déformables conjugués à différentes altitudes.

A partir des mesures dans plusieurs directions, la phase dans le volume de la turbulence est reconstruite, et la correction appropriée est appliquée à chaque

MD. Si le nombre de senseurs est suffisant et la reconstruction bien faite, il en résulte une correction uniforme dans la champ de vue de l'instrument.

Le Démonstrateur d'OAMC

Le démonstrateur d'OAMC MAD est un prototype de la prochaine génération d'instruments d'OA. Il est développé par l'Organisation Européenne de recherches astronomiques dans l'hémisphère austral (« European Southern Observatory » = ESO) et son but est de démontrer la faisabilité de l'OAMC sur le ciel, dans le cadre du développement des instrument de seconde génération pour le VLT (« Very Large Telescope ») et pour un futur grand télescope Européen, de 30 à 100 mètres de diamètre. C'est un banc de test remarquable pour l'expérimentation de nouveaux concepts d'OA.

MAD, comme tout autre instrument, doit être testé en laboratoire avant d'être monté sur un télescope. Cette opération est facilitée par l'utilisation d'un générateur de turbulences, un outil qui reproduit les effets de la turbulence atmosphérique sur le front d'onde reçu par le télescope. Celui de MAD a été baptisé MAPS (« Multi-Atmospheric Phase screens and Stars » = Multiples étoiles et écrans de phase atmosphériques). Il sera utilisé intensivement dans les laboratoires de l'ESO pour caractériser et optimiser les performances de MAD avant qu'il ne soit installée au foyer du télescope. Toutes les phases de son développement, de la conception à l'assemblage et aux tests, ont eu lieu dans le cadre de cette thèse, et sont détaillés dans le chapitre 3.

En ce qui concerne les performances, on s'attend à ce que la qualité d'un instrument soit fortement liée à la qualité de ses optiques. Quand on souhaite atteindre des performances élevées, les aberrations statiques de l'instrument lui-même deviennent une limitation. Elle sont évidemment réduites par conception et alignement, mais pour la nouvelle génération d'instruments contenant de nombreuses optiques et transmettant un large champ de vue, elles ne peuvent être négligées. En Optique Adaptative, nous avons la chance d'avoir un Miroir Déformable (MD) dans le chemin optique pour les compenser. Les aberrations communes aux voies d'imagerie et d'analyse sont corrigées par la boucle d'asservissement, mais la qualité des images au niveau de l'instrument scientifique est encore dégradé par les aberrations non vues pas l'analyseur de front d'onde : les aberrations non communes. Dans le chapitre 4 de cette thèse est décrit comment nous avons amélioré une technique existante de correction des aberrations non communes grâce au MD du système, et étendue celle-ci à la correction des aberrations dans le champ d'un instrument d'OAMC.

L'OAMC utilise plusieurs étoiles guide dans le champ pour calculer la meilleure correction à appliquer, ce qui cause une complexification à la fois de la conception et de l'utilisation de l'instrument. En particulier, la procédure d'étalonnage (détermination de la relation entre les perturbations mesurées et la correction à appliquer) doit être répétée pour chaque nouvelle configuration d'étoiles guides. Dans le chapitre 5 de cette thèse nous proposons une méthode simplificatrice basée sur l'interpolation d'un nombre limitée de mesures d'étalonnage.

MAPS, un générateur de turbulence pour OAMC

Présentation

Les récents développements en OA et particulièrement en OAMC rendent les instruments de plus en plus complexes. Ceux-ci visent des performances et une stabilité croissantes, alors que les temps alloués sur les télescopes de classe 8 mètres sont de plus en plus précieux. En conséquence, il semble logique de vouloir tester le plus intensivement possible l'instrument en laboratoire avant de le soumettre aux conditions plus rudes de l'environnement d'un grand observatoire. C'est dans cette optique qu'ont été développés les simulateurs de télescopes et autres générateurs de turbulence.

Un simulateur de télescope peut permettre de tester l'interface (optique et/ou mécanique) de l'instrument avec le télescope, et d'évaluer l'effet de la gravitation sur les performances du système. Un générateur de turbulence quant à lui permet de tester les performances de l'instrument en laboratoire en reproduisant optiquement l'effet de la turbulence atmosphérique sur le front d'onde provenant d'un objet astronomique.

Au cours du temps plusieurs techniques ont été proposées dans le but de produire des fronts d'onde turbulents : flux d'air chaud, Miroirs Déformables, écrans à cristaux liquides, ... mais la méthode la plus réaliste et reproductible (bien que limitée à un nombre fini de réalisations) reste l'utilisation d'écrans de phase, éléments optiques utilisés en réflexion ou transmission, et au sein lesquels sont imprimées des cartes d'aberrations ayant les mêmes propriétés que l'atmosphère (spectre de Kolmogorov ou de Von Kármán). Ces écrans (souvent circulaires) sont utilisés sur une surface annulaire à leur pourtour, et mis en rotation pour simuler la(les) couche(s) d'air se déplaçant au dessus de la pupille du télescope sous l'action du vent.

Le générateur de turbulence développé pour l'instrument NACO du VLT est un modèle du genre. Il simule une étoile sur l'axe optique perturbée par la turbulence typique du ciel de Paranal grâce à 2 écrans de phase en réflexion. Dans le cadre du démonstrateur MAD de l'ESO, il a été évalué de première importance la mise au point d'un générateur de turbulence pour OAMC qui permettrait de faire des tests les plus poussés possibles en laboratoire avant d'envoyer MAD à Paranal pour validation des résultats en environnement réel. Cet outils doit permettre de simuler simultanément jusqu'à 12 étoiles dans un champ de 2 minutes d'arc, et un volume de turbulence typique du ciel de Paranal. Ainsi était lancé le développement de MAPS (Multi-Atmospheric Phase screens and Stars = « Multiples étoiles et écrans de phase atmosphériques »).

Conception

La solution retenue pour la conception optique de MAPS est 100 % transmissive : à partir de fibres sources, un bloc d'optique image la pupille du télescope (ainsi que le volume d'atmosphère au dessus), et un autre bloc permet de recréer le foyer Nasmyth du VLT. Trois écrans de phase en transmission sont conjugués à la bonne altitude et mis en rotation grâce à un système de moteurs et de courroies. Le tout est aligné sur un support mécanique qui place l'axe optique

à la hauteur de celui de MAD et qui sera lui-même aligné précisément afin de faire coïncider le plan focal de sortie de MAPS avec le plan focal d'entrée de MAD.

La fabrication des deux blocs optiques de MAPS a été confiée à la société Winlight Optics à Marseille (France). Une fois livrées, les optiques ont été testées et trouvées conformes aux spécifications.

La source d'éclairage constitue un système auxiliaire à MAPS. En effet il a fallu utiliser une source assez puissante pour simuler des étoiles de magnitude 8, en l'occurrence une lampe halogène de 150 W, et concevoir un système de relais optique permettant de simuler simultanément 4 groupes d'environ 8 étoiles chacun et de 4 magnitudes différentes.

Enfin les moteurs faisant tourner les écrans de phase sont équipés de boîtes de vitesses contrôlées par 3 potentiomètres indépendants permettant de régler précisément la vitesse du vent simulé à chaque altitude.

Ecrans de phase

Comme indiqué précédemment, la turbulence atmosphérique est reproduite grâce à l'utilisation d'écrans de phase.

La première étape de leur développement a consisté à simuler des cartes de phase pour chaque altitude ayant les propriétés de l'atmosphère de Paranal. Ces cartes ont ensuite été testées pour vérifier qu'elles produisaient bien les effets escomptés sur les images et les front d'ondes, plus précisément la largeur à mi-hauteur d'images longue pose, la variance du front d'onde, et l'évolution de ces deux paramètres avec la longueur d'onde.

Une fois les cartes définies, il a fallu trouver parmi un nombre limité de fournisseurs potentiels celui qui fabriquera les écrans les plus proches de ceux définis par les spécifications de l'ESO, en tenant compte aussi du prix unitaire des écrans. Après une phase de prototypage, la meilleure solution a été trouvée chez SILIOS qui proposait de fabriquer les écrans par gravure ionique sur verre.

Une commande groupée de 23 écrans de phase a été placée, et 9 mois plus tard toutes les pièces étaient délivrées. La qualité de production des pixels individuels des écrans a été testée grâce à un profilomètre. Les propriétés statistiques de la turbulence ont été évaluées quant à elles de la même manière que pour les cartes de phase simulées, c-à-d par calcul de la variance des fronts d'onde mesurés projetés sur les polynômes de Zernike, ou par évaluation directe de la largeur à mi-hauteur d'images longue pose du spot turbulent, à différentes longueurs d'onde.

Ce travail a permis de comparer les écrans réels aux écrans simulés et ainsi de valider la technique de fabrication. De plus, cela a apporté une grande connaissance dans le domaine de la conception et fabrication d'écrans de phase en transmission pour des télescopes de classe 8 mètres. Enfin, nous en sommes venus à souligner une fois de plus l'importance de l'échelle externe de la turbulence, même si celle-ci a une valeur 3 fois supérieure au diamètre du télescope. Les conséquences en sont importantes sur les relations entre le Seeing et la largeur à mi-hauteur d'images longue pose, et cela nous oblige à être prudent lors de la caractérisation de turbulence, atmosphérique ou bien produite par des écrans de phase en laboratoire.

Correction des aberrations statiques

Présentation

Malgré tous les efforts faits au niveau de la conception, fabrication ou alignement d'un instrument d'OA, il reste toujours un certain niveau d'aberrations statiques qui dégradent le front d'onde. Si celles-ci se trouvent dans la voie commune de l'instrument, elles sont vues par l'Analyseur de Surface d'Onde (ASO) et donc corrigées par la boucle d'asservissement (dans la limite des fréquences spatiales corrigées par le système) comme le sont les distorsions de front d'onde engendrées par l'atmosphère.

Cependant dans tout système d'OA, la voie optique commune se sépare entre une voie d'analyse et une voie dite scientifique. Si les aberrations statiques se trouvent après cette séparation (souvent matérialisée par une lame dichroïque), elles sont soit non vues par l'ASO et donc restent présentes dans la voie scientifique, soit vues et corrigées par l'ASO et donc introduites injustement dans la voie scientifique. Dans les deux cas, la conséquence est une dégradation de la qualité du front d'onde dans cette dernière. En effet la boucle d'OA a pour but de produire un front d'onde le plus plan possible au niveau de l'ASO, ce qui n'est pas synonyme d'un front d'onde plan au niveau de l'instrument.

Cet effet indésirable peut être compensé par une utilisation de l'ASO en boucle fermée autour de valeurs de référence appropriées. L'obtention de ces valeurs de référence passe par 2 étapes :

- Mesures des aberrations dans la voie scientifiques
- Correction appropriée des aberrations

Dans le cas où l'instrument placé dans la voie scientifique est un imageur, la solution proposée ici est de l'utiliser comme un ASO en plan focal grâce à la technique de diversité de phase.

Le diversité de phase permet, grâce à un couple d'images séparées par une quantité connue d'aberrations, de reconstruire le front d'onde en amont des images. Dans le cas de l'algorithme que nous utilisons et qui a été développé à l'ONERA, la seconde image est obtenue en introduisant une quantité connue de defocus dans le chemin optique, et les aberrations estimées sont projetées sur les polynômes de Zernike.

La mesure des aberrations à l'endroit où elles doivent être corrigées (sur le détecteur de la caméra d'imagerie) élimine le phénomène d'aberrations non vues. Cette méthode a précédemment été implémentée sur le système NAOS-CONICA (NACO) pour le VLT. Dans ce cas, les aberrations non vues étaient estimées par diversité de phase et la correction était appliquée en changeant les pentes de référence de l'ASO, et donc la forme de référence du Miroir Déformable en boucle fermée. Le lien entre les aberrations mesurées et les pentes de référence était déterminé par l'application d'un modèle du système ASO-MD.

Dans cette thèse nous proposons une méthode de mesure permettant de remplacer l'utilisation de ce modèle par une matrice de contrôle, inverse généralisée d'une matrice d'interaction mesurée.

Correction des aberrations grâce à une matrice d'interaction

Pour simplifier, le modèle utilisé dans le cas de NACO lie les aberrations mesurées et projetées sur les polynômes de Zernike avec les modes produits par la surface du MD (par l'intermédiaire des pentes de référence associées, étant donné que la correction se fait lorsque la boucle d'OA est fermée). Une liste d'aberrations mesurée multipliée par ce modèle donne la combinaison linéaire des modes à appliquer au MD pour les corriger.

L'idée que nous avons cherché à appliquer est de remplacer ce modèle par une mesure de la réponse de la camera à des actuations du MD. Pour cela, il faut produire successivement des modes du MD, et analyser les aberrations qu'ils créent au niveau de l'image par diversité de phase. Ceci étant fait pour des modes appliqués en valeur positive et négative, il est possible par soustraction de séparer la contribution du mode seul. Cette opération est répétée pour plusieurs modes, et permet de construire ce que nous appelons la matrice d'interaction IM entre les N_m modes produit par le Miroir Déformable et les N_z polynômes de Zernike estimés par diversité de phase :

$$N_z \begin{bmatrix} \text{IM} \end{bmatrix} = \begin{bmatrix} \begin{bmatrix} M_1 \end{bmatrix} & \begin{bmatrix} M_2 \end{bmatrix} & \begin{bmatrix} M_3 \end{bmatrix} & \dots & \begin{bmatrix} M_{N_m} \end{bmatrix} \end{bmatrix}$$

Cette matrice est factorisée par décomposition en valeurs singulières, et inversée pour obtenir la matrice de contrôle CM :

$$N_m \begin{bmatrix} \text{CM} \end{bmatrix} = \text{IM}^+$$

où A^+ dénote l'inverse généralisée de la matrice A .

Enfin, une liste d'aberrations « Ab » mesurée (et projetée sur les N_z premiers polynômes de Zernike) multipliée par CM donne la combinaison linéaire des modes à appliquer au MD pour les corriger :

$$N_m \begin{bmatrix} \text{Corr} \end{bmatrix} = - \begin{bmatrix} \text{CM} \end{bmatrix} \times \begin{bmatrix} Ab \end{bmatrix}$$

Après une première correction, le processus peut être répété plusieurs fois dans le but d'atteindre un niveau résiduel d'aberrations de plus en plus bas.

Cette méthode a été appliquée avec succès à la correction des aberrations non communes sur l'axe optique de MAD, bien que cet instrument d'OAMC ne soit pas le plus approprié à une correction efficace des aberrations sur l'axe (faible nombre d'actuateurs, aberrations de champ prédominantes).

La première étape consiste à déterminer les paramètres importants pour une bonne estimation des aberrations par diversité de phase :

- Qualité, amplitude et nombre des modes produits par le MD à appliquer.
- Qualité des images enregistrées : bruit, échantillonnage, présence d'images secondaires.

Dans le cas de MAD, les images sont prises grâce à une caméra infrarouge de test (« Infrared Test Camera » = ITC) équipée d'un filtre à bande étroite centrée autour de 2200 nm de longueur d'onde.

La correction des aberrations statiques de MAD qui est présentée dans cette thèse a été faite alors que le Miroir Déformable d'altitude était remplacé par un miroir plan, dans le but de tester MAD comme un système d'OA classique sur axe. La quantité d'aberrations statiques est estimée par l'intermédiaire du rapport de Strehl mesuré sur les images de la caméra. Il était de 83.2 % et a été élevé à hauteur de 93.4 % après application de la technique détaillée plus haut.

En plus de la qualité des images obtenues après correction, un autre point remarquable est la rapidité avec laquelle la technique peut être mise en place et appliquée. En effet il suffit d'être capable d'appliquer des modes au MD, l'algorithme de diversité de phase se charge d'estimer les aberrations présentes dans les images, et la matrice de calibration prends en compte toutes les spécificités du système (désalignements, rotation entre le détecteur et le MD, fonctions d'influence du MD) qui doivent au contraire être finement ajustées lors de l'utilisation d'un modèle.

La facilité d'implémentation de cette technique a été prouvée à deux autres reprises :

- Sur le banc MAD équipé d'une caméra visible et d'un filtre à 1064 nm, utilisée lorsque l'ITC n'était pas disponible. Une matrice d'interaction a été mesurée malgré les contraintes liées à la faible longueur d'onde, et les aberrations ont été en partie corrigées (rapport de Strehl passant de 14 à 44 % à cette longueur d'onde).
- Sur le Banc d'Optique Adaptative (BOA) de l'ONERA. Une expérience organisée sur ce banc a permis de combiner notre méthode de correction des aberrations avec la stabilité du banc et l'expérience acquise sur celui-ci depuis des années. Le rapport de Strehl initial était de 76.2 % à 633 nm, et il fut élevé à 96 %. Cette expérience nous a aussi énormément appris sur les limitations de la méthode (nombre de modes corrigés, qualité de la matrice d'interaction) et sur les améliorations possibles (stabilité apportée par le fait de travailler en boucle fermée).

Correction des aberrations de champ

De la même façon que les performances d'un système d'OA classique sont limitées par l'anisoplanétisme atmosphérique, la correction des aberrations statiques décrite plus haut est valide seulement sur l'axe optique et laisse les bords du champ dégradés par les aberrations de champ des optiques. Cet effet devient important en OAMC, technique qui vise à fournir une performance la plus uniforme possible dans un large champ.

Il a été observée sur MAD une perte de plus de 5 % en rapport de Strehl absolu sur les bords du champ par rapport au centre quand la correction des aberration sur l'axe est appliquée.

Une solution possible pour uniformiser le résidu des aberrations est inspirée de la correction de la couche au sol en OA (« Ground Layer Adaptive Optics » = GLAO). Les aberrations sont mesurées dans plusieurs directions dans le champ de vue, la correction à appliquer est calculée et moyennée pour toutes les directions, corrigeant ainsi la contribution commune à toutes, qui est assimilée à la contribution de la couche de turbulence au niveau du sol en OA.

Dans un système d'OAMC comme MAD, nous avons à notre disposition un MD conjugué à une différente altitude pour corriger ces aberrations de champ. La méthode est cette fois-ci inspirée par la correction du volume de la turbulence en OAMC : les aberrations sont mesurées dans plusieurs directions, reconstruites par tomographie aux altitudes où on estime qu'elles se trouvent, et projetées sur les altitudes des Miroirs Déformables pour être corrigées.

Pour notre application il n'y a pas plusieurs ASO, mais une seule camera qui enregistre les images de diversité (donc non limitées en nombre). Les altitudes où se trouvent les aberrations ne sont pas des couches atmosphériques, mais les altitudes équivalentes auxquelles sont conjuguées les optiques aberrantes. Enfin les propriétés statistiques du bruit de mesure et du spectre de la turbulence ne sont pas ici d'une aussi grande importance.

L'application de cette méthode requière la construction d'une méta-matrice d'interaction entre les différentes directions d'analyse et les différents Miroirs Déformables. Celle-ci est engendrée en agissant successivement sur les actuateurs des MDs et en mesurant la réponse sur le détecteur de la camera (images focalisée et defocalisée pour analyse par diversité de phase). La partie correspondant au miroir dans la pupille est identique dans toutes les directions, alors que celle correspondant au miroir d'altitude (8.5 km dans le cas de MAD) est différente pour chaque position, étant donné que l'empreinte du faisceau est différente sur la surface de ce miroir.

La méthode la plus simple est alors d'inverser directement cette méta-matrice. La matrice résultante multipliée par les aberrations mesurées dans le champ donne directement la combinaison de modes à appliquer au MDs.

Une méthode plus élaborée consiste à analyser les modes mesurés par tomographie (ce qui revient à une simple multiplication matricielle en fait). Les aberrations mesurées sont elles aussi analysées par tomographie, et la meilleure correction peut ainsi être calculée miroir par miroir.

L'algorithme de reconstruction que nous avons mis au point a été validé par des simulations qui incluaient l'ajout de défauts sur différentes optiques à différents niveaux, la mesure des aberrations dans plusieurs directions, et leur

analyse par tomographie. La correction s'est avérée efficace, et un système de poids sur les directions de mesure permet d'améliorer encore l'uniformité des aberrations résiduelles dans le champ de 2 minutes d'arc.

La correction des aberrations dans le champ n'a malheureusement pas pu être testée sur MAD, mais le sera dès que le banc sera fonctionnel dans sa configuration OAMC.

Application au contrôle de l'optique active de OWL

Depuis quelques années, l'ESO développe des concepts pour un futur très grand télescope : OWL. Le train optique de celui-ci est constitué de 6 miroirs, dont 2 segmentés, et 2 adaptatifs conjugués à des altitudes de 0 et 8 km pour être utilisés par des instruments d'OA et d'OAMC. Parmi les 6 miroirs, tous sont actifs et 3 sont conjugués avec le plan pupille (0 km), les autres étant à 0.25, 2 et 8 km.

L'optique active d'un télescope est le système qui permet de contrôler la courbure du (des) miroir(s) pour lui (leur) donner la forme la plus proche de celle parfaite, et aussi compenser les déformations due à la gravité en temps réel (à une fréquence de l'ordre du Hertz). Dans le cas de OWL, les miroirs actifs sont conjugués à différentes altitudes, donc il est logique d'essayer d'appliquer la méthode de reconstruction présentée précédemment au contrôle de ces miroirs.

Ici les senseurs seront des ASO déployés dans le plan focal du télescope, et le nombre de miroirs à contrôler sera compris entre 1 et 3 (les miroirs dans le plan pupille sont considérés comme un seul pour simplifier). En utilisant une version modifiée de l'algorithme présenté dans la partie précédente, nous avons simulé la présence d'aberrations sur 1 à 3 des miroirs actifs, l'analyse (supposée parfaite) dans 1 à 5 directions, la reconstruction par tomographie et enfin la correction des défauts mesurés, éventuellement après plusieurs itérations.

Les résultats de ces simulations préliminaires sont que :

- 1 étoile guide et 1 itération sont requises pour contrôler 1 miroir conjugué à 0 ou 2 km d'altitude
- 3 étoiles guide et 3 itérations pour 1 miroir à 8 km
- 3 étoiles guide et 2 itérations pour 2 miroirs à 0 et 2 km
- 3 étoiles guide et 3 itérations pour 2 miroirs à 0 et 8 km
- il n'est pas possible de contrôler 3 miroirs à 0, 2 et 8 km simultanément, peu importe le nombre l'étoiles guide ou d'itérations.

Si nécessaire, cette étude devra être complétée par des simulations plus précises, incluant des modèles d'ASO et de MD par exemple.

Interpolation de Matrices d'interaction

Problématique

Dans un système d'OAMC basé sur des étoiles guide naturelles (non laser), la configuration de celles-ci change d'une cible scientifique à une autre. Si l'analyse des fronts d'onde se fait avec un senseur par direction (façon « star-oriented »), cela signifie que les ASO doivent se déplacer pour aller chercher l'étoile source.

Une autre conséquence concerne la matrice d'interaction du système. Celle-ci regroupe la réponse des ASO à l'excitation des électrodes des Miroirs Déformables. Pour un miroir situé en altitude, l'empreinte du faisceau est différente dans la méta-pupille pour différentes positions d'étoile guide, et donc une matrice d'interaction doit être enregistrée par étoile.

Dans cette partie de la thèse nous souhaitons trouver une solution alternative qui éviterai d'avoir à répéter l'étalonnage du système à chaque nouvel astérisme d'étoiles. L'idée proposée est de mesurer réellement les matrices d'interaction pour un nombre fini de directions dans le champ, et d'interpoler ces mesures à n'importe quelle combinaison d'étoiles. Cette approche est certaine de fonctionner pour une grille de point suffisamment serrée, aussi la question est de déterminer l'espacement optimal entre les points de cette grille qui, après interpolation, n'engendre pas de perte de performance remarquable. Le nombre de points de mesure peut encore être réduit grâce à l'utilisation d'un algorithme d'interpolation optimisé.

La méthode décrite ici a été testée et validée grâce à des simulations, premièrement assez simples et en boucle ouverte, puis plus complètes en boucle fermée, et sera appliquée au banc MAD durant sa phase de tests.

Simulations en boucle ouverte

Ces simulations ont été faites grâce à des modèles de Miroirs Déformables et d'ASO sous Matlab. Le Miroir Déformable d'altitude (le seul simulé) prend en compte les fonctions d'influences mesurées sur le vrai miroir. L'ASO de type Shack-Hartmann quant à lui a les mêmes caractéristiques que celui utilisé sur MAD, et sa réponse a été comparée à celle fournie par des mesures sur le banc.

Dans ces simulations, une matrice d'interaction est mesurée pour chaque point d'une grille de positions dans le champ. Des directions d'analyse sont choisies aléatoirement et pour chacune, l'ASO est soumis à une série de fronts d'onde turbulents. Après multiplication par la matrice de contrôle (mesurée ou interpolée), le miroir déformable corrige les aberrations vues. La qualité de la correction est moyennée sur une centaine de réalisations de la turbulence. La variance du front d'onde résiduel est comparée entre l'utilisation de la matrice mesurée et de celle interpolée. Si la différence est négligeable, l'échantillonnage de la grille peut être élargi.

Ces simulations nous ont permis de trouver une géométrie de grille composée de 53 points de mesure et de perfectionner l'algorithme d'interpolation pour qu'il donne de bons résultats dans tout le champ.

Simulations en boucle fermée

Forts des résultats obtenus en boucle ouverte avec une seule étoile guide, nous sommes passés à une simulation plus complète d'un système d'OA. En fait il s'agit du code qui a été écrit pour simuler les performances de MAD. Grâce à sa procédure d'étalonnage, les matrices d'interaction sont mesurées dans différentes directions du champ. Elles sont ensuite interpolées grâce au même algorithme que précédemment, et combinées de façon à former la méta-matrice d'interaction d'OAMC (regroupant les matrices individuelles entre les 3 ASO et les 2 miroirs).

La simulation de la boucle fermée est alors lancée avec soit la méta-matrice mesurée dans cette configuration, soit celle interpolée. La qualité de la correction de la turbulence est estimée en terme de rapport de Strehl sur une ligne de points d'évaluation en travers du diamètre du champ. Les résultats montrent comme prévu en OAMC une correction plus ou moins uniforme suivant l'éloignement des étoiles guides et leur positions relatives. La perte relative de Strehl maximale dans le champ est utilisée pour évaluer l'impact de l'interpolation sur les performances. Pour une grille de 33 points, nous avons observée une perte maximale inférieure à 1 %.

L'étape suivante consistera à appliquer l'interpolation des matrices d'interaction sur le banc MAD, ce qui nous permettra d'étudier l'impact de tous les paramètres qui n'ont pu être simulés tels que les erreurs de mesure des matrices d'interaction, les désalignements possibles, ...

Conclusion et perspectives

L'objectif du travail présenté dans cette thèse était de développer de nouvelles stratégies d'étalonnage et de test pour les systèmes d'OAMC. Le démonstrateur d'OAMC MAD construit par l'ESO est le premier instrument de ce genre, ce qui en fait le support parfait pour l'application de nouveaux concepts.

Dans le but de tester MAD en laboratoire, nous avons réalisé un nouveau type de simulateur de télescope et de générateur de turbulence : MAPS. L'innovation principale dans cet outil est l'utilisation d'écrans de phase en réflexion qui sont quasi-achromatiques entre 500 et 2500 nm. Ceci est très important car le front d'onde est mesuré grâce aux ASO dans le visible, mais les performances de l'instrument sont évaluées dans le proche infrarouge, et donc le chromatisme de la turbulence produite par les écrans pourrait résulter en une estimation biaisée des performances mesurées en laboratoire. Dans le cadre de cette thèse, les écrans de phase ont été soigneusement conçus, fabriqués, et caractérisés avant d'alimenter l'instrument d'OAMC avec un front d'onde reproductible et étalonné.

MAPS est utilisé intensivement pour caractériser et améliorer les performances de MAD. Le même concept d'écrans de phase est déjà envisagé pour de futurs générateurs de turbulence à l'ESO, dans le cadre des bancs de test APE (« Active Phasing Experiment ») et HOT (« High Order Test bench »), du système d'OA GALACSI pour le VLT, des concepts d'instruments d'OA pour OWL, et aussi dans d'autres observatoires comme le GTC. Les leçons tirées de l'utilisation des écrans de phase de MAPS sont utilisées pour mieux concevoir la prochaine génération d'écrans de phase et de générateurs de turbulence.

Les aberrations non communes limitent la qualité des images obtenues par la camera d'imagerie d'un instrument d'OA. La solution suggérée dans cette thèse est d'utiliser la camera elle-même comme Analyseur de Surface d'Onde en plan focal, et de compenser les aberrations statiques grâce au Miroirs Déformable présents dans le chemin optique. L'enregistrement d'une matrice d'interaction entre le(s) MD et la camera permet d'obtenir une correction efficace par simple multiplication matricielle. La procédure dans son ensemble, inspirée de la correction en temps réel de la turbulence atmosphérique en OA, est rapide et facile d'implémentation sur tout système.

Dans le cas des instruments d'OAMC, nous avons aussi montré comment utiliser une approche tomographique pour reconstruire les aberrations au niveau des optiques qui les créent, et les corriger uniformément dans le champ de vue grâce à l'utilisation des différents Miroirs Déformables.

Les limitations principales de ces techniques sont la précision de correction des aberrations par le(s) MD, et la stabilité du système entre le moment où les aberrations sont estimées et le moment où elles sont corrigées. Ces différents points n'ont pas encore été testés sur MAD, mais le seront dans un proche avenir.

Enfin, et spécifiquement à l'OAMC, nous avons testé par simulation la possibilité d'interpoler les matrices d'interaction mesurées en quelques points à tout le reste du champ. C'est une solution hybride entre la mesure de ces matrices pour chaque nouvel astérisme d'observation et l'utilisation de matrices

synthétiques, et combine en ce sens les avantages des deux : rester proche du système réel et de ses spécificités, mais aussi être flexible et automatisé pour une utilisation plus efficace de l'instrument. Dans le cas de MAD, les simulations sont prometteuses et tendent à montrer qu'un nombre relativement faible de points de mesure est suffisant pour l'interpolation de la matrice d'interaction à tout le champ.

L'efficacité de l'interpolation des matrices d'interaction peut probablement encore être améliorée en réduisant le nombre de point de mesure tout en utilisant un algorithme de reconstruction plus élaboré, qui prendrait en compte les fonctions d'influence des Miroirs Déformables par exemple. Cette technique pourrait devenir très pratique pour les futurs systèmes d'OAMC qui comprendront beaucoup plus d'actuateurs et d'analyseurs.

En parallèle à MAD, l'ESO est en train de développer ce qui est appelé le « AO facility » et qui comprend un miroir secondaire adaptatif pour le VLT, plusieurs étoiles guide laser, et la partie OA de la seconde génération d'instrument pour le VLT : GALACSI pour MUSE et GRAAL pour HAWK-I, qui sont tous deux des systèmes « GLAO ». Depuis le succès de la première génération d'instruments, le groupe d'OA de l'ESO pousse la recherche en avant pour atteindre le meilleur dans toutes les phases du développement : conception, fabrication, assemblage, étalonnage, test et optimisation.

Dans l'avenir, les temps d'observation sur les télescopes deviendront de plus en plus précieux, et alors les outils de test et d'étalonnage se devront d'être extrêmement sophistiqués pour permettre une analyse complète de l'instrument. L'ESO et d'autres instituts européens travaillent en collaboration dans le cadre du programme de recherche commun (« Framework Program 6 » = FP6) de la Commission Européenne, qui finance la recherche concernant un très grand télescope. D'autre part, l'ESO explore depuis plusieurs années des concepts pour construire un télescope de 60 à 100 mètres de diamètre OWL, et aux Etats-Unis la production d'un télescope de 30 mètres (« Thirty Meters Telescope » = TMT) a été lancée. Tous ces projets ont pour but de collecter le plus de lumière possible, mais leur avantage en terme de résolution angulaire ne peut être atteint qu' à travers l'Optique Adaptative.

SUMMARY IN FRENCH / RESUME EN FRANÇAIS

1. Introduction

For more than a century, progresses in technology allowed building larger and larger telescopes, until they reached the diameter of 8-10 meters in the last years. The light collecting power has in the same time increased with the surface of the telescope, and together with the quality of the optics and coatings produced, it helped providing astronomers with data on the faintest objects in the sky.

However, another advantage one could expect from a large aperture is an increase of the resolution, but this one limited in the visible wavelengths to the resolution of a telescope of a few tens of centimeters only. The reason for this is the turbulence in the Earth's atmosphere which, in the last kilometers before it reaches the ground, distorts the wave front coming from an astronomical object after it has traversed unchanged sometimes billions of light-years.

Since this effect is known, methods have been proposed to restore *a posteriori* the high angular resolution of the object [55] [72]. Adaptive Optics (AO) is another solution [3] that consists in measuring and correcting in real-time the aberrations in the incoming WF. Most of the largest telescopes in the world are now equipped with AO which allows reaching the diffraction limit of their aperture.

The next generation of AO systems is currently under study. Their goals are to improve the performance of the correction (Extreme AO) and/or to extend the size of the corrected Field of View (FoV) normally limited by anisoplanatism (wide field AO like Multi Conjugate AO or Ground Layer AO), while dealing with the constraints dictated by the use of large telescopes, mainly the reduction of the night-time used for commissioning and calibration of the instrument.

On one hand, enhancements can be made by a better design of the instrument, optimization of the reconstruction algorithms, prediction of the performances by simulation, ... and on the other hand there will always remain practical problems (static aberrations, calibration errors, ...) that can be dealt with only once the instrument has been built.

The MCAO Demonstrator (MAD) is a prototype for the next generation of AO instruments. It is developed by the European Southern Observatory (ESO) and its goal is to demonstrate the on-sky feasibility of MCAO, in the framework of the 2nd generation of instruments for the VLT (Very Large Telescope) and of a future European Extremely Large Telescope, of 30 to 100 meters diameter. It is an exceptional test bench for experimenting new AO concepts with their implementation difficulties and limitations.

MAD, as any other instrument, requires to be tested and evaluated in a laboratory before being mounted on a telescope. Such experimentations will be eased by the use of a Turbulence Generator (TG), a device that reproduces dynamically the effects of the atmospheric turbulence on the WF collected by the telescope. The TG of MAD has been baptized MAPS (Multi-Atmospheric Phase screens and Stars). It will be used intensively in the laboratories of ESO to characterize and enhance the performances of MAD, before installing it at the

focus of the telescope. All the phases of its development, from design to integration and test, occurred within the framework of this PhD thesis, and are detailed in the chapter 3.

Concerning performances, it is expected that the quality of an instrument is strongly linked to the quality of its optics. When one wants to reach high performances, the static aberrations introduced by the instrument itself can become a limitation. They are obviously reduced to a minimum value by a proper design and alignment, but for the new generation of instruments containing numerous optics and/or accommodating a large FoV, they cannot be neglected. In Adaptive Optics we have the chance to have a Deformable Mirror (DM) in the optical path to correct for them. The aberrations present in the common path are eliminated when the loop is closed, but the quality of the image at the level of the scientific instrument is still degraded by the aberrations unseen by the AO WFS, also known as the Non-Common Path Aberrations (NCPA). In the chapter 4 of this PhD thesis is described how we improved an existing technique of compensation of the NCPA by the use of the DM in the system, and extended it to the correction of aberrations in the FoV of an MCAO instrument.

MCAO makes use of several Guide Stars (GS) in the FoV to produce the best correction, which causes a complexification of both the opto-mechanical design of the instrument and its operation. In particular, the procedure of calibration (determination of the relationship between the perturbations measured and the correction to perform) becomes as crucial as it is delicate, for it has to be redone for each new configuration of GS. In the chapter 5 of this PhD thesis we propose a simplifying method, based on the interpolation of a limited sample of actual calibrations.

Finally I will conclude on this 3 years' work that combined research with practical realization, and open perspectives on the continuation to give to this PhD, on the MAD prototype and more generally on the future AO instruments.

2. From classical AO to MAD

This chapter is a brief overview of Adaptive Optics, from its most classical form (Single-Conjugated AO) to the one tested thanks to the MAD prototype (Multi Conjugate AO). It contains also several sections introducing notions that will be used thoroughly in this thesis, namely the Zernike polynomials, the Kolmogorov and Von Kármán models of atmosphere, the concept of Shack-Hartmann Wave Front Sensor (SHWFS), the calibration of an AO system, and the technique of Strehl Ratio (SR) measurement.

2.1. Adaptive Optics

Atmospheric turbulence severely limits the angular resolution of ground-based telescopes. Adaptive Optics is a powerful technique that allows, thanks to an opto-mechanical system, correcting in real-time for the phase error introduced in a Wave Front (WF) by its crossing of the atmospheric turbulence. A complete description can be found in [82], and we will here give only a brief overview of its principle and main characteristics.

2.1.1. Principle

The turbulent WF is measured by a Wave Front Sensor (WFS) using the light from a Guide Star (GS) and optically corrected by a Deformable Mirror (DM) located in a pupil conjugate plane (see Figure 2.1). They operate in closed feedback loop: the DM is the first hit by the WF and corrects for its distortions, then part of the light is diverted toward the WFS to estimate the residual aberrations which remain to be compensated. The control system uses the WFS signal to update the values of the voltages applied to the DM. As the incoming WF evolves, these operations are repeated indefinitely, at a frequency which has to be high enough to follow the fast evolution of the turbulence (typically several hundreds of Hertz).

The DM has a finite number of actuators A that one can control, and the WFS provides a finite (always larger) number of measurements M . In general, there is no one-to-one relationship between the sensor signal and the actuators: acting on one actuator modifies more than one of the sensor signals. The response of the sensor to each actuator is then described by a $[A \times M]$ matrix called the Interaction Matrix (IM).

In closed loop, the signal measured by the WFS is multiplied by the Control Matrix (CM) to get the voltages to apply to the DM to correct for the residual aberrations measured. The simplest way to get the CM is by Truncated Singular Value Decomposition (TSVD) and generalized inversion of the IM (see section 2.4.4).

This compensation allows the recording of long-exposure images with a resolution close to the diffraction limit of the telescope. However, one can notice that the correction of the WF is optimized to get the smallest residual on the

WFS, but not on the camera. The presence of static aberrations in the non-common path (between the dichroic and the camera) leads to a decreasing of the performance. The evaluation and compensation of those aberrations is the subject of the chapter 4 of this PhD.

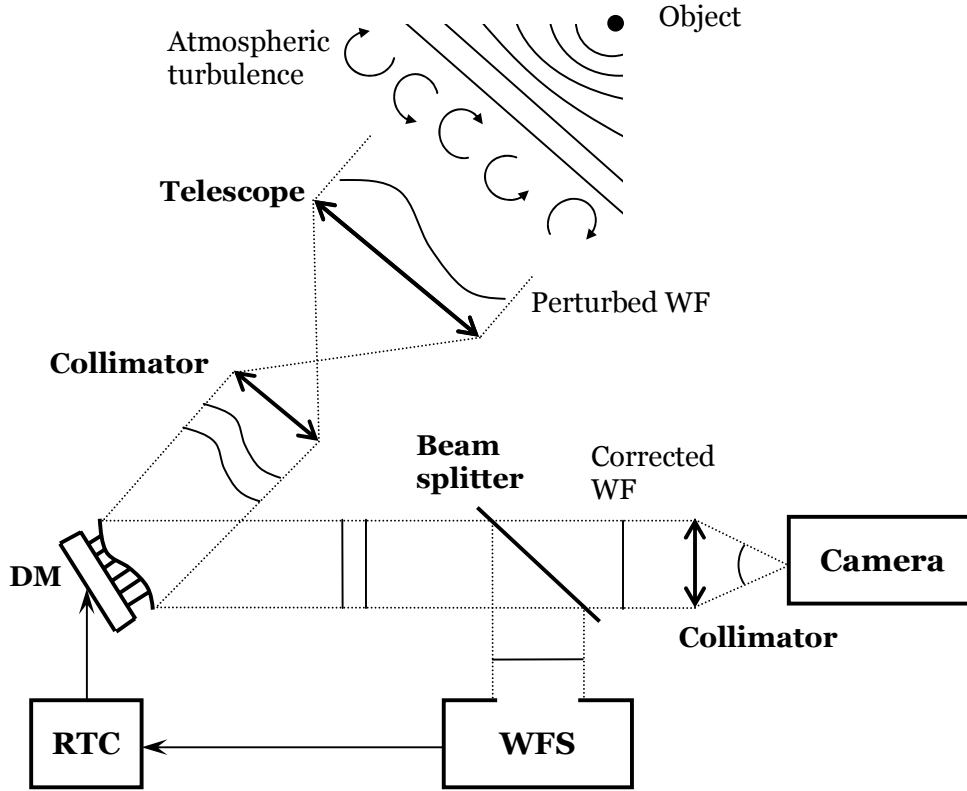


Figure 2.1: General layout of an Adaptive Optics imaging system. The Wave Front Sensor measures the residual of the turbulence, and the Real-Time Computer converts it into voltages to apply to the Deformable Mirror in order to have a turbulence-corrected image on the Camera.

2.1.2. Limitation

When the seeing conditions are favorable, the performance of the AO correction are limited by the availability of a bright GS in the vicinity of the object to observe. If the GS found is too faint, the noise on the WFS is limiting, and if it is too distant, the anisoplanatism effect becomes important.

Anisoplanatism [23] appears when one starts to observe the AO performance on an object far from the GS. As the wave coming from the two objects doesn't cross the same part of the atmosphere (thus the same turbulence), the aberrations are different in the two directions, while the correction is optimized only for one (Figure 2.2).

One can define an isoplanatic angle θ_0 [83] inside of which the phase difference is smaller than 1 rad^2 :

$$\theta_0 = 0.314 \frac{r_0}{h} \quad (2.1)$$

2.1 ADAPTIVE OPTICS

θ_0 depends only on the strength of the turbulence (expressed through the Fried parameters r_0) and its vertical profile $C_n^2(h)$ through the weighted average \bar{h} :

$$\bar{h} = \left[\frac{\int_0^\infty h^{5/3} C_n^2(h) dh}{\int_0^\infty C_n^2(h) dh} \right]^{3/5} \quad (2.2)$$

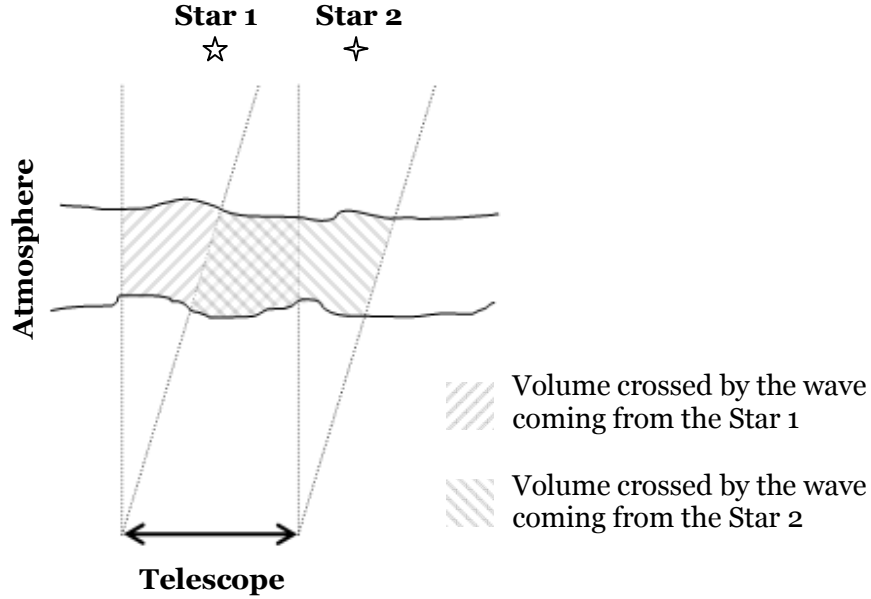


Figure 2.2: Illustration of the anisoplanatism effect. The wave coming from two separated objects doesn't cross the same volume of atmosphere on its way to the telescope.

2.1.3. Application

The first idea for building an AO system rose in 1953 [3], but it was made into practice only when the computing power became sufficient some 35 years later, with the system COME-ON [87] [86] installed on ESO's 3.6 meters telescope in La Silla (Chile). This one has been successively upgraded to COME-ON+ [85] and ADONIS [7]. Later on ADONIS, Hokupa'a [84] and PUEO [80] were installed on the CFHT in Hawaii and gave astronomical images of great quality.

Today, while the first generation of AO instrument on 8-meters class telescopes is working routinely (NAOS [88], Altair [34], Keck AO [96] and Subaru AO [69]), the second generation is being designed (Gemini MCAO [30], GALASCI [35], MAD, ...), and concepts for AO on Extremely Large Telescopes are under study.

2.2. Multi Conjugate Adaptive Optics (MCAO)

MCAO ([18], [5], [6], [21]) is a generalization of classical AO (or SCAO). As we have seen in the section 2.1.2, the main limitation of SCAO comes from the fact that the DM is conjugated to the pupil plane of telescope. Thus the phase minimization is done in the pupil and in one direction of the FoV (the direction of analysis). This correction is then applied to the whole FoV, which results in the deterioration of the performances of the system in function of the angular position in the FoV. This deterioration is due to the volume of the atmosphere that creates anisoplanatism effects that a classical system cannot compensate.

The concept of the MCAO is to analyse and correct the turbulence in the volume (Figure 2.3). It involves:

- Several Guide Stars (GS) allowing to record the resulting phase in several direction of the FoV.
- A reconstruction algorithm that retrieves information about the volume of the turbulence.
- Several Deformable Mirrors conjugated to different altitudes.

From the measurements in different directions, the phase in the volume of turbulence is reconstructed, and the appropriate correction is applied to each of the DMs. If the reconstruction is well done, the result will be a uniform correction in the FoV. Different approaches for MCAO correction have been proposed in the last years like for instance the atmospheric tomography [92] [26].

One can also imagine another practical implementation of MCAO, called Layer-Oriented [76], in which the reconstruction at the level of the DMs is optically made by conjugating the WFS to those altitudes (Figure 2.3.b).

2.2 MULTI CONJUGATE ADAPTIVE OPTICS (MCAO)

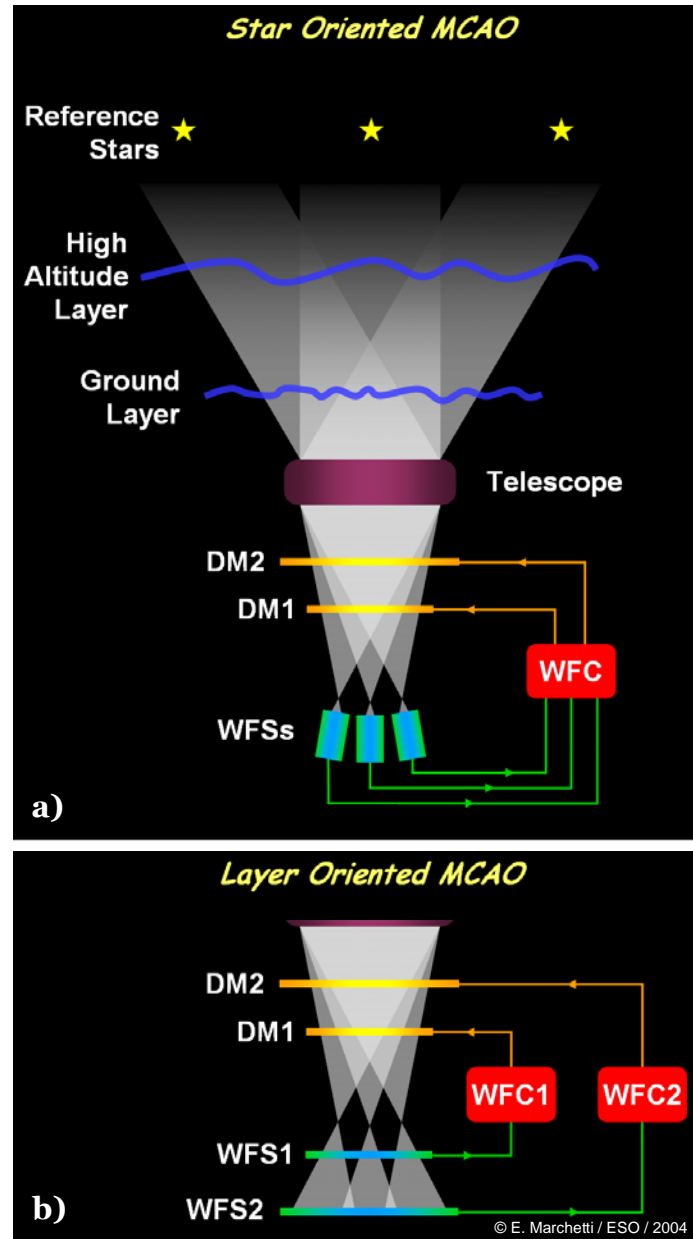


Figure 2.3: Schematic view of two practical implementations of MCAO. a) In Star Oriented (SO) MCAO, the WF is measured in a pupil plane in several directions simultaneously, and the Wave Front Corrector (WFC) reconstructs the contribution of each layer. b) In Layer-Oriented (LO) MCAO, the WF is sensed at the same altitudes to which the DMs are conjugated and the reconstruction is straightforward.

2.3. The MCAO Demonstrator

The European Southern Observatory in collaboration with external research institutes has built an instrument prototype, the McAo demonstrator (MAD) [36], to prove on the sky the feasibility of the MCAO technique using both reconstruction approaches (SO and LO) in the view of the future 2nd generation of the VLT instrumentation and the 100-meters telescope OWL [19]. MAD will be installed at the Nasmyth focus of a VLT unit telescope and the actual timeline foresees to have the on-sky operations for late 2006 using only natural guide stars (NGSs).

The following sections contain an overview of MAD and some of its sub-systems to which it will be referred in the chapters 3, 4 and 5 of this thesis. More details can be found in [62].

2.3.1. General overview

MAD is a prototype MCAO system performing wide FoV AO correction over 2 arcmin on the sky by using bright ($m_v < 14$) Natural Guide Stars. It is implemented using existing technology and re-using as much as possible key components developed in the scope of existing AO systems. MAD will be used to investigate two different approaches of MCAO correction with two independent wave front sensing techniques: the Star Oriented MCAO sensing simultaneously 3 NGS with 3 Shack-Hartmann WFS (see section 2.4.3) and the Layer Oriented MCAO based on a Multi-Pyramid WFS [77] sensing simultaneously 8 NGS. The MAD Real-Time computer architecture is designed in order to support both reconstruction approaches.

The correction is based on two Deformable Mirrors. One mirror is conjugated to the telescope pupil for ground layer turbulence correction, the second is conjugated at 8.5 Km above the telescope aperture, enabling a larger FoV correction. The MCAO correction is optimized for the K band (2200 nm) under median Paranal seeing conditions and the performance will be evaluated at this wavelength.

MAD uses a 1 arcmin FoV IR camera, called CAMCAO [1], to evaluate the correction. During the laboratory testing is also uses the ESO IR Test Camera (ITC) with smaller FoV (17 arcsec). The optical design of those two cameras is given in the appendix 8.5.

2.3.2. Opto-mechanical layout

The optical and opto-mechanical designs of MAD are provided in the Figure 2.4 and Figure 2.5. The input beam is F/15. A 2 arcmin FoV is de-rotated by an optical derotator and collimated by a doublet lens to re-image a telescope pupil of 60 mm in diameter. A 100 mm DM is conjugated at an altitude of 8.5 Km (DM-2) and a 60 mm DM is conjugated to the re-imaged telescope pupil (DM-1). A Tip-Tilt Mount (TTM) is supporting the DM-1 for the tip-tilt correction. A dichroic transmits the infrared light (1000-2500 nm) toward the IR camera and reflects the visible light (450-950 nm) toward the WFS path. A lens objective provides a telecentric F/20 input beam to the WFS.

2.3 THE MCAO DEMONSTRATOR

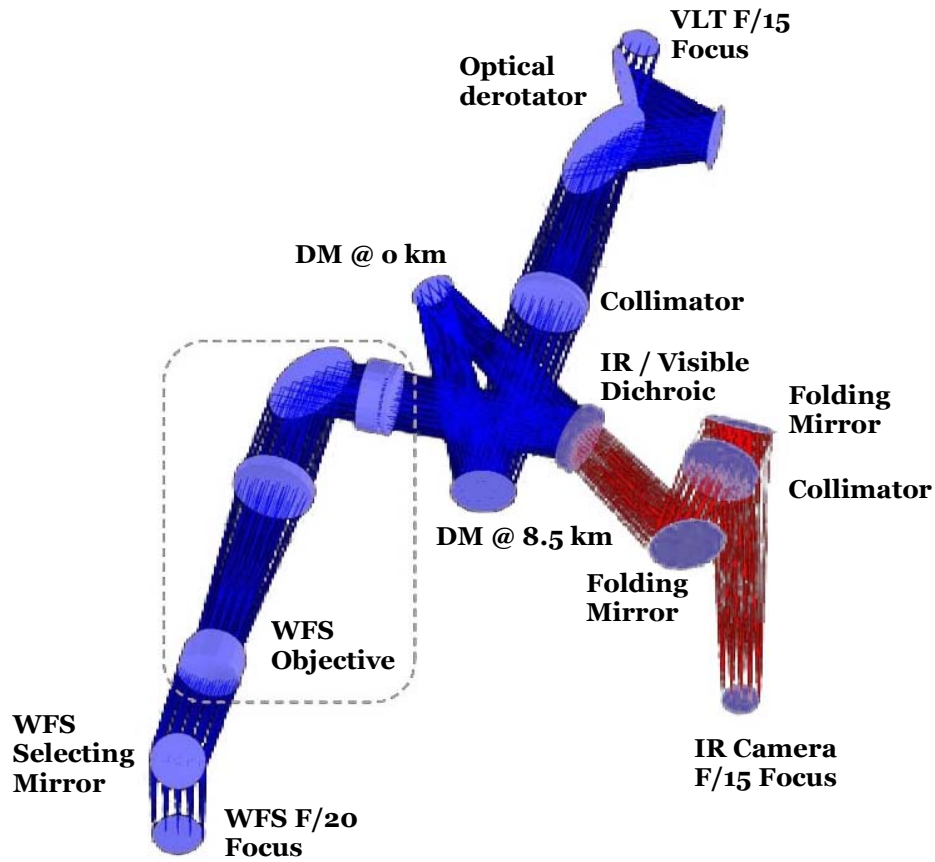


Figure 2.4: Optical design of MAD.

After passing through the dichroic, the IR beam is folded and then focused by a second collimator (copy of the first one) to form an F/15 focus at the entrance of the IR camera. This collimator is mounted on a translation stage that is used to assure the focusing on the camera detector (and eventually to introduce a defocus to record images for the Phase Diversity analysis in the chapter 4 of this thesis). A second folding mirror provides to direct the focused beam perpendicularly through the bench. The IR camera, located below the bench, is interfaced with an XY table for scanning the 2 arcmin FoV .

The turbulence generator MAPS (see chapter 3) is located in proximity of the input F/15 to inject the turbulence inside the optical train.

Two calibration units are implemented: one at F/15 input focus (Calibration Unit 1) and one at the input of the WFS optical path (Calibration Unit 2). These units consist of a set of movable illuminated fibers.

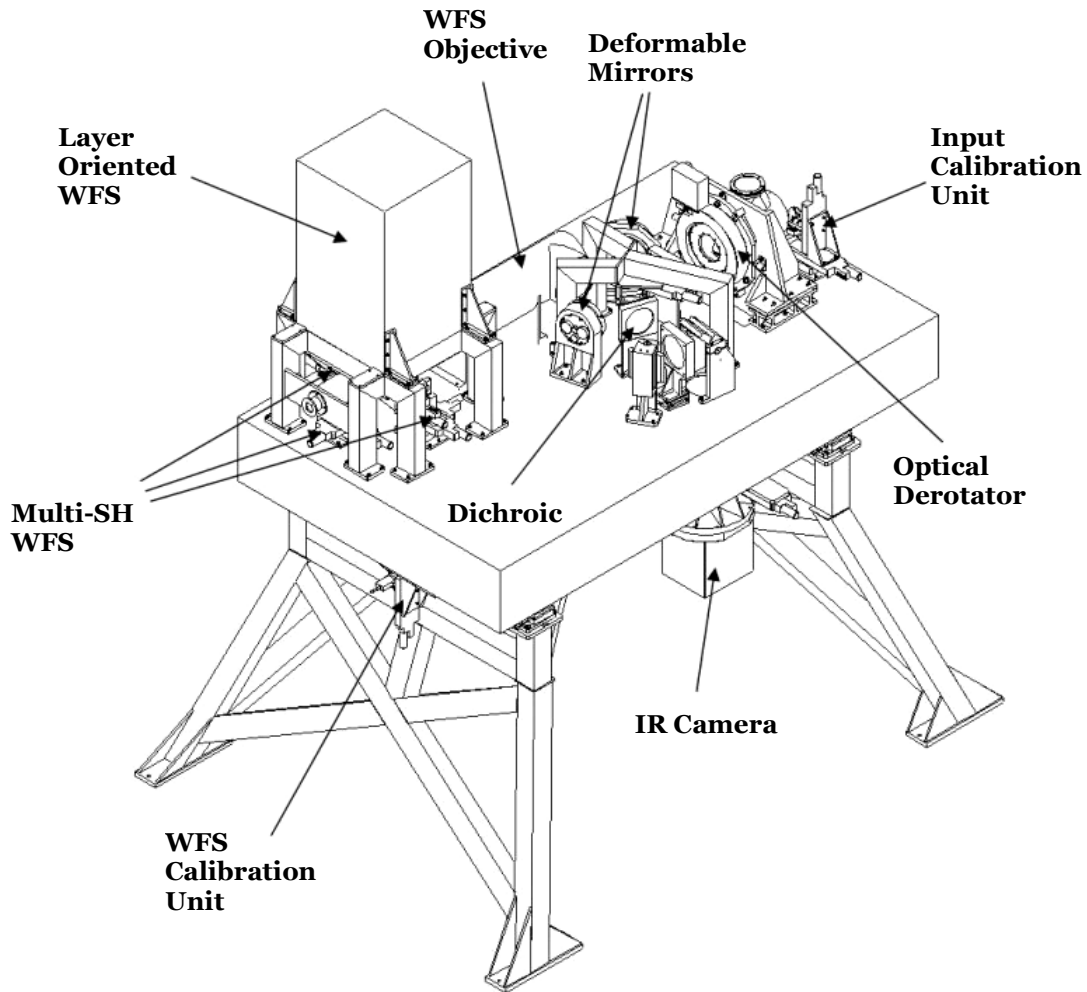


Figure 2.5: MAD bench 3D view.

2.3.3. Wave Front Sensors

Multi Shack-Hartmann WFS

The Multi SHWFS consists of 3 Shack-Hartmann units (SHU) capable to scan the whole 2 arcmin FoV to pick-up the NGSs for the wavefront sensing (see Figure 2.6). Each SHU is provided with an arm supporting a pick up mirror folding the light through the SHU optics, a FoV diaphragm of 2.4 arcsec located at the F/20 focus and doublet lenses that re-image the telescope pupil on the lenslet array. The lenslet array is an 8×8 sub-apertures, $192 \mu\text{m}$ pitch, 3.2 mm focal length. Each small lens focuses the NGS light on the WFS camera detector over 8×8 pixels, $24 \mu\text{m}$ size (scale 0.3 arcsec/pixel). Each SHU is mounted on a XY motion scanning the 2 arcmin FoV and the three arms are slightly displaced in altitude with respect to the table plane in order to avoid mutual collisions.

2.3 THE MCAO DEMONSTRATOR

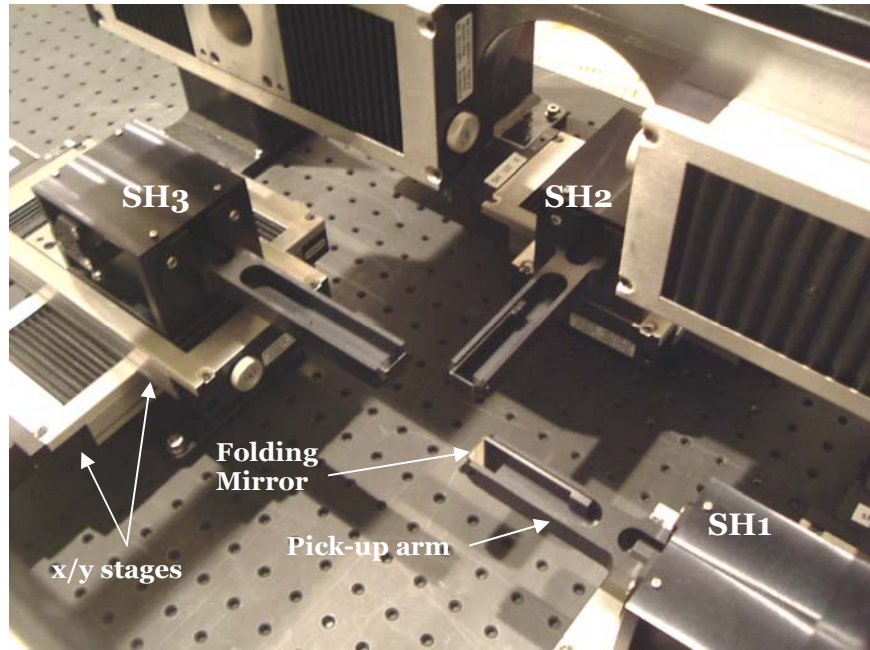


Figure 2.6: SHWFS area.

Layer Oriented WFS

The LOWFS for MAD [97] is based on a multi pyramid WFS with eight pyramids to observe simultaneously eight NGSs (Figure 2.7). Each pyramid is supported by a small cylinder containing some re-imaging optics to enlarge the system focal ratio by a factor ~ 10 on the top of the pyramid. The light modulated by the pyramid is then re-imaged through two groups of lenses and the pupil image of the observed NGS is created on the plane where the WFS camera detectors are located. Between the two groups of lenses a dichroic splits the light toward two WFS cameras slightly displaced along the optical axis in order to provide the footprint geometries corresponding to of the conjugation altitudes of the two DMs of MAD.

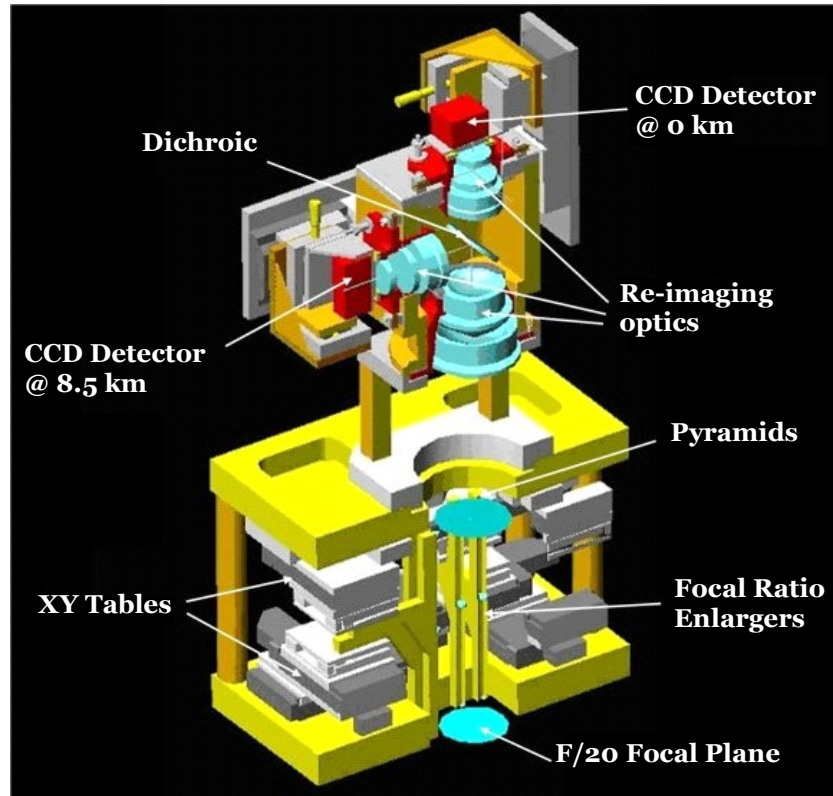


Figure 2.7: Opto-mechanical layout of the MAD LOWFS.

2.3.4. Deformable Mirrors

The Deformable Mirror conjugated to the ground is the MACAO SINFONI [10] bimorph DM, 60mm pupil, radial geometry (Figure 2.8.a). The Deformable Mirror conjugated to the altitude of 8.5 Km is the MACAO-VLTI [2] bimorph DM, 100mm pupil, radial geometry (Figure 2.8.b). The tip-tilt correction is provided by the SINFONI Tip-Tilt supporting the MACAO SINFONI DM.

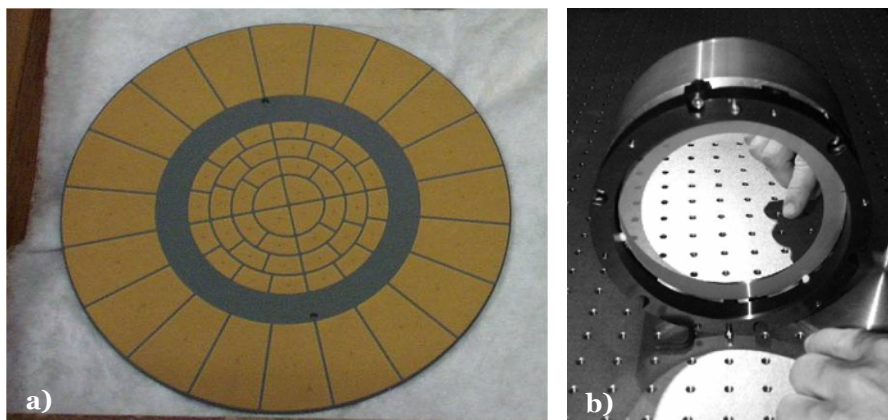


Figure 2.8: a) Radial geometry of the sub-apertures in the MAD Deformable Mirrors. b) The MCAO-VLTI DM.

2.3 THE MCAO DEMONSTRATOR

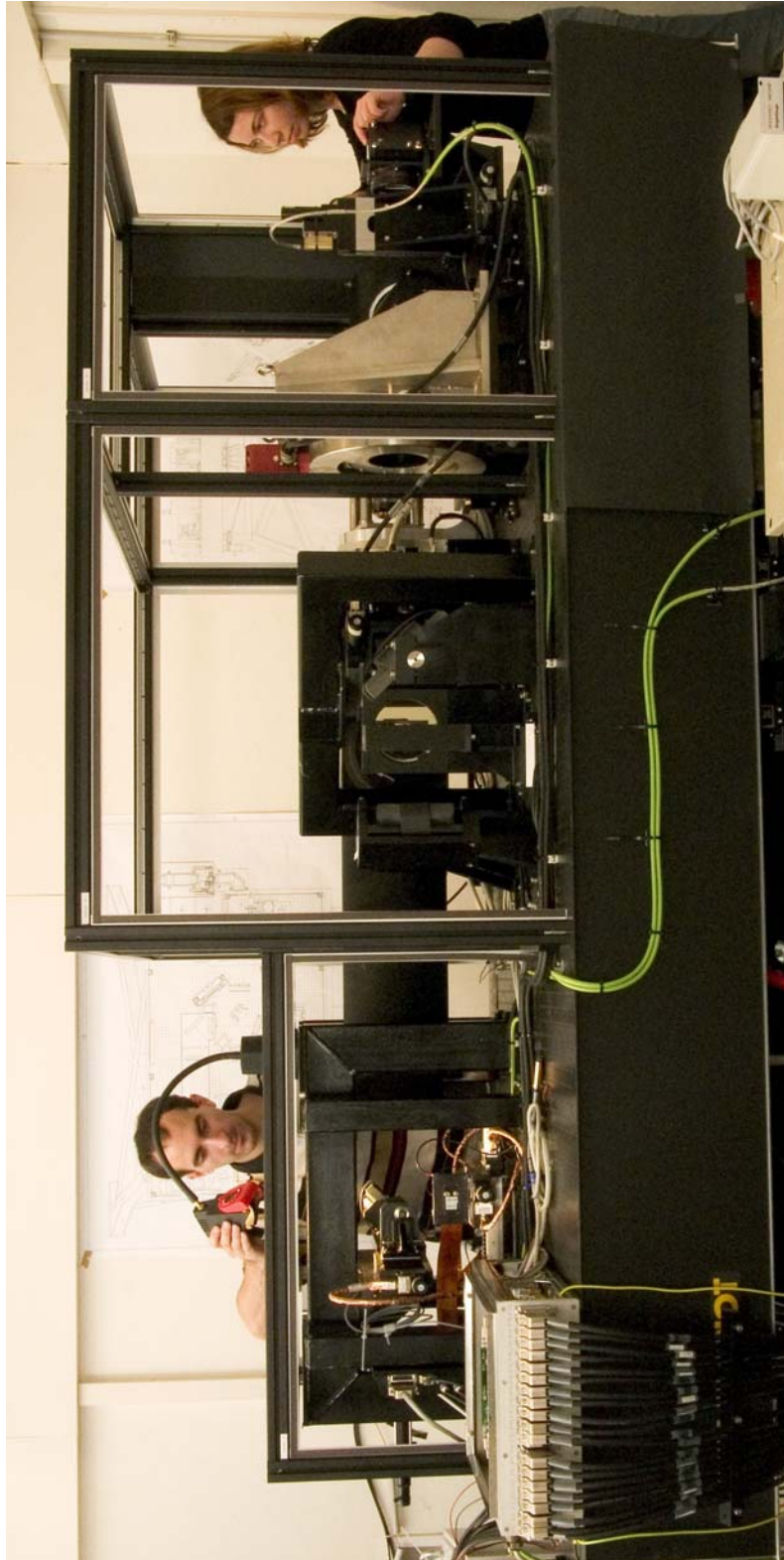


Figure 2.9: Final configuration of the MAD bench, including the cabling, the derotator, and the beams supporting the enclosure panels. Only the LOWFS is missing.

2.4. Useful notions

2.4.1. The Zernike polynomials

In order to characterize the turbulent phase, it is often interesting to project it on a basis of modes. A basis commonly used is the one of the Zernike polynomials for it has a simple analytical expression defined over a circular aperture, and its first modes describes well the low order optical aberrations (defocus, astigmatism, coma...).

For a circular aperture without obstruction and using polar coordinates, the Zernike modes are defined by:

$$\left. \begin{array}{l} Z_{n,\text{even}}^m(\rho, \theta) \\ Z_{n,\text{odd}}^m(\rho, \theta) \\ Z_n^m(\rho, \theta) \end{array} \right\} = \sqrt{n+1} R_n^m(\rho) \left\{ \begin{array}{ll} \sqrt{2} \cos(m\theta) & m \neq 0 \\ \sqrt{2} \sin(m\theta) & m \neq 0 \\ 1 & m = 0 \end{array} \right\} \quad (2.3)$$

where θ and ρ are the polar coordinates, m and n respectively the radial degree and azimuthal frequency. As explained in [11], the radial polynomials $R_n^m(\rho)$ can be derived from the Jacobi polynomials and are finally found to be:

$$R_n^m(\rho) = \sum_{s=0}^{(n-m)/2} \left(\frac{(-1)^s (n-s)!}{s! ((n+m)/2 - s)! ((n-m)/2 - s)!} \right) \rho^{n-2s} \quad (2.4)$$

From this expression several classifications of Zernike polynomials have been made. In the present thesis and as often in AO applications, we will use the classification given by Noll [75]. The Table 2.1 shows the expression of those polynomials up to the 5th azimuthal frequency, as well as the corresponding optical aberration for the first ones. The shape of the same polynomials is shown in the appendix 8.1.

Any turbulent phase can be decomposed on the basis of the Zernike polynomials:

$$\phi(r) = \sum_{i=1}^{\infty} a_i Z_i(r) \quad (2.5)$$

Noll	m	n	Zernike polynomial	Definitions
1	0	0	1	Piston
2	1	1	$2\rho \cos \theta$	Tip
3	1	1	$2\rho \sin \theta$	Tilt
4	0	2	$\sqrt{3} (2\rho^2 - 1)$	Defocus
5	2	2	$\sqrt{6} \rho^2 \sin 2\theta$	Astigmatism (3 rd order)
6	2	2	$\sqrt{6} \rho^2 \cos 2\theta$	Astigmatism (3 rd order)
7	1	3	$\sqrt{8} (3\rho^3 - 2\rho) \sin \theta$	Coma
8	1	3	$\sqrt{8} (3\rho^3 - 2\rho) \cos \theta$	Coma

2.4 USEFUL NOTIONS

Noll	m	n	Zernike polynomial	Definitions
9	3	3	$\sqrt{8} \rho^3 \sin 3\theta$	Trefoil
10	3	3	$\sqrt{8} \rho^3 \cos 3\theta$	Trefoil
11	0	4	$\sqrt{5} (6\rho^4 - \rho^2 + 1)$	Spherical
12	2	4	$\sqrt{10} (10\rho^4 - 3\rho^2) \cos 2\theta$	Astigmatism (5 th order)
13	2	4	$\sqrt{10} (10\rho^4 - 3\rho^2) \sin 2\theta$	Astigmatism (5 th order)
14	4	4	$\sqrt{10} \rho^4 \cos 4\theta$	Ashtray
15	4	4	$\sqrt{10} \rho^4 \sin 4\theta$	Ashtray
16	1	5	$\sqrt{12} (10\rho^5 - 12\rho^3 + 3\rho) \cos \theta$	
17	1	5	$\sqrt{12} (10\rho^5 - 12\rho^3 + 3\rho) \sin \theta$	
18	3	5	$\sqrt{12} (5\rho^5 - 4\rho^3) \cos 3\theta$	
19	3	5	$\sqrt{12} (5\rho^5 - 4\rho^3) \sin 3\theta$	
20	5	5	$\sqrt{12} \rho^5 \cos 5\theta$	
21	5	5	$\sqrt{12} \rho^5 \sin 5\theta$	

Table 2.1: Expression of the Zernike polynomials as classified by Noll and corresponding optical aberrations.

2.4.2. Atmosphere models

The atmosphere of the Earth is a turbulent medium. The kinetic energy produced by the motion of air masses creates the turbulence at a characteristic scale L_0 called the outer scale. This energy is transferred to smaller and smaller scales (Kolmogorov's cascade theory [54]) until the inner scale l_0 at which point it is dissipated by viscosity. The orders of magnitude are of tens to hundreds of meters for L_0 and of millimeters for l_0 .

The domain comprised between those characteristic scales, where the turbulence is fully developed, is called the inertial scale range. The Kolmogorov model of the turbulence is valid for distance in this range, i.e. in the field of imaging through turbulence, for telescopes diameters with a size much smaller than L_0 . In this range the following expression for the phase structure function is valid [83]:

$$D_\phi(r) = 6.88 \left(\frac{r}{r_0} \right)^{5/3}, \quad (2.6)$$

where r_0 is the Fried parameter [25] characterizing the strength of the turbulence (see also the section 3.4.3).

For telescope diameters larger than a couple of meters, the condition $D \gg L_0$ is no longer respected, and Von Kármán proposed an *ad hoc* model taking into account the outer scale of the turbulence. Using this model, the phase structure function has been derived in [16]:

$$D_{\varphi}(\mathbf{r}) = \frac{\Gamma(11/6)}{2^{11/6} \pi^{8/3}} \left[\frac{24}{5} \Gamma\left(\frac{6}{5}\right) \right]^{5/6} \left(\frac{r_0}{L_0} \right)^{-5/3} \left[2^{-1/6} \Gamma\left(\frac{5}{6}\right) - \left(\frac{2\pi r}{L_0} \right)^{5/6} K_{5/6}\left(\frac{2\pi r}{L_0} \right) \right] \quad (2.7)$$

where $K_{5/6}(x)$ is the modified Bessel function of the third kind and $\Gamma(x)$ is the gamma function.

A direct consequence is that the spectrum of the turbulence projected on the Zernike polynomials is dependant on the value of the outer scale (Figure 2.10). We notice that the influence of the outer scale is mainly on the low order modes, and that for a telescope of 8 meters diameter under an atmosphere of 22 m outer scale (as measured in Paranal), the variance of the tip and tilt modes is divided by 10 with respect to the Kolmogorov case.

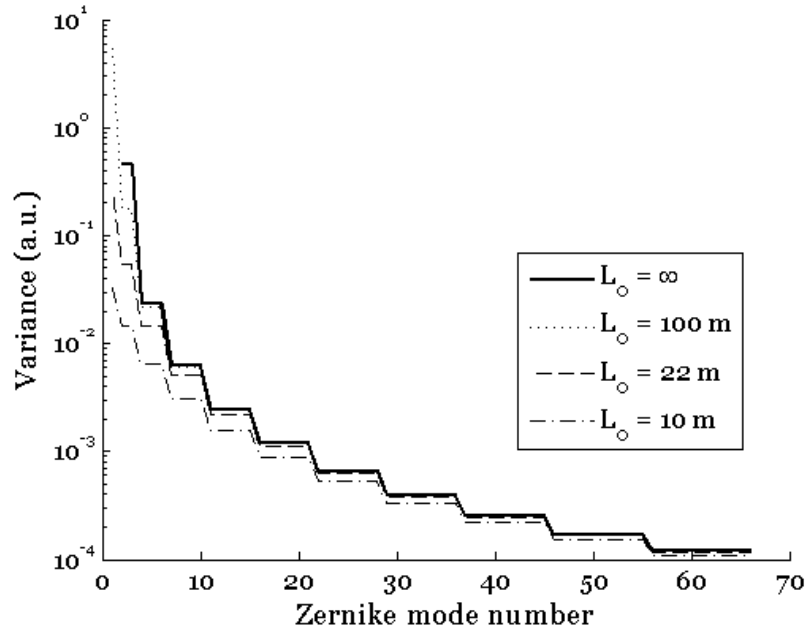


Figure 2.10: Variance of the turbulent phase projected on the Zernike polynomials for a telescope diameter of 8 meters and different values of the outer scale: ∞ (Kolmogorov case), 100, 22 and 10 meters (Von Kármán cases).

2.4.3. SHWFS

A well-known Hartmann test devised initially for telescope optics control was adapted for AO and is the most frequently used type of WFS [82]. An image of the exit pupil is projected onto a lenslet array, a collection of small identical lenses. Each lens takes a small part of the aperture, called sub-pupil, and forms an image of the source. All images are formed on the same detector, typically a CCD.

When an incoming wave-front is plane (Figure 2.11.a), all images are located in a regular grid defined by the lenslet array geometry. As soon as the wave-front is distorted (Figure 2.11.b), the images become displaced from their nominal positions.

2.4 USEFUL NOTIONS

Each spot is imaged on a $[n \times n]$ sub-array (minimum 2×2) of the CCD. A simple estimation of the center of gravity position (c_x, c_y) is:

$$c_x = \frac{\sum_{i,j} x_{i,j} I_{i,j}}{\sum_{i,j} I_{i,j}} \text{ and } c_y = \frac{\sum_{i,j} y_{i,j} I_{i,j}}{\sum_{i,j} I_{i,j}}, \quad (2.8)$$

where $I_{i,j}$ and $(x_{i,j}, y_{i,j})$ are the signal and the position coordinates of the CCD pixel (i, j) . The sum is made on all the pixels devoted to a lenslet field.

Displacements of the image centroids in two orthogonal directions $[x, y]$ are proportional to the average wave-front slopes in $[x, y]$ over the sub-apertures. Thus, a Shack-Hartmann WFS measures the WF slopes. The WF itself can be reconstructed from the arrays of measured slopes. The spatial sampling of a SHWFS is equal to the sub-aperture size.

The alignment of the lenslet array is made in a way that this grid coincides with the grid formed by the junction between the CCD's pixels, so that when a plane WF hits the lenslet array, the slopes measured are zero in all the sub-apertures (for a perfect SHWFS with lenslets perfectly aligned and aberrations-free).

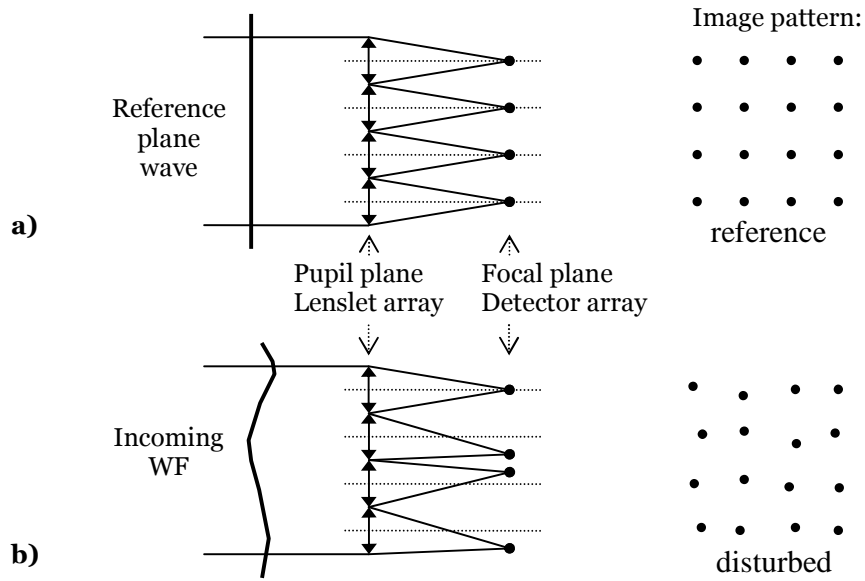


Figure 2.11: Principle of the Shack-Hartmann wave front sensor: a) plane wave, b) disturbed wave.

2.4.4. Calibration of a single-AO system

In Adaptive Optics, the Interaction Matrix (IM) links the deformations of the DM to the WF distortions measured by the WFS [12]. The basic idea for recording it is to deform the DM by pushing its actuators one after the other (zonal approach), and for each of them record the WFS measurement, i.e. a list of $2 \cdot N_{\text{subap}}$ slopes in the case of a SHWFS composed of N_{subap} useful sub-apertures. The response to the actuation i is then:

$$\begin{bmatrix} M_i \end{bmatrix} = \begin{bmatrix} \begin{bmatrix} S_{xi,1} \\ S_{xi,2} \\ \dots \\ S_{xi,N_{subap}} \end{bmatrix} \\ \begin{bmatrix} S_{yi,1} \\ S_{yi,2} \\ \dots \\ S_{yi,N_{subap}} \end{bmatrix} \end{bmatrix} \quad (2.9)$$

The concatenation of the M_i gives the Interaction Matrix of the AO system:

$$\begin{matrix} & N_m \\ & \begin{bmatrix} IM_{AO} \end{bmatrix} \\ 2N_{subap} \end{matrix} = \begin{bmatrix} \begin{bmatrix} M_1 \end{bmatrix} & \begin{bmatrix} M_2 \end{bmatrix} & \begin{bmatrix} M_3 \end{bmatrix} & \dots & \begin{bmatrix} M_{N_m} \end{bmatrix} \end{bmatrix} \quad (2.10)$$

Some improvements can be brought to improve the SNR (apply Zernike or even system modes to the DM: modal approach) or the temporal behavior (fast recording, closed loop recording). The number of modes applied N_m is usually kept equal to the number of actuators of the DM.

Once the IM measured, it can be decomposed by SVD. In the equation (2.11), U is the matrix of the eigen modes of the system and V the matrix of its eigen values.

$$\begin{matrix} IM_{AO} \\ 2N_{subap} \end{matrix} = \begin{matrix} \begin{bmatrix} U \end{bmatrix} \\ 2N_{subap} \end{matrix} \times \begin{matrix} \begin{bmatrix} S \end{bmatrix} \\ 2N_{subap} \end{matrix} \times \begin{matrix} \begin{bmatrix} V^T \end{bmatrix} \\ N_m \end{matrix} N_m \quad (2.11)$$

After generalized inversion we obtain the Control Matrix (equation (2.12)), where S^\dagger is obtained by inverting the values in the diagonal of S after filtering. At this point, some badly seen modes can be filtered out (Truncated SVD). The CM can also be computed by taking into account the turbulence spatial (Maximum A Posteriori approach [29]) and temporal (Kalman filtering [56]) behaviors.

$$\begin{matrix} 2N_{subap} \\ N_m \end{matrix} \begin{bmatrix} CM_{AO} \end{bmatrix} = IM_{AO}^\dagger = V \cdot S^\dagger \cdot U^T \quad (2.12)$$

2.4 USEFUL NOTIONS

2.4.5. Strehl Ratio computation

The Strehl Ratio (SR) [91] is a criterion that is commonly used to measure the quality of (astronomical) images, in particular of ones corrected by AO. It is defined as the ratio of peak focal intensities in the aberrated and ideal point spread functions [11]. There is quite a number of different methods to retrieve the SR from an image [81], and they can be more or less accurate.

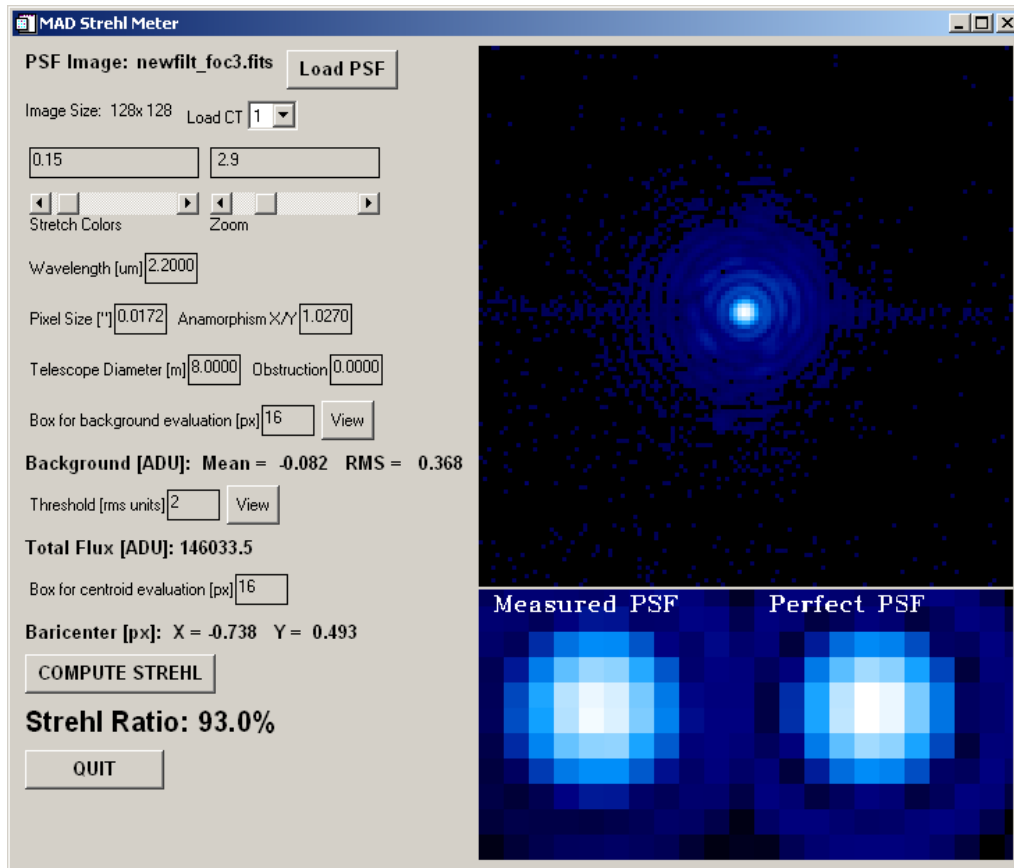


Figure 2.12: Graphical Interface of the Strehl Ratio computation routine for MAD.

In order to analyze the performances of the MAD instrument, its system engineer Enrico Marchetti has written a routine in IDL that computes the SR from images taken by the Infrared Test Camera. It can also be adapted to other camera's images. A snapshot of its graphical interface is shown on the Figure 2.12. The input parameters are the ones of the camera (pixel scale, anamorphism, noise) and of the optical system (telescope diameter, pupil obstruction). The different steps of this routine are the following:

- Load an image and a background files, subtract them
- Find the spot and crop a square area centered on it
- Compute the background value from square areas at the corners of the image and subtract it
- Apply a threshold to the image, i.e. set to zero the pixels with a value smaller than a defined number of times the rms of the background

- Normalize the image to 1
- Find accurately the centroid of the image
- Create a perfect PSF (10 times over sampled) centered on the centroid and bin it to have the same sampling as the aberrated image (this reproduces the natural sampling done by the pixels of any detector)
- Compute the ratio of the perfect PSF's maximum to the aberrated PSF's maximum. This is the Strehl Ratio.

For given conditions of measurements (integration time especially), it is very easy to compare the SR of several images thanks to this routine, and thus to evaluate the performance of the AO loop.

By submitting to this routine a bunch of simulated AO-corrected images [60], it was possible to evaluate the accuracy of the SR estimated. It turned out that this routine estimates quite badly the SR below 35 % (with an error of up to 15 % of SR relative, depending on the sampling of the images and the true SR of the image), but overestimates only slightly (<1.5 % relative) the SR higher than 35 %, unlike many other routines, and this even for images not better than Nyquist-sampled (see Figure 2.13).

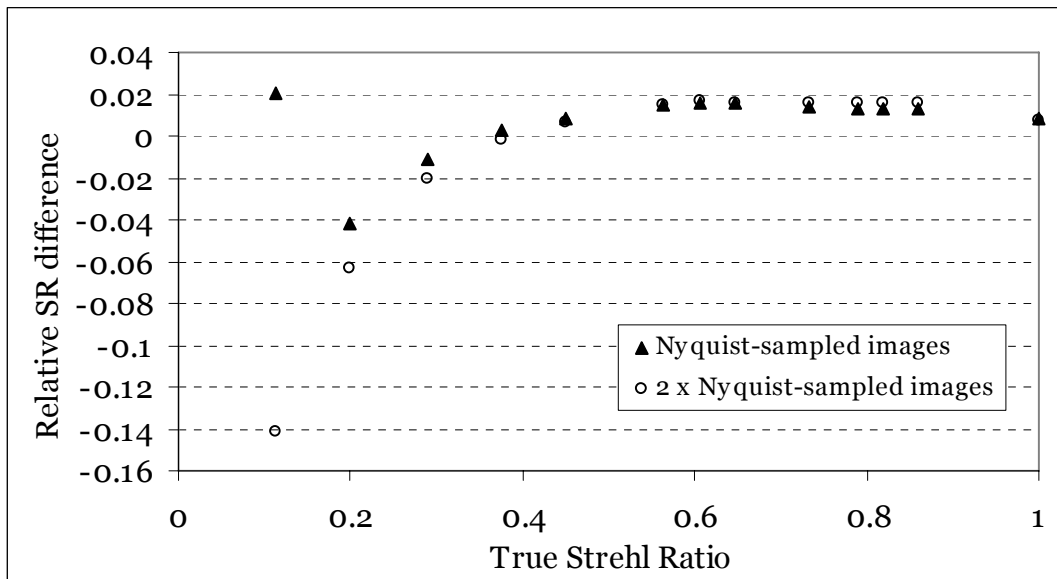


Figure 2.13: Estimation of the error in the SR estimation in the case of Nyquist sampled (triangles) or twice Nyquist sampled images (circles).

On the other hand, the repeatability of the SR computation (giving an error bar on the value) can be estimated by submitting the routine to several images of a spot supposed unchanged, or to evaluate its sensibility to arbitrary parameters such as the threshold defined by the user. The question here is to determine the amount of signal that really belongs to the image compared to the contribution of the noise, and the influence on the estimation of the SR. For images with a SNR of about 40000 as we regularly record with the ITC, we observed that the fluctuation of the estimated SR is within approximately ± 0.3 % **rms absolute** (absolute means that it does not scale with the SR).

2.4 USEFUL NOTIONS

This routine has been used to evaluate the quality of the turbulence-corrected images by MAD in all its modes (SCAO, GLAO, MCAO), but also to evaluate the quality of the bench after correction of the static aberrations, described in the chapter 4 of this thesis.

We have also been brought to use another SR routine, developed at ONERA, in order to evaluate the quality of images taken on their BOA bench (in the course of the experiment described in the section 4.7.2). This routine computes the SR of a given PSF using the ratio between the integral of the Optical Transfer Function (OTF) and the integral of the aberration-free OTF (Figure 2.14).

The users of the routine at ONERA determined that the fluctuations of SR were within the range of **± 0.2 % rms absolute**.

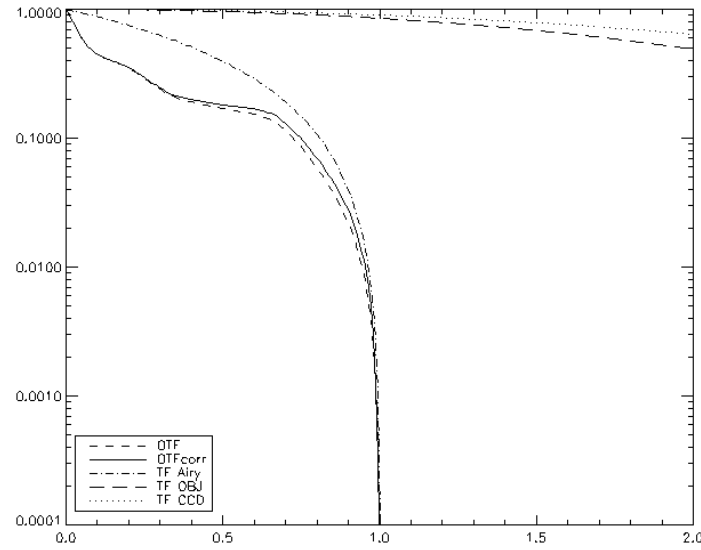


Figure 2.14: Comparison between the measured (solid line) and aberration-free (dot-dashed line) OTFs by the ONERA Strehl Ratio code.

3. MAPS, a turbulence generator for MCAO

3.1. Former systems / need for MAPS

With time, Adaptive Optics systems increase in complexity. They aim at always better performance and/or Field of View correction. Meanwhile, commissioning time on 8-meters class telescopes is precious and one wants to limit the risks of seeing an instrument delivering poor results once on the sky. This leads to longer laboratory testing periods and to the development of turbulence generation systems. Their goal is to reproduce a distorted WF similar to the one reaching an instrument before correction. They are to be placed in front of the AO system in order to test it and even predict its performances on the sky for a given turbulence configuration.

A first idea is to use turbulent air or another fluid [17] with a temperature gradient, similarly to what actually happens in the atmosphere. This kind of “air-dryer” system is quite easy to implement, but it is voluminous and dissipates a lot of heat. Moreover the turbulence produced is weak and not reproducible, which make it unsuited for full system testing.

In the family of the all-optical turbulence generator, which general layout is shown on the Figure 3.1, one can think of using a DM or liquid crystal plates [59] to distort the WF, but their drawbacks are the low number of electrodes (producing not enough high frequencies) and the high cost. Moreover the turbulence produced in the case of liquid crystal plates is strongly chromatic.

In the end the most practical optical devices are the so-called Phase Screens (PS), passive optical elements in which the optical path difference is modified locally in order to produce a phase shift in an electromagnetic wave passing through it. Properly placed in the optical setup, being hit off-axis and set in rotation, they simulate layers of turbulence at different altitudes moving above the telescope pupil at a given wind speed, in agreement with Taylor’s hypothesis [93]. Their drawback is the limited number of realizations they produce, but it can be compensated by the use of several desynchronized PS.

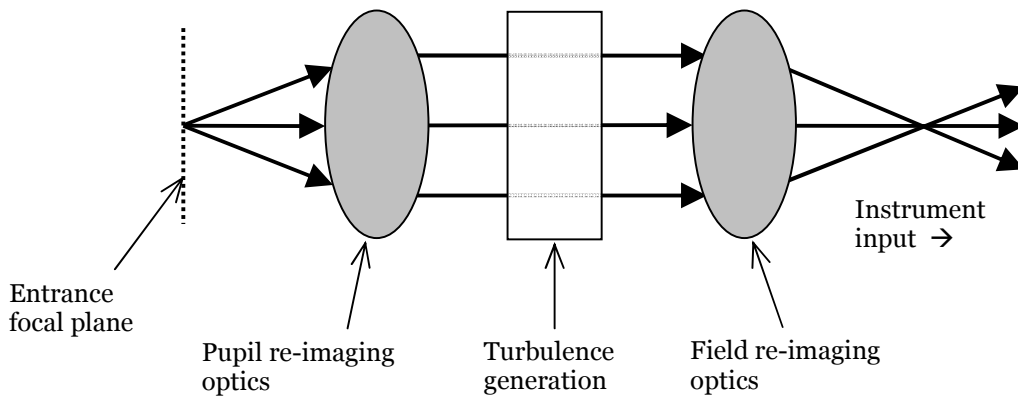


Figure 3.1. General layout of an all-optical turbulence generator.

3.1 FORMER SYSTEMS / NEED FOR MAPS

The methods to produce such Screens are numerous: computer-generated holography, laser writing, plastic molding, resine photolithography, near-index matching method, ion-exchange technique, ion etching, ... Each of them has pros and cons, but the constraints dictated by the MCAO turbulence generation leaves only a few possibilities (see section 3.4).

A remarkable TG is the one that has been developed for the laboratory testing of the (Single-)AO system NAOS for the VLT, by the Observatoire de Paris (France) [40]. It is a quite compact on-axis system (Figure 3.2) composed of relay parabolic mirrors and of 2 PS both conjugated with the pupil of the telescope. There are two screens in order to produce a strong amount of turbulence, and so that when they are set in rotation at slightly different speed, they create many more different realizations of the turbulence.

The reflective Phase Screens are produced by depositing a layer of resine on a substrate, and insulate it by an ultraviolet beam through a 256 grey levels mask. The insulated resine is then removed, and the PS is coated with aluminum. The mask used contains 4096 pixels in the PS diameter of 50 mm, and the size of the beam footprint is 6.5 mm. Several sets of those PS were manufactured in order to produce a variety of seeing conditions.

Drawbacks of this technique are that it cannot create more than 8 microns of WF shift per PS, and also that it is quite sensitive to aging (deterioration of the resine and the coating with time). However this TG was successfully used to test NAOS, was then shipped to ESO and used to characterize the performances of not less than the 6 MACAO-like curvature AO systems (4 MACAO-VLTI, SINFONI and CRIRES [70]).

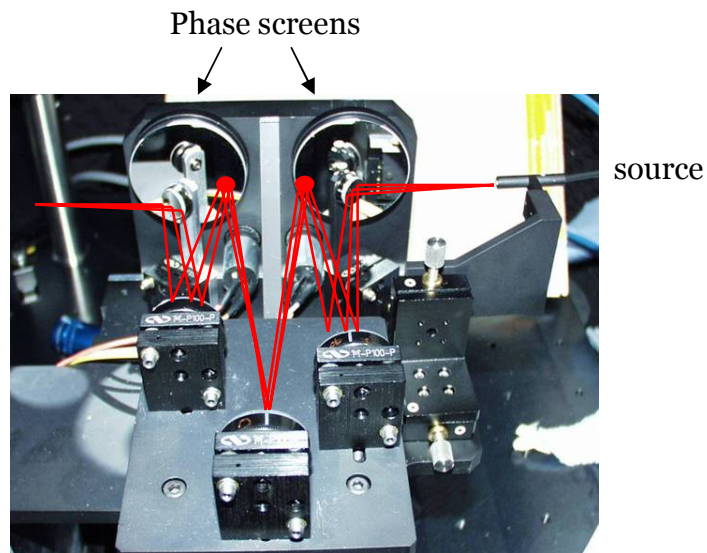


Figure 3.2: The NAOS turbulence generator.

3.2. MAPS concept

Generating turbulence for MCAO requires a higher level of complexity in order to implement the rather large FoV and the several turbulent layers. Indeed the characterization of the instrument requires a well-known and reproducible seeing, the FoV makes the optics larger, and the amount of turbulent layers to simulate pushes the development of a new generation of Phase Screens.

In the framework of the ESO's MCAO Demonstrator, MAPS (Multi-Atmospheric Phase screens and Stars) has been identified as a strategic tool for the laboratory tests [36]. The goal of MAPS is to emulate a time evolving three-dimensional atmosphere whose induced aberrations are injected into MAD. The characteristics of the atmospheric turbulence shall be similar to those of the Paranal observatory during typical seeing conditions. MAPS creates a 2 arcmin FoV beam as seen at the F/15 Nasmyth focus of one of the VLT Units [63].

The strategy is to use an all refractive solution because of its versatility in changing the atmospheric characteristics without increasing the complexity of the system, as for an all reflective or hybrid solution. Indeed the use of a NAOS-like TG would have required a complex reflective optical design, large optics including off-axis parabolas, and make impossible any change in the altitude of the layers for instance.

The evolving atmosphere is emulated by rotating Phase Screens (see section 3.4). The distribution of the phase shift shall follow a typical distribution given by a Von Kármán spectrum with a finite outer scale (section 2.4.2). The PSs are positioned along the optical axis in order to emulate the turbulence at different altitudes with the desired spatial and temporal behavior.

The general concept of MAPS can be represent by the Figure 3.1. The Natural Guide Stars (NGS) are reproduced by visible-IR light transmitting fibers. Their positions are changeable to create the desired star configuration. A first group of lenses collimates the light beams from the NGSs and allows the telescope pupil to be created. Several refractive PSs are located in the collimated beam to emulate the atmospheric layers at different altitude. One phase screen is located in the telescope pupil as the ground layer of the atmosphere. The PSs have different turbulence power according to the expected vertical C_n^2 distribution. The evolving atmosphere is reproduced by rotating the PSs at different speeds according to the wind speed vertical profile. The position of the high altitude PS can be slightly varied in order to modify the atmospheric anisoplanetism and the speeds can be adjusted to create a wide range of atmospheric correlation times. Moreover the PSs are interchangeable in order to emulate a selected range of seeing conditions.

A second group of lenses re-images the artificial NGSs whose wavefront quality is degraded by the PSs. The distorted wavefronts are then injected into MAD for MCAO correction and performance evaluation.

Particular care has to be taken when selecting the location of the beam footprints on the different PSs. Because of the rotation, each footprint will experience a differential speed at the edges located along the PS radius. In order to keep this effect as small possible, large PSs have to be considered as well as smaller footprint dimensions [14]. Both conditions are difficult to achieve: large

3.3 OPTO-MECHANICS

PSs are difficult to manufacture and small footprints require the PSs to be very close to each other, in addition to a small pixels size. A reasonable trade-off in the selection of these reduces the differential speed disturbance. The goal achieved is to keep the differential speed smaller than $\pm 50\%$, which is the average variation of the wind speed inside an 8 meter VLT pupil at Paranal.

3.3. Opto-mechanics

3.3.1. MAPS design

The optical and mechanical designs of MAPS are shown on the Figure 3.3 and Figure 3.4. A more detailed information is given in the SPIE paper “*MAPS, a turbulence generator for MCAO*” [52], also in the appendix 8.1.

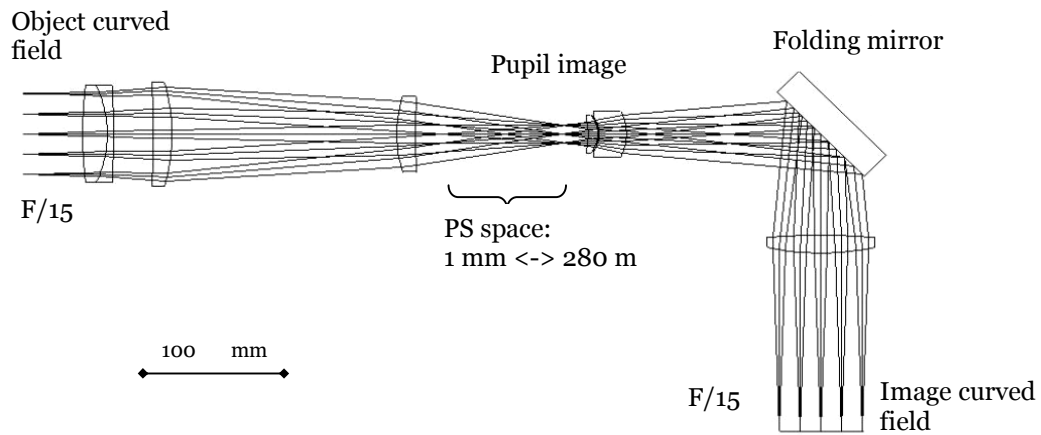


Figure 3.3: Optical concept for MAPS. A 1:1 imaging system provides to re-image the NGS at the MAD input F/15 focus. The size of the pupil is 15 mm in diameter.

3. MAPS, A TURBULENCE GENERATOR FOR MCAO

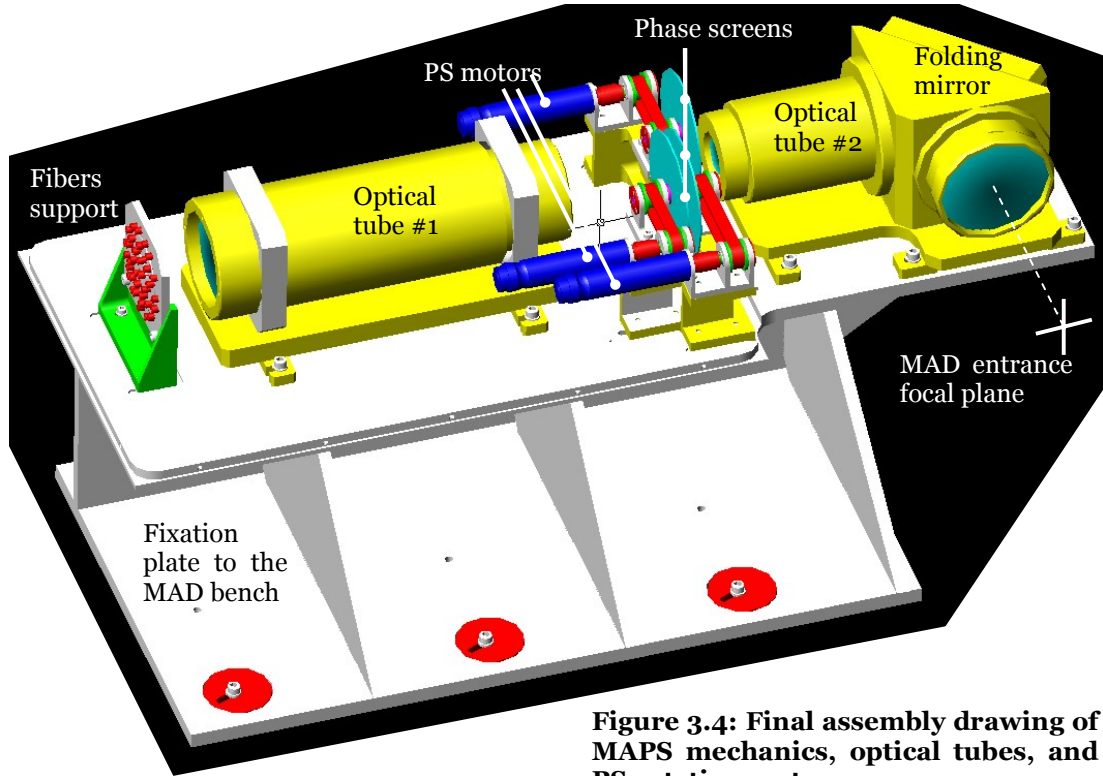


Figure 3.4: Final assembly drawing of MAPS mechanics, optical tubes, and PS rotation system.

In summary, optical fibers are plugged to the entrance plate which is crowded with connectors. The basic plate has 37 of them on 5 concentric circles of diameters up to 2 arc minutes (69.84 mm at F/15), but it can be exchanged to a custom plate simulating any real star asterism.

The first optical tube re-images the pupil in the PS area, where the refractive glass plates create the turbulence. The Phase Screens are placed at different altitudes to emulate the turbulent atmospheric layers. They are set in motion thanks to a system of belts and motors, electronically controlled to a great accuracy [61]. The second optical tube re-images the focal plane to feed MAD. The whole is mounted on a structure that brings the beam height to the same one as MAD [44] [22].

3.3.2. Alignment

The technical specifications of MAPS are detailed in [63]. The alignment of the instrument [43] was performed thanks to a dedicated mechanical reference from the manufacturer and some additional tools, such as pupil masks or a holding device for the alignment with MAD, that had to be designed (Figure 3.5).

3.3 OPTO-MECHANICS

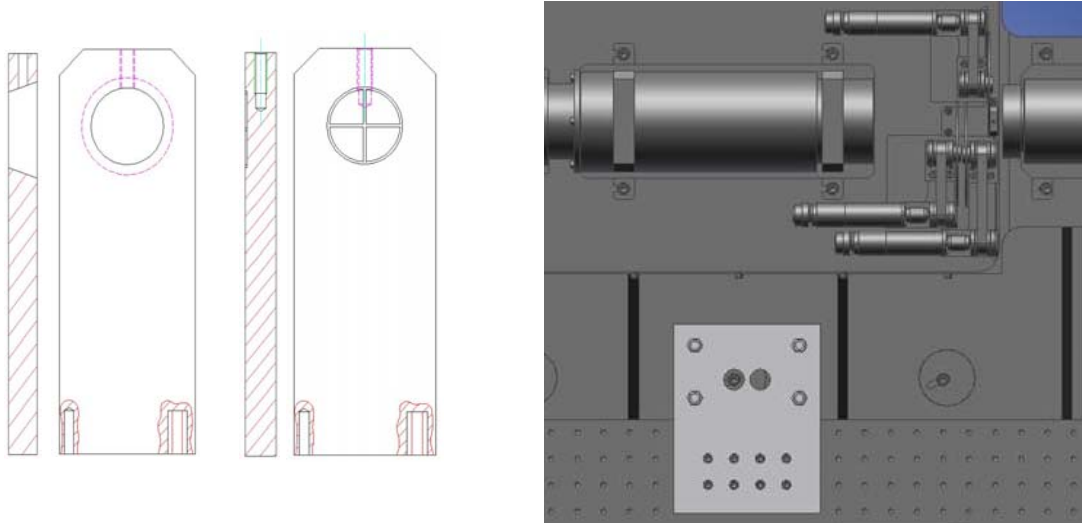


Figure 3.5: Alignment tools for MAPS. Masks for pupil finding (left) and tool allowing to keep MAPS in tight contact with MAD while moving it laterally, thanks to ball casters (right).

One crucial point is the positioning of the PSs at the right altitude:

- The ground layer PS should be as close as possible from the pupil, and in any case lower than 0.50 km. In MAPS it has to be put close from the pupil mask without touching it. We achieved placing it at 0.4 mm, equivalent to **0.11 km** in the atmosphere (as 1 km \Leftrightarrow 3.6 mm).
- The intermediate PS is supposed to be placed at an equivalent altitude of 6 km. The limitation of the drilled parts in the MAPS structure allow us to bring it down to **6.22 km** only. The altitude is measured relatively to the pupil mask thanks to a caliper, which brings the accuracy on the altitude to about 0.03 km.
- The altitude PS was set successfully to the specified height of **8.5 km**.

To comfort the measurements made with the caliper, we set up an optical technique to measure the altitude of the Phase Screens (see Figure 3.6). In this setup, we plug 2 laser-fed fibers at the borders of the FoV of MAPS, and the simultaneous exit beams are projected on a screen (thanks to 2 folding mirrors). As the screen is not in a plane conjugated to the PS, we see the shape of the PS's dig levels on the screen (details on the PS are given in the section 3.4). Thanks to the folding mirrors mounted on tip-tilt mounts, we make the 2 images overlap in a way so that the patterns coincide. Then by simply measuring the ratio between the pupil and the 'meta-pupil' diameters (overlap), and knowing the angular separation θ between the two stars simulated, we get the altitude of the PS through the formula:

$$\text{alt} = \frac{D}{\theta} \times \text{Overlap}, \quad (3.1)$$

where D is the telescope diameter .

3. MAPS, A TURBULENCE GENERATOR FOR MCAO

The accuracy of this method is very good: around 1 %. We found the following values for the altitude of the 3 PS:

- 8.59 ± 0.08 km
- 6.25 ± 0.06 km
- 0.23 ± 0.01 km

This method being not so easy to implement, we decided to rely in the future on the measurements made with a caliper.

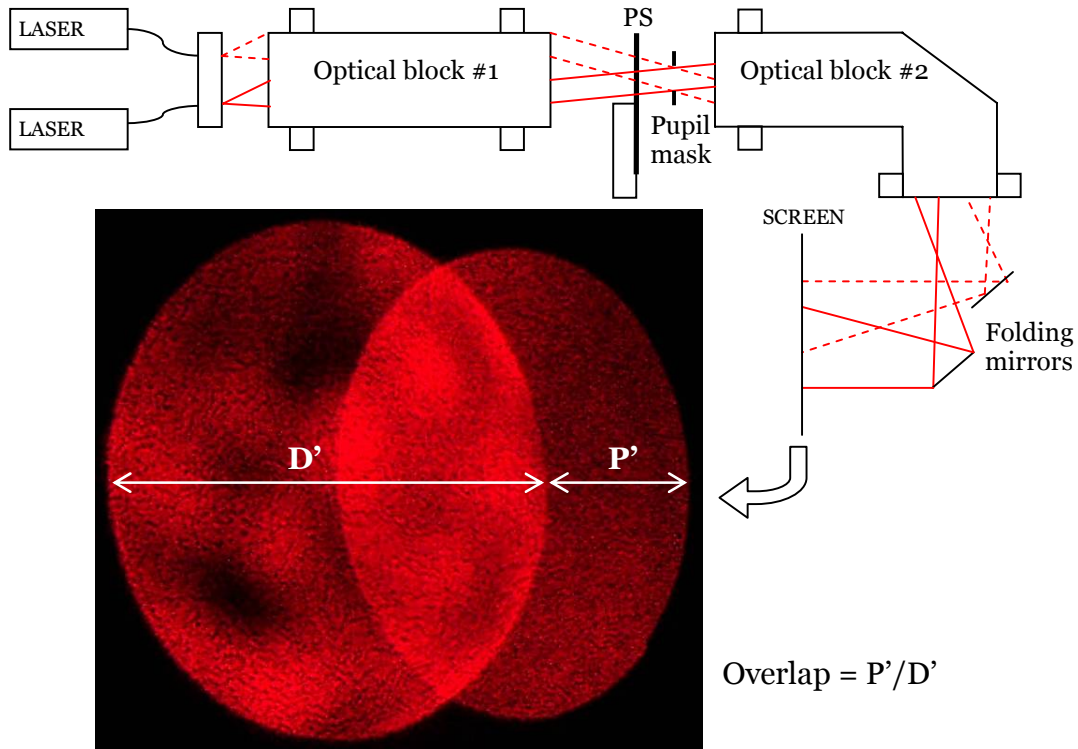


Figure 3.6: Setup used for positioning the altitude of the PS blocks.

3.3.3. Optical quality testing

Once aligned, MAPS has been tested in its flat configuration, i.e. with “dummy” PS mounted instead of the real ones (glass plates of the same material as the PS, but with no turbulence imprinted in them). The goal was to determine the aberrations produced in the 2 arcmin FoV. The measurement was made in double-path thanks to a compact Fisba interferometer (Figure 3.7).

3.3 OPTO-MECHANICS

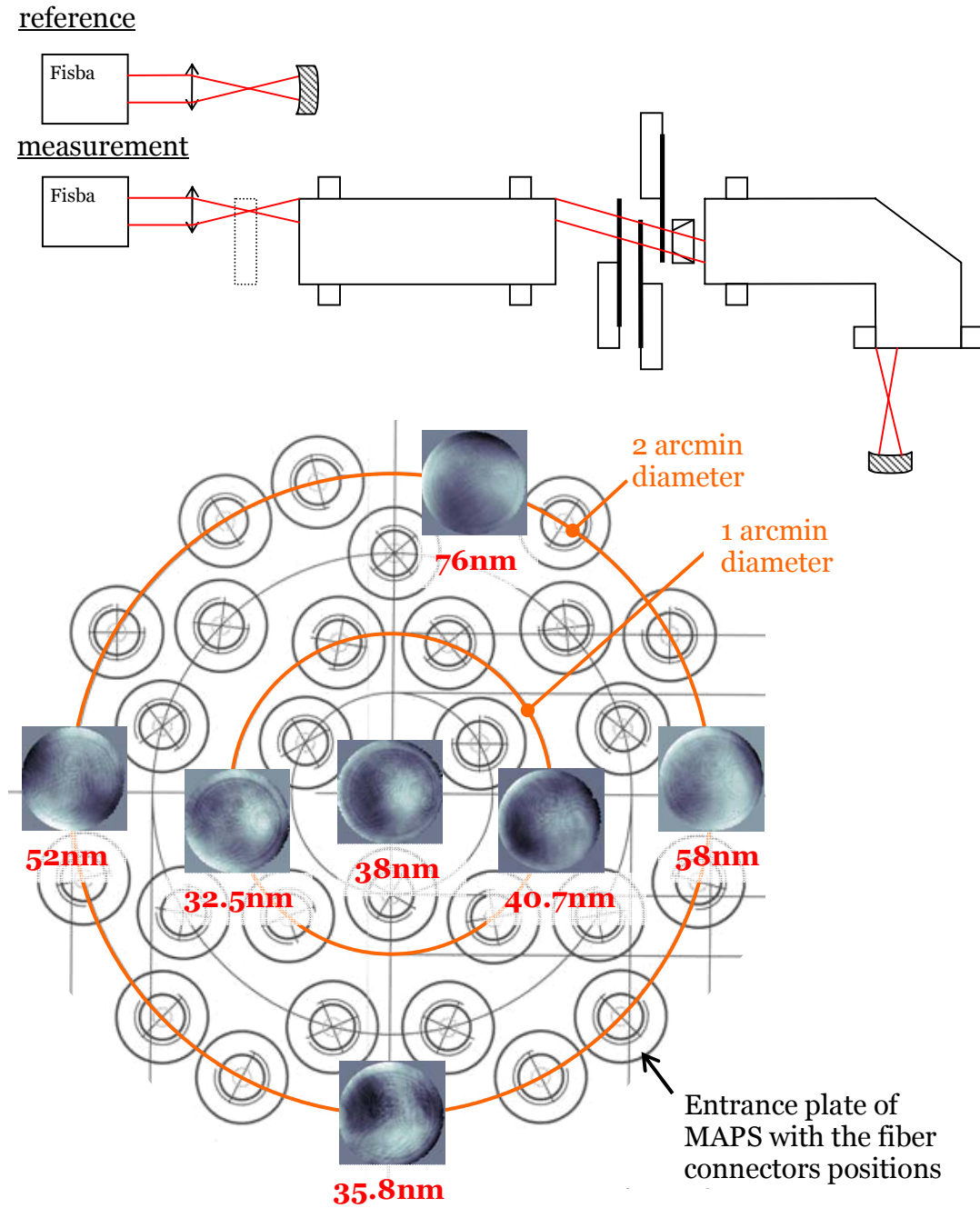


Figure 3.7: Setup for testing of the optical quality of MAPS, and result of the measurements in the FoV: interferometer WF measurement and rms WF error.

The amount of aberrations measured is less than 40 nm rms in the first arcmin of the FoV, and it goes up to 76 in one side of the 2 arcmin FoV. Those values are in agreement with the ones measured by the manufacturer, and almost in the specifications, which were 40 nm on-axis and 55 nm at the border. Anyway, those are low order and static aberrations in the common path of MAD, so they will be easily corrected by the AO loop.

3.3.4. Side effects

Rotation of the image

When one dummy PS is set in rotation, we notice that the image of a star simulated by MAPS rotates. This is due to the non parallelism of the 2 faces of a PS, and doesn't depend on the perpendicularity of the PS to the beam. Integrated images taken by rotating 3 different dummy PSs are shown in Figure 3.8. We measured amplitudes of 0.13, 0.21 and 0.23 arcsec equivalent on the sky.

To get the angle of shift produced by the PS, we have to multiply by the ratio of the apertures of the full telescope to the one of the beam in MAPS (8 m to 15 mm) and finally multiply by 2 to get the angle between the two faces of the PS. We obtain values of **2.3, 3.7 and 4.1 arc minutes** for the three dummies we have, while the specification was of 10 arc minutes.

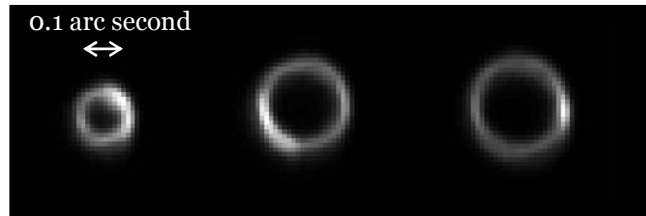


Figure 3.8: Integrated images of the rotation of the spot.

Ghosts

Without PSs, MAPS appears to create no ghosts in the output focal plane, although not all the optics are coated. When we introduce one PS in the beam, one ghost appears, due to the reflection on the two sides of the glass window (the screens haven't been coated against reflection). When we put a second window, a second ghosts appears, plus 4 more ghosts due to the reflections between the screens. In the end, with 3 PSs, 15 ghosts appear in the focal plane (Figure 3.9) rotating with the Phase Screens, and with all approximately the same amplitude measured as **0.1 %** of the amplitude of the main image.

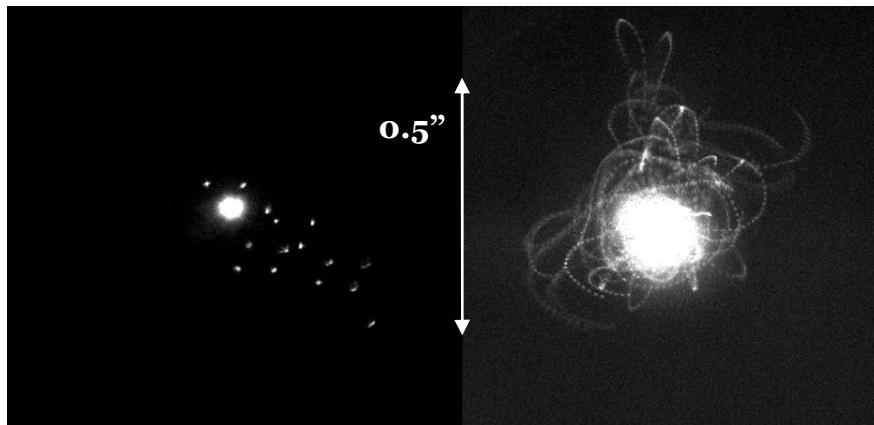


Figure 3.9: Short (left) and long exposure (right) images of the ghosts around the main spot; saturated images with logarithmic scale.

3.3 OPTO-MECHANICS

3.3.5. Light source system

Fibers

MAPS shall emulate up to 12 NGSs for correction and performance evaluation with MAD. The NGS are simulated using single-mode fibres, 9 μm core, transmitting from 500 to 2500 nm of wavelength. The size of the core is dimensioned to reproduce diffraction limited images of NGSs down to 600 nm. The fibres are mounted in so-called V-groove assemblies (Figure 3.10) that allows fitting a large number of fibres in a small area, and prevents us from having to route a great amount of individual fibres around the MAD bench. Such assemblies are constituted at one end of the V-groove itself, that is several fibres (4,8,12,32,...) rigidly mounted in array with a spacing of 250 μm , and at the other end the termination for the fibres are standard SMA connectors. A breakout box assures the transition between bare fibres and jacketed fibres.

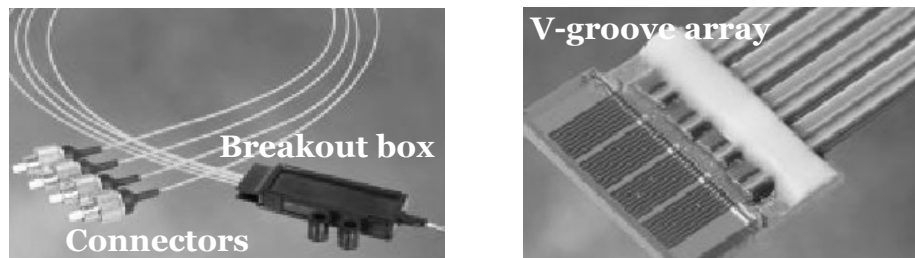


Figure 3.10: V-groove assembly. The V-groove endface is attached to the light source while the other end's FC connectors are attached to the interface in the input plane of MAPS.

The fibres are distributed in four bunches: one of 12 fibres and three of 8 fibres, so a total of 36 fibres. While the 12 fibres bunch face directly the source, neutral density filters are placed in front of the 8 fibres bunches in order to dim the light entering. The filters are chosen so that they let respectively 40, 16 and 6.4 % of the light pass through, leading to an attenuation of respectively 1, 2 and 3 magnitudes. Thus MAPS permits to simulate 4 different star magnitudes at the same time (with a maximum of 12 fibres for the brighter magnitude and 8 fibres for the others), the magnitude of the brightest star being determined by the dimmer of the source.

Light source

It turned out that the light source foreseen for MAD (integrating sphere containing a 50W halogen-tungsten lamp and on which are plugged single-mode fibers) was not powerful enough for the high flux tests we intended to perform with MAPS, although it was still enough for the calibration procedures (possibility to integrate longer). The brighter magnitude achievable was around 12, and a value of 8 would have been desirable. Thus a new source had to be designed and tested.

This new source system (Figure 3.11.a) includes a power supply, a lamp, a fiber bundle, a relay box to the V-groove fibers, and ND filters to simulate the 4

3. MAPS, A TURBULENCE GENERATOR FOR MCAO

different magnitudes. The source itself is a standard ACE light source from Schott, containing the DDL lamp (giving the most uniform output). An IR filter is mounted at the output to limit the heating of the fiber bundle; it had to be removed for our use. In order to bring the light from the light source to the 4 channels of the relay box, we use another standard part from Schott: a randomized and calibrated fiber bundle. It can be connected to the ACE light source, and splits the light in 4 arms, with a uniformity of $\pm 10\%$. Those arms are plugged to a custom-made relay box (Figure 3.11.b), which allows placing simultaneously the 4 arms of the fiber bundle in front of the 4 V-groove arrays for an optimal illumination, and insert in-between the ND filters dimming the light for the different magnitudes simulation.

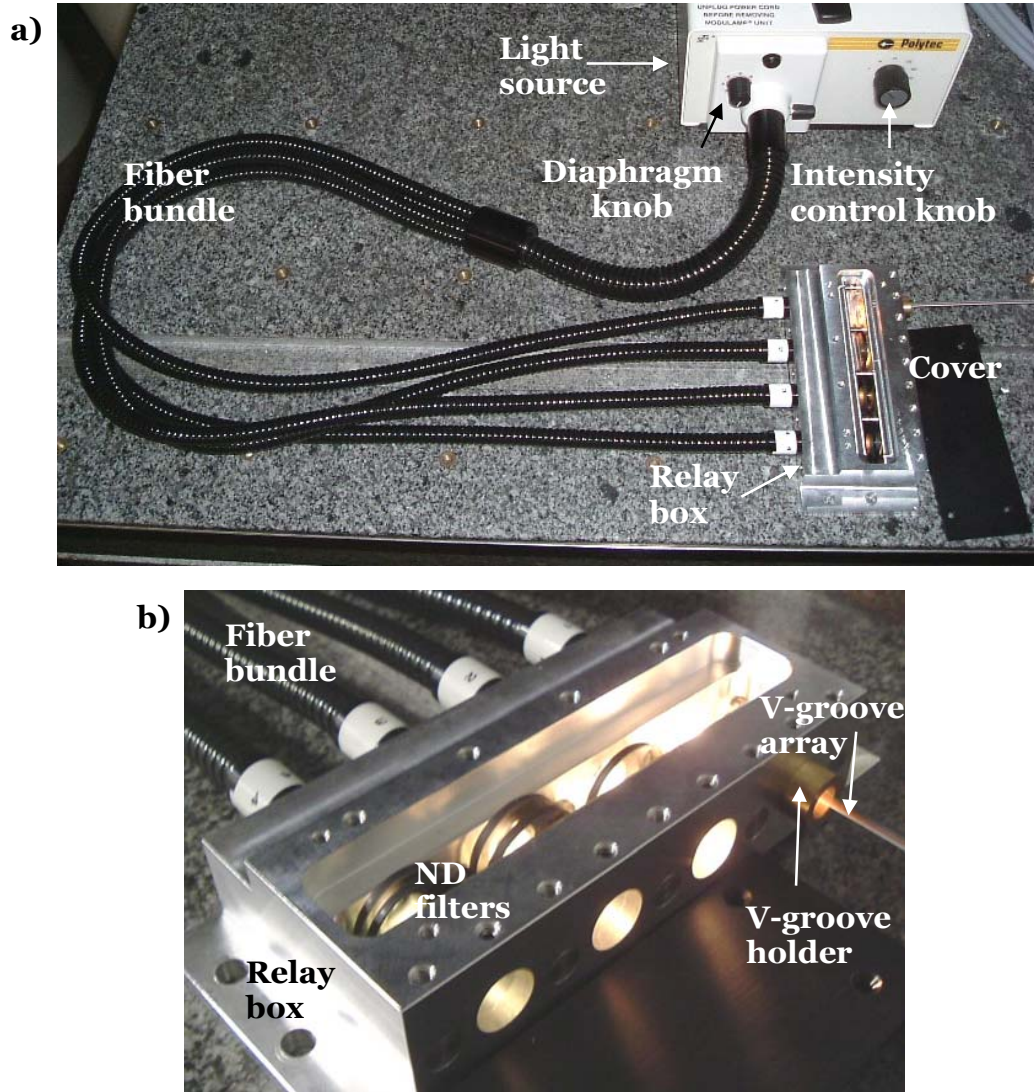


Figure 3.11: Source system for MAPS (a) and close-up view of the relay box (b).

3.3 OPTO-MECHANICS

Flux measurements

In order to characterize the flux delivered by the source described in the previous section and by the full MAPS system, we used several means:

- The datasheets or optical design of some parts give a first value of the transmission.
- The transmission of small refractive parts (PS blanks, ND filters, narrow band filters used for the characterization) could be measured with a spectrophotometer.
- To measure absolute flux from 400 to 1100 nm, we could use a calibrated Newport Si photodiode.
- To measure absolute flux from 800 to 1650 nm, we could use a calibrated Newport AsGa photodiode.
- To reach the highest wavelengths (from 900 to 2200 nm), we could use a Hamamatsu PbSe detector (not calibrated) with a lock-in technique.

The goal being not only to measure the throughput of MAPS but also to determine from which component could come an eventual drop of light intensity at a given wavelength, it was important to try as much as possible to test the components independently.

By combining those several techniques of flux measurement and narrow-band filters, we managed to cover the full wavelength range of MAPS (from 550 to 2200nm actually) [38]. The calibrated Si and AsGa probes allow getting an absolute value of the flux measured in Watts/nm, overlapping at 900nm. The PbSe source is calibrated thanks to measurements at 1193 and 1649nm overlapping with AsGa measurements.

The Figure 3.12 shows the maximum flux delivered by MAPS at 6 different wavelength. We can see that the flux is decreasing slowly between 650 and 1700 nm (star magnitude constant to 5.5), is significantly lower at 550 nm (magnitude 7) and drops dramatically at 2200 nm (flux 200 times lower). This is consistent with what we observed when trying to record images with the IR camera and the narrow K band filter.

We identified the fiber bundle as the responsible for the drop of flux in the K band. This problem has been partially solved by using a shorter bundle (0.5 meter instead of 2), bringing 100 times more flux at 2200 nm.

3. MAPS, A TURBULENCE GENERATOR FOR MCAO

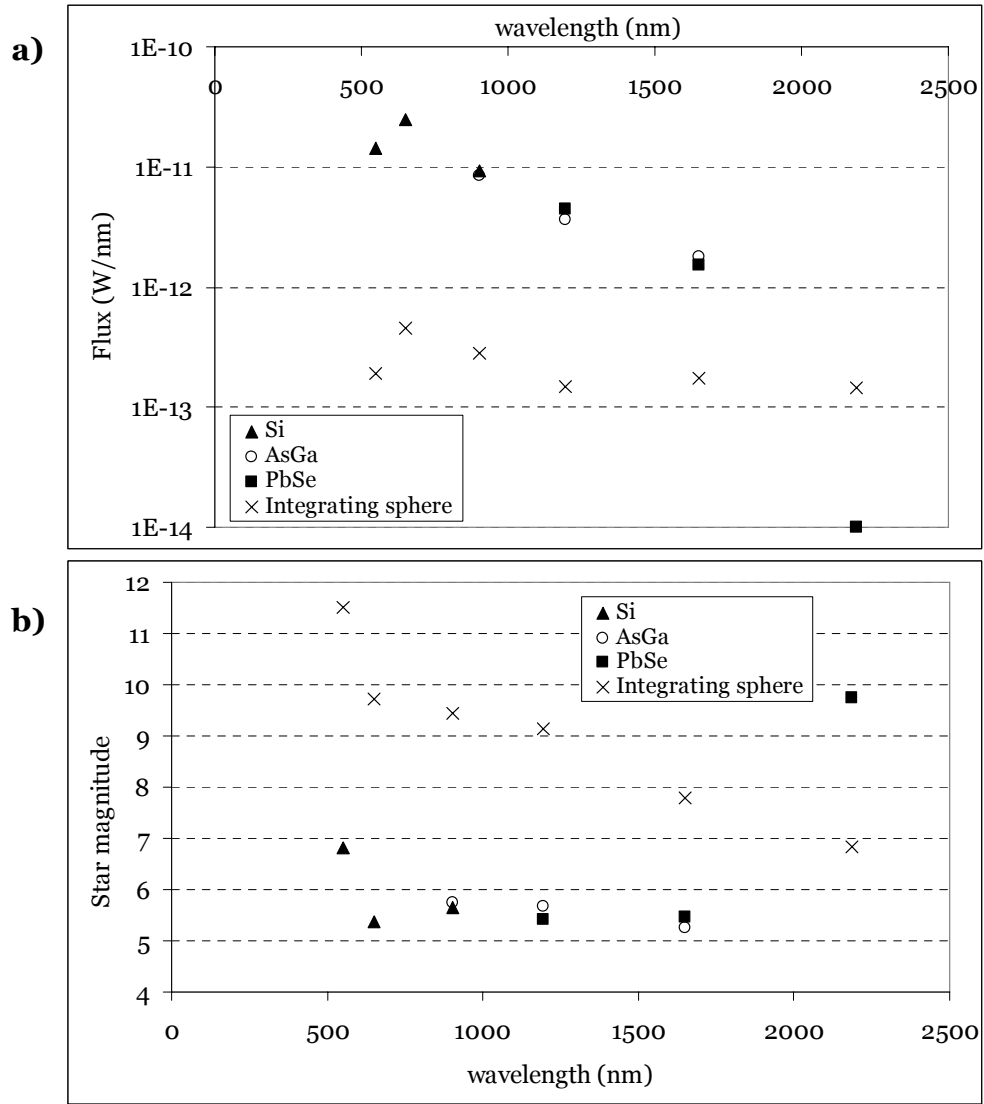


Figure 3.12: Maximum flux (a) and equivalent magnitude (b) delivered by MAPS in different bands, and comparison with the original plan to use the integrating sphere of MAD.

3.4 PHASE SCREENS

3.4. Phase Screens

3.4.1. General Assumptions

MAPS is required to have a set of four phase screens, only 3 of which will be used at any time to simulate two different seeing conditions. The PSs are optical elements capable to transmit the light. They are circular plates (100 mm in diameter) with a hole at the centre for fixation of the rotation axis. The PSs has encoded on their surface a bi-dimensional aberrations map with spatial distribution typical of the atmospheric turbulence. The mechanical dimensions of a PS are shown in Figure 3.13.

A plane WF passing through the PS emerges distorted accordingly to the aberrations encoded in the glass. The useful surface of the PS is an annular ring around its centre, so that the WF shift seen through a 15 mm pupil centered on the annulus is evolving when the PS is set on rotation. The rotation speed gives the value of the wind speed simulated for this altitude.

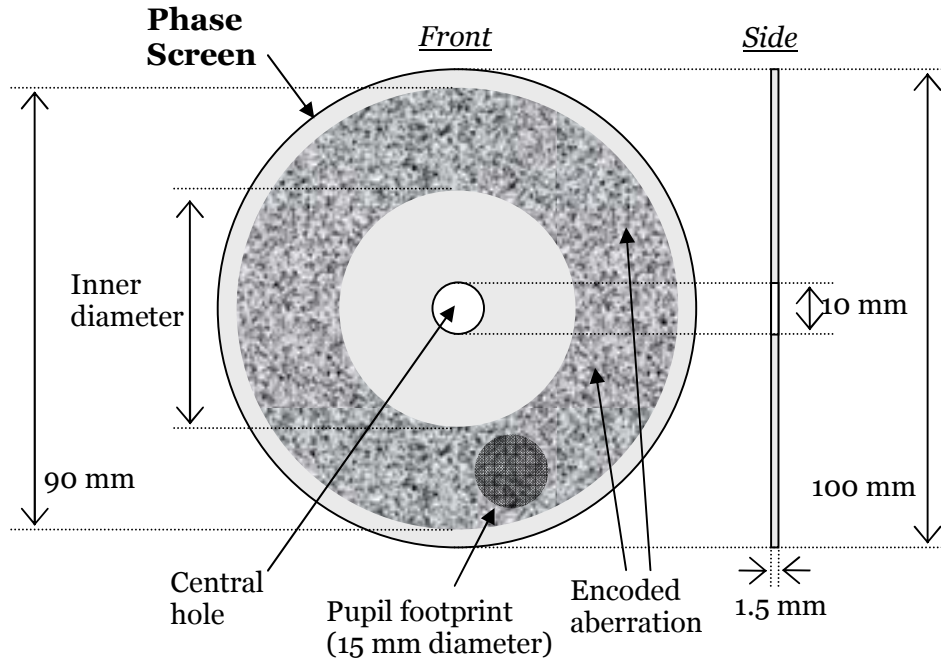


Figure 3.13: Dimensions of a Phase Screen. The inner diameter varies depending on the altitude at which the PS is intended to be used.

3.4.2. Designing the Phase maps

A finite outer scale of 22 m is considered [64] (the outer scale and other atmospheric parameters are defined in the section 2.4.2) and the properties of the turbulent layers we wish to simulate are summarized in the Table 3.1 [63]. PS-01 to PS-04 label four different phase screens, which combination allows reproducing the aberrations induced by the atmosphere above Paranal in two different conditions. The resulting simulated turbulence parameters at the level of the telescope are given in the Table 3.2.

3. MAPS, A TURBULENCE GENERATOR FOR MCAO

	Median @ ZD=30°				Good @ Zenith		
	Altitude (km)	r_0 (cm @ 0.5 μm)	Wind speed (m/s)		Altitude (km)	r_0 (cm @ 0.5 μm)	Wind speed (m/s)
PS-01	0.0 ± 0.2	20 ± 1	7 ± 3	PS-02	0.0 ± 0.2	30 ± 2	7 ± 3
PS-02	6.0 ± 0.2	30 ± 1	13 ± 6	PS-03	6.0 ± 0.2	50 ± 2	13 ± 6
PS-03	8.5 ± 0.2	50 ± 1	30 ± 15	PS-04	8.5 ± 0.2	80 ± 2	30 ± 15

Table 3.1: Atmospheric parameters for the MAPS phase screens allowing to produce two seeing conditions: median (left) and good (right).

Parameter (@ 500 nm)	Median	Good
r_0 (cm)	14.4 ± 0.6	22.4 ± 1.2
Seeing (arcsec)	0.73 ± 0.03	0.46 ± 0.03
τ_0 (ms)	3.4 ± 0.2	5.5 ± 0.3
θ_0 (arcsec)	2.2 ± 0.1	3.6 ± 0.1

Table 3.2: Theoretical global atmospheric parameters resulting from the use of the Phase Screens combinations defined in the Table 3.1.

The phase screen turbulence data is produced using the inverse Fourier transform of a Von Kármán spectrum (Figure 3.15). Among numerous possible random maps were kept the ones that show the smallest Peak-To-Valley (PTV) phase over their surface, while keeping the global atmospheric properties and particularly the phase variance in the pupil. This property helps for the realization of the PS as a high PTV is always practically hard to achieve. The size of the phase maps is 900 x 900 pixels, leading to pixels of 100 microns in the case of a ring of aberration of 90 mm in diameter.

Four phase maps in agreement with those requirements were found (Figure 3.14).

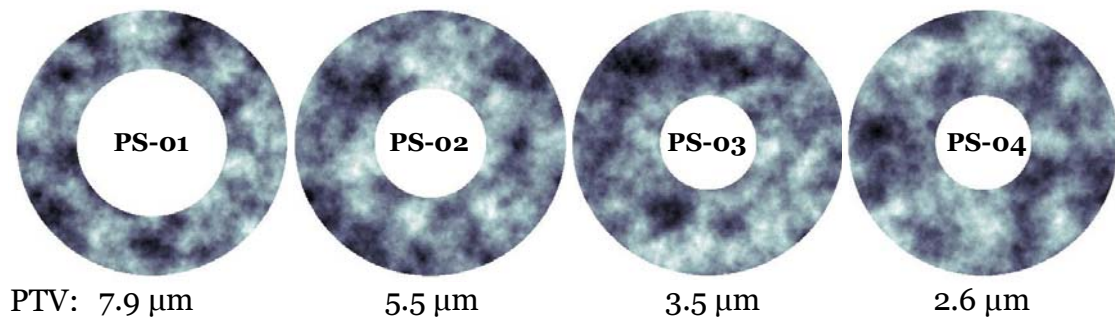


Figure 3.14: Phase maps to be imprinted on the 4 phase screens. The width of the imprinted annulus differs, as the footprint of the 2 arcmin meta-pupil increases with the altitude to which the PS is conjugated. The external diameter is 90 mm for all while the internal diameter is respectively 50, 37, 32 and 32 mm for the Ps-01 to PS-04.

3.4 PHASE SCREENS

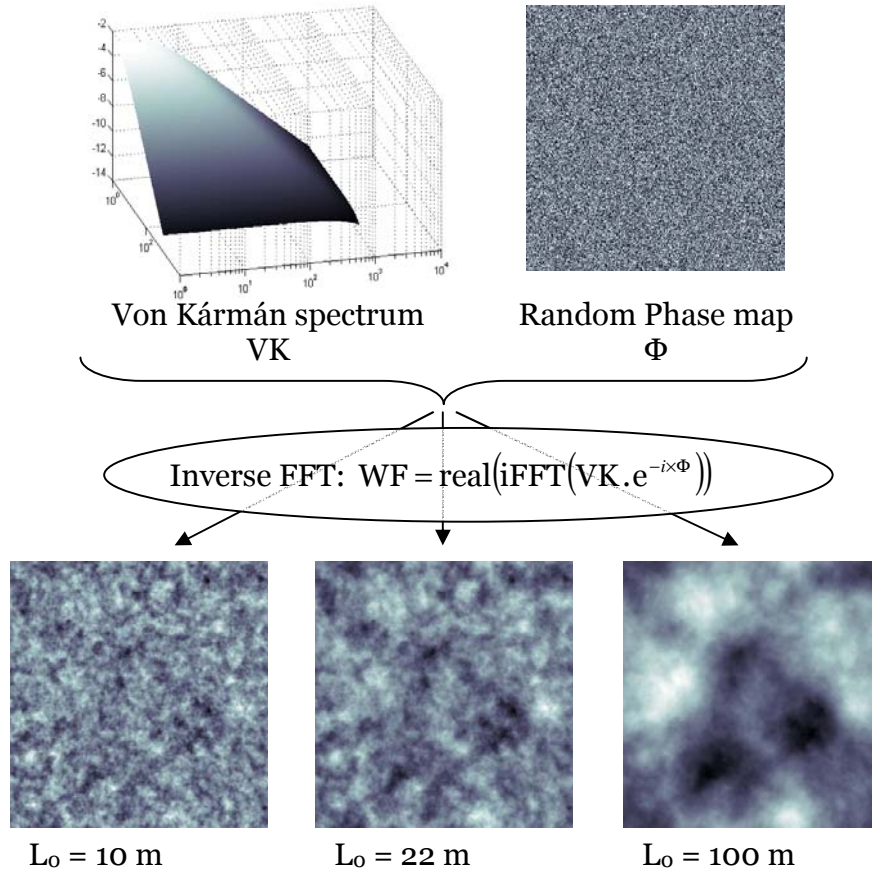


Figure 3.15: Generation of Phase screens with different outer scales, using the inverse Fourier transform of a Von Kármán spectrum. We can recognize the same structures on the WFs being generated from the same phase map, but with a different repartition of the spatial frequencies.

Several simulation were performed using those phase maps, the first one being the production of a long-exposure PSF for both combinations of screens (see how it is done in the next section), and the fine scaling of the WF map. Indeed the equation used to create the phase maps doesn't take into account the strength of the turbulence to produce; this is a parameter to set afterwards by scaling the WF according to a given parameter defining the seeing.

At that point we have decided to scale the PS turbulence so that the FWHM of the PSF is equal to the seeing specified in the Table 3.2, although this is not the way the seeing is defined and measured at Paranal by the Differential Image Motion Monitor (DIMM) [89]. The consequences of this choice are discussed in the conclusion of this chapter (section 3.5).

3.4.3. Testing the phase maps

Seeing, r_o and FWHM at 500 nm

More simulations were done on the phase maps once scaled (i.e. the maps sent to the manufacturer for imprinting on the PSs), such as the decomposition on the Zernike polynomials and the measurement of the variance over one rotation. Those tests have been carried out for individual PS as well as for theoretical combinations of the three PS. They are all summarized on the Figure 3.16 and described hereafter.

The FWHM is measure on a simulated long exposure PSF. By FFT, we image 100 WF realizations around the PS (or the combination of PSs) and sum their intensities. The PSF cannot be assimilated to a Gaussian in the case the outer scale of the atmosphere is not infinite. Thus the FWHM of the images cannot be computed after Gaussian fitting, and we designed instead a routine that finds accurately the centroid of the spot, and sorts all its points relatively to their distance to it. We obtain the kind of plot shown on the Figure 3.17, and the value of the FWHM is measured on an average fit of the data (red curves). The residual speckles that we observe on the images are due to the fact that the simulation is monochromatic.

The Fried parameter r_o is deduced from statistics on the simulated WF measurements. For a given set of $N=100$ realizations around the PS, we used 3 different procedures to retrieve 3 values of r_o :

a) For each WF realization n , the variance σ_n^2 over the aperture is computed, and the N values are averaged to get the mean variance $(\sigma^2)_a$.

b) Each WF realization n is projected on the $Z=60$ first Zernike polynomials. The outputs are N lists of Z coefficients $a_{i,n}$. The variance σ_i^2 of each coefficient over the N realizations is computed. The quadratic sum of all the variances gives us the variance of the turbulence $(\sigma^2)_b$.

c) The list of variances σ_i^2 obtained in b) are fitted to a theoretical Van Kármán spectrum, and it is the variances of the fit $\sigma_{i,VK}^2$ which are added to get the variance of the turbulence $(\sigma^2)_c$. On the example of the Figure 3.17 one can see how the theoretical and measured spectra agree.

The variance is linked to the Fried parameter:

$$\sigma^2 = f(L_o) \times \left(\frac{D}{r_o} \right)^{5/3}, \quad (3.2)$$

where D is the telescope diameter, and $f(L_o)$ a scaling factor that depends only on the value of the outer scale; it is equal to 1.029 for an infinite L_o and to 0.207 when $L_o = 22m$. For the 3 different values of variance $(\sigma^2)_x$ we can then get the values of r_o :

$$(r_o)_x = D \times \left(\frac{f(L_o)}{(\sigma^2)_x} \right)^{3/5} \quad (3.3)$$

3.4 PHASE SCREENS

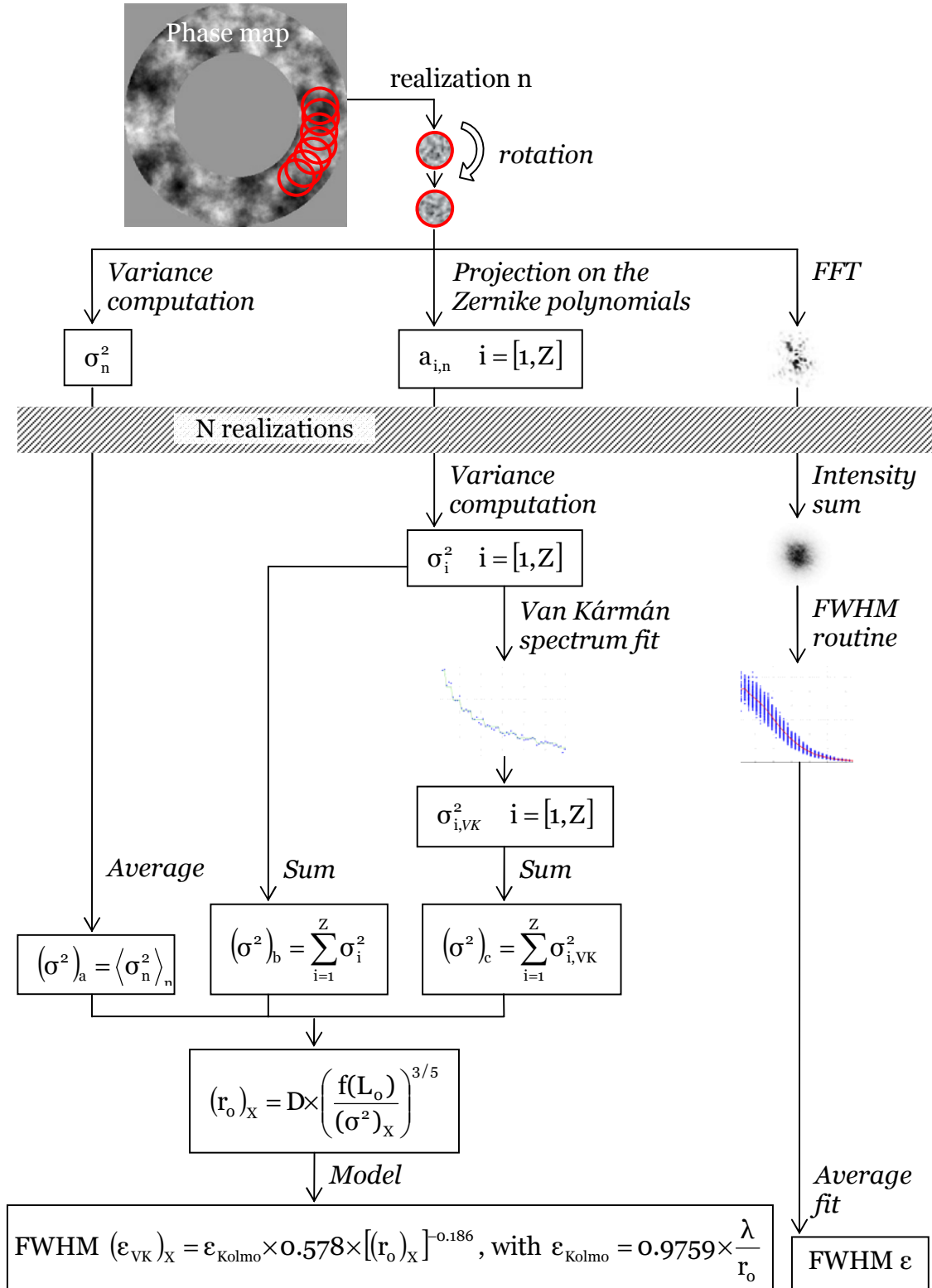


Figure 3.16: Summary of the different methods used to compute the seeing and the FWHM of the Phase Screens. We obtain then one direct value of the FWHM, and 3 values of r_o (indexed a, b and c) that can be converted into 3 more values of FWHM.

3. MAPS, A TURBULENCE GENERATOR FOR MCAO

The results of the measurements on the simulated PSs are given in the Table 3.3.

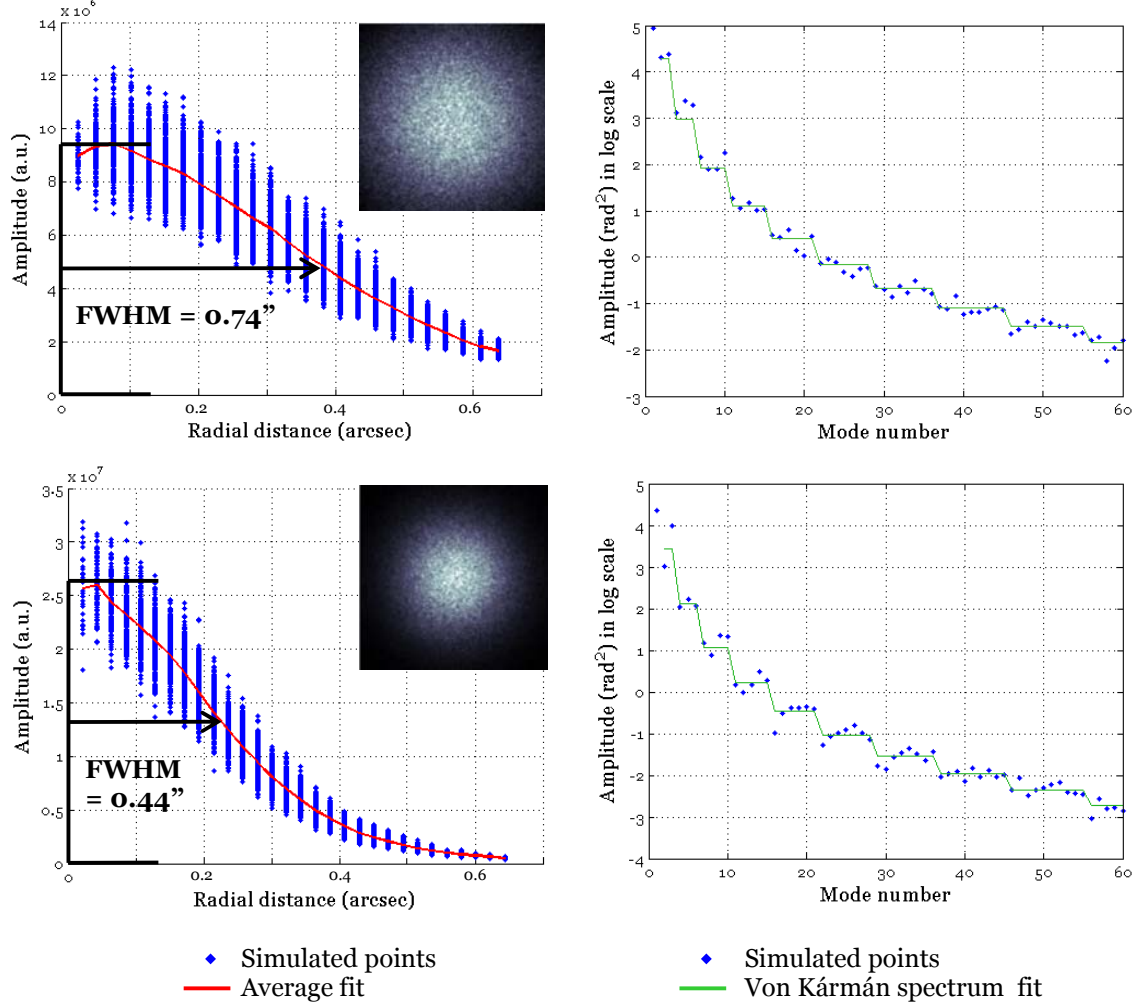


Figure 3.17: Simulation results at 500 nm: integrated PSF, PSF profile and variance of the projection on the Zernike polynomials in the case of the combination PS-01/02/03 (top) and PS-02/03/04 (bottom). Data obtained from a series of 100 realisations all around the imprinted annulus.

Linking the FWHM to r_0 through a model

With two independent ways of measurement (one on the WF and one on the PSF) we have at this point obtained values for the FWHM ε and for the Fried parameter r_0 . The 2 results can be cross-checked if one knows the law that links those 2 parameters.

The Seeing is **defined** in [89] (and demonstrated in [16]) to be:

$$\text{Seeing} = 0.9759 \times \frac{\lambda}{r_0} \quad (3.4)$$

3.4 PHASE SCREENS

In the Kolmogorov case, the Seeing is equal to the FWHM of a long-exposure image:

$$\varepsilon_{\text{Kolmo}} = \text{Seeing} \quad (3.5)$$

The Van Kármán case has been studied by R. Conan in [16] and leads to an expression of the FWHM as a function of r_o and L_o much more complex than (3.4). In this case there are 3 ways of linking the FWHM to r_o :

1. Using the code written by R. Conan. It computes the theoretical FWHM of the long-exposure image of a WF perturbed by turbulence characterized by $[L_o, r_o]$. Its drawback is that it doesn't give an analytical expression for the FWHM, thus one cannot get back r_o from a given FWHM for instance.
2. For a practical use, the results given by this code has been approximated by:

$$\left(\frac{\varepsilon_{\text{VK}}}{\varepsilon_{\text{Kolmo}}} \right)^2 \approx 1 - 2.183 \times \left(\frac{r_o}{L_o} \right)^{0.356}, \quad (3.6)$$

which was obtained by Tokovinin [95] by fitting the numerical results, and gives relative errors within ± 1 % for $L_o/r_o > 20$. For $L_o = 22$ m, we have then:

$$\left(\frac{\varepsilon_{\text{VK}}}{\varepsilon_{\text{Kolmo}}} \right)^2 \approx 1 - 0.726 \times (r_o)^{0.356} \quad (3.7)$$

3. In our case of use of weak PS alone and at IR wavelengths, we rather used another *ad hoc* expression valid down to $L_o/r_o = 7$, with $L_o = 22$ m:

$$\left(\frac{\varepsilon_{\text{VK}}}{\varepsilon_{\text{Kolmo}}} \right)^2 \approx 0.334 \times (r_o)^{-0.371}, \quad (3.8)$$

leading to the expression used in the Figure 3.16:

$$\frac{\varepsilon_{\text{VK}}}{\varepsilon_{\text{Kolmo}}} \approx 0.578 \times (r_o)^{-0.186} \quad (3.9)$$

Using such a simplified expression, one can get back r_o from a given FWHM, and establish a trend for the evolution of the FWHM with the wavelength.

The comparison between the numerical results and the two approximations is shown on the Figure 3.18, and justifies our use of the second one, which gives larger errors (within ± 5 % for r_o between 0.1 and 1 m) but is still valid until $r_o = 3$ m (within ± 15 % of error).

In the following, we will use as much as possible the 1st solution (the code itself) to estimate the FWHM, and use the 3rd solution only for drawing trends.

3. MAPS, A TURBULENCE GENERATOR FOR MCAO

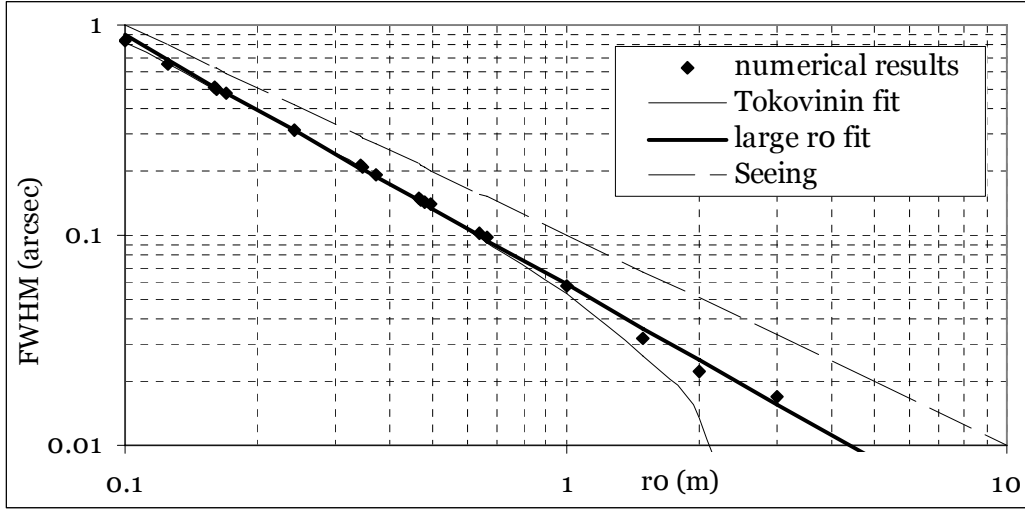


Figure 3.18: Fitting error due to the approximation of the numerical results of the FWHM as a function of r_0 , for both the equations (3.7) and (3.8). The Seeing, equal to the FWHM in the Kolmogorov case and defined in the equation (3.4), is also plot for comparison. The wavelength considered is 500 nm.

The values for r_0 and the FWHM are given in the Table 3.3 for the 4 PS and their combinations. We can see that after scaling, the values of the **FWHM** reach well the **seeing values** specified in the Table 3.2.

In the same table one can compare the values for r_0 obtained with the 3 methods detailed on the Figure 3.16. We see that the methods a and b give always almost the same result, while the method c gives slightly larger values of r_0 . We decided to use as reference results the ones given by the method c (grey shaded in the Table 3.3), as they correspond better to the way r_0 is measured in practice, and as the fit is done on high orders, it is insensitive to the measurement error on the low orders.

	FWHM (arcsec)	r_0 (cm)			Seeing= ϵ_{Kolmo} (arcsec)	$(\epsilon_{\text{VK}})_c$ (arcsec)
		a	b	c		
PS-01	0.56	13.8	14.0	13.9	0.73	0.59
PS-02	0.345	21.5	21.8	24.1	0.42	0.320
PS-03	0.202	35.9	36.5	39.4	0.255	0.182
PS-04	0.127	55.4	56.3	61.4	0.173	0.107
PS-01+02+03	0.76	9.73	9.90	10.6	1.01	0.79
PS-02+03+04	0.43	16.3	16.5	17.8	0.60	0.45

Table 3.3: FWHM and r_0 values for all the PSs and their combinations, corresponding Seeing values (@ 500 nm), and prediction of the FWHM value from R. Conan's code using the values $(r_0)_c$ and $L_0=22$ m.

3.4 PHASE SCREENS

By applying the equation (3.4) we get the corresponding values of the Seeing, as it would be measured at Paranal by the DIMM. We notice that it is much higher than the FWHM we actually measure (from 30 to 40 % higher). This proves that an outer scale of 22 m cannot be considered as infinite with respect to a telescope aperture of 8 meters. So in the end the two sets of PSs for MAPS have been designed to create Seeings of **1.01 and 0.60 arcsec** and FWHM of respectively **0.79 and 0.45 arcsec** at 500 nm.

Finally in the Table 3.3 is also shown the prediction of the FWHM value from the equation (3.8) using the values $(r_0)_c$. The agreement with the values coming from direct measurement is very good, and the difference always smaller than 0.03 arcsec, for individual PSs as well as for the combinations.

Chromatism of the turbulence

Chromatism is defined as the sensitivity to color (= wavelength). In this sub-section we discuss about the chromatism of the turbulence (i.e. the influence of the wavelength on the FWHM), which is not to be confused with the chromatism of the PS substrate (variation of the refractive index with wavelength) which is discussed in the section concerning the PS manufacturing. Obviously the latter has an influence on the first.

Simulated PSFs (at 500 and 2200 nm, static and integrated) are shown on the Figure 3.19. It is interesting to notice the size of the speckles, much larger in the IR. As foreseen, the size of the integrated PSF is smaller in the IR than in the visible.

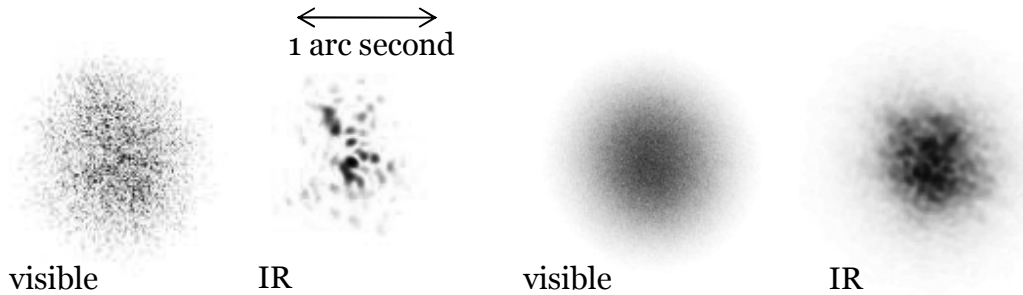


Figure 3.19: Simulated visible and IR PSFs, static (left) and integrated over one rotation of the slowest PS (right), resulting from the use of the combination PS-01+02+03 in MAPS.

The Figure 3.20 summarizes for all the PS and their combinations several values and trends (the trends are relative to the measurement at 500 nm):

- The values of the FWHM measured on images simulated from the phase maps to be imprinted in the PS (points). At 500 nm they are the values given in the previous section (Table 3.3). The other wavelengths are 550, 800, 1187, 1644 and 2188 nm, to match the further measurements on real PSs (section 3.4.7).
- The trend following the law in $\lambda^{-1/5}$ (solid lines), valid only in the Kolmogorov case.
- The trend following the approximation presented in the equation (3.8) and that follows a law in $\lambda^{-0.423}$ (dashed lines).

3. MAPS, A TURBULENCE GENERATOR FOR MCAO

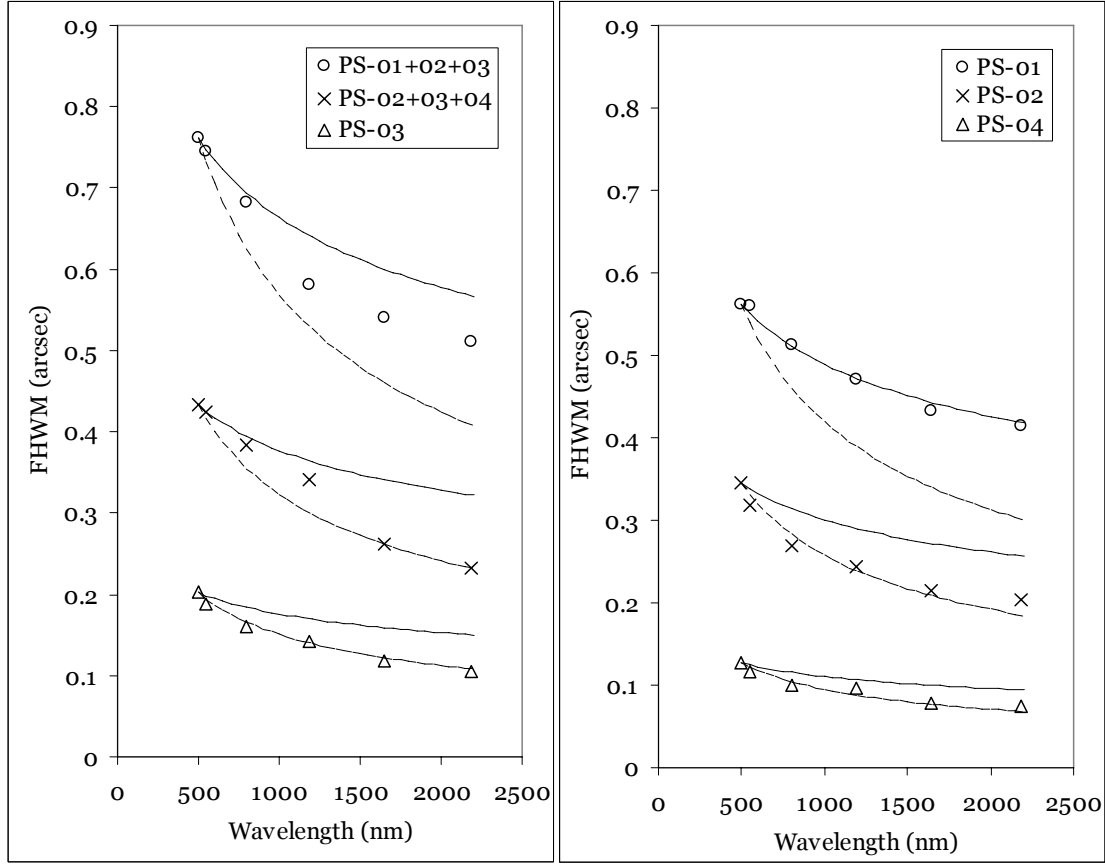


Figure 3.20: Chromatism of the turbulence. Simulated FWHM for all the PS and their combinations (points) and comparison with the expected behavior from the measurement at 500 nm according to the law in $\lambda^{-1/5}$ (solid lines) and to the approximation of the equation (3.8) (dashed lines). The accuracy on the measured FWHM with the routine we use is about ± 0.1 arcsec.

We notice that the measurement on the phase maps of the PS-02, 03 and 04 follow quite well the expected behavior in the case of a Van Kármán with a 22 meters outer scale. But concerning the PS-01 it follows almost perfectly the Kolmogorov case, which is surprising and contradictory with the results of projection on the Zernike polynomials and Van Kármán spectrum fit. As a consequence, the combination PS-02+03+04 follows also quite well the expected law, while the combination PS-01+02+03 shows FWHMs in the IR larger than they should.

3.4.4. Optical specifications

In addition to the phase maps to be reproduced, a set of detailed optical specifications was compiled [50] and sent to 14 possible manufacturers. The main specifications are:

- S1. WF Maps definition: The encoded aberrations shall have the same spatial resolution, phase resolutions and PTV of the Phase Maps (Figure 3.14).

3.4 PHASE SCREENS

- S2. Transmission efficiency: Each PS shall transmit >60 % (goal >80 %) of the light in the wavelength range 500-2500 nm.
- S3. Substrate chromatism: The refractive index change with respect to the wavelength in the material(s) of the PS shall be <2 % (goal 1 %) in the specified wavelength range for each PS.
- S4. WF quality: The WF quality in transmission over the full PS surface (100 mm diameter) before encoding the aberration shall be 60 nm rms.
- S5. Parallelism: The parallelism of the two faces of each PS shall be < 10 arcmin.
- S6. Spatial Resolution: The encoded aberrations shall have a resolution (pixel size) of $100 \pm 5 \mu\text{m}$.
- S7. Phase Resolution: The number of resolution steps is defined as the minimum number of equally spaced steps of phase in which the PTV of the WF Map can be divided. The number of phase resolution steps is 64 for PS-O1 and 32 for the others.
- S8. Phase Resolution step accuracy: The tolerance on the reproducibility of a single Phase Resolution step is ± 0.5 step.
- S9. Peak-to-Valley: The PTV of the 4 PSs WF maps are respectively 7.9, 5.5, 3.5 and $2.6 \mu\text{m}$, according to the phase maps.
- S10. Layer thickness: The atmospheric layer thickness, i.e. the thickness of the PS material(s) producing the turbulence, shall be smaller than $200 \mu\text{m}$.
- S11. Scattered light: The encoding technique shall not produce a scatter of more than 20 % of the light outside the area interested by perturbed image of the star. The encoding technique shall also prevent the creation of secondary perturbed images of the star (grating effect).

As already mentioned, the PSs were selected in order to have the smallest possible PTV while keeping the same variance. In the same way, most of the specifications were revised and relaxed in order to make the PS more easily feasible, less expensive, but still suited for our application. For instance the transmission doesn't need to be great as our star source is powerful, pixels of $100 \mu\text{m}$ are sufficient to have about 4 resolution elements per smallest r_0 , and we simulated that the discretisation in 64 steps imprinted with an accuracy of ± 0.5 step produces a negligible effect on the spectrum of the aberrations. The size of the imprinted area was also reduced to the minimum annulus in order to reduce the number of pixels to imprint.

However some specifications had to be kept strong due to the specificities of our application, especially the fact that the WF disturbance should remain almost unchanged over a wide wavelength range (500 to 2500 nm). This rules out fabrication techniques involving too "fancy" materials or combinations of materials, in particular Near-index matching technique, i.e. "sandwich" of oil between two glass plates that achieve at best a relative variation of index of 11 % in the sole visible range [79].

Eight companies answered positively, of which 3 seemed to be able to match the more stringent specifications [45], and finally ESO went through a prototyping phase with 2 of them (the third one being too expensive): SMOS from Mannheim (Germany) and SILIOS from Peynier close to Marseille (France).

3.4.5. Prototyping with SMOS

General assumptions

The company SMOS (Smart MicroOptical Solutions) is known for the fabrication of micro-lenses using the MSI (**Mask Structured Ion-exchange**) technology [4], and it has started to develop refractive Phase Screens for the Max Planck Institute for Astrophysics in Heidelberg [13] [20], to be used in a first version of MAPS [14] and in the framework of other projects.

The MSI technology is based on the principle that the diffusion of silver ions into a glass substrate increases its refractive index. In short, specific concentrations of silver ions in glass are achieved using a structured metallic mask (e.g. titanium) on the glass surface. For a small phase-shift value, the holes are spaced widely apart, while for a bigger value they are placed closer together. Thus, the refractive index of the diffusion layer can be varied in a systematic way, and a 2-dimensional map of phase-shifts can be produced. The glass is then immersed in a hot salt solution: some ions (e.g. Na^+) diffuse out of the substrate and are replaced by different ions (Ag^+) that come from the salt melt. After removal of the substrate from the salt solution, the metallic mask is removed by chemical etching, leaving behind a glass substrate with local differences in refractive index.

For the PS material, off-the-shelf glass substrates of 1.6mm thick HOYA SLW (Soda Lime White) were used. The glass is mostly composed of SiO_2 and Na_2O_3 . For the fabrication of each screen, the number density of 1.8 μm wide holes per 100 μm -wide square pixel in the metal mask ranged from about ten for the smallest phase-shift to about 1000 for the biggest phase-shift. Each screen was placed in a chemical solution to remove its metal mask. After fabrication, the glass substrates has a yellow color, being darker for longer diffusion times.

Prototypes

SMOS has been ordered one exemplar of the PS-01 (the most stringent one) in order for us to test the compliance with the specifications. After a non-compliant first prototype (Figure 3.21) [48], SMOS sent another one (Figure 3.22) corrected from the mistakes of the previous element: shape, undesired diffusion of the ions in the useful area, melting of the mask.

Some obvious advantages of the SMOS technique are that the aberrations imprinted in the PS are continuous (creating thus no grating effect) and that the process doesn't alter the roughness of the surface, which limits the light diffusion far from the PSF.

3.4 PHASE SCREENS

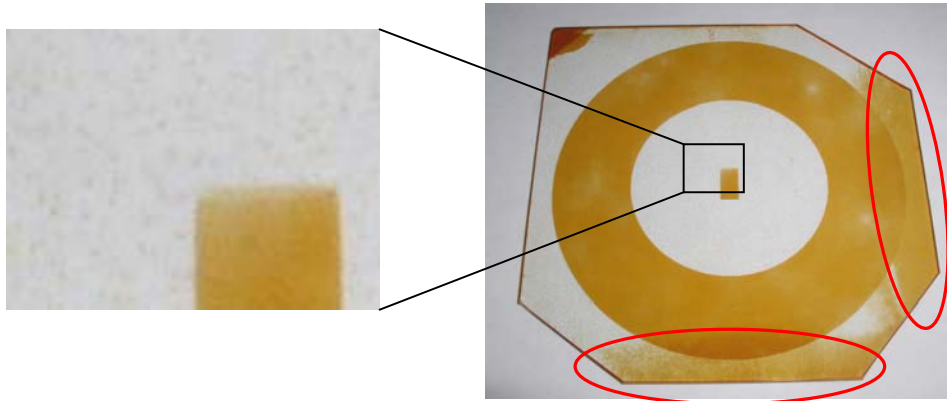


Figure 3.21: Visual aspect of the first SMOS prototype and enlargement of a non imprinted area. One can notice the two areas (encircled in red) of the PS where SMOS encountered some problems with the durability of the titanium mask during the ion exchange process. The marks at the top-left and at the center of the PS are for orientation. On the enlargement one can see the silver ions ‘spots’ present on back side of the screen.



Figure 3.22: Second SMOS prototype.

Testing

As foreseen the imprinted annulus on the PS is yellow, so one could wonder about the transmission in those areas. We have measured it between 500 and 2500 nm thanks to a spectro-photometer (Figure 3.23). Although we see a drop of transmission in the visible stronger than what the specification S2 allows, it is acceptable. However we can see on the PS that when the WF distortion is higher, the concentration of silver ions is higher and thus the transmission of the PS lower. The undesired effect on the PSF is that the spot intensity is proportional to the local aberrations imprinted in the PS.

3. MAPS, A TURBULENCE GENERATOR FOR MCAO

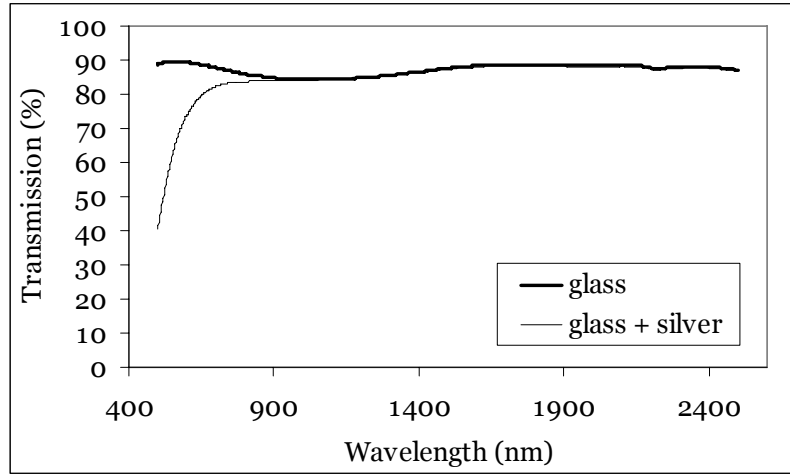


Figure 3.23: Transmission curve of the PS substrate (bold line) and imprinted area.

Another worry we had about the SMOS technique was its ability to create strong WF disturbances (PTV), as it has already been noticed by the Heidelberg team. This can be verified by placing the PS in rotation in a collimated beam, and imaging the turbulent spot onto a visible CCD camera (Figure 3.24, left). The expected FWHM (specification S1) of the long exposure PSF @ 550 nm is 0.54 arcsec, while we measured only **0.33 arcsec** on the prototype.

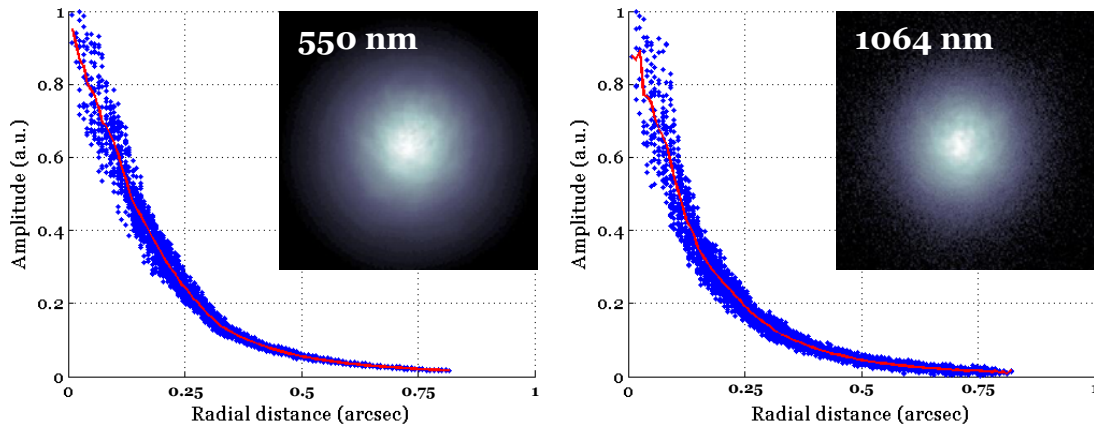


Figure 3.24: Integrated PSF and PSF profile measured over 1 rotation of the SMOS PS, at 550 (left) and 1064 nm (right). The estimated FWHM are respectively 0.33 and 0.24 arcsec.

One last specification to check about the SMOS PS was the chromatism of the turbulence produced (S3). The same procedure as previously described was repeated at 1064 nm (Figure 3.24, right) and we measured then a FWHM of **0.24 arcsec**. It is in agreement with the expected value of 0.25 arcsec in the case of the Von Kármán model of the atmosphere.

It is interesting to notice that the integrated PSF measured were never smooth at the center, but show a peak which could be the sign of a lack of low spatial frequencies.

3.4 PHASE SCREENS

3.4.6. Prototyping with SILIOS

General assumptions

SILIOS Technologies is known for manufacturing Micro-Optical Components including diffractive optical elements such as gratings. The specific technique proposed for the manufacturing of the PS is a **wet etching on glass substrate**, which description is given below (excerpt from [52]).

SILIOS manufactures the PS in its clean room facilities. 100 mm diameter substrates are compatible with off the shelf 4 inches silicon wafer equipments. The basic principle for encoding the 2^N levels of the phase map is to process N individual etching steps which either cumulate or not. The pattern of each step is defined by a photolithography process (photo-resist deposition, insulation, development). The N patterns are realigned with an accuracy of 0.5 micron (1/200 of a pixel width). A typical master mask pattern is presented in Figure 3.25. 21 master masks were designed (6 for the PS-O1 and 5 for the each of the PS-O2, PS-O3 and PS-O4). The main issues in the fabrication of the PS are linked to the accuracy of each etching depth and to the uniformity inside the wafer. The technique proposed by SILIOS provides $\pm 0.7\%$ as etching depth accuracy (max etching depth is about 20 microns) and $\pm 0.45\%$ as uniformity inside the wafer.

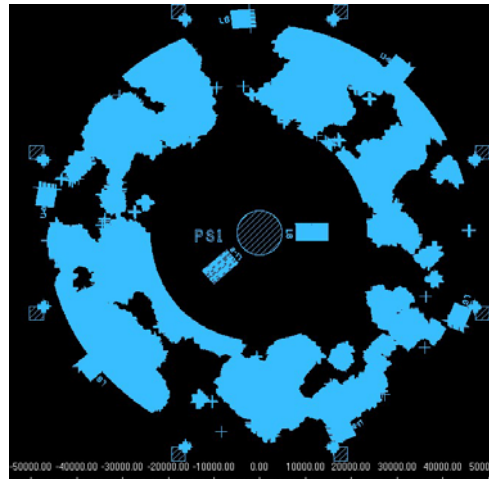


Figure 3.25: First mask (out of 6) used to create the PS-O1.

Prototypes

Manufacturing a full PS being too expensive, we have asked SILIOS to provide us with a sample prototype representative of the problems that would be encountered during the full PS manufacturing [49]. To this aim we designed a small (10 x 10 mm) phase map with some characteristics of a full PS-O1 (Figure 3.26):

- The area 1 is a discretisation to 4 levels of an area of the PS-O1, scaled to the PTV of this same PS. The goal was to check the ability of SILIOS to reach the high PTV, with a simplified number of masks (4 levels = 2 masks).

3. MAPS, A TURBULENCE GENERATOR FOR MCAO

- The area **2** shows the same pattern as the area **1**, but scaled so that the height between the levels is equal to the minimum height to be achieved in all the PSs (81 nm). The goal was to check the ability of SILIOS to imprint small steps with a great accuracy.
- The area **3** is a random phase maps with a Gaussian statistic, discretised to 4 levels, with a height between the levels equal to the one in the area **2**. The goal was to check the shape of the pixels and the ability of SILIOS to accurately imprint a great number of adjacent pixels with different levels, as it will be the case in the final PSs (the statistic in the area **3** was based on the statistic between adjacent pixels in a final PS).
- The area **4** is not imprinted, so that we could check the flatness, roughness and transmission of the raw material.

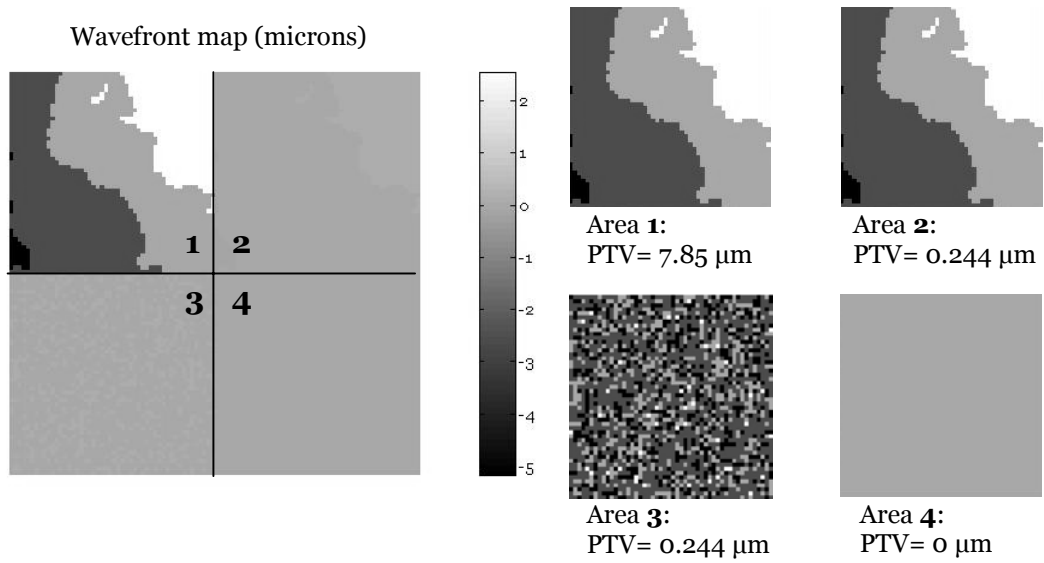


Figure 3.26: Wavefront map of the SILIOS prototype (left) and scaled views of the areas to be imprinted with the aberrations (right). Note that on the left map mainly only the area 1 is visible, because the range covered by the aberrations is much smaller in the other areas. The grey scale of the separated maps on the right has been scaled to cover the whole range so that the aberration can be seen clearly.

It required 4 successive prototypes to SILIOS to achieve one fully in the specifications (shown on the Figure 3.27 in its mount). The characterization of each prototype was done in the SILIOS premises thanks to a surface profiler, at ESO thanks to a simple optical setup (Figure 3.28) for testing statistical properties and a spectro-photometer for the transmission [47], and also at the IMT (Institut de Micro-Technologie) in Neuchatel (Switzerland) with a surface profiler coupled to a microscope [46].

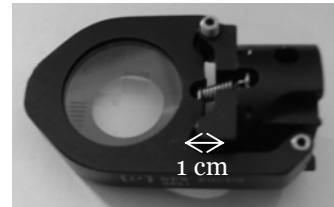


Figure 3.27: Mounted SILIOS PS prototype.

3.4 PHASE SCREENS

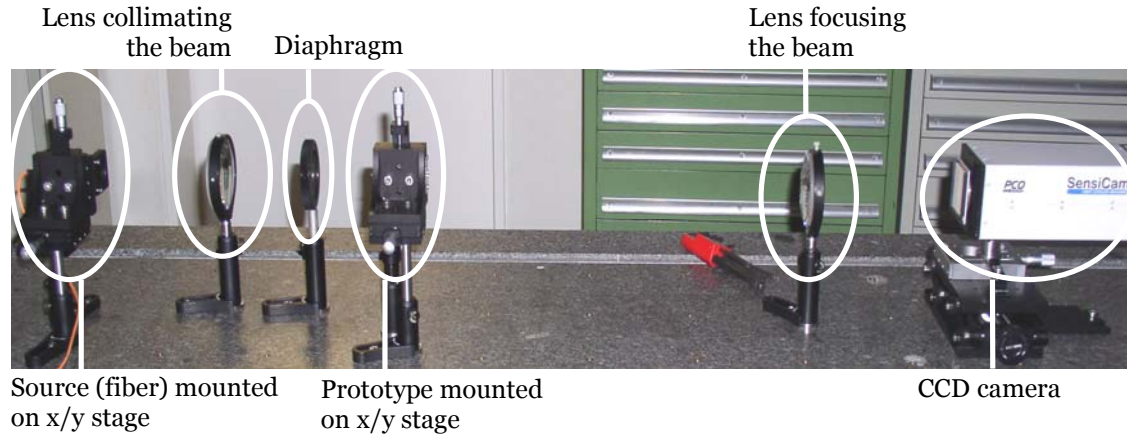


Figure 3.28: Test bench for the PS prototype. The sample is placed in a collimated beam, and an image is made on a CCD camera. A WF sensor can also be placed in a plane conjugated with the prototype. The x/y motion of the sample allows choosing the area hit by the beam, while the x/y motion of the source allows different incident angles on the prototype.

Testing at ESO

The Figure 3.29 shows the transmission in the area 3 and 4 of the prototype (with and without aberrations), well in the specification S2.

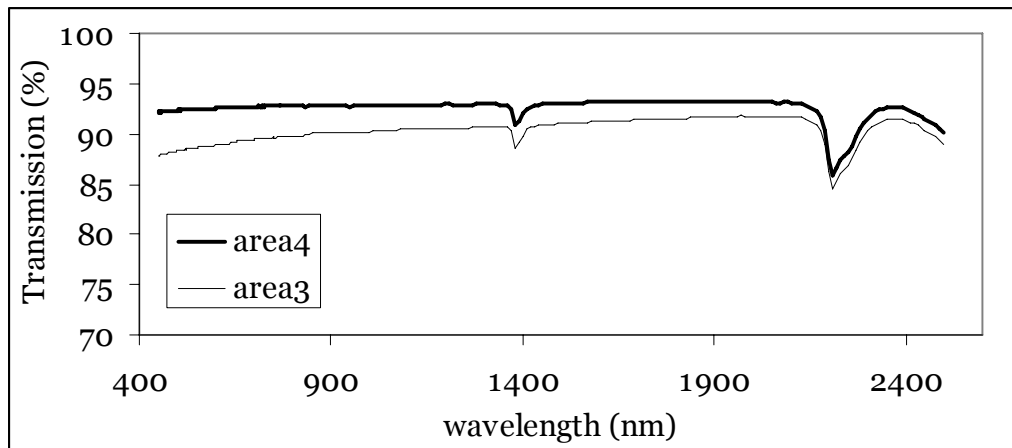


Figure 3.29: Transmission curve of the prototype from SILIOS. Substrate (bold line) and imprinted area (thin line).

The index variation of the substrate (Fuse Silica KU-1) is given in Figure 3.30, as furnished by the supplier. The chromatism of a PS after manufacturing is the same as the one of the raw material, as nothing is implanted in the glass during the photo-lithography. The relative index variation in the range 500-2500 nm is of 2.25 %, which is slightly out of the specifications S3 but that we accepted.

3. MAPS, A TURBULENCE GENERATOR FOR MCAO

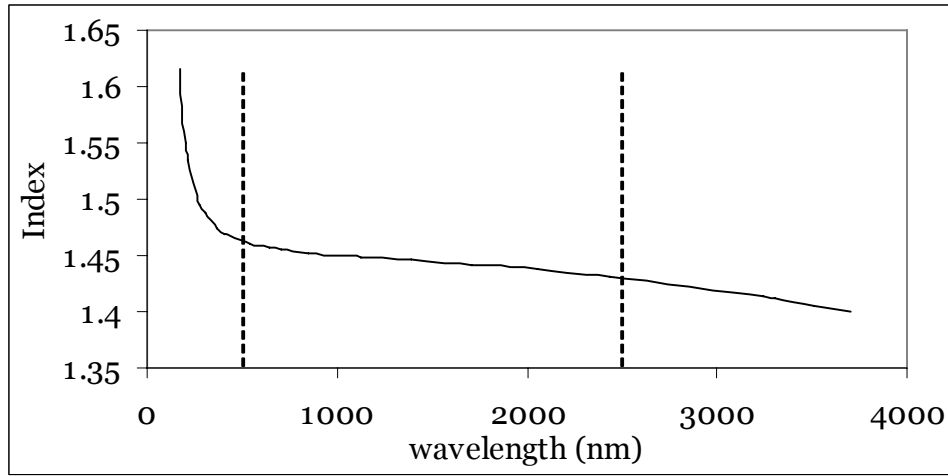


Figure 3.30: Chromatism of the glass used as the prototype substrate (Fuse Silica KU-1), and limits of our range of interest (vertical lines).

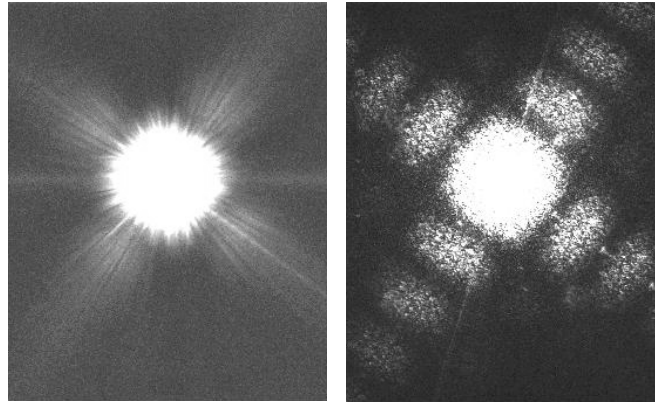


Figure 3.31: Static PSFs created by the area 3 of the prototype, in white light (left) and with a laser source (right). The images are highly saturated and in log scale to show the secondary spots. At least the ones due to the first and second grating orders are visible on the laser image.

It is specified that the encoding technique shall not produce a scatter of more than 20 % of the light outside the area interested by perturbed image of the star (S11). The cause of the scattering is a too high roughness of the glass surface after etching the levels. Its contribution is difficult to separate from the one of the PSF wings due to the turbulence. Another consequence of the use of an area of pixels etched with sharp edges is the apparition of grating effect (secondary images). This effect should be reduced to the minimum. The Figure 3.31 shows saturated images of the spot. We notice the presence of secondary images, 1500 times fainter than the main spot (~ 8 magnitudes). Those parasite images are quite far away: 2.6 arcsec, thus outside of the FoV of the MAD SHWFS, as a consequence of the design of the pixels size of $100 \mu\text{m}$. Moreover they are attenuated when one uses broadband light and when the PS will be set in rotation, although they might be intensified by a higher PTV of the final PS.

3.4 PHASE SCREENS

The tests made at ESO validated most of the specifications, while the tests at IMT aimed at measuring accurately the height of the steps created by the photo-lithography process.

Testing at IMT Neuchatel

The laboratory of the IMT is equipped with an Alpha-Step 500, a surface profiler coupled with a microscope for an accurate targeting of the measurement area. An example of measurement is shown on the Figure 3.32. Thanks to those measurements one can evaluate accurately the depth of individual pixel levels, measure the roughness in the pixels, their size, the steepness of the transitions and eventual spikes, the flatness over large surfaces (like in the areas 1 and 2)...

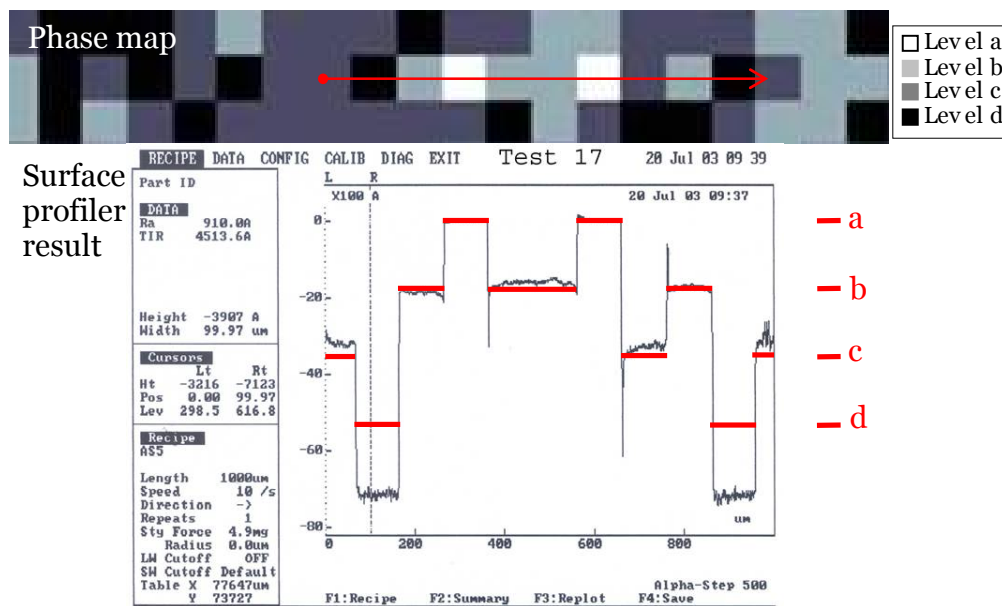


Figure 3.32: Result of a profile in the area 3 of the first SILIOS prototype. The arrow on the area sample (top) shows the line of pixels which depths have been measured. The horizontal lines on the lower plot represent the depths expected. It is then clear that on this example the level d was imprinted much lower than specified.

After several iterations and 4 prototypes, SILIOS managed to bring all the levels at the right depth (Figure 3.33), fulfilling then the last pending specifications (S1, S6, S8). The main difficulty came from the fact that the surface of the substrate didn't have the same hardness than its depth, making the etching non uniform ; it was solved by etching a flat level over the whole PS before digging the levels themselves. An accurate control of the depth, thanks to reference gratings (visible outside of the useful area on the Figure 3.25) and dichotomic etching, also brought a great enhancement.

Measurements made on references at IMT allowed SILIOS calibrating their surface profiler and thus measuring accurately the depths of the PS before delivering them.

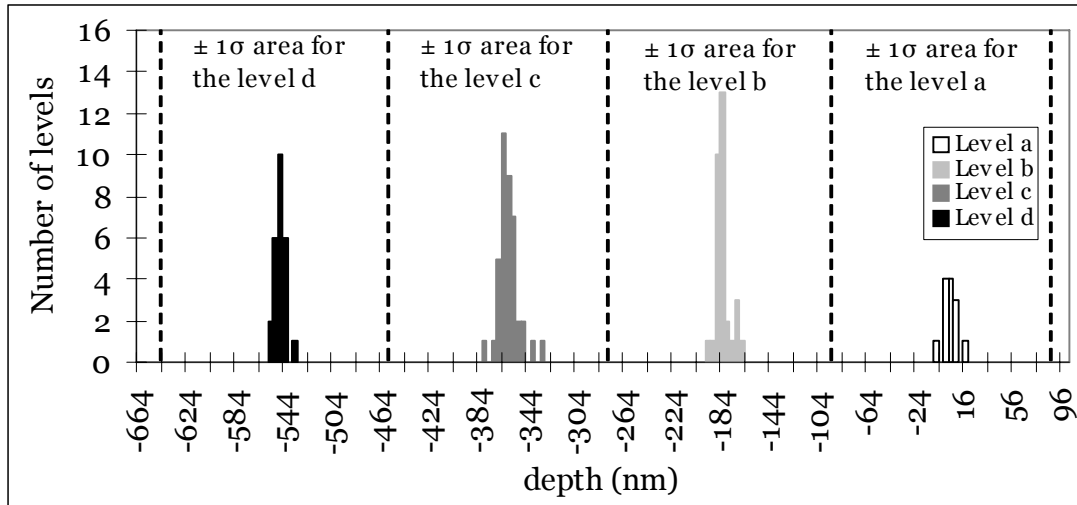


Figure 3.33: Repartition in depth of the levels measured in the area 3 of the SILIOS prototype. The color corresponds to the levels specified by the phase map. The $\pm 1\sigma$ areas refer to the specification on the rms accuracy of the levels depth (S8), thus more than $\sim 70\%$ of the measurements for a given level should be in this area to fulfill the requirements. It is largely the case.

Phase Screens order

The outcome of the prototyping phase was that the Phase Screens for MAPS would be ordered to the company SILIOS.

The specificities of the technique and tools used by SILIOS made very expensive to manufacture a single PS (from 20 to 25 k€), while the second exemplar of the same PS sees its price divided by 10. It was then advantageous to place a group order in order to decrease the unitary price of a PS. This has been done in collaboration between ESO, ONERA (France), the Observatoire de Paris (France), the Heidelberg Max-Planck-Institut for Astronomy (Germany) and the university of Galway (Ireland), leading to the group order of 23 Phase Screens of 4 different kind (6 exemplars of the PS-01, PS-02, PS-03 and 5 of the PS-04) and thus a substantial cost reduction for all the partners.

The ordered was placed in December '03, and the PS were delivered between July and December '04 [94], in time for being tested before used in MAPS for turbulence generation and correction with MAD.

3.4.7. Final screens testing

Each PS is delivered together with a brief test report from SILIOS (see Appendix 8.3), summarizing random profile measurements they have made over the PS and their compliance with the specifications.

The procedure used to retrieve the characteristics of the PS once delivered is the same as for the simulations (Figure 3.16), except for the conditions of measurement:

- The WF measurements were obtained thanks to a HASO SHWFS: 20 random positions around each individual PS and 50 positions for the combinations.

3.4 PHASE SCREENS

- The FWHM measurements @ 550 nm were done by rotating the PS (or combinations) of more than one turn and imaging the integrated PSF on a commercial Peltier-cooled PCO camera. A narrow-band filter is placed after the source.
- The FWHM measurements in the IR were done once MAPS mounted and aligned on the MAD bench, thanks to the ITC and narrow-band filters placed before the source fiber (@ 1187, 1644 and 2188 nm).

ESO received 14 PS from SILIOS (2 of which were then hand over to ONERA). Each of them has been tested at 550 nm (WF variance and FWHM), and once the compliance verified, only one of each type was tested in the IR, as well as 2 combinations of them.

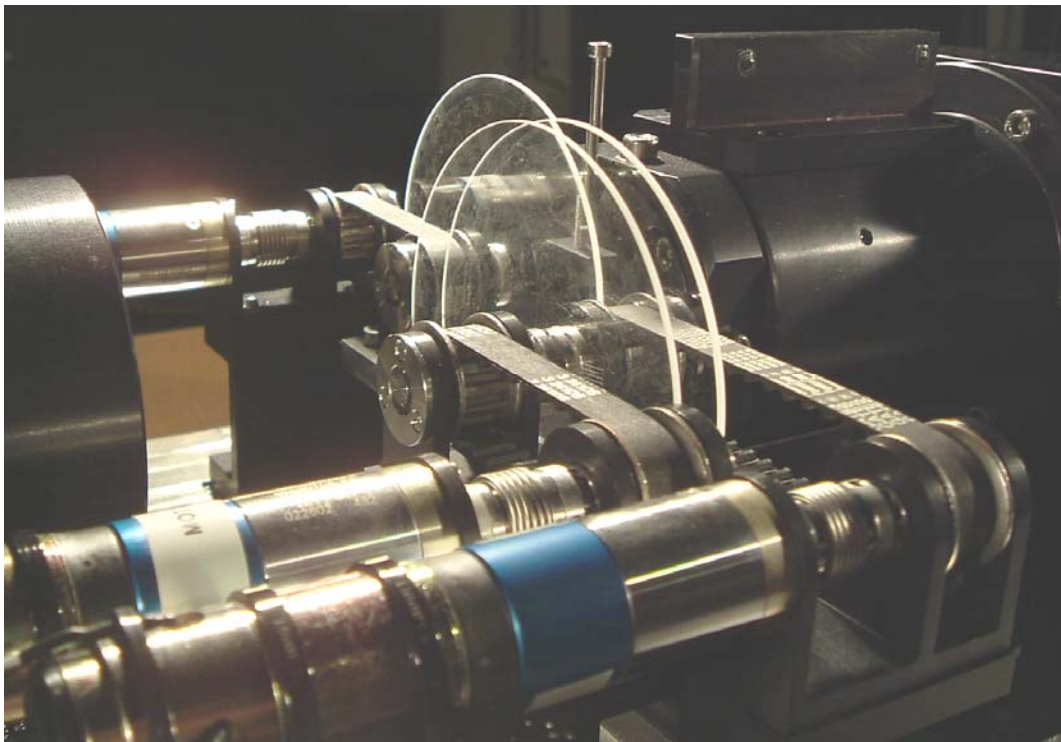


Figure 3.34: Close-up view of the SILIOS Phase Screens installed in MAPS, and of their rotation system.

FWHM @ 550 nm

Examples of FWHM measurements are shown on the Figure 3.35 for the 2 combinations of PS and for 2 individual PS. We see that for the combinations the PSF is very smooth and symmetric, while for one PS alone it is not the case due to a limited number of realizations over 1 turn.

The measured FWHM for all the PSs are given in the Table 3.4 (The PSs have been labeled by SILIOS with a letter in order to differentiate them). They vary of less than 5 % for a given PS type, and are very close to the values simulated from the Phase maps (section 3.4.3). For the combinations PS-

3. MAPS, A TURBULENCE GENERATOR FOR MCAO

01b+02a+03a and PS-02a+03a+04g, we measured respectively **0.82** and **0.48 arcsec** of FWHM, while the simulations gave **0.73** and **0.42 arcsec** @ 550 nm. The explanation for this difference is most probably the small angle between the faces of the PS (fulfilling the optical specification S5 of the section 3.4.4) that create an additional slow image motion.

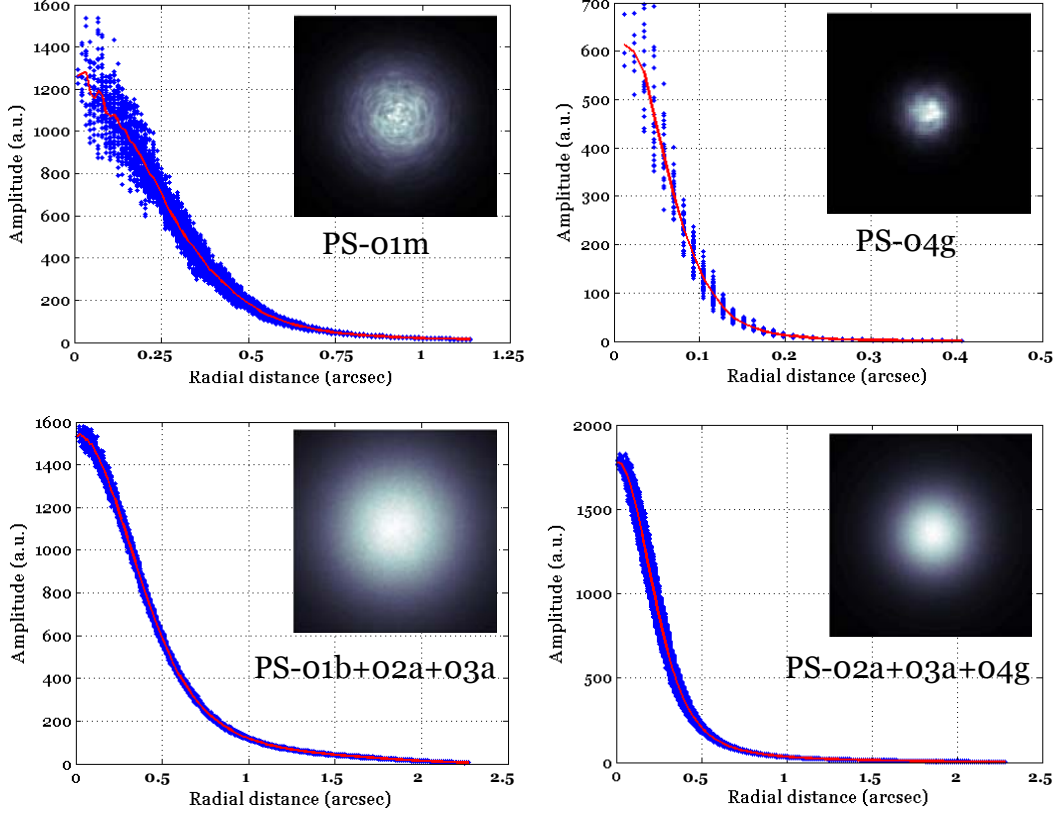


Figure 3.35: Integrated PSFs and average fit for the two possible combinations of PSs and 2 individual PSs @ 550 nm. The FWHM measured are 0.82 and 0.48 arcsec for the combinations.

PS	FWHM (arcsec)	PS	FWHM (arcsec)	PS	FWHM (arcsec)	PS	FWHM (arcsec)
01	0.54	02	0.33	03	0.194	04	0.122
01b	0.53	02a	0.32	03a	0.185	04b	0.124
01k	0.54	02e	0.33	03d	0.186	04c	0.123
01m	0.53	02f	0.33	03e	0.196	04g	0.129
				03f	0.193	04h	0.127

Table 3.4: FWHM measurements for all the PSs, individually labeled with a letter. In bold are recalled the values given by the simulations on the phase maps. All values @ 550 nm.

3.4 PHASE SCREENS

We noticed on the integrated PSF of the Phase Screen labeled PS-01b a spike at the center, 3 times higher than the expected maximum. It might be caused by the zero order of the grating created by the impression of the square pixels of the Phase maps, but it doesn't appear in the other exemplars of the same PS. The peak disappears when the PS-01b is used together with others PSs in rotation, but this annoying effect could re-appear in close loop, thus we recommend to keep this PS as spare.

Variance @ 550 nm

The Table 3.5 summarizes the r_0 values (@ 500 nm) measured on all the PS, as well as the values from the simulations for comparison, all obtained thanks to the method c) detailed on the Figure 3.16.

The values measured on the final PS are systematically higher than the simulated ones, with a difference of up to 60 % ! As a consequence the r_0 values for the 2 combinations of PS are **12.6 and 24.1 cm** instead of the **9.7 and 16.3 cm** simulated. Using the methods a) or b) produces the same results.

It is astonishing that the FWHM values match so well between the simulations and the measurements while the r_0 values don't. The cause of the difference is not known, and it doesn't seem to be a too low number of realizations, an under-sampling of the WF by the HASO or a vignetting of the pupil in the set-up.

Indeed we have used yet another independent measurement to cross-check the results given by the HASO. Once MAPS aligned on MAD, the SCAO loop was closed to correct for the turbulence induced by the combination of PS-02+03+04, and we collected the real-time data. By combining the voltages applied in closed loop to the DM and the residual aberrations seen by the WFS, it is possible to retrieve all the information about the turbulence (except for the high orders modes not seen by the system). After analyzing those results, we found a value of **25 cm** for r_0 , coherent with the HASO measurement of 24.1 cm.

The Figure 3.36 summarizes the measured and simulated FWHM values, as well as the values predicted from the r_0 measurements (equation (3.8)) and scaled from 550 to 500 nm with the law in $\lambda^{-0.423}$ when necessary.

PS	r_0 (cm)	PS	r_0 (cm)	PS	r_0 (cm)	PS	r_0 (cm)
01	13.9	02	24.1	03	39	04	61
01b	16.2	02a	38	03a	45	04b	61
01k	16.1	02e	33	03d	45	04c	-
01m	15.3	02f	33	03e	45	04g	-
				03f	44	04h	65

Table 3.5: r_0 measurements for all the PS. In bold are recalled the values given by the simulations on the phase maps. All values @ 500 nm. The PS-04c and PS-04g haven't been measured.

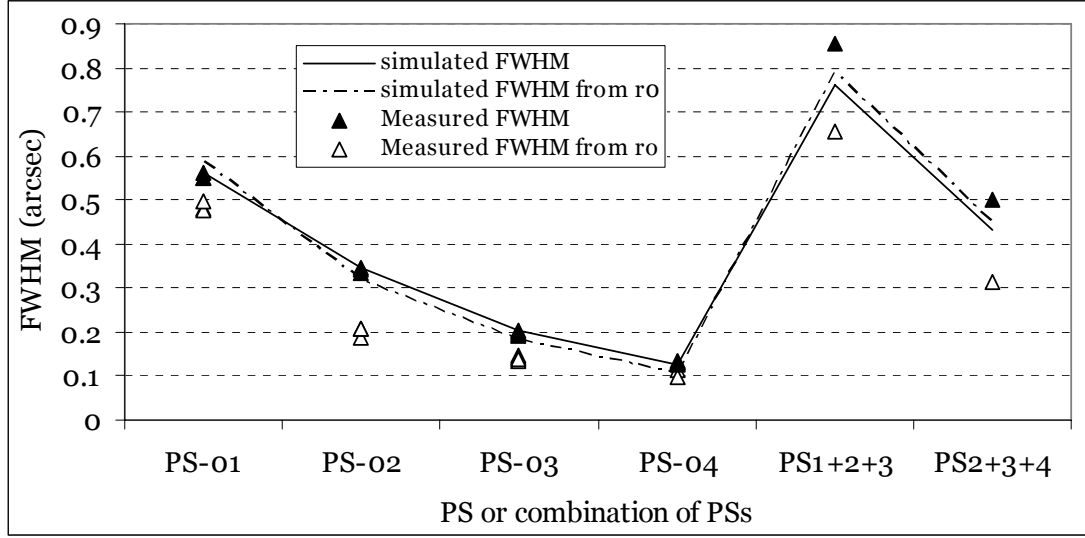


Figure 3.36: Simulated (lines) and measured (points) FWHM for all the PS, direct and estimated from r_0 .

It is interesting to notice the agreement between the two methods used in simulation to retrieve the value of the FWHM: direct measurement and computation from the r_0 measurement, validating the algorithm wrote by R. Conan.

The FWHM measurements made on real Phase Screens are very similar from one PS to the other and in good agreement with the simulations. The difference observed in the case of the combinations of screens can be easily explained by the fact that the non-parallel faces of each PS create a slow additional tilt in the image, resulting in an enlargement of the long-exposure PSF.

The abnormally high r_0 values measured on the real PS are unexplained. They cannot be due to an error of measurement, as the results are the same for all the PS of a same kind, even considering measurements taken months apart. We have checked by simulation that it is not due to an under-sampling of the WF by the HASO. The comparison with measurements made with another SHWFS (the one of MAD) gives the same result.

Chromaticism

The chromatism of the turbulence produced by the PSs has been measured over the full useful range of MAD (Figure 3.37) and compared to the results of the simulations on the Phase maps. The agreement is excellent for the PS-01 and 02, but for the PS-03 and 04 the measurements are quite larger than the simulations (probably a measurement bias as the PSF is very narrow at those wavelengths). For the combinations, the trend is as expected, and the measured values are slightly higher, probably due to the slow image motion created by the PS non parallel faces as explained before.

3.4 PHASE SCREENS

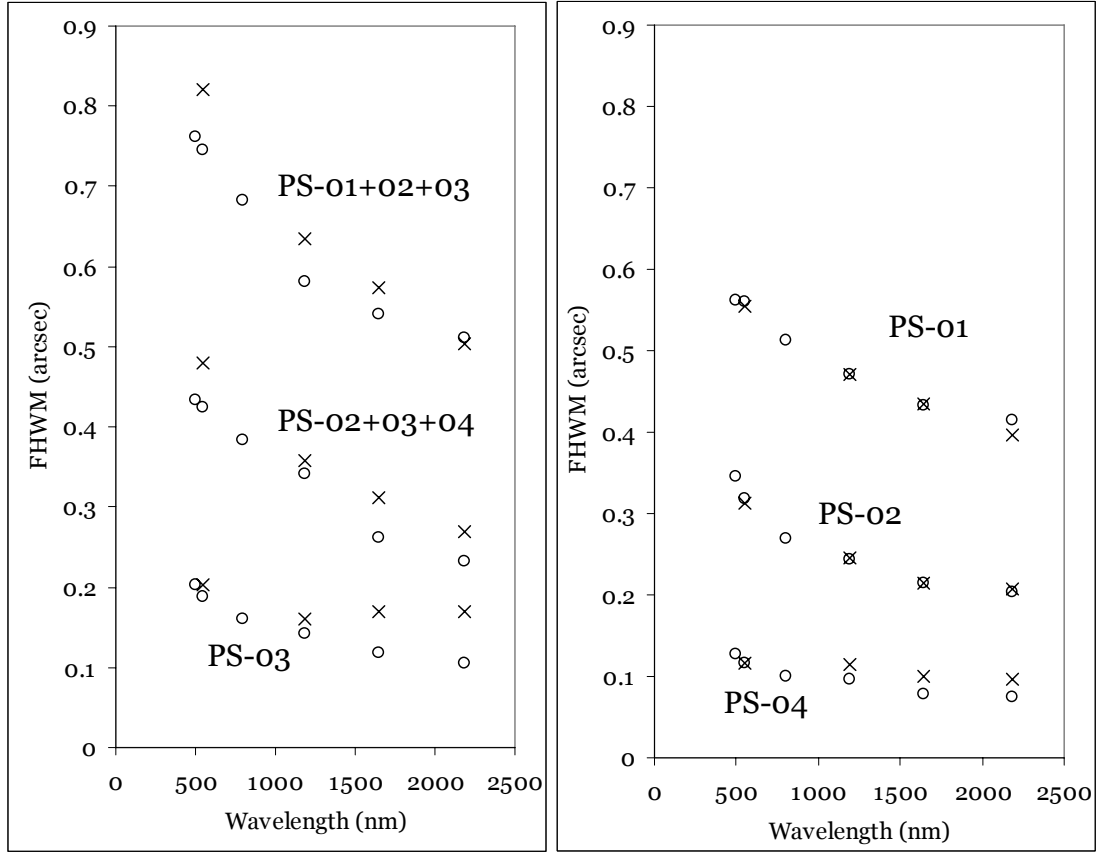


Figure 3.37: Comparison between the simulated (circles) and measured (crosses) FWHM values for each PS and their combinations. The measurement wavelengths are 550 (visible PCO camera), 1187, 1644 and 2188 nm (ITC on MAD).

3.5. Conclusion / Discussion

MAPS

During this PhD internship at ESO, the MCAO turbulence generator MAPS has been successfully brought from a concept to an instrument fully characterized and installed on the MAD bench.

On the design point of view, the complexity came from the constraints related to the wide FoV and the accommodation of refractive Phase Screens. The mechanical design had to be simple and limit the number of degrees of freedom in the alignment of MAPS. A combination of good optical and mechanical designs and a fine alignment allowed getting MAPS delivering an optical quality within the specifications in almost all the FoV.

The large wavelength and magnitude ranges that had to be covered by MAPS made it difficult to find a proper light source. The solution found combines a powerful source and an optical system splitting the light to simulate up to 36 stars with 4 different magnitudes.

In the future MAPS will be used intensively to perform the laboratory tests and optimizations on MAD before sending it to the VLT at Paranal, saving in this way precious nights of telescope time. MAPS is already foreseen to be used with other ESO instruments such as APE, and will inspire the next generation of Telescope simulators reproducing even larger FoV, Laser Guide Stars,...

Phase Screens

Designing Phase maps that follow the theoretical Von Kármán model of the atmosphere is not a difficult task. But finding the right set of maps that ease the manufacturing of the PS, characterize them in all the configurations required, and especially make a comparison with real refractive PS is another story.

Before characterizing Phase Screens (real or simulated), it is important to agree on the definitions used. The problem doesn't appear in the Kolmogorov case, but in the more realistic case of finite outer scale (like 22 m over a telescope diameter of 8 m) things are different.

One should always keep the practical definition of the Seeing as “the FWHM of a long-exposure PSF in the case of infinite outer scale”. The Fried parameter r_0 is completely independent from the outer scale L_0 . It can be obtained from WF or differential image motion measurements, for instance by fitting of the high orders of the power spectrum of the phase (orders not influenced by the outer scale) as does a DIMM seeing monitor.

In all cases the following equation is valid:

$$\text{Seeing} = 0.9759 \times \frac{\lambda}{r_0},$$

where λ is the wavelength of operation, but only in the Kolmogorov case the Seeing is also equal to the FWHM of a long-exposure image $\varepsilon_{\text{Kolmo}}$.

The effect of the outer scale on the image characteristics has been theoretically studied by R. Conan in [16]. In particular it came out that the

3.5 CONCLUSION / DISCUSSION

FWHM of long-exposure images is significantly reduced by a finite outer scale. For $L_o = 22$ m, a good approximation to the numerical results of Conan is:

$$\left(\frac{\epsilon_{VK}}{\epsilon_{Kolmo}} \right)^2 \approx 0.334 \times (r_o)^{-0.371},$$

valid for r_o between 0.1 and 3 m.

Using those definitions, we have verified that the Phase maps designed for MAPS followed the expected behavior, i.e. the ratio between the Seeing and the FWHM at 500 nm, and also the evolution of the FWHM vs. the wavelength. Indeed this is a crucial parameter because the instrument MAD senses the WF with a peak sensitivity around 700 nm but characterizes the performances at 2200 nm, and a wrong scaling factor can lead to a biased estimation of the performances in the lab. We came out with an approximated law of the FWHM evolving in $\lambda^{-0.423}$ while the Seeing goes with $\lambda^{-0.25}$ (still for $L_o = 22$ m).

The knowledge we acquired of the atmospheric parameters can be summarized by the following consideration: when describing atmospheric turbulence with outer scale to be corrected by (MC)AO, two parameters should always be given, and it is essential to distinguish between them:

- **The Seeing.** Commonly given to characterize an observation site, it is linked to the Fried parameter r_o , itself measured by instruments such as the DIMM.

- **The FWHM** of long-exposure images, often measured at a different wavelength than the Seeing, and following a different chromatic law than this one.

The outcome of the lab work performed on the Phase Screens is that the elements manufactured by SILIOS produce the expected FWHM of the long exposure images at any wavelength, but the results of the HASO measurements are not yet fully understood.

It will require some additional work to find out the source of the discrepancies, and if the PS actually produce a too large r_o , why is it not seen on the surface profiles delivered by SILIOS with the Phase Screens.

3. MAPS, A TURBULENCE GENERATOR FOR MCAO

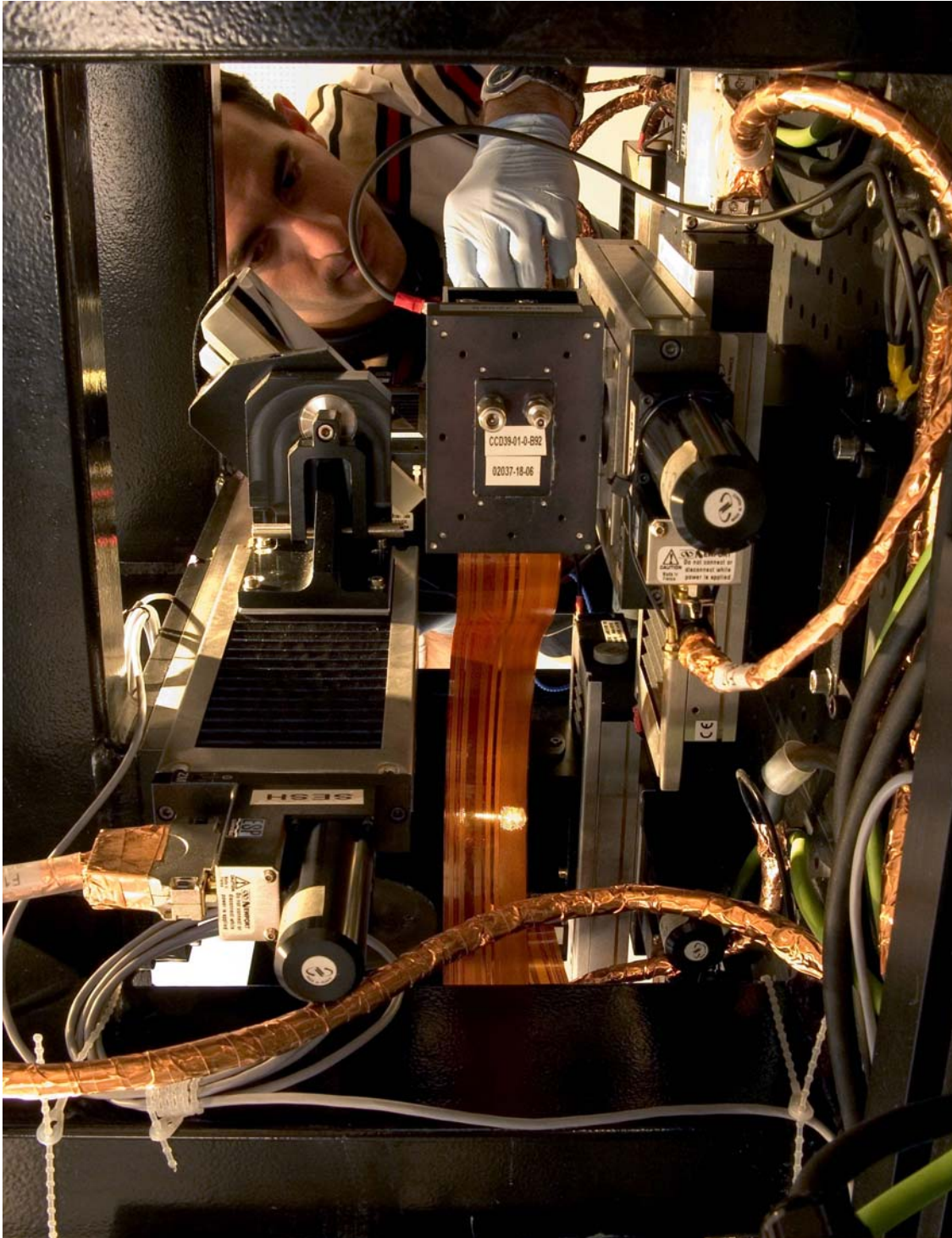


Figure 3.38: Working around the WFS area.

4. Correction of the static aberrations

An overview of this work on the pre-compensation of static aberrations has been presented as a poster at the “Journées Scientifiques de l’ONERA - MCAO” that were held on March 14th - 15th in Châtillon close to Paris, France [39].

4.1. Presentation of the problem

Since the first developments of adaptive optics, it was clear that trying to get the best beam quality at the level of the WFS didn’t mean getting the best image at the scientific focus. Indeed the beam doesn’t cross the same optics before reaching those two points, and is deformed by the Non-Common Path Aberrations (NCPA), ones that lay after the dichroic of the system (Figure 4.1). For “simple” AO systems, the residual is generally not important, but when the system is composed of numerous optics, large ones for FoV correction, and/or aims to high performances, the NCPA can decrease the quality of the images of several percents of SR.

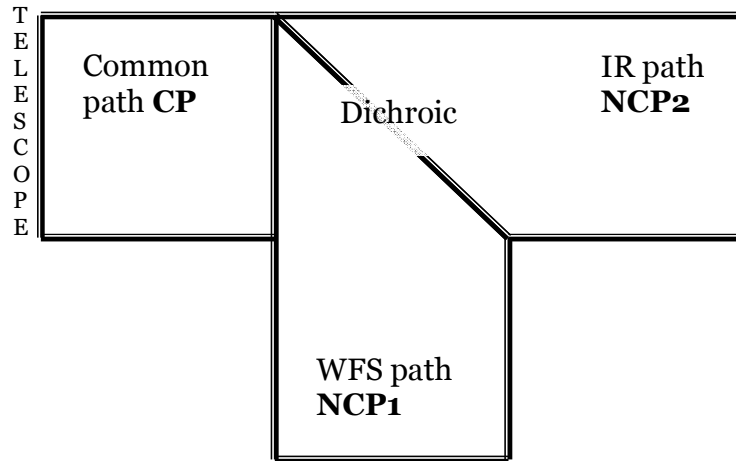


Figure 4.1: Schematic view of an AO system.

As shown on the Figure 4.1, in open loop the aberrations seen by the WFS are equal to CP+NCP1, while the ones seen by the scientific instrument are CP+NCP2. If the loop is closed around the zero reference values (flat WF on the WFS), the residual aberrations at the level of the science instrument are (if we neglect the non corrected high order aberrations):

$$Ab1 = (CP + NCP2) - (CP + NCP1) = NCP2 - NCP1 \quad (4.1)$$

This drawback can be compensated by using the system in closed loop around a different functioning point, i.e. change the reference for the WFS. This is done by subtracting at each iteration a set of reference values to the WFS measurements, in a more or less efficient way depending on the sampling, FoV and linearity of the WFS, as well as its nature. It is for instance very easy to

implement for a well sampled SHWFS like the ones we use on MAD. If the reference values are well calibrated, the static aberrations (mainly low order) are “pre-”compensated in closed loop by proper DM deformations.

The critical point remains the estimation of the aberrations. A partial solution is to record the WFS reference values with a calibration source placed at a focus just before the dichroic of the system (when possible). The residual aberrations resulting from the use of those values are then:

$$Ab2 = (CP + NCP2) - (CP + NCP1) + NCP1 = NCP2 \quad (4.2)$$

But this still does not compensate for the NCPA in the science path. Moreover, in some case there is no focal plane in front of the dichroic, like in MAD for which the light from a calibration source goes through 1 collimator and 2 mirrors before feeding the WFS path. Obviously the aberrations introduced in the calibration path itself (of the same amplitude of the ones we want to compensate for) make the process inaccurate.

The best estimation would be one done at the level of the scientific instrument, where in the end the quality of the beam has to be the best. For the first AO instruments this was done by using an empiric method: checking “by eye” the quality of the PSF at the scientific focus and guessing which modes to apply to the DM (coma, astigmatism...) to increase the SR. This technique was somehow efficient to roughly correct for the low order aberrations in the instrument COME-ON for instance [87] [86].

Another solution, chosen by the Gemini South MCAO team [30], is to deploy one or several High Resolution WFS (HRWFS) in the scientific FoV, just before the instrument. The WF quality is measured as close as possible from the instrument, and converted into reference values for the AO WFS. This method requires a very well calibrated HRWFS, a good modeling of the system to change the reference values, and even though, the aberrations of the instrument after the HRWFS are not seen.

The ultimate solution is to use the scientific instrument itself as a WFS. This is possible, for an imaging instrument Nyquist sampled at the wavelength of use, thanks to the phase retrieval technique named Phase Diversity (ΦD) as proposed and implemented first by ONERA on a number of AO systems. In particular it has been applied to the correction of the NCPA in the AO instrument NAOS coupled with the IR camera CONICA [33].

4.2. Phase diversity

Retrieving the WF from a sole focused image is not possible without indetermination. The phase retrieval technique called Phase Diversity was proposed to add information and remove the indeterminations [31]. The idea behind it is to record at least one additional image, separated from the first one by a well known amount of phase variation. Then the ΦD uses a maximum-likelihood approach to identify a combination of object and aberrations that is consistent with all the images collected. This technique has been successfully used to determine aberrations and restore images [71] [58] [66] [65] [8]. One

4.2 PHASE DIVERSITY

drawback of this low-cost procedure is that it requires a complex numerical and iterative processing to restore the unknowns from the images.

There can be several ways to introduce aberrations between two images. The simplest one to add is a defocus by using a beam-splitter and a second detector (Figure 4.2), or by shifting the unique detector of a known distance and supposing that the static aberrations don't evolve between the times when the two images are taken, which is often the case.

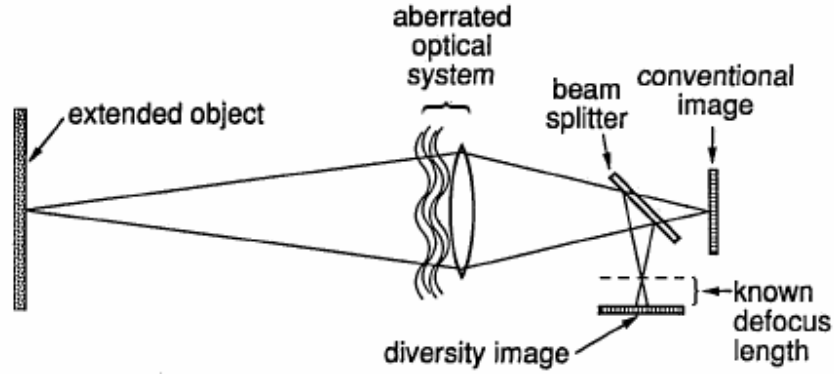


Figure 4.2: Optical layout of a Phase Diversity system.

From the focused and defocused images and the parameters of the system (wavelength, pixel scale of the camera, pupil central obstruction...), the ΦD software developed at ONERA [8] [27] [9] retrieves the aberrations present in the optical path from the calibration source to the camera detector, and estimates as well the shape of the object. Indeed we use most of the time a diffraction-limited calibration source, but it is not an obligation as the ΦD software accommodates extended objects.

The choice of the known amount of defocus between the two images (expressed by Δ , the PTV of the WF of defocus in nm) is essential to obtain accurate results. It has been shown [66] that it should be in the range $[\lambda/2, 3\lambda/2]$ and that a value of λ gives the most accurate estimation, λ being the working wavelength. This amount of defocus can be obtained by several means:

1. placing a second detector after a beam-splitter at a distance d behind the first one (Figure 4.2), d being given in the equation (4.4)
2. measuring a second image by shifting the detector of the same distance d
3. apply a focus mode on the DM of amplitude a_4 given by the equation (4.3)
4. shifting the entrance calibration source (less accurate)
5. shifting a collimator in the optical path of the distance d

If applied with the DM, the coefficient of the focus mode is:

$$a_4 = \frac{\Delta}{2\sqrt{3}}, \quad (4.3)$$

otherwise the distance of shift required is given by:

$$d = 8\Delta(F/D)^2 \quad (4.4)$$

where F/D is the F ratio of the beam at the level of the element shifted (source, detector or collimator)

4. CORRECTION OF THE STATIC ABERRATIONS

The results of the ΦD estimation by the ONERA software are a list of Zernike coefficients (result of the projection of the aberrations on the Zernike polynomials, described in the section 2.4.1 of the introduction), an image of the object, and the amount of tip and tilt between the two images. The images have to be carefully centered because a tip-tilt value of more than 2π results in the failure of the estimation. In a general manner, the ΦD is not able to estimate aberrations greater than 2π , which is greatly sufficient for the static aberrations of the concerned AO system.

The ΦD algorithm is based on several assumptions which must be well verified to obtain a good accuracy on the results [9]. The most critical possible error sources are listed below:

- Defocus distance d : it has to be known very accurately.
- SNR of the images: the ΦD gives good results for SNR on the focused image higher than 200. As in [9], the SNR is defined as the ratio of the maximum flux in the focused image over the rms noise.
- Sampling and size of the images: they have to be at least Nyquist sampled (2 pixels per λ/D), and their size about 32 times λ/D , preferably a number of pixels multiple of 2.
- Residual features such as ghosts or imperfect background subtraction.
- Number of estimated Zernike polynomials: an empiric law tells us to project on a number of polynomials twice larger than the one we want to correct, in order to limit the aliasing of the high orders on the low orders.
- Quality of the defocus produced.

The ΦD code developed at ONERA in IDL has been delivered to ESO. It has been there translated in C [57] in order to be integrated in the automatic calibration procedure for NACO. The IDL version is still in use for the preparation of the calibration of future ESO instruments, MAD in particular. For the test of the software we have submitted it to simulated images from a WF distorted by a known quantity of aberrations. A list of the input coefficients and of the result of the phase estimation is given in Table 4.1, for the case of images containing no noise. On this example the ΦD algorithm manages to estimate successfully the aberrations between 4 and 15 with a total error of 6nm rms, over a total WF of about 100 nm rms. The noisy case shows that the ΦD software can also deal with such images (Figure 4.3).

Zernike #	4	5	6	7	8	9	10	11	12	13	14	15
Input (nm)	60.5	-39.3	58.1	-16.2	-14.1	-2.5	13.7	-24.3	0.5	-3.2	2.8	-2.4
Estimated (nm)	61.2	-39.0	58.7	-16.2	-14.0	-2.5	13.5	-23.0	0.8	-2.8	8.5	-2.4

Table 4.1: List of coefficients used to simulate the input images for the ΦD algorithm and result of the phase estimation.

4.3 NACO

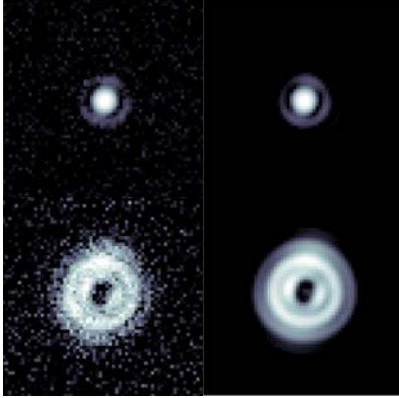


Figure 4.3: Simulation of the performances of the ΦD algorithm. Focused (top) and defocused (bottom) images of a calibration source, as measured (left) and as reconstructed from ΦD estimation (right). Logarithmic scale is considered for all images.

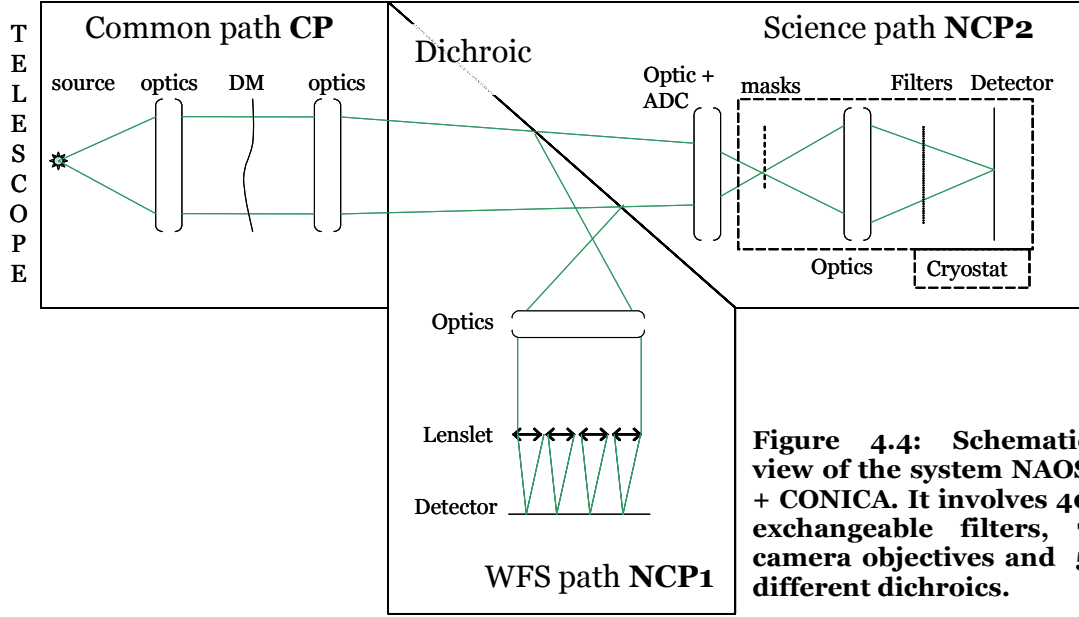
4.3. NACO

We have seen how it is possible to use Phase Diversity to estimate the aberrations present in an optical setup. But its implementation on an already existing instrument (not designed to ease the use of ΦD) can reveal quantities of problem, starting from the impossibility to shift the detector of the camera or to introduce a beam-splitter and another detector.

The NACO team had to face those constraints and find smart ways to overcome them [33]. A schematic view of the system is shown on the Figure 4.4. Moreover, the number of possible combinations of optics is tremendous (40 filters, 7 objectives and 5 dichroics!) and for each of them the aberrations are different. The solution found is described below:

- The masks wheel inside the cryostat of the camera was used to house different pinholes at different distances. Lit by the proper source, they create a calibration reference at the entrance of CONICA. The diversity images were then recorded thanks to a pair of pinholes shifted on the optical axis.
- The median value of the measurements for the 40 filters gives the aberrations of the objective, and the residuals from the subtraction of this median values gives the aberrations of the filters. Once this known, it is easy to retrieve the aberrations for the other 6 objectives.
- Then for 1 combination of objective/filter, the aberrations of the different dichroics have to be recorded. For this the calibration source used is the one simulating the telescope focus at the entrance of NAOS, and the defocus is introduced in closed loop in the WFS path, immediately compensated by the right focus amount on the DM in the common path.
- Finally for each mode of the instrument, the aberrations are loaded, combined, and converted into reference slopes thanks to a model of the WFS. Closing the loop around this set of slopes ensures the correction of the static aberrations for the actual combination of dichroic, objective and filter.

4. CORRECTION OF THE STATIC ABERRATIONS

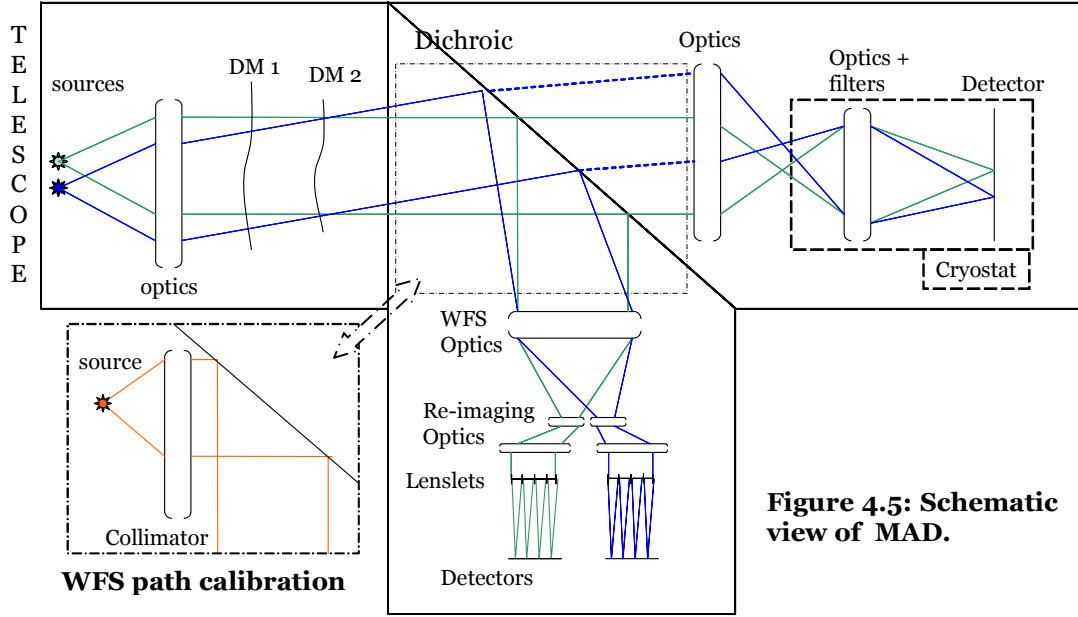


This procedure has been successfully applied to NACO, achieving great performances in terms of SR on the camera [9] [33]. The conclusions of this work are positive but underline the fact that for future instruments, the implementation of the technique of ΦD should be thought from a very early phase in the design.

4.4. MAD

Similarly as for NACO, MAD (see [62] or the section 2.3) was already in a final design phase when the choice was made to use Phase Diversity to correct for the NCPA. Thus the implementation of the ΦD had to be done within the range of the existing possibilities. The optical layout of MAD is shown on the Figure 2.4 and a schematic view on the Figure 4.5. We notice that the beam is collimated on the dichroic, so there is no possibility to place a calibration source near it. Instead, there is a calibration path under the MAD bench that collimates the beam from a point source and feeds the WFS path. The detector of the camera cannot move along the optical axis; the focusing of the camera is indeed done by displacing a collimator in the IR path. Finally and unlike in NAOS, there is no device to create a defocus in the WFS path.

4.4 MAD



In the framework of this PhD, the measurement of aberrations in MAD were performed mainly thanks to the Infrared Test Camera (ITC) [53] belonging to the Integration group of ESO. For a period when the ITC was not available we have been using a visible camera, a commercially available astronomical SBIG camera ST-9XE (section 4.6.6). In the end, MAD will be used together with the wide FoV IR camera CAMCAO [1], developed by a Portuguese consortium. The parameters of those 3 cameras are summarized in the Table 4.2 (see also the appendix 8.5). The pixel scale for the ITC and the SBIG camera are values measured on the bench. We notice a distortion of the field of respectively 2.6 % and 0.7 %.

Camera	ITC		SBIG	CAMCAO
Wavelength (nm)	2188	2200	1064	2200
Pixel size (μm)	18.5		20	18
Detector size (px)	1024 x 1024		512 x 512	2048 x 2048
Pixel scale : x / y (mas/px)	17.76 / 17.30		8.29 / 8.23	28 / 28
FoV (arcsec)	18.2 / 17.7		4.24 / 4.21	57.34
PSF Sampling: x / y	3.18 / 3.26	3.19 / 3.28	3.31 / 3.33	2.026
Rms WF a_4 to produce 1λ of focus (nm)	631.6	635.1	307.15	635.1
Defocus distance d at F/15 (mm)	3.938	3.960	1.915	3.960

Table 4.2: Parameters for the cameras used with MAD. The ITC has been used alternatively with its own 2200 nm narrow band filter, or with its K wide band filter and a light source for MAD at 2188 nm. The parameters for CAMCAO are given by design. The values for a_4 and d are given by the equations (4.3) and (4.4).

4. CORRECTION OF THE STATIC ABERRATIONS

In MAD, the possibilities to introduce the defocus required by the ΦD are:

- Apply a focus on the DM in open loop. This option is the most attractive, as it introduces pure focus in a pupil plane, but it requires a very good knowledge of the Influence Functions of the DM, and one might have to deal with creep effect.
- Shift the entrance calibration source of the distance d along the optical axis. This is possible thanks to the micrometric stage on which the entrance calibration plate is mounted. This option is not recommended as it changes the path of the beam through all the optics between the focused and defocused images.
- Shift the IR camera focusing collimator of the distance d . This make change the path of the beam only on the camera optics. It requires a good alignment, especially the parallelism of the axis of motion of the collimator with the optical axis.
- Apply a focus on the DM in closed loop. This is done by using the appropriate set of reference slopes for the WFS.

We have chosen to use the collimator during the open loop corrections (section 4.5), and the DM (+SHWFS) during the closed loop corrections (section 4.7).

Another difference between MAD and NACO is the size of the FoV of the instrument. It is reduced for NACO, but the MCAO FoV of MAD is 2 arc minutes. This implies the presence of field-dependant aberrations, that can be also compensated thanks to a clever use of the altitude DM of MAD.

We will first study the case of the correction of the on-axis aberrations and explore the possibilities to enhance it with respect to the NACO procedure (sections 4.5 to 4.7) before investigating the correction of the static aberrations in the FoV (section 4.8).

As we will develop in the next sections, we don't make any use of the calibration path of MAD ; we always use the calibration source at the entrance of MAD and measure the ΦD images with the IR camera. Thus it becomes useless to differentiate between the common and non-common paths aberrations, and we rather use in the following the generic name of static aberrations, which we define as the aberrations in the common plus IR path of the instrument.

4.5. Correction of the static aberrations using a calibration matrix

4.5.1. Correction of the NCPA in NACO

We have seen previously how it is possible to measure the aberrations present in an image thanks to the addition of a second image and the use of Phase Diversity. This measurement can be done with a great accuracy if one tunes accurately the most sensitive parameters. The output of the measurement is a list of Zernike coefficients. In the case of NACO, this list is multiplied by a model of

4.5 CORRECTION OF THE STATIC ABERRATIONS USING A CALIBRATION MATRIX

the WFS (more exactly a model of the way it measures the Zernike polynomials) in order to get the right reference slopes:

$$2N_{subap} \begin{bmatrix} \text{Corr} \end{bmatrix} = - \frac{N_Z}{2N_{subap}} \begin{bmatrix} \text{Model} \end{bmatrix} \times \begin{bmatrix} \text{Ab} \end{bmatrix} \quad (4.5)$$

where N_Z is the number of Zernike polynomials we wish to correct (starting from the mode # 4, the focus) and N_{subap} is the number of useful sub-apertures in the WFS (144 in NAOS and 52 in MAD). The matrix “*Model*” contains the reference slopes that allow, in closed loop, producing Zernike polynomials with the DM.

Finally, the AO loop is closed around the reference slopes contained in the matrix “*Corr*” in order to correct for the NCPA of NACO.

4.5.2. Improvement / Analogy with AO calibration

The method used for NACO relies strongly on the quality of the model, and is limited when one tries to correct for modes that are not perfectly produced by the system. Thus the method we propose here consists in replacing this “*Model*” matrix by a Control Matrix, generalized inverse of a measured Interaction (or calibration) Matrix.

In the following sections we will often draw the parallel between this new approach and the calibration of a classical AO system, from which it is inspired in the general idea but also in the means to improve it, as described in the section 2.4.4. Indeed, the equation (4.5) describes as well the closed loop of an AO system, temporal terms excluded. For such a system, it has been shown that recording an IM and invert it to get a CM is more efficient than using a synthesized matrix [12], even though those ones are being considered for the current highly complicated system or on-sky calibrations [68].

For the present analogy we will consider only the case of the TSVD.

4.5.3. Building of the IM

For correcting the static aberrations, the IM we measure links the shape of the DM to the aberrations estimated by ΦD , projected on the basis of the Zernike polynomials (equation (4.6)). The number of modes N_m in this case will be smaller than for the atmospheric turbulence correction, the static aberrations of the optics being generally of low orders.

$$N_Z \begin{bmatrix} \text{IM} \end{bmatrix} = \begin{bmatrix} \begin{bmatrix} M_1 \end{bmatrix} & \begin{bmatrix} M_2 \end{bmatrix} & \begin{bmatrix} M_3 \end{bmatrix} & \dots & \begin{bmatrix} M_{N_m} \end{bmatrix} \end{bmatrix} \quad (4.6)$$

4. CORRECTION OF THE STATIC ABERRATIONS

In practice, Zernike polynomials are applied to the DM for building the IM. The list of voltages to apply is determined thanks to the prior knowledge of the Influence Functions of the DM and are the columns of the matrix $m2V$ of modes to voltages:

$$\begin{matrix} & N_m \\ & \left[\begin{array}{c} \\ \\ \\ \end{array} \right] \\ N_V \left[\begin{array}{c} \\ \\ \\ \end{array} \right] m2V & = & \left[\begin{array}{c} \left[\begin{array}{c} \\ \\ \\ \end{array} \right] V_1 \\ \left[\begin{array}{c} \\ \\ \\ \end{array} \right] V_2 \\ \left[\begin{array}{c} \\ \\ \\ \end{array} \right] V_3 \\ \dots \\ \left[\begin{array}{c} \\ \\ \\ \end{array} \right] V_{N_m} \end{array} \right] \quad (4.7)$$

For each mode, two images are taken with the IR camera (playing here the role of WFS): one focused and the other one defocused of a precise amount. As said before, the defocus is introduced by shifting the collimator in the IR path. Each couple of images is then analyzed by ΦD , and the lists of coefficients obtained fill the columns of the IM (equation (4.6)).

4.5.4. Critical parameters for recording a good IM: aberrations subtraction

In fact the modes recorded as described in the previous section are not pure, and contain the contribution of the aberrations, even if our starting point is an image already corrected. To eliminate this contribution, there are two solutions:

- Record positive and negative modes and make the difference of the estimations to keep only the mode contribution (Figure 4.6, equation (4.8)). With this method we also average the difference between the positive and negative modes produced by the DM (non-linearity). This is the method we decided to use at first.
- To each mode estimations, subtract the contribution of the aberrations estimated by ΦD for a couple of images taken when no mode is applied. This method is a bit less accurate, but twice faster. Thus we will use it when applying the closed loop procedure in the section 4.7.

4.5 CORRECTION OF THE STATIC ABERRATIONS USING A CALIBRATION MATRIX

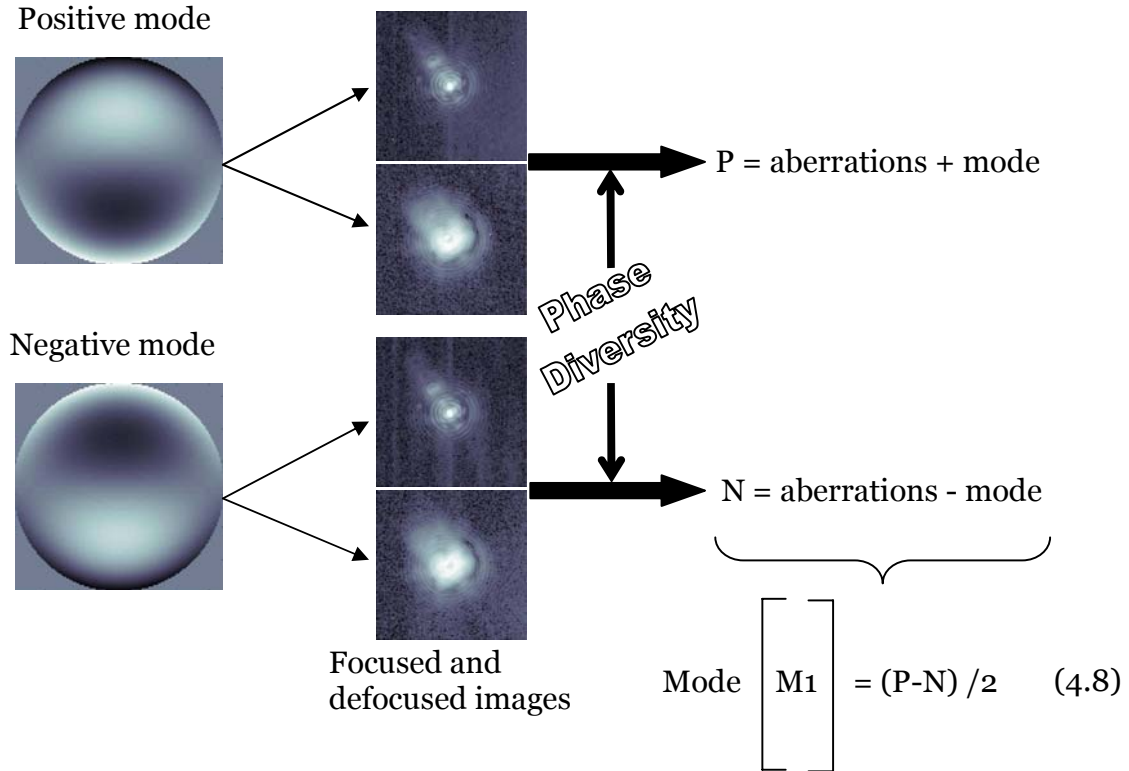


Figure 4.6: Method used to remove the contribution of the static aberrations from the estimation of the modes.

4.5.5. Critical parameters for recording a good IM: amplitude of the modes to apply

In AO calibration, the IM is the most efficient when recorded in conditions similar to the ones of a closed loop. Thus the IM is recorded by showing to the WFS modes that have an amplitude similar to the ones seen in closed loop. In addition, it is an advantage to use fast methods to record the IM (apply modes at 400 Hz to build an IM used in closed loop at 400 Hz for instance) to take into account the temporal response of the DM.

For the correction of the static aberrations, the temporal behavior is not an issue, but the amplitude of the DM modes is. The constraints are listed below:

- The ΦD cannot deal with aberrations greater than 2π per mode (equivalent to about 250-300 nm rms), which gives an upper limit to what can be applied.
- For the same reason as in AO calibration, the amplitude of the modes should be of the same order as the residual aberrations. By experience, we know that at the first iteration (no static aberrations corrected) we can have to correct 100 nm for some modes, but quickly the residuals fall to less than 10 nm for all the modes (the iterative process is described in the section 4.5.8).
- The lower limit is given by the ability of the ΦD to estimate correctly small amounts of aberrations in noisy images. For perfect images the accuracy of the ΦD is a few nm per mode (1-2 nm), but on real data it is not as good, and has to

4. CORRECTION OF THE STATIC ABERRATIONS

be estimated for each system. For example, images taken with the ITC and its narrow band K filter have an SNR of 40000 (the SNR is defined as the ratio of the maximum flux in the focused image over the rms noise). In those images we estimated that modes of amplitude 25 nm are correctly extracted from the background [41]. In the Table 4.3, the discrepancy between the amplitude of the mode we think we apply and the ΦD estimation illustrate our bad knowledge of the IF of the DM, and prove the usefulness of a measured IM for the correction of the static aberrations.

Applied on the DM(nm)	25	50	100	150	200	300
Measured by ΦD (nm)	28.5	60.3	121.3	205.2	192.2	84
Applied on the DM(nm)	-25	-50	-100	-150	-200	-300
Measured by ΦD (nm)	-42.6	-71.6	-127	-192	-215	-319.5

Table 4.3: Quality of the estimation of high amplitude aberrations on the example of the mode #7.

Therefore the amplitude of the modes to apply should be the minimum one that allow accurate ΦD estimations, and depend fully on the quality of the images recorded with the camera.

4.5.6. Critical parameters for recording a good IM: Number of Zernike polynomials produced by the DM

Any basis of polynomials could be applied to the DM for recording the IM, but we have chosen the basis of the Zernike polynomials in order to ease the ΦD estimations, to improve the conditioning of the CM, and because they describe very well the optical aberrations over circular apertures, which is more intuitive if one wants to check visually the shape of the aberrations in the images. However, those polynomials can be produced by a DM only to a certain extend.

Using the measured Influence Functions of the ground DM of MAD (measured on a dedicated bench thanks to a commercial SHWFS), we can simulate the ability for the DM to take the shape of the Zernike polynomials. We can see on the Figure 4.7 that the residuals remain very small for the orders smaller than 10, and that it increases and decreases periodically with the radial order of the polynomials. From those results we have decided to use the modes from 4 to 28 and that they should be enough to correct for most the aberrations (statistically decreasing with the square root of the radial order of the Zernike polynomials).

4.5 CORRECTION OF THE STATIC ABERRATIONS USING A CALIBRATION MATRIX

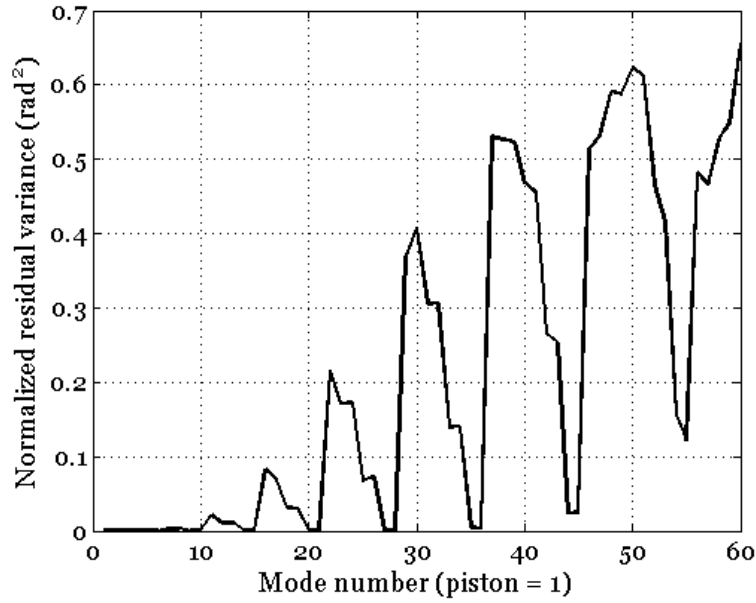


Figure 4.7: Quality of the Zernike modes produced by the MAD bimorph DM (spare of the MACAO-VLTI systems): difference between Zernike polynomials (of variance 1 rad²) and their best fit as produced by the DM, according to the measured IFs.

4.5.7. Correction

Once the IM recorded, it is factored by SVD and inverted, similarly as for an AO IM (section 2.4.4), as described in the equations (4.9) and (4.10). Here the number of Zernike coefficients estimated by Φ D N_Z can be much larger than the number of modes applied N_m .

$$\text{IM} = \begin{matrix} & \begin{bmatrix} U \\ N_Z \end{bmatrix} \\ N_Z & \end{matrix} \times \begin{matrix} & \begin{bmatrix} S \\ N_Z \end{bmatrix} \\ N_Z & \end{matrix} \times \begin{matrix} & \begin{bmatrix} V^T \\ N_m \end{bmatrix} \\ N_m & \end{matrix} \quad (4.9)$$

$$\begin{matrix} & \begin{bmatrix} CM \\ N_m \end{bmatrix} \\ N_m & \end{matrix} = \text{IM}^\dagger = V \cdot S^\dagger \cdot U^T \quad (4.10)$$

The correction vector (in the space of the modes applied to the DM) is obtained by application of the CM to the vector of aberrations measured:

4. CORRECTION OF THE STATIC ABERRATIONS

$$N_m \begin{bmatrix} \text{Corr} \end{bmatrix} = - \begin{bmatrix} N_Z \\ \text{CM} \end{bmatrix} \times \begin{bmatrix} \text{Ab} \end{bmatrix} N_Z \quad (4.11)$$

We notice the similarity with the equation (4.5) describing the correction of the NCPA in NACO, except that the “*Model*” matrix is replaced by the Control Matrix, generalized inverse of a measured Interaction (or calibration) Matrix.

The vector “*Corr*” contains the coefficients for the linear combination of modes to apply to the DM to correct for the actual aberrations. It is converted into voltages thanks to the matrix m2V (defined by the equation (4.7)) applied as follows:

$$N_V \begin{bmatrix} \text{Volts} \end{bmatrix} = \begin{bmatrix} N_m \\ \text{m2V} \end{bmatrix} \times \begin{bmatrix} \text{Corr} \end{bmatrix} N_m \quad (4.12)$$

In order to produce the expected enhancement of the quality of the images at the IR focus, the correction voltages “*Volts*” have to be added to the reference voltages of the DM, i.e. the ones applied while the images for ΦD are recorded:

$$V_{\text{Tot}} = V_{\text{Ref}} + \text{Volts} \quad (4.13)$$

The reference voltages are different from zero, as most of the time the rest position of a DM is strongly curved thus they might be, as it is the case in MAD, the ones that bring the DM surface physically flat.

In closed loop operations, those voltages cannot simply be applied to the DM, otherwise they would be corrected by the control loop. The right procedure is to apply the voltages of the equation (4.13) in open loop and to record in this configuration the reference values for the WFS. Closing the loop around this reference will ensure that the system will aim to reach the best image possible at the level of the camera.

4.5.8. Iterations

The usefulness of an iterative process has been proven during the correction of the NCPA of NACO, and later on applied to the BOA bench at ONERA [90] (the characteristics of this bench are detailed in the section 4.7.2). The idea behind it is to correct for the static aberrations a first time, then measure a new couple of focused/defocused images and estimate the residual aberrations. This allows us quantifying the quality of the correction performed, but it is also the starting point for another application of the CM in order to get even better correction voltages (by application of the equations (4.11) and (4.12)). This procedure can be repeated several times in order to reach the best

4.6 APPLICATION TO MAD

correction. The voltages correcting for the aberrations measured at the iteration i are then:

$$\text{Volts}_i = -m \times 2 \text{ V} \times \text{CM} \times \text{Ab}_i \quad (4.14)$$

As a result, the total voltages to apply to compensate for the aberrations measured after j iterations are:

$$V_{\text{Tot},j} = V_{\text{Ref}} + \sum_{i=1}^j \text{Volts}_i \quad (4.15)$$

4.6. Application to MAD

In this chapter is described the application to MAD of the technique previously detailed, that we name “**open loop correction for the on-axis static aberrations of the system MAD-ITC by the use of Phase Diversity and a calibration matrix**”.

It is done in open loop, in contrast to what is described in the section 4.7, thus we do not make any use of the WFS path, and indeed the first series of measurements were performed while the WFS path of MAD was not even aligned! As described previously, we focus here on the optimization of the technique for the correction of the on-axis aberrations with the ground DM, so for those tests a dummy mirror was installed at the position of the altitude DM.

Obviously the presence of a camera at the IR focus is required, and this was mainly what drove the scheduling of the tests. Indeed the ITC is an instrument very demanded, and it was possible to have it plugged on MAD only for limited periods of time. It was the case on the week from October 12th to 19th 2004, from January 23rd to February 2nd 2005 and finally beginning of June 2005 it has been installed on MAD for an undetermined period of time. During those runs we proceeded to more and more tests to learn the practical implications of the proposed technique, and the periods in between were dedicated to the analysis of the data and the preparation of the next run. In the following sections is described the outcome of those tests.

The ITC (Figure 4.8) is a cryogenic camera housing a 1064 x 1064 IR detector, cooled by a liquid Nitrogen bath. It has been developed at ESO by the Integration and Detector groups, and is controlled through an ESO standard IRACE rack.

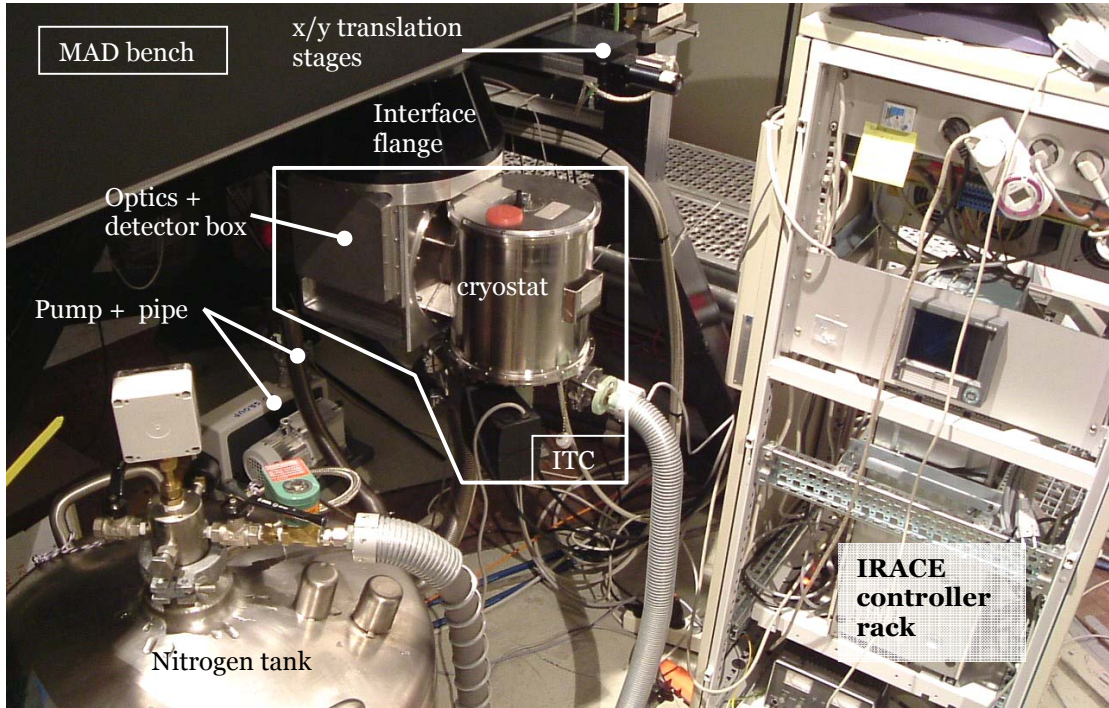


Figure 4.8: Picture of the Infrared Test Camera plugged to MAD, as well as its control rack, pump and nitrogen refilling tank.

End of February 2005, while the ITC was not available, an optical relay was set up to image the IR focus of MAD onto the visible detector of the commercial SBIG camera with the proper sampling and a narrow band filter at 1064 nm. The correction of the static aberrations in this case is described in the section 4.6.6.

4.6.1. Dummy mirrors

Before the installation of the DMs, they were substituted by dummy flat mirrors. An IR image taken in this configuration is shown on the Figure 4.9, together with the comparison with a perfect PSF. We can see on this image that the aberrations are not important, and we can recognize the typically 'X' shape of the PSF due to astigmatism. The origin of the ghosts seen on this image is discussed in the section 4.6.3.

The analysis of this image by a SR routine gives a values of 85.6 ± 0.3 % (for details on the SR routine used, see the section 2.4.5). Another routine (developed at ONERA) based on a different method gives 82.4 ± 0.2 %.

On the other hand, a defocused image allows us performing the ΦD estimation of the aberrations (Figure 4.10). For comparison, we made the quadratic sum of the first 55 Zernike coefficients, and found 141 nm (equivalent SR of 85.0 % at 2200 nm).

4.6 APPLICATION TO MAD

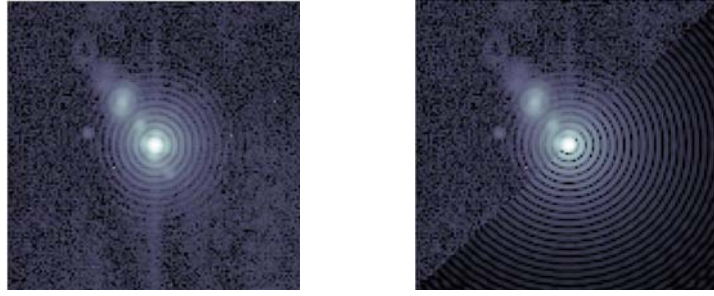


Figure 4.9: ITC image of a diffraction limited fiber (9 μm core) obtained with the flat mirrors in place of the DMs (left), and comparison with the theoretical best PSF (right). The wavelength considered is 2200 nm and the images are displayed in logarithmic scale.

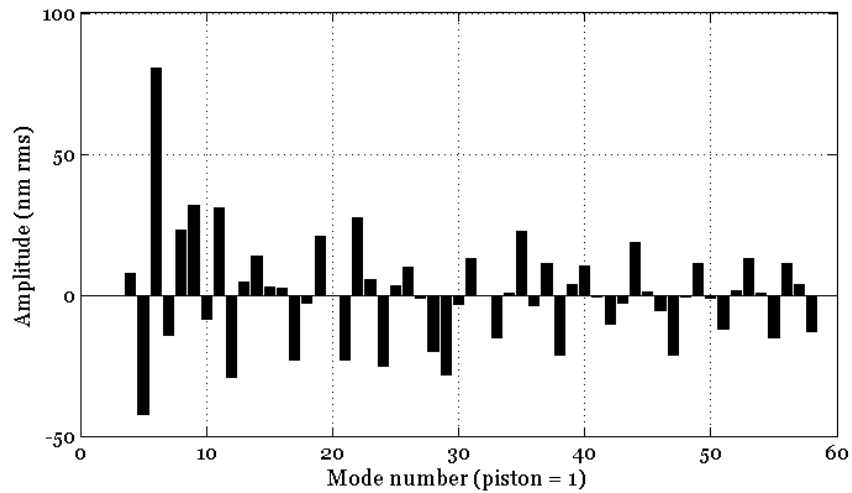


Figure 4.10: Estimation of the aberrations by Phase Diversity for the image shown on the Figure 4.9. The quadratic sum of all the coefficients is 141 nm.

4.6.2. Best criterion for the image quality

The result on the previous image brings us to discuss the criterion we will use in the following sections to quantify the quality of the images. The value of SR obtain through the dedicated routine is a direct measurement on the image, while the sum of the aberrations estimated by ΦD is only an indication (especially due to the fact that we estimate the aberrations on a finite number of Zernike polynomials). This is nevertheless the parameter that the ΦD algorithm enhances at each iterations. We have noticed that for SR below 90 %, both estimations give very similar result, but above 90 % the ΦD overestimates strongly the quality of the images (see as example the comparison in the Table 4.4). Finally we notice that in spite of those discrepancies, the relative quality between 2 images is always going in the same direction, whatever the criterion used.

So we can conclude that above 90 %, the SR on the images has to be estimated thanks to the dedicated routine. However, in order to evaluate the

quality of the ΦD convergence loop, it is more logical to use as criterion the amount of aberrations estimated by ΦD at each iteration.

4.6.3. Ghosts of the ITC

Although it is still valid for images recorded with a large bandwidth (up to 400 nm), the ΦD algorithm is more efficient when used with narrow band filters. The ITC is equipped with a 5 positions filter wheel: blind, J, H, K and K'. This last filter has a narrow bandwidth (about 40nm) centered around 2200 nm. An advantage of using this cold filter to record the images is also that it blocks a great amount of warm background (for example the image of the Figure 4.9 shows a SNR of 40000). Unfortunately it is an interferential filter, moreover placed in the vicinity of the detector of the camera. This has for effect to create secondary images (ghosts) close to the main one.

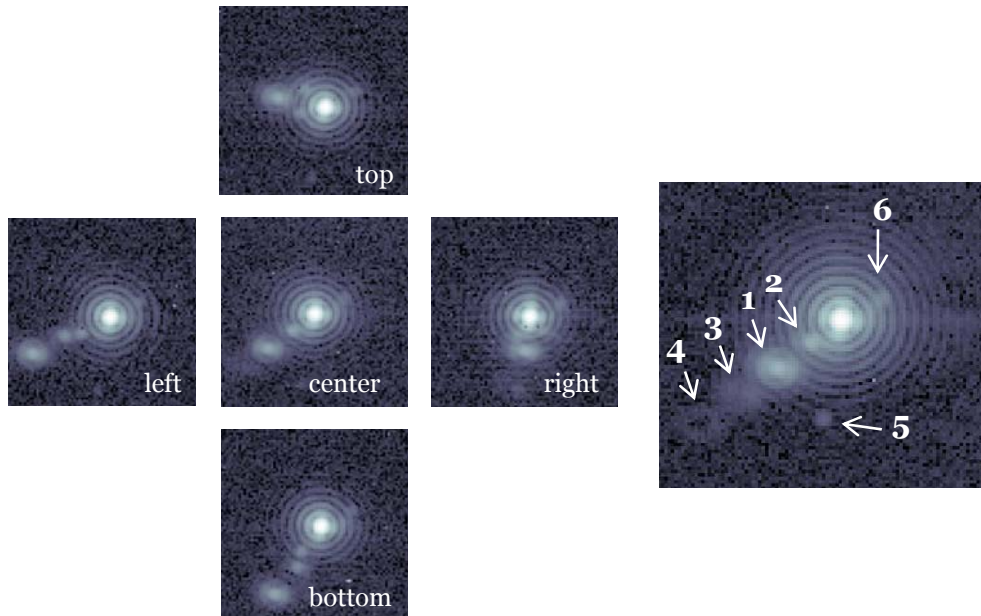


Figure 4.11: PSF at the center and borders of the FoV of the ITC plugged to MAD, with 2 dummy mirrors in place of the DMs (left) and ghosts inventory on a higher SNR image (right). Logarithmic scale.

The Figure 4.11 shows the positions of the ghosts relatively to the main spot at the center and borders of the ITC FoV. The variation of those positions shows that the ghosts are created by a optical element which is in a non telecentric beam. In the center of the ITC FoV, the most annoying spot (that can disturb the ΦD estimation) is the #2, as it is located at the same distance as the 3rd Airy ring of the main spot. The images taken in the FoV of the camera show that the ghosts #6 doesn't move with the others, so it is the only one that might be caused by the entrance window of the camera (also close to a focal plane) and not by the K' filter.

In the end, in order to deliver reference values to use on the MAD bench, it was decided to work always at the same position on the ITC (close to the center of

4.6 APPLICATION TO MAD

the field). The IM is measured at this position and so are the aberrations. The effect of the ghosts is then identical during the estimation of the aberrations and their correction.

However it would be interesting to disentangle the effect of the ghost from the real limitations of the technique. To this aim, we have rather used the K broad band filter of the ITC, but placed a narrow-band filter (@ 2188 nm) before the fiber feeding the bench. In this way we have on the detector of the camera a narrow-band light ideal for the ΦD estimations, but no ghosts are present (see for example the Figure 4.15). The only drawback is that the broad-band filters lets through more background, but we made certain that the performance of the ΦD is not effected by this drop of SNR. It is in those conditions that were obtained the IM and correction shown in the following sections 4.6.4 and 4.6.5.

4.6.4. Building of the IM

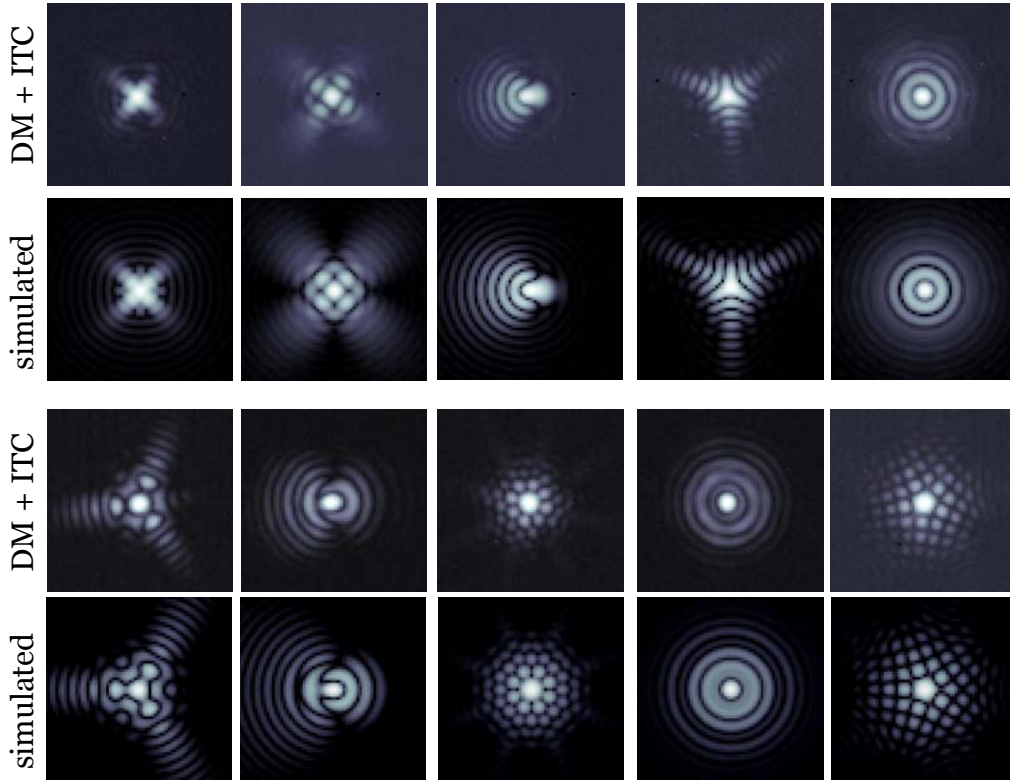


Figure 4.12: Example of modes produced by the DM as seen by the ITC (amplitude of 250 nm rms) and comparison with the theoretical PSFs.

The Ground DM has now been aligned and replaces one of the dummies. The other one remains in place of the Altitude DM. Following the procedure described on the section 4.5.3, we have recorded the required images to build the Interaction Matrix. The Figure 4.12 shows the PSFs measured when applying the modes with an rms amplitude of 250 nm, although the amplitude used to record a valid IM is 25 nm. The size of the images recorded is 128 x 128. We chose to estimate the aberrations with ΦD over 55 Zernike coefficients (radial order 11)

and to use the modes 4 to 28 for the correction (radial order 8), thus the size of the IM is 52 x 25 (Figure 4.13).

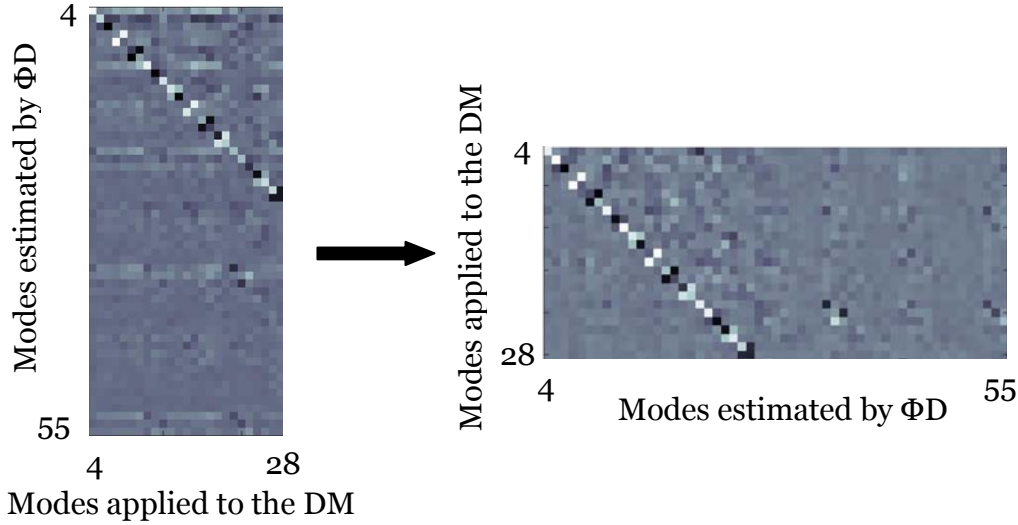


Figure 4.13: Measured Interaction Matrix (left) and corresponding Control Matrix obtained after generalized inversion (right).

As we produce Zernike polynomials with the DM and measure the same polynomials by ΦD , one could expect to see in the CM a main diagonal full of ones. The spreading of the values in the measured IM is simply due to a difference between the Zernike polynomials used by the ΦD and ours produced by the DM, and to an angle between the axis of the DM and of the camera. The Figure 4.14 shows a reshaped version of the CM with the highest values on the diagonal.

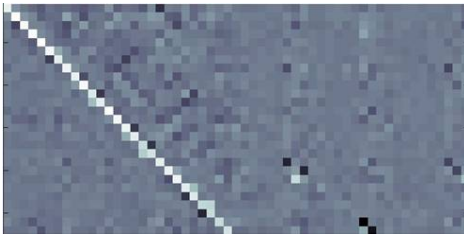


Figure 4.14: Reshaped Control Matrix

4.6.5. Correction

By applying the equations (4.11) and (4.12) and going through the iterative process described in the section 4.5.8, we recorded the convergence loop detailed in the Table 4.4. The Figure 4.15 shows the image recorded when no correction of the static aberrations is done, and the image after correction. The first image is obtained when the DM is set to its 'flat' shape, thus the aberrations are the same as the ones of the image in the Figure 4.9, plus the residual non-flatness of the newly installed ground DM. The corrected image is obtained after 5 iterations, but we can notice that after only one, the enhancement is already significant.

4.6 APPLICATION TO MAD

Iteration	0 (initial)	1	2	3	4
SR after correction (± 0.3 %)	83.2	92.6	92.6	93.1	93.4
Aberrations (nm rms)	138.2	47.1	39.9	37.5	37.0
Equivalent SR (%)	85.6	98.2	98.7	98.9	98.9

Table 4.4: Convergence loop in the case of 28 modes corrected in open loop.

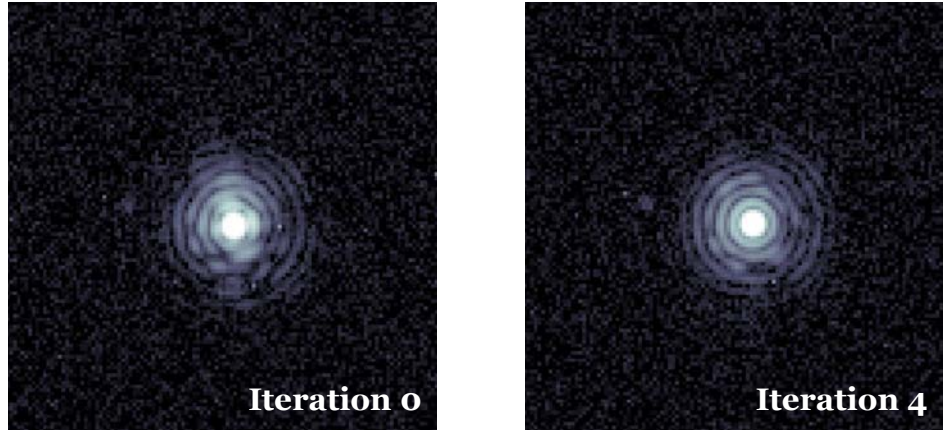


Figure 4.15: Starting point (left) for the correction of the aberrations (SR = 83.2 %) and best image (right) obtained after 5 iterations (SR = 93.4 %). Logarithmic scale.

4.6.6. MAD + visible camera

Between February and April '05 included, the ITC was not available, thus we installed a visible Peltier-cooled SBIG camera (Figure 4.16) at the IR focus of MAD, together with a narrow band filter at 1064 nm and a relay lens ensuring a good sampling on the CCD chip. We faced different problems in this configuration:

- Higher noise on the camera. The detector of the SBIG camera is cooled down to -10°C thanks to an integrated Peltier system. At 1064 nm and with the light sources available on MAD, we managed to reach a SNR on focused images of ~ 3200 , by taking the average of 9 images of 1 second integration time. This reduces the accuracy in measuring the IM.
- Shorter wavelength. The working wavelength of 1064 nm makes the aberrations larger compared to the diffraction limited spot, thus more difficult to estimate by ΦD .
- Camera software not integrated to the MAD environment.
- Second DM of MAD plugged for first MCAO tests, creating additional aberrations and eventually creep.

Once more, the IM was recorded following the previously described procedure and the static aberrations compensated (they are not the same as with the ITC because this one contains many aberrant optics and the visible camera does not). The process was much more difficult in this case, as most of the images the ΦD analysis failed, so they had to be manually re-centered and/or background subtracted, or even measured again. In the end the IM built contains

4. CORRECTION OF THE STATIC ABERRATIONS

only the modes 4 to 17 (Figure 4.17). We managed nevertheless to correct efficiently for the aberrations (Figure 4.18). The SR of the image before correction is **14.2 %** at 1064 nm (the ΦD estimates 235 nm), and after 4 iterations we reach **43.6 %** (155 nm). For information, the corresponding SR at 2200 nm are respectively 63.5 and 82.5 %.



Figure 4.16: ST-9XE CCD imaging camera.

This result shows several things. First, the technique of correction of the static aberrations with an IM has been applied to another system (DM + camera) quickly and with no big problem, proving its easiness of implementation. Also we saw that the building of the IM can be performed at a much shorter wavelength as long as the sampling and the SNR are good enough. Given the present system, we have also seen that the use of the first 14 modes is already enough to correct for most of the optical static aberrations.

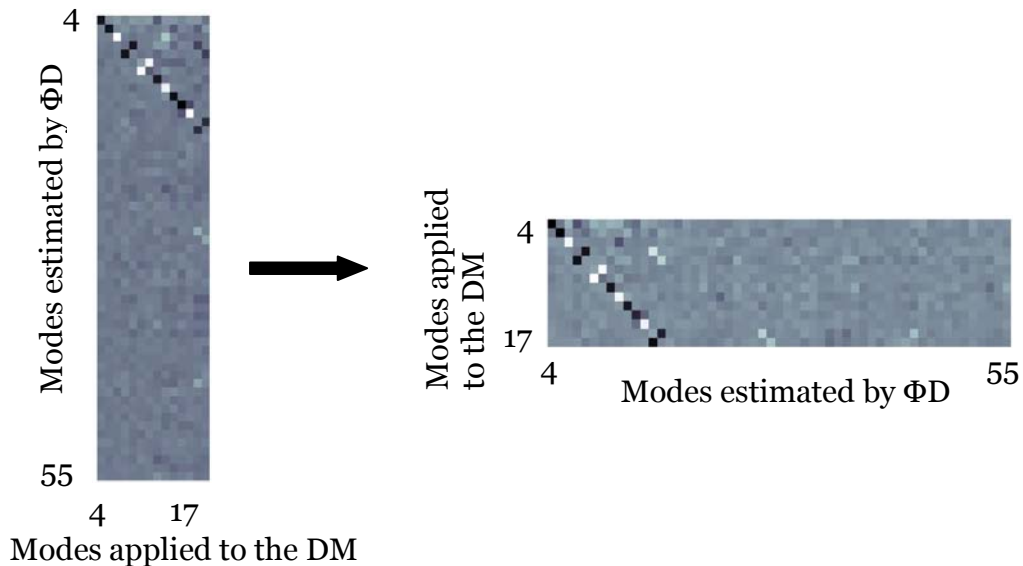


Figure 4.17: IM measured with the SBIG CCD camera (left), and corresponding CM (right).

4.6 APPLICATION TO MAD

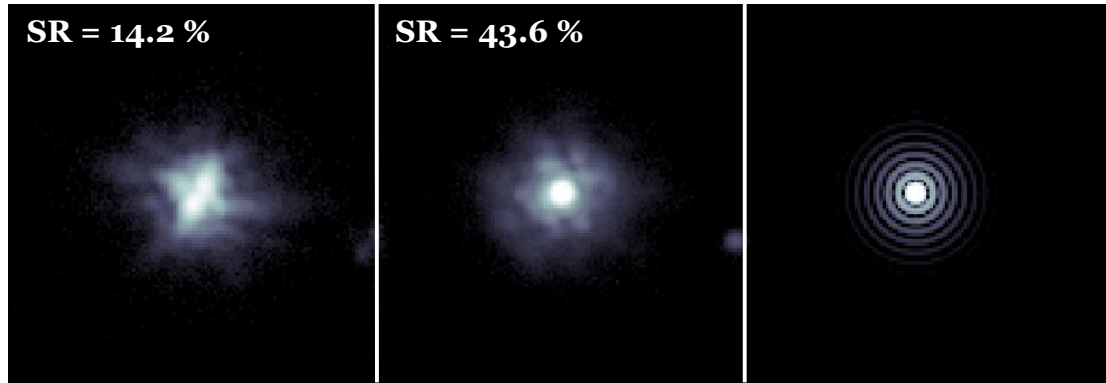


Figure 4.18: PSFs recorded with the visible camera, before (left) and after (center) correction, and theoretical diffraction limited PSF (right) in the same conditions. The ghost on the camera images is probably due to a reflection in the filter.

4.6.7. Discussion

The method we have used up to now has been named “***open loop correction for the on-axis static aberrations of the system MAD-ITC by the use of Phase Diversity and a calibration matrix***”. Its major improvement compared to existing techniques lies in the recording of an Interaction Matrix between the device compensating for the aberrations (the DM) and the device measuring the aberrations where they have to be minimized (the camera), in open loop.

By implementing it on two different systems, we have proved that it can be adapted easily to any configuration and uses only the common and science paths, but none of the calibration and WFS paths. This “all-measured” technique requires some knowledge of the DM’s IF in order to produce modes close to Zernike polynomials, but it is not compulsory. As for an AO system calibration, the first IM recorded might not be fully satisfying, and the next one bring an improvement. Indeed when the system is aligned, less than one day is enough to perform to full measurement of the IM and correction of the aberrations. No long and demanding fine tuning of a model is required.

However, some parameters have to be set carefully in order to achieve the best correction in the minimum number of iterations, like for instance the number of modes to correct or the amplitude to use when applying those modes to build the IM. The raw IM we have used up to now could be enhanced by applying clever filtering, or diagonalisation.

The way of recording the IM itself could be improved. Unlike for the calibration of an AO system, the recording an IM for the correction of the aberrations is a slow process, as well as the analysis of the images by Phase Diversity. Optimization of parameters such as the size of the image, the number of modes or the usefulness of the positive/negative modes technique could speed up the whole process.

Last but not least, it seems like after reaching a certain level of correction, the performance is limited by the stability of the system itself, in particular the evolution of the system between the moment when the IM is recorded and when

it is applied. Thermal expansions can change the aberrations of the bench, but against this there is no solution. The air flow in the bench can also alter the measurement ; this effect can be lowered, like on MAD, by enclosing the bench in a “turbulence-proof” box, playing at the same time the role of stray light shield. But the major effect appears to be the creep of the DM, especially important in the case of bimorph mirrors. We have effectively noticed that the DM voltages giving the best SR in the evening are not so good anymore when using the system the following morning. The difference is of the order of several SR percents. It is due to the fact that a DM that was under stress for hours doesn’t behave the same as when it is first plugged. The focus is especially concerned, and the variation can reach 2 mm at F/15.

It is logic to think that this effect would be strongly attenuated by working with the DM in closed loop with the MAD WFS, i.e. by using as reference modes ones defined on a (stable) WFS rather than on a (creeping) Deformable Mirror. This is what we intend to demonstrate in the following chapter. The step of the open loop technique was however necessary for the cases where the implementation of the closed loop is not possible or too complex, as in the FoV correction (section 4.8).

4.7. Improvements: close loop corrections

4.7.1. Description

The improvement to the previous technique that will be presented in this section is the “**closed loop correction for on-axis static aberrations by the use of Phase Diversity and a calibration matrix**”. The basic idea behind it is to “shortcut” the DM by recording the IM between the camera and the WFS in closed loop, and as a consequence to apply the correction by changing the reference functioning point of the WFS instead of the reference voltages of the DM (see the section 2.4.3 about the functioning of a SWFS). This way of getting the reference is more straight-forward than the one described at the end of the section 4.5.7, therefore more accurate.

The implementation of the technique we describe here requires more from the AO system: the WFS path has to be aligned, and the Real Time Computer (RTC) must be in a state where the loop can be closed at a frequency high enough to compensate for the residual turbulence in the bench (at least 50Hz). If we want this improvement to be really one, another constrain is to use the WFS in the most accurate and reproducible manner. To this aim, one has to study parameters such as the linearity and the noise of the sensor. In particular, one should be able to close the loop and acquire IR images on the same calibration source, which (contradictorily) should better be diffraction limited for a good ΦD estimation, and an extended source for a good linearity of a WFS as the Shack-Hartmann.

The first step is to know the reference points of the WFS that make the DM take the shape of Zernike coefficients in closed loop. This one can be obtained through the IM of the system, or measured directly by the WFS when applying

4.7 IMPROVEMENTS: CLOSE LOOP CORRECTIONS

the proper voltages to the DM (contained in the matrix $m2V$ of the equation (4.7)). We then build the matrix $m2Ref$ from those measurements:

$$\begin{matrix} N_m \\ \\ N_{Ref} \end{matrix} \begin{bmatrix} \\ \\ m2Ref \end{bmatrix} = \begin{bmatrix} \begin{bmatrix} \\ \\ R1 \end{bmatrix} & \begin{bmatrix} \\ \\ R2 \end{bmatrix} & \begin{bmatrix} \\ \\ R3 \end{bmatrix} & \dots & \begin{bmatrix} \\ \\ R_{NRef} \end{bmatrix} \end{bmatrix} \quad (4.16)$$

One could think that this introduction of an open loop measurement could cancel the advantage of the closed loop technique, but once again, here the important is not to be able to produce modes very close to Zernike ones, but to use them only as a basis to build the IM, and most of all be able to reproduce those modes as accurately as possible at will. The reproducibility in time is the key point, and the effects of other considerations are dealt with when we used the measured IM technique.

Each mode is applied to the system by closing the loop successively around the reference values contained in the columns of the matrix $m2Ref$ (equation (4.16)). Focused and defocused images are recorded, analyzed by ΦD and the resulting coefficients fill the IM (the same as in the equation (4.6)). The CM is computed as for the open loop technique, and from a ΦD estimation of the aberrations, a list of references correcting for the static aberrations is deduced:

$$\begin{matrix} \\ \\ N_{Ref} \end{matrix} \begin{bmatrix} \\ \\ Ref \end{bmatrix} = - \begin{matrix} N_m \\ \\ N_{Ref} \end{matrix} \begin{bmatrix} \\ \\ m2Ref \end{bmatrix} \times \begin{matrix} N_Z \\ \\ N_m \end{matrix} \begin{bmatrix} \\ \\ CM \end{bmatrix} \times \begin{matrix} \\ \\ N_Z \end{matrix} \begin{bmatrix} \\ \\ Ab \end{bmatrix} \quad (4.17)$$

The iterative process described in the 4.5.8 can be applied to this technique as well.

4.7.2. Experiment on BOA

Introduction

In the laboratories of ONERA in Châtillon (close to Paris, France) lies BOA (Banc d'Optique Adaptative), an optical bench used to perform tests on AO techniques being developed by the local AO group, the DOTA. This bench (Figure 4.19) is equipped with:

- A system for turbulence generation
- On- and off-axis calibration sources, fed by a laser at 633 nm
- A piezo-stack DM placed in a pupil plan (10 x 10 actuators, with 9 x 9 useful ones)
- A tip-tilt mirror
- A 8 x 8 SHWFS, with 52 useful sub-apertures and 15 x 15 pixels per sub-aperture
- A visible imaging camera for performance estimation: sampling = 4.1, electronic noise = 4 e⁻ (1,2 ADU)

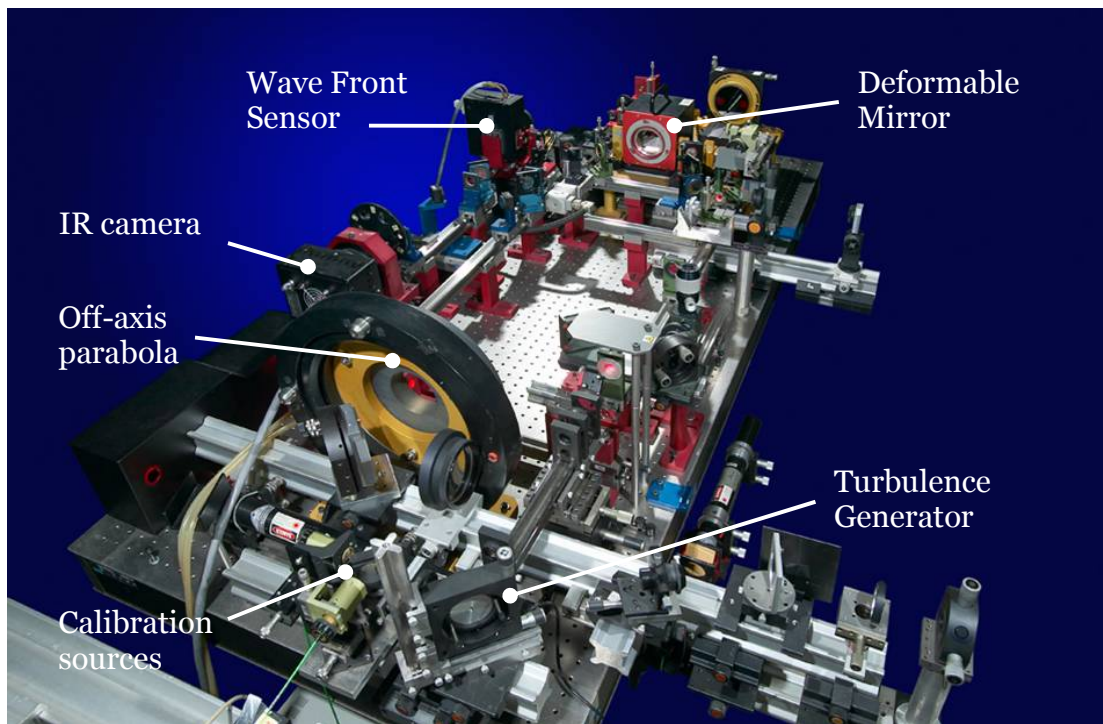


Figure 4.19: The BOA test bench at ONERA.

The tests usually performed on this bench are dealing with optimization of the reconstruction in AO, prediction of the turbulence in the command, off-axis optimization, and correction of the NCPA. There have been validated for the first time the ΦD technique before being implemented on NACO. The AO loop is closed routinely at a frequency of 270 Hz with a gain of 0.3 and a very good alignment of the bench together with a well-tuned model of the system allowed performing efficient experiments.

4.7 IMPROVEMENTS: CLOSE LOOP CORRECTIONS

For the NCPA compensation, the procedure used at ONERA involves closed loop DM control, correcting aberrations by the modification of the reference slopes, and recording the in and out of focus images by introducing the defocus through the reference slopes, therefore applying defocus deformation to the DM. The great advantage of it is that no optical element is moved between the recording of the images.

In the framework of the collaboration with ONERA for my thesis, I have organized the implementation of the closed loop technique with Interaction Matrix developed at ESO on the BOA bench at ONERA. This experiment shall benefit of the expertise of the ONERA team and the good knowledge they have of the bench, and include the IM technique to the already existing templates of correction of the aberrations, in order to compare different techniques, and try to reach higher performances. The criteria retained to make this comparison are the final SR and the speed of the convergence loop, but we will also take this opportunity to see how the technique applies to a different system, and experiment several improvements that have been thought without being implemented on the quite more complex system MAD.

The experiment parameters

After a test plan has been agreed, the BOA bench was available on the week from June 06th to 10th 2005. The work has been performed together with Benoît Neichel [67] and the support of Jean-François Sauvage for the bench, Thierry Fusco and Gérard Rousset for the theoretical aspects.

The first step was to use an already measured IM after “cleaning”, proper inversion and correction, as it is described in the previous section. The outcome was positive, and the performances achieved already better than the ones using the synthetic matrix (model). This first achievement also taught us more about the behavior of the system, and encouraged us to record a new IM, using the fresh experience on BOA and the lessons learned on the MAD bench at ESO, in details:

- The number of modes used to build the IM was increased from 36 to 45, 55 and finally 66, even if the DM can reproduce trustfully only 36 Zernike modes.
- The aberrations were estimated by ΦD over a larger number of Zernike coefficients: 133.
- The IM was not truncated before inversion.
- The modes were not recorded in positive and negative as previously implemented on MAD (section 4.5.4), but only in positive, and then the ΦD estimation of the aberrations was subtracted to the one of the mode, giving the same result provided that the system is stable:

$$\text{Mode} = (P - N) / 2 = P - \text{aberrations} \quad (4.18)$$

This allows recording twice more modes in the same amount of time.

- The amplitude of the modes was lowered from 50 to 20 nm rms in order to be closer to the aberrations to correct while keeping a good signal. The use of the right amplitude also make disappear artifacts due to the ΦD estimation. On the example shown on the Figure 4.20, it is clear that the estimation of the

4. CORRECTION OF THE STATIC ABERRATIONS

aberrations in the case of the amplitude 50 nm shows repetitive “peaks”, while it should show noise for high order Zernike modes.

- The defocus is introduced thanks to a proper change in the reference slopes of the SHWFS.
- The starting point is a configuration where the DM is flat. The SR is then **76.2 %** (Figure 4.23).

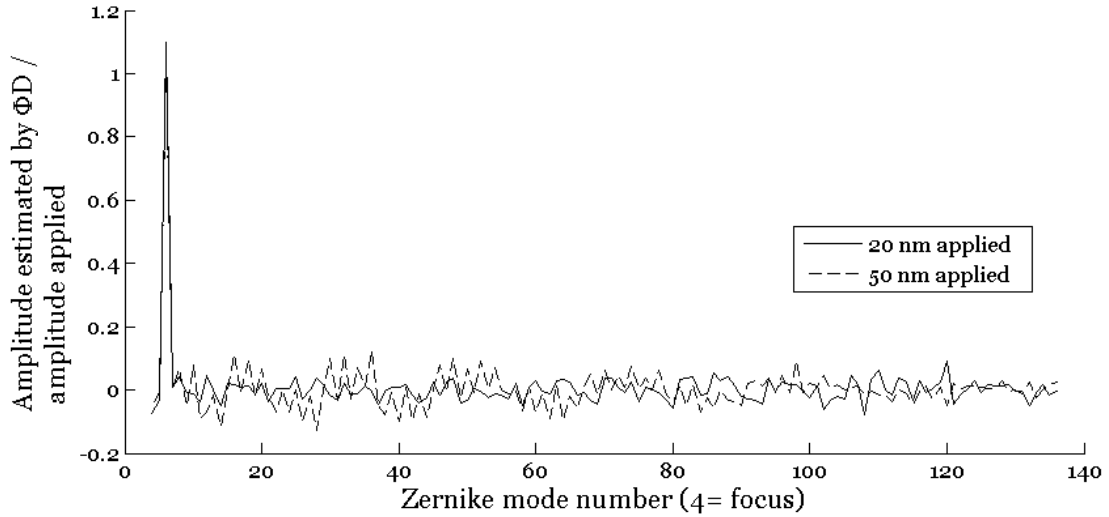


Figure 4.20: Comparison between the ΦD estimation of the 133 Zernike coefficients of the mode #6 applied with an amplitude of 20 (solid line) or 50 (dashed line) nm rms.

First results and comparisons

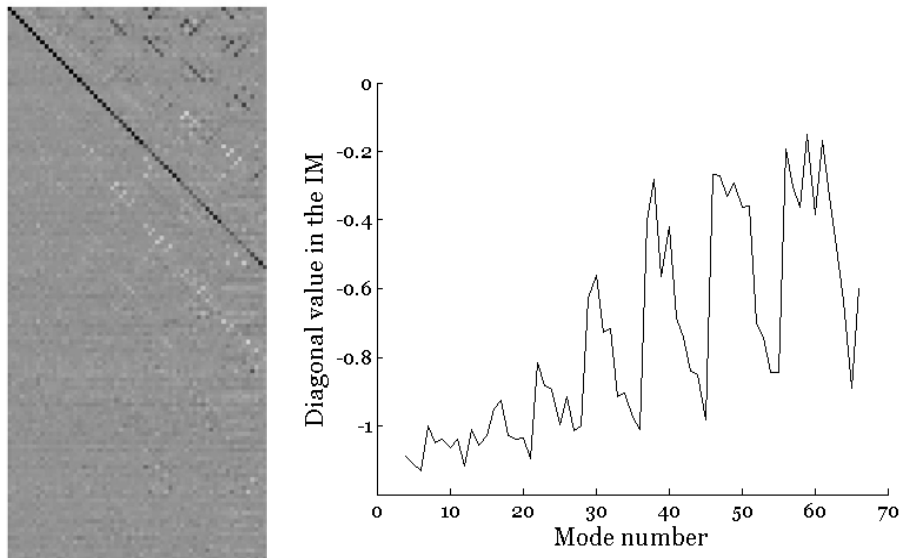


Figure 4.21: IM measured over the modes 4 to 66 and plot of the diagonal values.

4.7 IMPROVEMENTS: CLOSE LOOP CORRECTIONS

The IM measured is shown on the Figure 4.21. Several particularities come to our attention:

- The IM has the main values on the diagonal compared to the one obtained on MAD, especially for the modes lower than 36. This shows that the convention for the Zernike polynomials made by the DM is the same as the ones estimated by ΦD (even their orientation) and that the very well tuned system produces good Zernike polynomials. “Parasite” values on higher order modes are inherent to the system, but values on lower order modes should be attenuated by a better model.
- There are remnants of static aberrations in the modes measured, seen as horizontal lines in the IM. We tried to remove them by removing the median of the columns, but the performance is better without this modification.
- The plot of diagonal values shows us the amount of variance which is actually put in the mode we want to produce. We recognize a similar behavior as shown on the Figure 4.7 for the MAD bimorph DMs, i.e. a quality of the modes produces that increases and decreases periodically with the radial order of the polynomials.

The Figure 4.22 shows the convergence loop with or without the measured IM, for different number of modes used for the correction, and the Figure 4.23 the quality of PSF obtained after the first iteration with the matrix correcting for 66 modes.

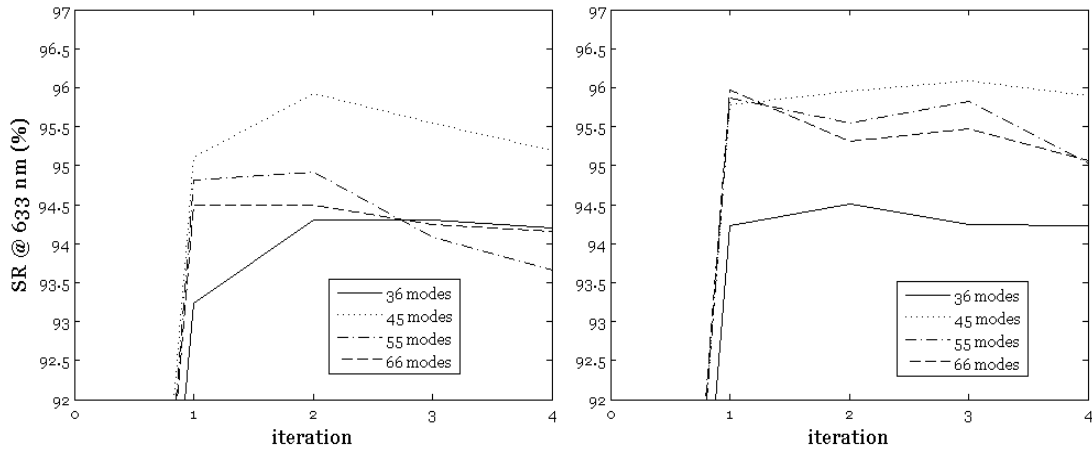


Figure 4.22: Convergence loop for different number of modes corrected, using the model (left) or the measured IM (right). The starting point (iteration 0) is a SR of 76.2 %. The error on a SR measurement is of ± 0.2 %.

4. CORRECTION OF THE STATIC ABERRATIONS

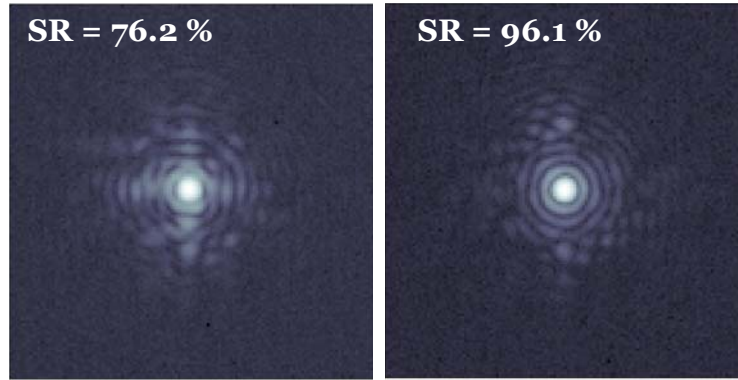


Figure 4.23: PSF before (left) and after (right) correction on the BOA bench using 66 mode. The SNR is > 10000 .

Clearly, the use of more than 36 modes, even with the model, enhances the quality and the speed of convergence. 45 modes seems to be a good value, while 55 and 66 create a decreasing of the performances after the first iteration, due to the poor quality of those modes as produced by the DM.

In the case we use the measured IM, the SR comes always at the first iteration close to its best value. If we correct 36 modes, the gain between the use of the model and of the IM is 1 iteration loop, but for 45 modes the SR of **96 %** reached surpasses the best performances obtained with the model, and is stable after several iterations.

Although working with the DM in closed loop, we noticed that the bench is not totally stable and the performances could vary for the same configuration between 95.9 and 96.5 %. The measurements leading to the results shown in the Figure 4.22 were taken in a lapse of time of 1 hour, and have been taken in parallel (doing for each iteration all the measurements before going to the next) so that the results for a given iteration can really be compared even if separated by less than 1 % of SR.

On the Figure 4.24 can be seen the Zernike coefficients remaining in the images after some iterations of correction using 36 modes. It is interesting to notice that the method without IM corrects better for the modes below 36 (vertical dashed line), while with the IM more modes are attenuated, giving approximately the same overall performance (Table 4.5). This has to be taken into account when one defines the criterion defining the best image: it can be either the best SR (bring more energy to the center of the PSF) or the less remaining aberrations in the first N Airy rings, more crucial in the case of close exo-planets detection for instance.

The Figure 4.25 shows the conditioning of the CM (diagonal values of the matrix S in the SVD). The conditioning number (ratio between the highest and lowest eigen values) is very small: 18, which explains that modes filtering is useless and doesn't improve the performances.

4.7 IMPROVEMENTS: CLOSE LOOP CORRECTIONS

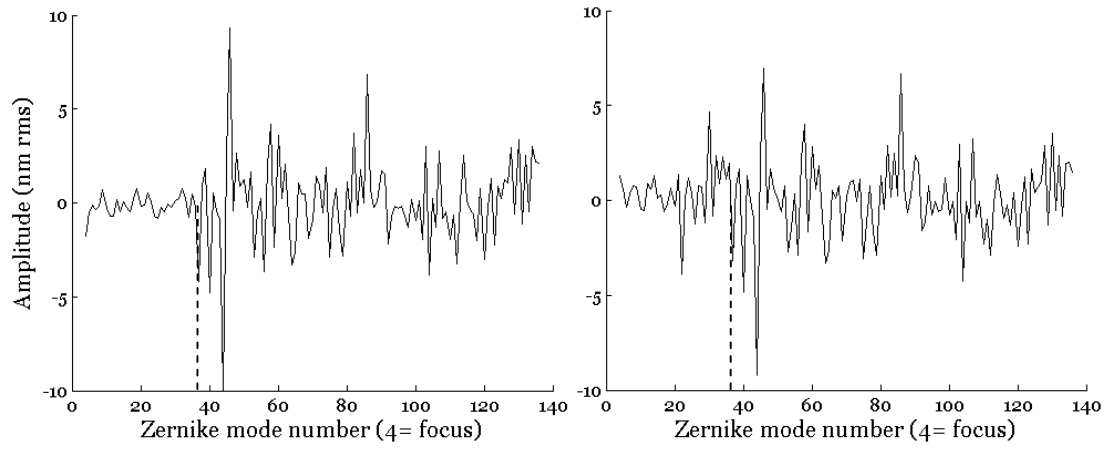


Figure 4.24: Estimation of the Zernike coefficients by ΦD , in the case of correction of 36 modes, after 3 iterations, without (left) and with (right) the use of the measured IM.

N	36	133
$\sqrt{\sum_{i=4}^N a_i^2}$ (nm)	Model	24.3
	Measured IM	23.5

Table 4.5: Aberrations estimated by ΦD , summed between the modes 4 and 36 or 4 and 133. The a_i are the Zernike coefficients estimated by ΦD shown on the Figure 4.24.

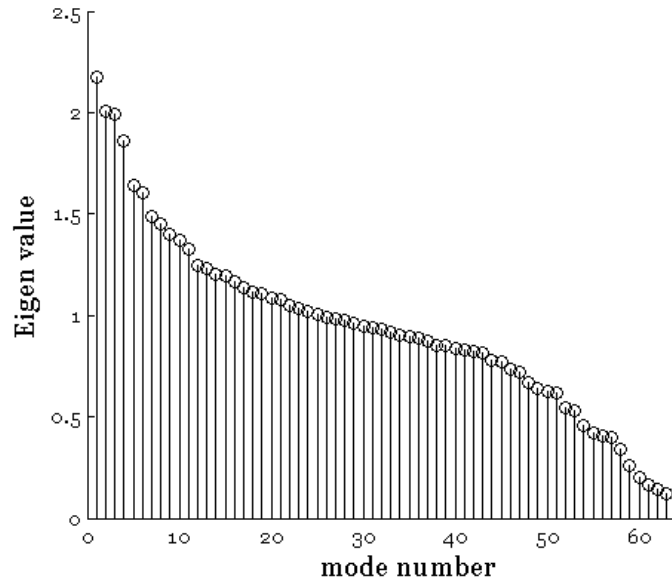


Figure 4.25: List of eigen values of the IM.

Possible improvements

A possible way to improve the quality of the IM is to enhance the diagonal values, i.e. to take out of the noise the modes that interest us. In order to achieve this, one has to modify the modes applied to record this IM. Instead of using modes coming from a model, we can now use the knowledge from the first IM measured to apply modes closer to the Zernike polynomials estimated by ΦD . To record this improved IM, we have to apply a linear combination of the modes applied previously, and the coefficients are contained in the CM. The modification is done at the level of the matrix $m2Ref$ (introduced in the equation (4.16) of the section 4.7.1):

$$\begin{matrix} N_m \\ N_{Ref} \end{matrix} \begin{bmatrix} m2Ref' \end{bmatrix} = \begin{matrix} N_m \\ N_{Ref} \end{matrix} \begin{bmatrix} m2Ref \end{bmatrix} \times \begin{matrix} N_Z \\ N_m \end{matrix} \begin{bmatrix} CM \end{bmatrix} \times \begin{matrix} N_m \\ N_{Ref} \end{matrix} \begin{bmatrix} Id \\ 0 \ 0 \ \dots \\ 0 \ 0 \ \dots \end{bmatrix} \quad (4.19)$$

where the role of the last matrix is to truncate the new $m2Ref$ to keep the same size as the original.

The modes contained in $m2Ref'$ are applied (still when working with the DM in closed loop) and a new IM is recorded, then inverted to get CM' . The correction of the aberration is performed similarly as before (equation (4.17)), with being careful of using $m2Ref'$ instead of $m2Ref$:

$$\begin{matrix} N_{Ref} \\ N_{Ref} \end{matrix} \begin{bmatrix} Ref' \end{bmatrix} = - \begin{matrix} N_m \\ N_{Ref} \end{matrix} \begin{bmatrix} m2Ref' \end{bmatrix} \times \begin{matrix} N_Z \\ N_m \end{matrix} \begin{bmatrix} CM' \end{bmatrix} \times \begin{matrix} N_Z \\ N_Z \end{matrix} \begin{bmatrix} Ab \end{bmatrix} \quad (4.20)$$

The goal of doing this is to measure an IM with smaller values outside of the diagonal. Qualitatively the advantage we see in doing this can be explained by the following example: if the modes used to build the first IM don't bring values only on the diagonal, the mode 6 could produce also some of the Zernike mode 10, and the mode 10 a little of the Zernike mode 6. Then if on the aberrated image one measures both the presence of the modes 6 and 10, the application of the CM will not allow correcting them properly.

It is obvious that the for the Zernike modes that the DM can not physically produce, the cross-terms are inevitable, but the for the other modes it could be valuable to implement this "diagonalisation".

As the new modes applied are a linear combination of the former ones (equation (4.19)), we can predict that the new Zernike modes measured are a combination of the old ones, leading to this prediction IM'_{pre} for IM' :

4.7 IMPROVEMENTS: CLOSE LOOP CORRECTIONS

$$\begin{matrix} N_m \\ \left[\begin{array}{c} \\ \\ \text{IM}'_{\text{pre}} \\ \\ \end{array} \right] \\ N_Z \end{matrix} = \begin{matrix} N_m \\ \left[\begin{array}{c} \\ \\ \text{IM} \\ \\ \end{array} \right] \\ N_Z \end{matrix} \times \begin{matrix} N_Z \\ \left[\begin{array}{c} \\ \\ \text{CM} \\ \\ \end{array} \right] \\ N_m \end{matrix} \times \begin{matrix} N_m \\ \left[\begin{array}{c} \\ \\ \text{Id} \\ \\ \end{array} \right] \\ N_Z \end{matrix} \quad (4.21)$$

Using the measurements performed on the BOA bench, the Figure 4.26 shows a comparison between the two matrices IM (a) and IM'_{pre} (b). We notice the vanishing of contribution of most of the low order modes on the higher order ones. However, the secondary diagonals prove (as expected) that some high order modes are not orthogonal and thus cannot be created independently. The enhancement of the diagonal values can be seen on the Figure 4.27.

To go even more in this direction, one can “boost” the diagonal values of the IM, and bring them all to the same value, by dividing the new modes to apply by the diagonal values of the predicted IM (Figure 4.26.b). The boosted predicted IM is shown on the Figure 4.26.c, and one can see on the Figure 4.27.c that the diagonal values are effectively all identical and equal to -1.

The new modes $m2Ref'$ have been used to record the second IM on the BOA bench. It is shown on the Figure 4.26/d. This matrix looks pretty much like the one predicted, although the diagonal values are not that uniform (Figure 4.27/d). The conditioning number of this matrix is improved (= 14.5), meaning that we managed effectively to improve the SNR of the IM.

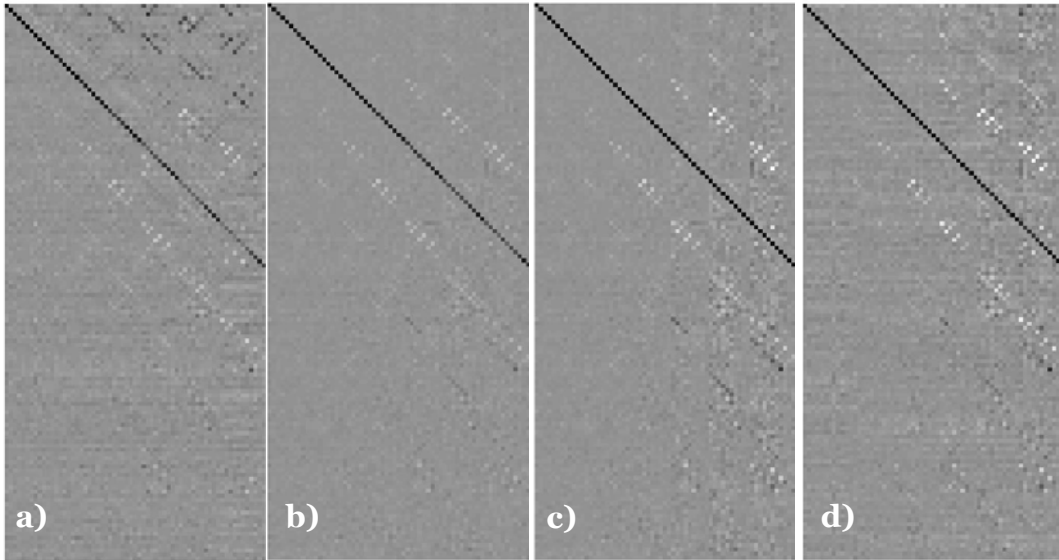


Figure 4.26: Interaction Matrices (same look-up table) measured over the modes 4 to 66 and projected on 136 Zernike polynomials: a) first measured, b) second predicted, c) second predicted and boosted, d) second measured.

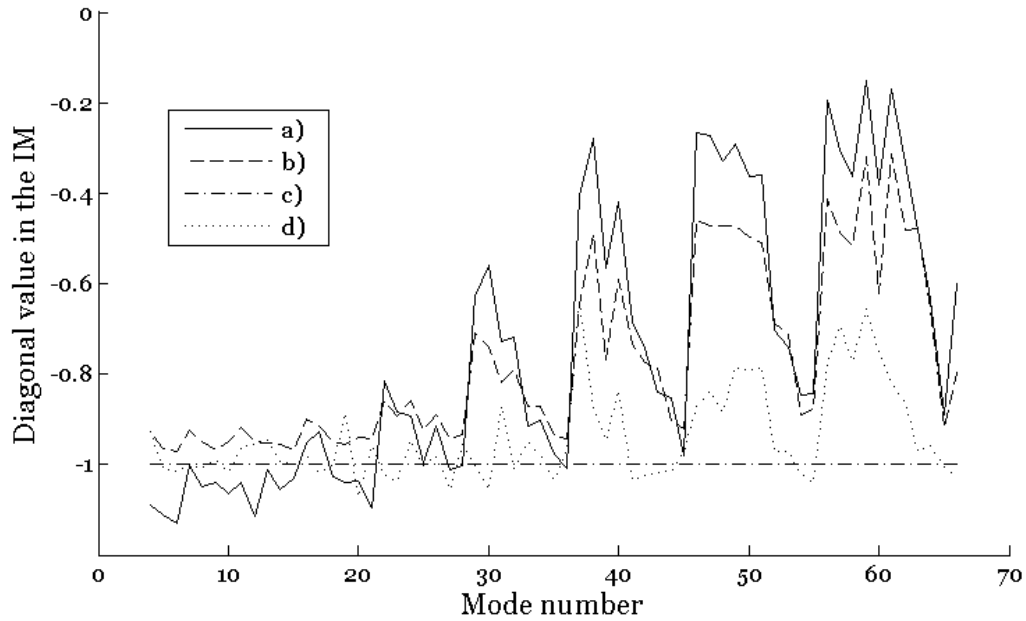


Figure 4.27: Diagonal values of the IMs shown on the Figure 4.26: a) first measured, b) second predicted, c) second predicted and boosted, d) second measured.

However, the application of this new IM didn't bring any enhancement to the correction of the aberrations. This can be explained by the fact that the first IM already had a very good conditioning.

Discussion

The implementation of the adaptive closed loop correction of the NCPA on the BOA test bench was a success. We proved once more the flexibility of the technique, easily adaptable to any new AO system. The quality of the correction was improved and this at the first iteration, giving a smaller importance to the iterative process, yet still required to compensate for changes happening between the recording of the IM and its application. We could use a number of modes much higher than what can produce the DM without degradation, with an IM built with Zernike modes and not even "diagonalisation".

In addition to those results, we took the opportunity of working on such a stable system to test some possible improvements on the measurement and application of the IM, which didn't appear to be better than the initial procedure. It is interesting to notice that most of the possible improvements are directly inspired from what is usually done for the calibration of an AO system (modes filtering, diagonalisation, enhancement of the IM by using measured modes as a basis instead of theoretical modes ...).

The improvement brought to the knowledge of the behavior of the BOA bench is a first step towards the implementation of the correction of the NCPA for future high order AO systems (Planet Finder-like), for which a very high SR is required, in spite of the greater and greater number of (aberrant) optics in the path.

4.7 IMPROVEMENTS: CLOSE LOOP CORRECTIONS

4.7.3. MAD + ITC

After the first corrections in open loop on MAD and the tests on BOA, the Single Conjugate AO loop was finally closed on MAD in March '05: 1 SHWFS looking at 1 calibrations source, or a simulated star through turbulence, and working at a frequency $> 100\text{Hz}$. This was the door open to the implementation of the adaptive closed loop correction of the NCPA, aiming to freeze the turbulence in the bench and to avoid the creep of the DM. Indeed we have followed the procedure described in the section 4.7.1 to produce Zernike modes in closed loop (4.16), build the IM, invert it and apply the CM to the aberrations measured (4.17) to get the set of reference slopes that bring the best WF at the level of the camera.

From the outcome of the measurements on BOA, we deduced the best parameters to use on MAD:

- The number of modes used to build the IM was kept to 28 in a first time.
- The aberrations were still estimated over 55 Zernike coefficients.
- The IM has not been 'diagonalised', boosted or filtered from noisy modes.
- The modes were recorded only in positive and then the ΦD estimation of the aberrations was subtracted to the one of the mode, like it was done on BOA.
- The amplitude of the modes was kept to 25 nm.
- The defocus for the Diversity image is still introduced by moving the collimator.
- We use the broadband K filter of the ITC to avoid ghosts, and place a narrowband filter at 2188 nm just before the calibration fiber.
- A direct effect of the previous point is that the visible WFS doesn't see the source we use for the ΦD . The fact that a diffraction limited calibration source is not Nyquist sampled on the CCD of the SHWFS of MAD, making it non linear, is also a problem. The solution we found is to use an off-axis extended calibration source, fed by a white light, for closing the loop on it. The IM is then built off-axis, but the measurement of the modes and the correction are made on the static aberrations measured on-axis. Once the best off-axis reference slopes determined, the on-axis fiber is replaced by an extended source, and the on-axis reference slopes are recorded while still closing the loop off-axis (this on 2 different SHWFS obviously).
- The starting point is a configuration where the loop is closed around the zero reference slopes of the WFS.

In this configuration, we didn't manage to record a satisfying Interaction Matrix. The CM computed from the IM measured allowed getting barely a better performance than without correction. Due to a problem with the ITC, it has not been possible to redo the experiment.

The results obtained on BOA (section 4.7.2) proved the validity of the method, which we were unable to put in practice on MAD. However, the "open loop" technique (section 4.6.5) allowed getting an already very satisfying performance on-axis, which converted into reference slopes became a solid reference to use in closed loop.

4.8. Aberrations correction in the Field of View

In this chapter we will extend the idea of correction of the static aberrations with a calibration matrix to the case of field-dependant aberrations. We will limit ourselves to the “open-loop” technique (based on the section 4.5), the “closed-loop” one (section 4.7) being more complicated to put into practice, and probably leading to an improvement barely noticeable on the performances of an MCAO system.

4.8.1. Idea

As the performances of an SCAO system are degraded in the FoV by the atmospheric anisoplanetism [23], the correction of the static aberrations described in the previous chapter is valid on-axis, and leaves the borders of the FoV degraded by the field-dependent aberrations of the optics. This effect becomes significant for an MCAO system, which aim is to provide the best uniform performance a wide FoV. We have experimented it when applying the best correction obtained in the section 4.7.3 to MAD, correcting thus for the on-axis static aberrations, and measuring the quality of the images around the 2 arc minutes FoV of the instrument: we measured a loss of SR of about 5 % percents at the edges, which is a bad starting point for who wants to perform a uniform MCAO correction of the atmospheric turbulence.

“Ground layer” correction

The next step in order to make uniform the residual aberrations in the large FoV of an instrument composed of 1 DM (wide field SCAO or GLAO) is to perform a “Ground Layer” correction of the static aberrations. The procedure would be to record an IM in one direction of the FoV (e.g. the center), and invert it exactly as described in the section 4.5 in order to get the CM. The difference with the previous method lies in the recording of the aberrations: not only one direction in the FoV is concerned but many (Figure 4.28).

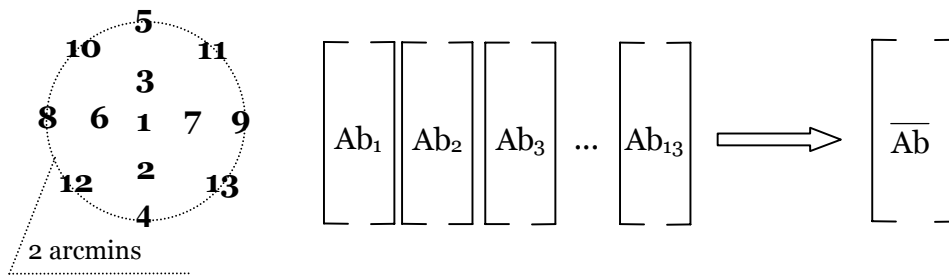


Figure 4.28: Example of grid of positions in a 2 arcmin FoV, and averaging of the aberrations estimated by ΦD to get the vector \overline{Ab} .

For each directions of a grid defined in the FoV, focused and defocused images are recorded and the aberrations are estimated by ΦD . The list of coefficients are then averaged to retrieve the common contribution \overline{Ab} of all the aberrations (“Ground layer” contribution). It is this vector which is multiplied to

4.8 ABERRATIONS CORRECTION IN THE FIELD OF VIEW

the CM to get the correction to apply (equation (4.22)). This procedure will have as effect the uniformisation of the static aberrations correction in the FoV. Several iterations can be done in order to reach better performances (section 4.5.8).

$$\begin{matrix} N_m \end{matrix} \begin{bmatrix} \text{Corr} \end{bmatrix} = - \begin{matrix} N_Z \\ \text{CM} \end{matrix} \begin{bmatrix} \end{bmatrix} \times \begin{bmatrix} \overline{\text{Ab}} \end{bmatrix} \begin{matrix} N_Z \end{matrix} \quad (4.22)$$

MCAO correction

In an MCAO system, the difficulty is increased by the large FoV and the complexity of the system, but the presence of several DMs can help correcting more efficiently the aberrations in the field. Indeed we can here also consider the camera as a WFS that allows taking several WF measurements in the FoV. The optics creating the aberrations can be assimilated to layers conjugated at different altitudes. In order to correct for this, it is then logic to apply a tomographic approach inspired by the atmospheric tomography for MCAO real-time correction [26].

The idea behind is to measure the WF in different directions of the FoV, reconstruct the aberrations at the level of layers where we guess they are present, and finally project on the altitudes at which are conjugated the DMs performing the correction. In atmospheric tomography, an approximation is done when considering thin turbulent layers, while in our case an error comes rather from the fact that the field-dependent aberrations of the optics cannot be described by a WF error at a fixed altitude. Tomography is nevertheless a very strong tool to analyse a volume of turbulence as well as a bunch of optics creating static aberrations.

A code has been written in Matlab in order to perform the tomography in the specific case of MAD. A summary of how tomography works is given in the following section.

4.8.2. Theoretical background about tomography

Let us suppose that the aberrations φ are produced in a discrete number of layers N_t . The expression of the phase measured in the N_{GS} directions is:

$$\Phi_{N_{GS}} = M_{N_{GS}}^{N_t} \varphi + n \quad (4.23)$$

where φ is the vector of the aberrations in the N_t layers, and n the noise on the measurement. The matrix $M_{\alpha}^{N_t}$ sums the contributions in the telescope pupil of the Wave Fronts in N_t altitudes and for a given direction α ; $M_{N_{GS}}^{N_t}$ is the concatenation of the matrices $M_{\alpha}^{N_t}$ for all the N_{GS} directions of interest.

The estimation $\hat{\varphi}$ of φ we seek has the shape:

$$\hat{\varphi} = W \times \Phi_{N_{GS}} \quad (4.24)$$

4. CORRECTION OF THE STATIC ABERRATIONS

where the unknowns are the elements of the reconstruction matrix W .

The criterion to be minimized is the residual phase variance in a FoV of interest $\{\alpha\}_{\text{fov}}$:

$$\varepsilon = \left\langle \int_{\{\alpha\}_{\text{fov}}} \left\| \mathbf{M}_{\alpha}^{N_{\text{DM}}} \hat{\phi} - \mathbf{M}_{\alpha}^{N_t} \phi \right\|^2 d\alpha \right\rangle_{\phi, \text{noise}} \quad (4.25)$$

where $\mathbf{M}_{\alpha}^{N_{\text{DM}}}$ is defined the same way as $\mathbf{M}_{\alpha}^{N_t}$ but for the N_{DM} altitudes.

The minimization of this equation gives [29]:

$$\mathbf{W} = \mathbf{P}_{N_{\text{DM}}, N_t} \times \mathbf{W}_{\text{MA}}, \quad (4.26)$$

$$\text{with } \mathbf{P}_{N_{\text{DM}}, N_t} = \left(\int_{\{\alpha\}_{\text{fov}}} \left(\mathbf{M}_{\alpha}^{N_{\text{DM}}} \right)^T \left(\mathbf{M}_{\alpha}^{N_{\text{DM}}} \right) d\alpha \right)^+ \left(\int_{\{\alpha\}_{\text{fov}}} \left(\mathbf{M}_{\alpha}^{N_{\text{DM}}} \right)^T \left(\mathbf{M}_{\alpha}^{N_t} \right) d\alpha \right) \quad (4.27)$$

$$\text{and } \mathbf{W}_{\text{MA}} = \mathbf{C}_{\phi} \left(\mathbf{M}_{N_{\text{GS}}}^{N_t} \right)^T \left(\mathbf{M}_{N_{\text{GS}}}^{N_t} \mathbf{C}_{\phi} \left(\mathbf{M}_{N_{\text{GS}}}^{N_t} \right)^T + \mathbf{C}_n \right)^{-1} \quad (4.28)$$

where \mathbf{C}_{ϕ} and \mathbf{C}_n are respectively the aberrations and noise covariance matrices. The matrix $\mathbf{M}_{N_{\text{GS}}}^{N_{\text{DM}}}$ is defined the same way as $\mathbf{M}_{N_{\text{GS}}}^{N_t}$ but for the N_{DM} altitudes of the DMs instead of the N_t altitudes of the layers. A^+ denotes a generalized inverse of the matrix A .

In the case where the number of layers containing the aberrations N_t is the same as the number of DMs N_{DM} , the projector $\mathbf{P}_{N_{\text{DM}}, N_t}$ is equal to identity and thus \mathbf{W}_{MA} is the reconstruction matrix. In the realistic case where there are $N_t > N_{\text{DM}}$ equivalent layers, \mathbf{W}_{MA} reconstructs the WF on the N_t layers and the multiplication by the projector gives the reconstruction matrix on N_{DM} layers.

From the matrix W , one can then compute $\hat{\phi}$ as in the equation (4.24). This gives the estimated correction phase on each DM that ensures a minimal residual phase variance for all the directions of the specified FoV $\{\alpha\}_{\text{fov}}$. It is then possible to optimize the correction in one direction of the field, one area, or the full FoV.

In addition to the directions of the GS, we can evaluate the quality of the correction in more directions in the field. The residual seen in those N_a directions of analysis is then:

$$\mathbf{R}_a = \Phi_{N_a} - \mathbf{M}_{N_a}^{N_{\text{DM}}} \hat{\phi} = \Phi_{N_a} - \mathbf{M}_{N_a}^{N_{\text{DM}}} \mathbf{W} \Phi_{N_{\text{GS}}} \quad (4.29)$$

where $\mathbf{M}_{N_a}^{N_{\text{DM}}}$ is defined the same way as $\mathbf{M}_{N_{\text{GS}}}^{N_{\text{DM}}}$, but for the N_a directions of analysis. \mathbf{R}_a is the residual WF seen in the N_a directions (its calculation requires the knowledge of the aberrations in those directions). From it we can derive the SR or the decomposition into Zernike coefficients of the residual.

A possibility is to limit ourselves to the evaluation of the performances in the direction of the GS:

$$\mathbf{R}_{\text{GS}} = \Phi_{N_{\text{GS}}} - \mathbf{M}_{N_{\text{GS}}}^{N_{\text{DM}}} \hat{\phi} = \left(1 - \mathbf{M}_{N_{\text{GS}}}^{N_{\text{DM}}} \mathbf{W} \right) \Phi_{N_{\text{GS}}} \quad (4.30)$$

4.8.3. Application to the correction of static aberrations, practical implementation.

The tomography requires some modifications in order to be applied to the correction of static aberrations.

4.8 ABERRATIONS CORRECTION IN THE FIELD OF VIEW

The aberrations measured are the output of the ΦD software, as a list of Zernike coefficients, which can be truncated to the useful number of N_Z coefficients. After making measurements in N_{GS} directions, we build the matrix $\Phi_{N_{GS}}$ of size $[N_{GS} \times N_Z, 1]$.

In order to get the matrix W , one need to compute first the meta-matrix $M_{N_{GS}}^{N_t}$, which depends only on the position of the calibration stars in the FoV and on the position of the N_t equivalent layers. The role of this matrix is to sample the Zernike polynomials in the meta-pupils at the N_t altitudes into Zernike polynomials in pupils of the appropriate size and position. It has been shown [78] that the number of polynomials required for such decomposition is smaller or equal to the number of polynomials used to define the meta-pupil. The analytical expression of the decomposition is demonstrated in [28]. However for the present simulations we use a numerical projection, accurate enough for our need and that shows the same behavior as the theory demonstrated: on the Figure 4.29 we see that from a polynomial of order N over the meta-pupil, it is possible to select any pupil and describe it thanks to a number of polynomials $\leq N$.

So for each couple GS/layer, we project Zernike polynomials from the meta-pupil to the pupil in order to create the transformation matrix M (size $[N_Z, N_Z]$), that we see on the Figure 4.29. For each GS (direction α), all the M matrices are concatenated to create $M_\alpha^{N_t}$ (size $[N_Z, N_t \times N_Z]$), and finally all the matrices $M_\alpha^{N_t}$ build $M_{N_{GS}}^{N_t}$ (size $[N_{GS} \times N_Z, N_t \times N_Z]$).

The same procedure is repeated for the couples GS/DM in order to build $M_{N_{GS}}^{N_{DM}}$ (size $[N_{GS} \times N_Z, N_{DM} \times N_Z]$).

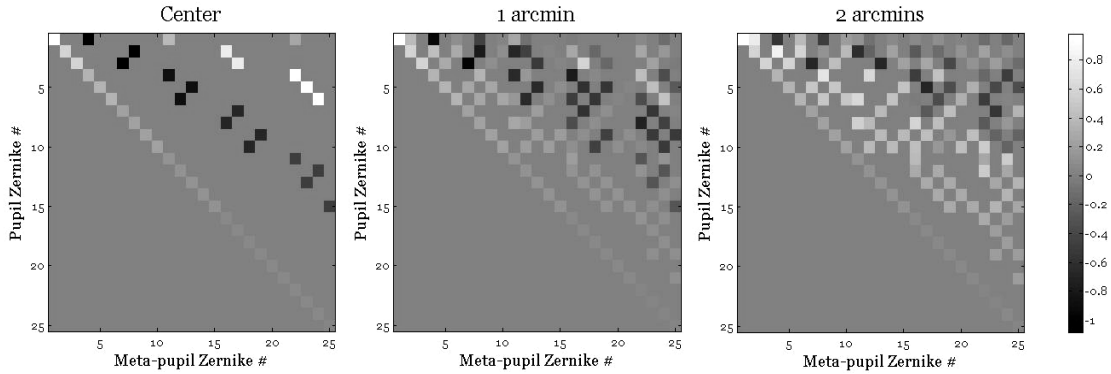


Figure 4.29: Result of the projection of Zernike polynomials from a meta-pupil at 8.5 km altitude to a pupil placed at the centered of the FoV (left), at 1 arcmin (middle) and 2 arcmins (right) from the center. The Zernike polynomial of order N in the meta-pupil can always be described by the polynomials of order $\leq N$ in the pupil.

At this level we need to compute C_φ (size $[N_t \times N_Z, N_t \times N_Z]$) and C_n (size $[N_{GS} \times N_Z, N_{GS} \times N_Z]$), which have a totally different meaning than in atmospheric tomography. In the present case the aberrations are measured at high flux and with the same accuracy for all directions, so the noise covariance matrix C_n is almost meaningless. Moreover the turbulence covariance matrix C_φ , normally

4. CORRECTION OF THE STATIC ABERRATIONS

computed from the Kolmogorov statistics, should rather be deduced from statistics on the amplitude of the aberrations in optical elements. Anyway, the aberrations being static and with the possibility to make several iterations, the importance of regularization thanks to this matrix is reduced compared to the atmospheric case.

In practice, the matrices C_φ and C_n represent the weight given respectively to the priors and to the measurements. If the measurement of good quality (mainly a good flux), C_n is predominant. On the contrary, in the case of noisy measurements, a relative importance of C_φ gives more weight to the priors on the statistics of the turbulence.

In our case, the measurements are perfect, thus contain no noise. Moreover we didn't wish to introduce any priors, because the phenomenon responsible for the aberrations is not statistical is the turbulence is. That's why we used for C_n an identity matrix and for C_φ an identity matrix multiplied by 1000.

The matrix W_{MA} (size $[N_t \times N_Z, N_{GS} \times N_Z]$) is easily computed from the knowledge of the previous elements.

Computing the projector P_{N_{DM}, N_t} (size $[N_{GS} \times N_Z, N_t \times N_Z]$) requires the knowledge of the matrices $M_\alpha^{N_t}$ and $M_\alpha^{N_{DM}}$ for each of the α where we want to optimize the correction. They can be one direction, the same directions as the ones of the GS, or a grid of directions in order to optimize part or all of the FoV.

The computation of the reconstruction matrix W (size $[N_{DM} \times N_Z, N_{GS} \times N_Z]$) is then immediate (equation (4.26)). Note that this matrix is built purely upon geometrical considerations, independently from the system and its aberrations.

4.8.4. Simulations

Framework of the simulations

The tomographic approach has been tested by simulation while the MAD bench was not yet integrated [42]. The optical elements mainly responsible for the degradation of the beam quality in the common and IR paths are (see the optical design of MAD in the Figure 2.4):

- Two collimators situated at equivalent altitudes of 16.2 Km
- Two folding mirrors at 13 and 14 Km
- The IR/visible Dichroic at 7.5 Km
- The residual non-flatness of the two DMs at 0 and 8.5 Km

When the derotator is active during on-sky operations, its optics is rotating in the FoV, thus it is not possible to calibrate it. Its optics are very close to the entrance focal plane (small footprints) and are constituted only of flat mirrors, so they shouldn't introduce much aberration.

All the ΦD images will be recorded on the axis of the IR camera, to disentangle the field-dependant aberrations of the camera from the ones of MAD. The optics of the camera are conjugated with altitudes of 0, 45 and 55 km, and the filters are higher than 100 km.

Only measurements on the bench once fully integrated and aligned will teach us the amount of aberrations to correct, but we can get an estimation of this

4.8 ABERRATIONS CORRECTION IN THE FIELD OF VIEW

value from the data on the separated optical pieces exaggerated to simulate a worst case situation (Table 4.6). In a first estimation, we consider that only four elements bring aberrations to the system, and that distortion can be modeled by a simple WF shift when the beam passes through a plane at the position of the optical element.

Thus, in order to simulate the real system, those aberrations were added to the optical design of MAD made by a ray-tracing software. By this way we combine the design aberrations, the chromatic aberrations and the expected optics aberrations.

A grid of 13 points has been defined in the FoV, following the geometry shown in Figure 4.30. Those points will be the measurement points of the aberrations. The SR in the K band (as calculated by the ray-tracing software) is also shown in Figure 4.30. We notice that it is always greater than 90 %, except some points at the border of the field where it drops down to 75 %, which is finally not unrealistic when we know the real aberrations as measured on the bench in its final configuration (with 2 DMs aligned).

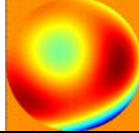
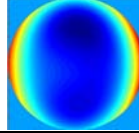
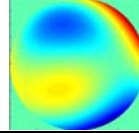
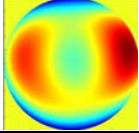
Optical element	Coll. # 1	Mirror IR1	Coll. # 2	Mirror IR2
Conjugation altitude (km)	16.2	13	16.2	14
Pupil footprint (mm)	60	60	60	60
Metapupil footprint(mm)	130	117	130	121
Aberr. added (nm rms)	85	65	100	105
Aberrations map				

Table 4.6: Aberrations on four optical elements of the common and IR paths, as implemented in the simulations. The rms value given refers to the aberrations over the whole surface of the optics.

Results

The WFs calculated by the ray-tracing software Zemax at the stars position are transformed into focused and defocused images. No noise is added to those images. They are analyzed by the ΦD algorithm that gives a table of Zernike coefficients for each position in the FoV. Those coefficients and the parameters of the system are used as input of our algorithm. As explained in the previous section, C_n is chosen to be an identity matrix and C_ϕ an identity matrix multiplied by 1000.

The reconstruction is done on eight layers (at 0, 4, 7.5, 8.5, 13, 14, 16.2 and 30 km) to take into account the position of the optics and to fill efficiently the equivalent volume occupied by the instrument. The projection is done at the levels of the two DMs (0 and 8.5 km). Finally the best correction computed for the 2 DMs is re-injected on the corresponding surfaces in Zemax, and the residual WFs are measured in the same directions as before. The quality of the correction is estimated thanks to the SR computed from the WF measurements:

4. CORRECTION OF THE STATIC ABERRATIONS

$$SR \approx e^{-\sigma^2} \quad (4.31)$$

where σ^2 is the variance of the phase.

The correction achieved is plotted in the Figure 4.30. At the positions of the measurements, the SR in K before correction (solid line) is ranging from 75.5 to 99 % in the FoV, with an average of **89.8 %**. After correction (dotted line) it is restricted to the range 93.3-98.8 % with an average of **97.2 %**. Note that those values might be underestimated because computed from the first 25 Zernike coefficients only, but that the most important is the comparison between before and after the correction.

This result proves that the tomographic reconstruction of the aberrations of the optics in the MCAO instrument is efficient, and that the projection on the two DMs brings a great enhancement of the quality of the images in the full scientific FoV.

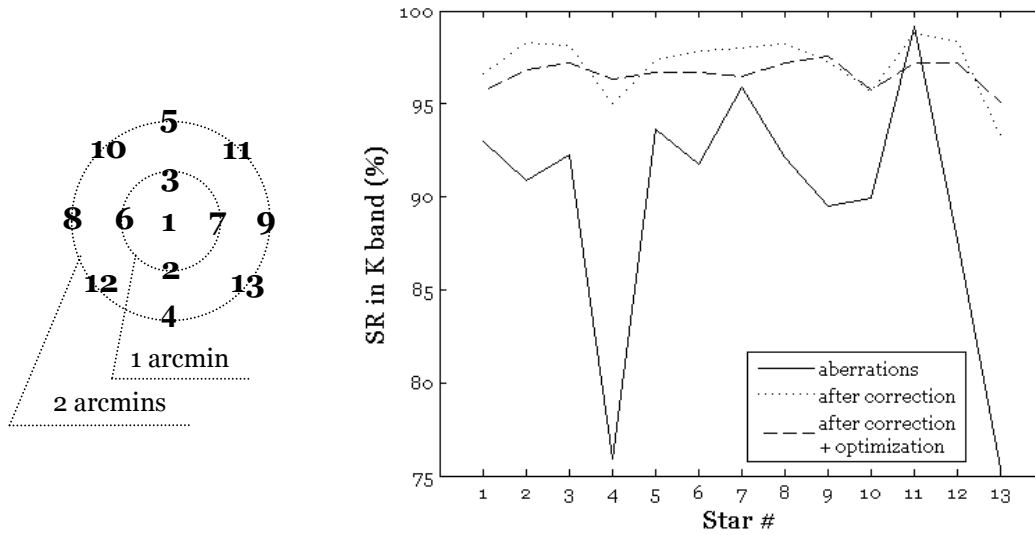


Figure 4.30: Configuration of stars used for the simulations. SR measurements before (solid line) and after correction by tomography (dotted line) and numerical optimization (dashed line).

Numerical optimization

Although the minimization of the criterion described previously (equation (4.25)) leads to the best average correction in the field, maybe it would be of an interest to define another one. In the case of the correction of the static aberrations in the FoV, an interesting criterion could rather be the dispersion of the residual variances in the directions of interest. The minimization of this criterion would lead to a solution with the best uniformity of the residual aberrations in the scientific field (or at least in the directions of interest) of the MCAO instrument, even if the average SR is a bit lower than the result obtained in the previous section. A possible expression of this estimator would be:

4.8 ABERRATIONS CORRECTION IN THE FIELD OF VIEW

$$\varepsilon' = \text{Var}_\alpha \left(\sum_i a_{\alpha,i}^2 \right) \equiv \int_{\{\alpha\}_{\text{fov}}} \left\| \sum_i a_{\alpha,i}^2 - \overline{\sum_i a_{\alpha,i}^2} \right\|^2 d\alpha \quad (4.32)$$

where \overline{X} denotes the average of X , the $a_{\alpha,i}$ are the coefficients of the decomposition on the Zernike polynomials of the residual aberrations R_α in the direction α , and:

$$R_\alpha = \Phi_\alpha - M_\alpha^{N_{\text{DM}}} W \Phi_{N_{\text{GS}}} \quad (4.33)$$

The drawback of this estimator is that it focuses on the uniformity of the residual variance in the FoV, but doesn't help for increasing its average value. Thus an estimator taking both into account would be:

$$\varepsilon'_G = \int_{\{\alpha\}_{\text{fov}}} \left\| \sum_i a_{\alpha,i}^2 - \text{Goal} \right\|^2 d\alpha \quad (4.34)$$

The constant "Goal" represents an average variance (that we can also express as a SR) we try to reach in addition to the minimization of the residual variance everywhere in the FoV. More precisely, instead of calculating the variance which is the deviation around the average value, this estimator represents the deviation of the residual aberrations around a goal value.

Here again we will limit ourselves to the evaluation of the performances in the direction of the GSs:

$$\varepsilon'_G = \sum_{N_{\text{GS}}} \left\| \sum_i a_{\alpha,i}^2 - \text{Goal} \right\|^2 \quad (4.35)$$

The analytical solution to the problem would come from deriving this estimator in order to find its minimum. In a first time we choose to adopt a numerical approach for solving the problem. Thus we considered that a way to make uniform the residuals in the FoV is to put weight on the reference stars measurements. This can be done by filling appropriately the matrix C_n . By default this matrix is set to identity, and its size is $[N_{\text{GS}} \times N_z, N_{\text{GS}} \times N_z]$. If we choose to put the same weight on all the coefficients of each GS, the number of parameters to resolve is equal to the number of GS (13 in our example).

So we have kept the solution W given by the equation (4.26), and modified the matrix C_n in it in order to minimize the new criterion ε'_G (equation (4.35)). Thanks to a routine that calculates the minimum of an unconstrained multivariable function, it is possible to numerically find the values of the 13 parameters that minimize ε'_G .

The result of this optimization for a Goal of 97 % of SR in K band is also shown in Figure 4.30. The average value of the SR is **96.6 %** (pretty close to the goal), and the variation is successfully limited to the range 95-97.6 %. The use of the new criterion, even if not analytically derived, brings a certain enhancement of the uniformity of the residual aberrations as measured in the directions of the GS.

In Figure 4.31 is shown the shape of the two DMs that brings this correction. We can notice that mainly low order aberrations are present. The amplitude of the correction is of a great importance, as it uses some of the stroke of the DM which then is no more available for the MCAO real-time correction.

4. CORRECTION OF THE STATIC ABERRATIONS

The two deformable devices in MAD are curvature mirrors, one of 60 mm useful diameter and the other one of 100 mm (fitting respectively the two altitudes of 0 and 8.5 km for a 2 arcmin FoV), both with about 3 microns of mechanical stroke. The stroke used to perform the correction is **146 nm** for the ground DM and **223 nm** for the altitude DM. If the aberrations in the real system, especially at the edges, turn out to be more greedy in DM stroke, we might have to select carefully the area for the field optimization during the tomographic reconstruction.

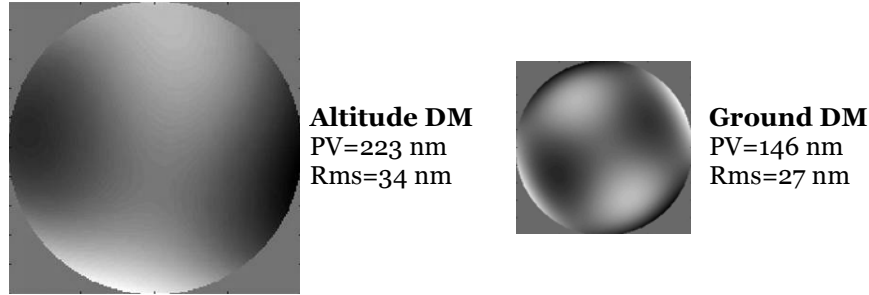


Figure 4.31: Shape of the DMs bringing the best correction in the case of the 8 layers tomography projected on 2 DMs, after numerical optimization.

The full simulation of the MAD system aberrations has been a good exercise to validate our tomography routine, and allowed us finding new ideas to optimize the correction in the FoV. Once the MAD bench aligned in its MCAO configuration, it will become possible to retrieve real aberrations data and apply the tomographic reconstruction.

4.8.5. Application to MAD

Without tomography

A simpler approach than tomography is to build a meta-IM from the measurements of the modes (equation (4.36)), invert it, and multiply the meta-CM straight by the aberrations to get the correction (equation (4.37)). This is equivalent to least-squares minimization, and is inspired by what is done to close the MCAO loop on MAD before the implementation of more “clever” algorithms such as MAP [29].

4.8 ABERRATIONS CORRECTION IN THE FIELD OF VIEW

$$\begin{aligned}
 & N_m = N_{mGnd} + N_{mAlt} \\
 & \begin{bmatrix} \text{metaIM} \end{bmatrix}_{N_{GS} \times N_Z} = \begin{bmatrix} \begin{bmatrix} M_{1,1} \end{bmatrix} & \begin{bmatrix} M_{2,1} \end{bmatrix} & \dots & \begin{bmatrix} M_{N_m,1} \end{bmatrix} \\ \vdots & \vdots & \ddots & \vdots \\ \begin{bmatrix} M_{1,N_{GS}} \end{bmatrix} & \begin{bmatrix} M_{2,N_{GS}} \end{bmatrix} & \dots & \begin{bmatrix} M_{N_m,N_{GS}} \end{bmatrix} \end{bmatrix} \quad (4.36) \\
 & \begin{bmatrix} \mathbf{V} \end{bmatrix} = \begin{bmatrix} V_{Gnd} \\ V_{Alt} \end{bmatrix} = - \begin{bmatrix} m2V_{Gnd} \\ m2V_{Alt} \end{bmatrix} \times \begin{bmatrix} \text{metaCM} \end{bmatrix} \times \begin{bmatrix} \Phi_1 \\ \Phi_2 \\ \dots \\ \Phi_{N_{GS}} \end{bmatrix} \quad (4.37)
 \end{aligned}$$

With tomography

The practical method we propose here to implement is the “**open loop correction for the FoV static aberrations of the system MAD-ITC by the use of Phase Diversity and a calibration matrix**”. It has been presented in the SPIE paper “*Calibration of the static aberrations in an MCAO system*” [51], also in the appendix 8.3.

It needs the second DM to be integrated to the instrument, but no closed loop tasks (SCAO nor MCAO) are required. The closed loop technique, maybe performing better but also much more difficult to implement, will not be implemented on MAD.

The chronologic order of actions required to implement this tomographic correction of the static aberrations is the following:

- Record IM_1 between the ground DM and the camera for 1 position in the FoV, in open loop. Zernike modes are applied to the DM, focused and defocused images are taken with the camera and analyzed by ΦD . Those modes are deduced from the Influence Functions of the ground DM and applied through the matrix

4. CORRECTION OF THE STATIC ABERRATIONS

$m2V_{\text{Gnd}}$ (equation (4.7)), as it is done in the on-axis case. If the ground DM is effectively in a pupil plan, recording the IM in one direction is enough. But the field effects can not be neglected, an IM has to be recorded for each direction and the procedure is then similar to the one for the altitude DM.

- Record IM_2 between the altitude DM and the camera for each direction of interest in the FoV, in open loop. Zernike modes are applied to the DM, focused and defocused images are taken with the camera in several directions and analyzed by ΦD . Those modes are deduced from the IFs of the altitude DM and applied through the matrix $m2V_{\text{Alt}}$. This is from far the longest measurement, and one should use the help of templates to have it done automatically. The number of positions in the FoV is a parameter to define.

- The two measured IMs link the modes applied to the DMs to aberrations measured in several directions. To be used to correct for the field aberrations, they have to be projected by tomography on the DMs' altitudes according to the equations (4.38) and (4.39). For the ground DM, there is only one direction of analysis, and the projection is done on the 0 km altitude, so the IM is identical ($IM_{\text{Gnd}} = IM_1$). For the altitude DM, there are N_{GS} directions of analysis and the projection is done on the altitude of the DM (8.5 km in the case of MAD).

$$\begin{array}{c} N_m \\ \left[\begin{array}{c} \mathbf{IM}_{\text{Gnd}} \end{array} \right]_{N_Z} = \mathbf{P} \times \mathbf{W}_{\text{MA}} \times \begin{array}{c} N_m \\ \left[\begin{array}{ccc} \left[\begin{array}{c} M_1 \end{array} \right] & \left[\begin{array}{c} M_2 \end{array} \right] & \dots & \left[\begin{array}{c} M_{N_m} \end{array} \right] \end{array} \right]_{N_Z} \\ \mathbf{IM}_1 \end{array} \end{array} \quad (4.38)$$

$$\begin{array}{c} N_m \\ \left[\begin{array}{c} \mathbf{IM}_{\text{Alt}} \end{array} \right]_{N_Z} = \mathbf{P} \times \mathbf{W}_{\text{MA}} \times \begin{array}{c} N_m \\ \left[\begin{array}{ccc} \left[\begin{array}{c} M_{1,1} \end{array} \right] & \left[\begin{array}{c} M_{2,1} \end{array} \right] & \dots & \left[\begin{array}{c} M_{N_m,1} \end{array} \right] \\ \vdots & \vdots & \ddots & \vdots \\ \left[\begin{array}{c} M_{1,N_{\text{GS}}} \end{array} \right] & \left[\begin{array}{c} M_{2,N_{\text{GS}}} \end{array} \right] & \dots & \left[\begin{array}{c} M_{N_m,N_{\text{GS}}} \end{array} \right] \end{array} \right]_{N_{\text{GS}} \times N_Z} \\ \mathbf{IM}_2 \end{array} \end{array} \quad (4.39)$$

4.8 ABERRATIONS CORRECTION IN THE FIELD OF VIEW

- The two IMs are decomposed by SVD (as in section 4.5.7) and inverted to get the Control Matrices CM_{Gnd} and CM_{Alt} .
- Take focused and defocused images of the aberrations in the same directions in the FoV and analyse them by ΦD .
- Use tomography to transform the aberrations vectors measured in the N_{GS} directions into the WF at the N_t different altitudes to which are conjugated the optics of the instrument. In the case of MAD we choose to consider 8 altitudes (at 0, 4, 7.5, 8.5, 13, 14, 16.2 and 30 km) that include the altitudes of the optics and additional ones in order to sample properly the equivalent height of atmosphere to which the instrument is conjugated.
- Project those WFs on the DMs' altitudes. We obtain then the 2 vectors of aberrations to correct: φ_{Gnd} and φ_{Alt} .
- After multiplication by the CM and by the matrices of modes to voltages, we get as result the lists of additional voltages to apply the DMs to perform the correction:

$$V_{Gnd} = -m2 V_{Gnd} \times CM_{Gnd} \times \varphi_{Gnd} \quad (4.40)$$

$$V_{Alt} = -m2 V_{Alt} \times CM_{Alt} \times \varphi_{Alt} \quad (4.41)$$

Comparison

The validity of using a simple inverted meta-IM has been proven by closing the MCAO loop on MAD. The advantage of this method is its simplicity, as it requires nothing more than a generalized inversion.

More than delivering the correction to apply at different altitudes, the tomographic approach gives also an estimation of the position of the aberration in the optical path. It can be also used as a way of testing and improving the instrument.

Anyway, both methods require to start from the measurement of the meta-IM, and their difference lie then in the computation of the correction (a numerical process). It is thus easy to compute the correction for the methods from the same set of measurements and compare their performance.

Unfortunately, the MAD bench has never been available in its MCAO configuration in the length of this thesis to compare both approaches, but it is certainly a study to follow in the further developments of the instrument.

4.9. Application to the Active optics of OWL

4.9.1. Introduction

Since a couple of years, ESO is developing concepts for a future Extremely Large Telescope: OWL [19]. Its optical design is shown in the Figure 4.32 and the details of the mirrors in the Table 4.7. The alignment of the segments of M1 and M2 is controlled by cophasing [32]. M5 will be active before being upgraded to an adaptive mirror for MCAO operations.

All mirrors are active so that their surface can be reshape in real-time in order to compensate for gravitational or thermal deformations. But if this technique is very well known for controlling one mirror (thanks to ESO's experience on the VLT), it is a whole different problem when it comes to control 6 of them, including 3 conjugated at the same altitude. At the VLT, a SHWFS picks up a star in the technical FoV (around the scientific FoV which size varies with the instrument), measures the aberrations integrated over 30 seconds (to average the effect of the turbulence), and sends commands to the active M1 at the same frequency.

One of the possible solutions to control the mirrors of OWL follows the same idea: having several moveable WFS in the focal plane of the telescope, and picking up stars in the technical FoV, situated for OWL between 1 and 5 arc minutes from the center. The combined information from all the sensors allows controlling the mirrors individually. The reconstruction of the shape of the mirrors to correct can be done by tomography, in the same way as presented in the section 4.8.2.

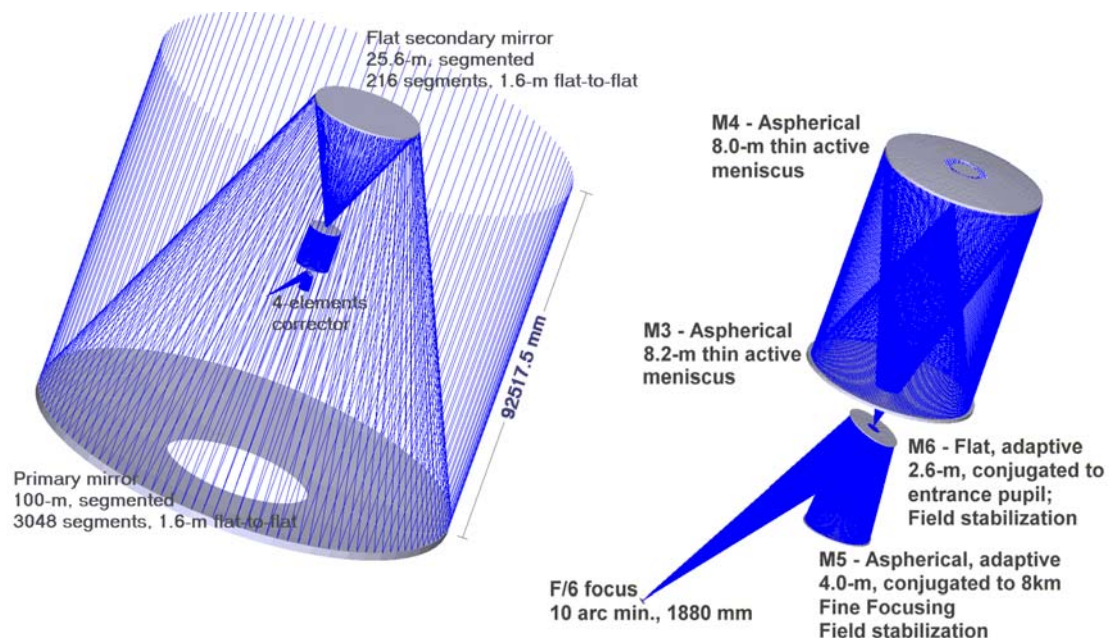


Figure 4.32: Optical design of the OWL telescope.

4.9 APPLICATION TO THE ACTIVE OPTICS OF OWL

Mirror	Diameter (m)	Shape	Segmentation	Control	Conjugation altitude (km)
M1	100	Spherical	Yes	Cophasing + Active	0.0
M2	25.6	Flat	Yes	Cophasing + Active	0.25
M3	8.2	Aspherical	No	Active	2.0
M4	8	Aspherical	No	Active	0.0
M5	4	Aspherical	No	Active (+Adaptive)	8.0
M6	2.6	Flat	No	Active + Adaptive	0.0

Table 4.7: Details of the mirrors in OWL.

4.9.2. Simulation tool

In this framework and given the similarities of the two problems, it is possible to apply the technique of correction of field-dependant static aberrations (section 4.8 of this thesis) to the control of several active mirrors. In this sense, we have slightly modified the tomography algorithm used for MAD in order to fit the parameters of the new system (mirrors size, altitude...) and to simulate the full chain of control from the measurement of the aberrations in the FoV to the correction applied to the Active Mirrors (AM) and the estimation of the performance after several iterations of the process.

The goal of this study is not to give an accurate estimation of the quality of correction that can be reached once the system is in place, but rather to prove the validity of the approach and its convergence. Thus we observe the following restrictions to eliminate all sources of noise:

- The sensors (which type is TBD) are considered perfect and give as output the WF projected on Zernike coefficients with no noise. The direct consequence is that the noise covariance matrix C_n is very small compared to C_ϕ .
- The mirrors are able to reproduce perfectly the shape of the first Zernike polynomials (up to the #21). By doing this we skip all the problems due to a practical implementation: on-sky open or closed-loop measurements, usefulness of an IM as we do in the section 4.5...
- The aberrations are not projected on M2. This might be also the case in the real system as M2 is too close from the pupil to be treated independently.
- All the pupil mirrors are considered as one. The disentanglement will be done by a process TBD, maybe offload of the deformations to the mirrors using the less mechanical stroke.
- We consider that only the active mirrors create the aberrations (i.e. there are no static aberrations due to optics at other altitudes).

The simulation will be done more complex in the future if a more realistic approach is required.

The first thing the code does is to build the matrices $M_a^{N_t}$ between the mirrors altitudes and the direction of observation (and eventually of

4. CORRECTION OF THE STATIC ABERRATIONS

optimization). Then it generates WF errors (inputs at the first iteration and residuals afterwards) for each mirror: $\phi_{N_{AM}}^o$, projects them in the directions of observation, makes the analysis by tomography and gets the correction to apply. All those actions are done in one operation that gives the shape of the mirrors at each iteration $i+1$ as a function of the shape it had at the iteration i :

$$\phi_{N_{AM}}^{i+1} = (1 - P_{N_{AM}, N_t} \times W_{MA} \times M_{N_{GS}}^{N_t}) \times \phi_{N_{AM}}^i \quad (4.42)$$

where N_{AM} is the number of Active Mirrors. The diagnostic we use is the residual variance of the WF on each mirror j at the iteration i (tip-tilt excluded):

$$\text{Var}_j^i = \sum_{k=4}^{N_Z} \|\phi_{j,k}^i\|^2 \quad (4.43)$$

The input aberrations (projected on the 21 first Zernike polynomials) follow a statistics of the variance in the power -2 of the radial order of the polynomial, as do the aberrations in optics. The amount of aberrations is then scaled to have for any mirror 200 nm rms at the first iteration (the absolute amplitude of the aberrations is not a limiting factor in the framework of those simulations).

The meta-pupil sizes at different altitudes are shown on the Figure 4.33.

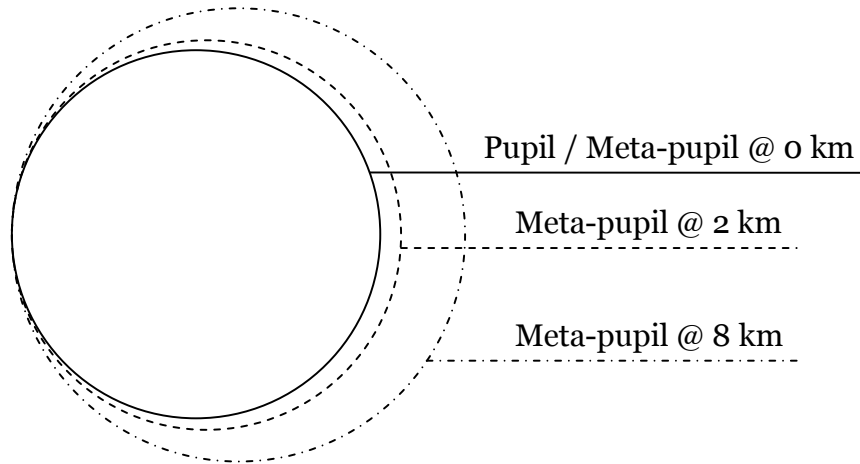


Figure 4.33: Relative size of the pupil and of the meta-pupils at different altitude for a 100 meter telescope and a 10 arc minutes FoV.

4.9.3. Results

1 Active Mirror at different altitudes

The first case we wanted to study is the control of a single AM conjugated to 0, 2 or 8 km with only 1 WFS. The Figure 4.34 shows the 10 first iterations of the convergence loop in those cases, for one example representative of several realizations of aberrations and of GS position we tried.

For one AM at 0 km, the best correction is obtained after the 1st iteration (the residual is of the order of 0.1 nm rms and is due to numerical approximations in the projection of the Zernike polynomials). For the AM at 2 km, the convergence takes one more iteration, to reach around 0.3 nm, due to a

4.9 APPLICATION TO THE ACTIVE OPTICS OF OWL

non complete sampling of the meta-pupil (see Figure 4.33). In the case the AM is at 8 km, the portion of the meta-pupil not sampled by the beam is significantly larger, which explains that the convergence is much slower, and that the residual can still be as large as 40 nm rms after 10 iterations, depending on the initial conditions (the Figure 4.34 shows a better case where the residual is 10 nm).

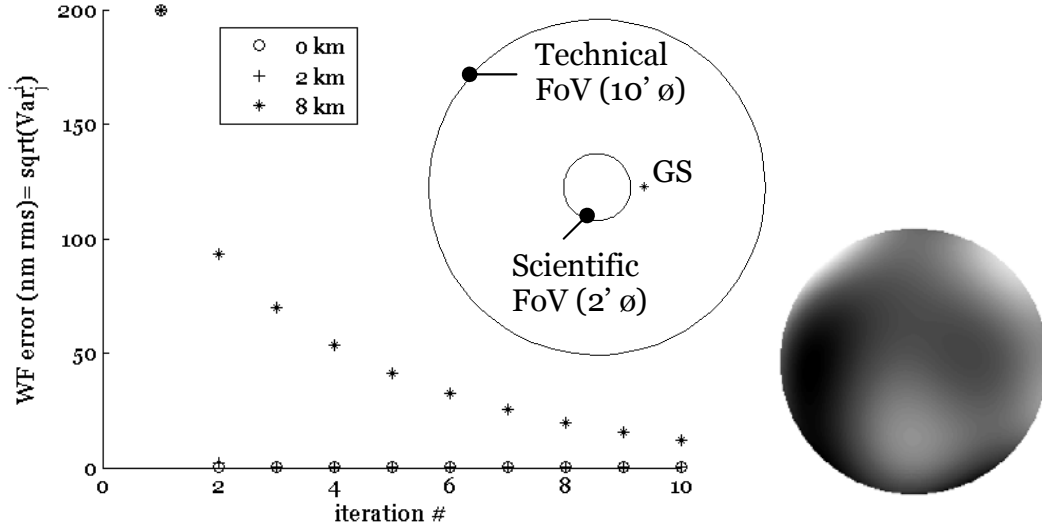


Figure 4.34: Example of the quality of correction for one AM placed at 0, 2 or 8 km altitude, position of the single GS in the technical FoV, and shape of the initial WF error for any AM.

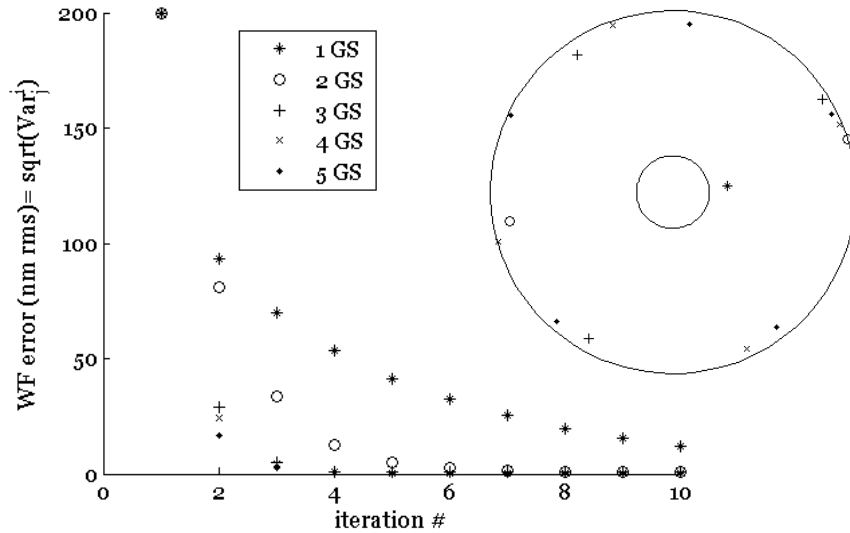


Figure 4.35: Example of the quality of correction for one AM placed at 8 km altitude and 1 to 5 GS for the WF sensing. The shape of the initial WF error is the same as on the Figure 4.34.

This problem is solved by the use of several GS in the FoV. For the simulations they were placed at the border of the FoV, and regularly spaced in angle. Small random variations in this position were introduced in order to avoid

4. CORRECTION OF THE STATIC ABERRATIONS

symmetric geometries, not desirable for an optimal performance of the tomography algorithm. The Figure 4.35 shows how an increasing number of GS improves the convergence loop for a same input WF error. We can see for instance that in the case we use 3 GS, a WF error smaller than 1 nm is reached after 3 iteration only.

2 Active Mirrors

In the case where we control 2 Active Mirrors placed at 0 and 2 km, the Figure 4.36 shows that 3 GS are required to separate properly the contribution of the 2 mirrors from the aberrations measured, and that the residual is smaller than 1 nm rms after 3 iterations.

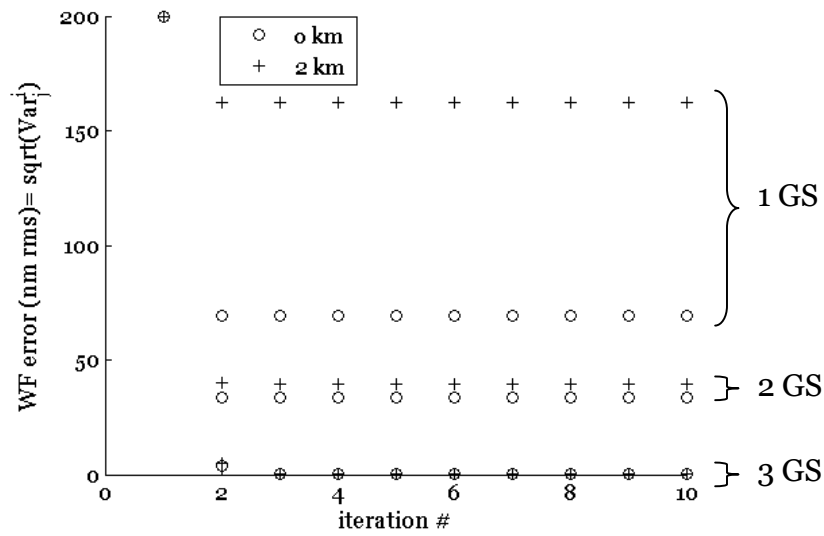


Figure 4.36: Example of the quality of correction for 2 AMs placed at 0 and 2 km of altitude and 1 to 3 GS for the WF sensing.

If we choose to control only the mirrors at 0 and 8 km (as it could be the case on OWL if it was decided that M3 is passive), the performance with 3 GS is a bit worse than for the 0/2 km case, but then with 4 GS the residual aberrations are smaller than 1 nm for both mirrors after 2 iterations only.

3 AMs: 0, 2 and 8 km

The Figure 4.37 shows one of the best results we obtained in the correction of the shape of 3 AMs with 5 GS for the WF sensing. The residual WF errors on each AM decreases to reach a plateau between 20 and 50 nm. But for some other stars configurations, the values could as well increase to more than 200 nm and stabilize there! We noticed that increasing the number of GS doesn't bring any improvement.

However, for any configuration and number of GS, the residual WFs in their direction after 10 iterations is lower than 0.1 nm rms. This means that the algorithm corrects efficiently for the aberrations it sees, and that if doesn't bring the mirrors to their flat shape it is because of modes that cancel each other

4.9 APPLICATION TO THE ACTIVE OPTICS OF OWL

between the different altitudes (like in AO the unseen modes between different turbulent layers).

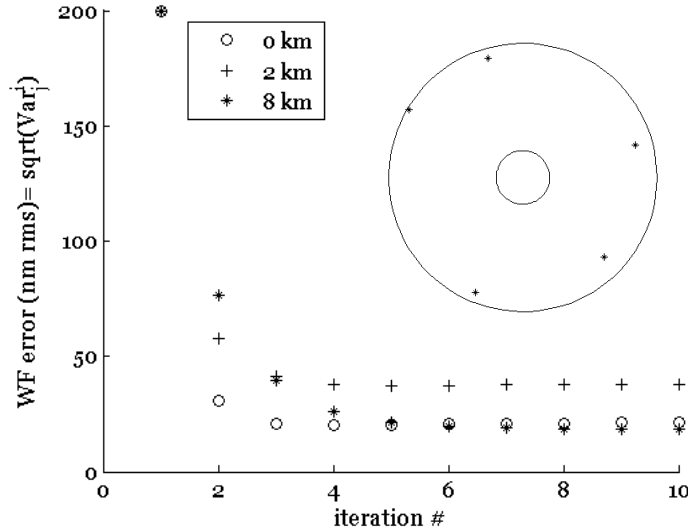


Figure 4.37: Example of the quality of correction for 3 AMs placed at 0, 2 and 8 km of altitude and 5 GS for the WF sensing.

Conclusions

We have seen that the tomographic approach seems suited for the control of 2 active mirrors, and allows “flattening” the Active Mirrors after a few iterations. In order to put more realistic numbers on the performances of such a system, it will be required to introduce the simulation of a WFS, including all sources of noise such as the photon or read-out noises.

Unfortunately it turned out that even in the no noise case, it is not possible to determine independently the shape of the 3 AMs controlled simultaneously. Tentative tries of correcting the mirrors one by one led to the same results as for the tomography, and changing the stars configuration at each iteration led to a slight enhancement, but is not practically feasible. A possible solution could be to use two stages of WFS, one before and one after M5, in order to disentangle the contribution of each mirror, but to find a definite answer this problem deserves to be studied more in details.

4.10. Discussion

In this chapter we have seen that the deformable device(s) present in an AO instrument can be used not only to correct in real-time for the dynamical aberrations induced by the atmosphere, but also to pre-compensate for the static aberrations of the optical elements in the path. The crucial point is to know HOW to convert the aberrations measured into a configuration of the bench that corrects for them.

We have proposed an all-measured technique to solve this problem, that involves a calibration matrix between the measuring device and the compensating device. The best accuracy is obtained by using the scientific instrument itself as a Wave Front analyzer, through the Phase Diversity technique. This method requires the stability of the bench for an accurate recording of the calibration matrix, but once this is done the correction becomes straight-forward, and doesn't make use of a model of the system. Depending on the application, this method can be used in different ways:

- For "simpler" systems, the open-loop method is applicable by controlling only the DM and the camera. It has been proven to give good results on the MAD test bench in different configurations.
- For more stability and performance, an improvement of this method is to do it by controlling the DM in closed loop through the WFS. The advantage is to freeze the turbulence inside the bench and prevent any change during the process (thermal expansion...). The result is a set of reference values for the WFS. This method is the most accurate, and can be applied to the correction of the on-axis aberrations in Extreme AO instruments for instance.
- In the different case of AO systems correcting the aberrations in the FoV, we have developed a way to apply the tomographic approach, usually applied to the atmosphere, to the static aberrations. The information coming from different directions of measurement are combined and converted into the correction to apply with one or several DMs, still through the use of a calibration matrix. It will be validated experimentally on the MAD bench.

The great advantage of this method in general is that it can be easily applied to any AO system, as we have seen on different configurations of the MAD bench and on the BOA bench of ONERA. Working in closed loop improves the stability of the process, but the results in open loop are already very satisfying if the stability of the bench is ensured.

Some sources of error are inherent to the technique (limited number of measurements and of DMs,...) but some others could be reduced if the compensation of the static aberrations was thought more in the design of the instrument. It could for instance give a more accurate way to apply the defocus for the Diversity images, or allow recording the meta-IM faster by using several calibration sources simultaneously in the FoV.

5. Interaction Matrix interpolation

5.1. Problematic

In an MCAO system based on NGSs, the configuration of those ones changes from one scientific target to the other. If the WF sensing is “Star Oriented”-like, this implies that the sensing devices have to be able to pick-up the GS, as it is the case in MAD (section 2.3.3).

Another implication concerns the Interaction Matrix of the system. This one gathers the response of the several WFS (located at the position of the GSs) to the excitation of the DMs. For an altitude DM the footprint of the beam is different across the meta-pupil for different GSs (as shown on the Figure 5.1 in the specific case of MAD for which the geometry of the sensor and of the DM don’t match), so one IM has to be recorded for each GS position. This problem obviously doesn’t occur in Single Conjugate AO systems (SCAO) where the unique DM is in the pupil and the GS is always placed on-axis.

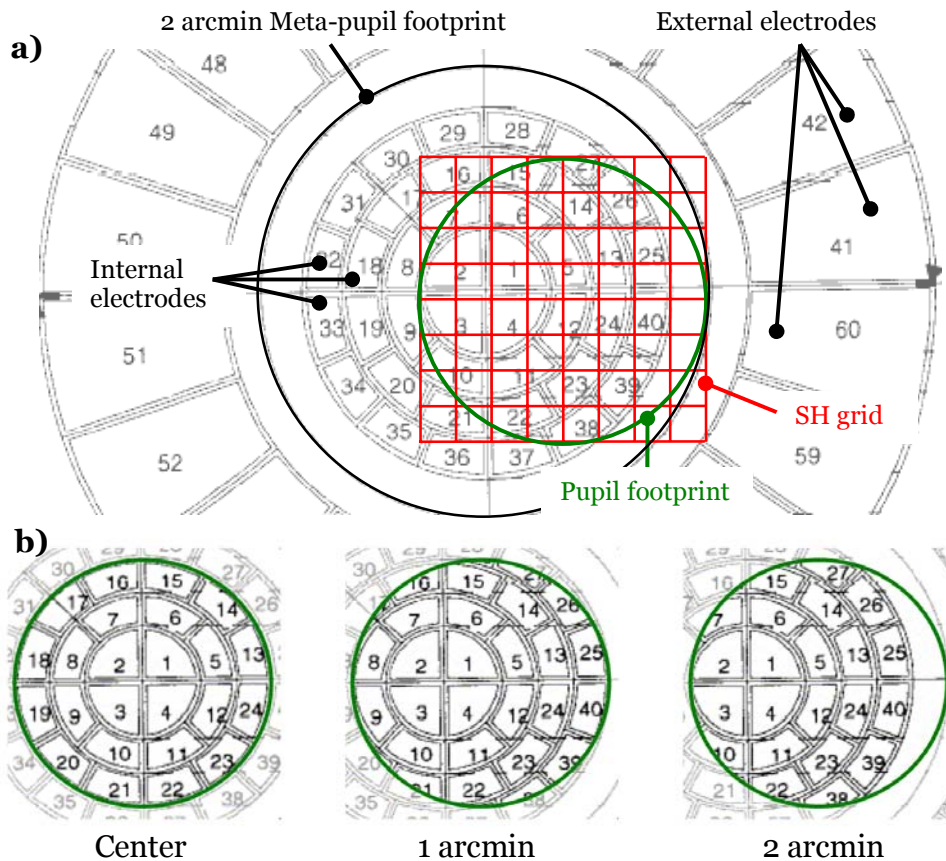


Figure 5.1: a) SH grid and pupil size superimposed to the MAD high altitude DM electrodes configuration. b) Beam footprint on the altitude DM for different GS positions in the FoV. We notice the changing overlap with the DM's electrodes.

The calibration of the IM in MCAO is the same one as for Single-AO, but repeated for each GS position. It is a day-time operation that involves knowing the exact positions of the GS, placing there a calibration source, running the calibration procedure (synchronous DM actuations and WF measurements), and once this done for each GS, filling in the meta-IM and inverting it so as to get the Control Matrix (see section 2.4.4).

A possible way to avoid this time-consuming procedure could be to use synthetic Interaction Matrices, computed from the knowledge of the Influence Functions of the DM, as well as its orientation in the optical path. Although it can be tuned accurately, this kind of model misses some details like the optical defaults in the WFS and other optical aberrations, that are present in the system and taken into account in a measured IM. Also the model has to be revised often to take into account the inevitable changes occurring in the system with time.

Another solution could be to combine measurements (to keep the information on the specificities of the system) and numerical approximation (to be able to easily generate the IM corresponding to any stars asterism). What we propose here to do is to record a set of Interaction Matrices for a grid of GS positions, and then to interpolate them to any position in the FoV (Figure 5.2). If one uses a tight enough sampling of the FoV, it is logical to think that this procedure works. The problem we choose to address is more the determination of the minimal number of GS positions in the grid (and eventually their geometry) that allows extrapolating an IM that bring performances of the AO system identical to the ones with a measured IM (or deteriorated only by an acceptable amount). We will restrict ourselves to the case of MAD in its Star-Oriented mode.

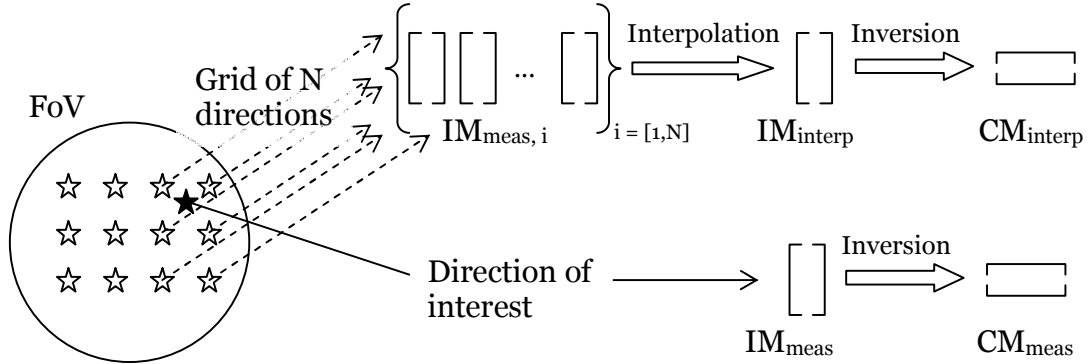


Figure 5.2: Creation of measured and interpolated Control Matrices.

In order to study the validity of the interpolation technique we have developed a set of routines in Matlab and run simulations in the specific case of MAD (same characteristics of DM and WFS), which results are detailed in the section 5.2. Those first simulations are limited to the simplified case of Single Conjugate AO (SCAO) correction.

After finding an appropriate grid size and interpolation method, we have used an existing closed loop code to simulate the effect of the interpolation on the MCAO performances of MAD (section 5.3). It will be then possible to compare the outcome of the simulations with performances measured in the laboratory with MAD and the reproducible turbulence of MAPS (see chapter 3).

5.2 SCAO OPEN LOOP SIMULATIONS

5.2. SCAO open loop simulations

5.2.1. Simulation tools

Deformable Mirror

In the present simulations we consider only the altitude DM of MAD (conjugated to 8.5 km), and assume that the calibration of the ground DM (conjugated with the pupil of the telescope) is done as for a Single-AO system, and that the resulting IM is the same for any direction in the FoV.

The altitude DM can be simulated either by its measured Influence Functions (see a sample on the Figure 5.3) or by the Zernike modes, assumed to be produced perfectly (ideal case, quite true for the first 20 polynomials).

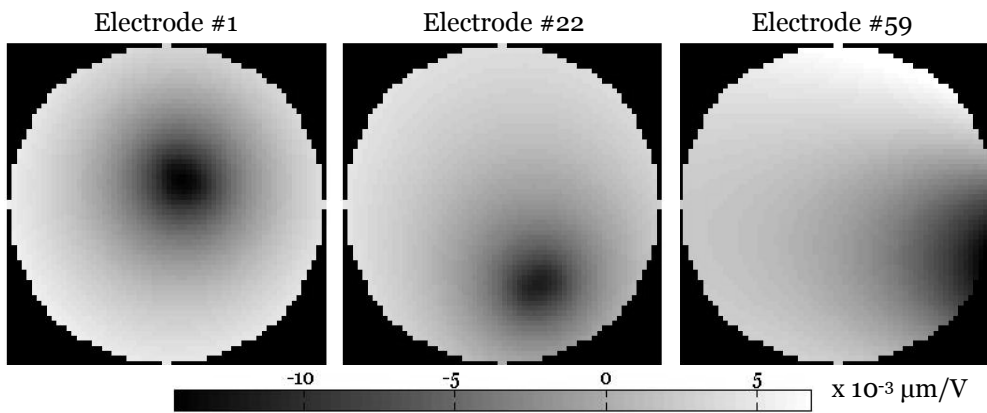


Figure 5.3: Example of IF for 3 different electrodes of the altitude DM of MAD.

SHWFS model

In order to simulate the effect of the MAD Star Oriented WFS, we have created a diffractive model of SHWFS in Matlab (Figure 5.4.a). It reproduces this WF sensing process by sampling the WF in square sub-pupils, imaging the PSF for each of them and computing the slopes in both x and y directions (see the section 2.4.3 of the introduction for details on the SHWFS). Although we used it in to simulate the MAD case (8 x 8 square sub-apertures including 52 useful ones, 8 x 8 pixels per sub-aperture), this code can be easily generalized to simulate any SHWFS.

Its main feature is the possibility to use diffraction-limited sources (for star simulation) as well as extended objects (for simulating an extended calibration source). Some other setting parameters are:

- Number of sub-apertures and of pixels per sub-aperture
- Pixel scale
- Working wavelength
- Possibility to take into account the first neighboring sub-apertures (Important for large slopes measurements).

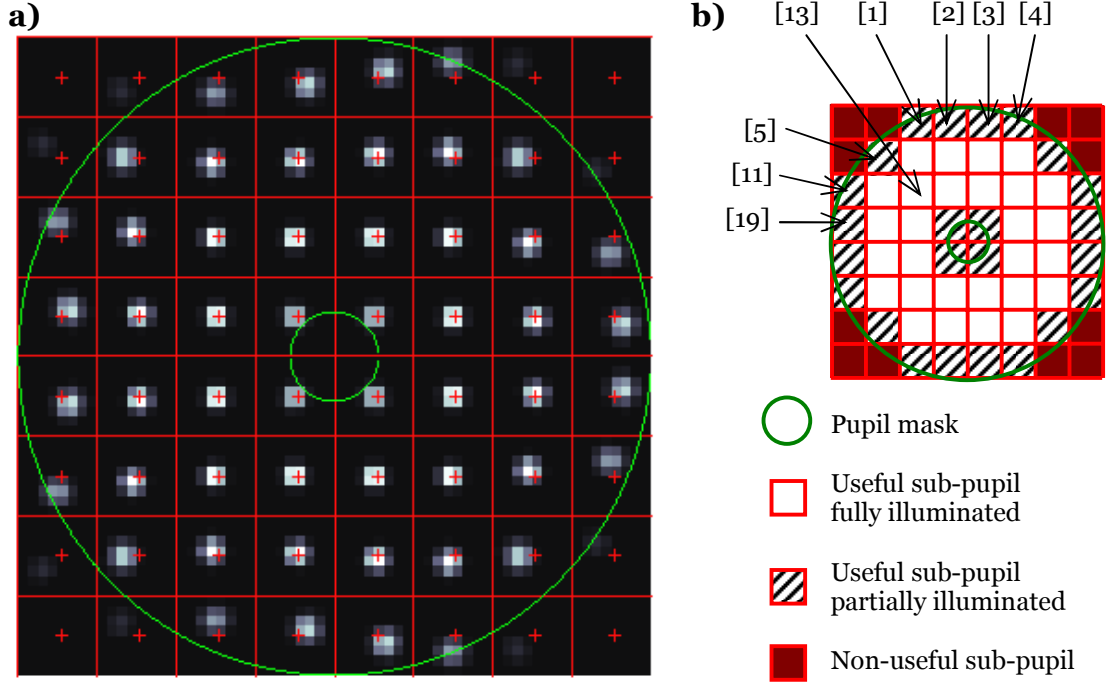


Figure 5.4: a) Display from our model of SHWFS applied to MAD. The red lines represent the limit of the sub-apertures, the crosses their centre and the green lines the shape of the pupil (including central obscuration). b) repartition of the sub-apertures with their numbering.

This model has been validated by studying the response of one of its sub-apertures to a tilt, and comparing it to the results of measurements made on the MAD bench. A 365 μm core fiber is used as extended calibration source, and the tilt is produced by shifting this source in one axis. On the Figure 5.5 are plot the results of the comparison. We can see that simulating the right source size is important to reproduce the correct behavior in the linearity range (in our case ± 0.7 arcsec), and that including the effect of the first neighbors is required when the spot reaches the border of the pixels area dedicated to one sub-aperture. There are several causes to the small difference between the model and the measurement, by order of importance:

- The response of each lenslet to a large tilt becomes non linear.
- The source is assimilated to a uniform disk, which is quite realistic but not completely.
- The pixel scale might be a bit different.
- The axis of the tilt introduced on the bench is not perfectly aligned with the ones of the SHWFS.

5.2 SCAO OPEN LOOP SIMULATIONS

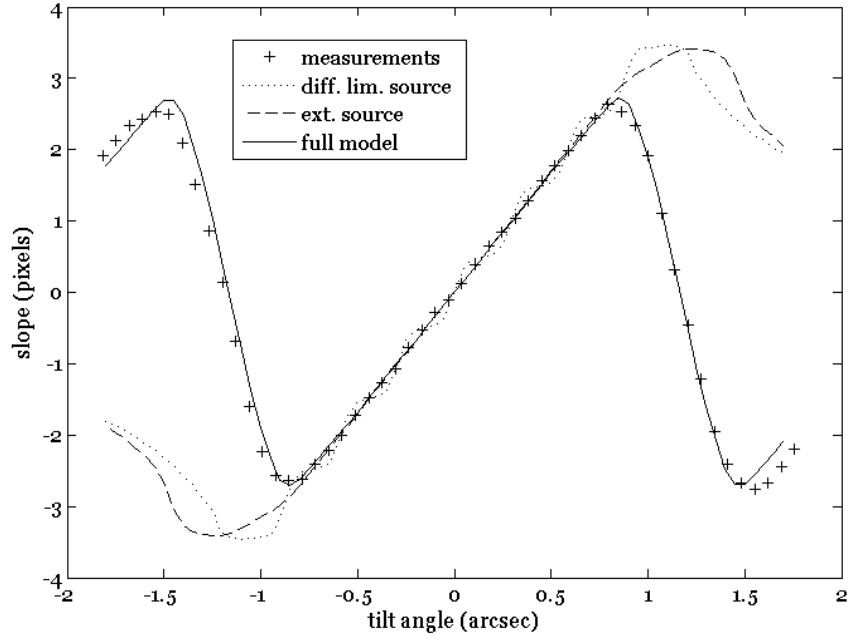


Figure 5.5: Comparison of the MAD SHWFS measurements (crosses) with different models: single sub-aperture and diffraction limited source (dotted line), single sub-aperture and extended source (dashed line), full model taking into account the first neighboring sub-apertures (solid line).

We have also compared the shape of the spots produced by our SHWFS model with the ones produced by the lenslet array of MAD (Figure 5.6), especially in the case of partially illuminated sub-pupils (Figure 5.4.b).

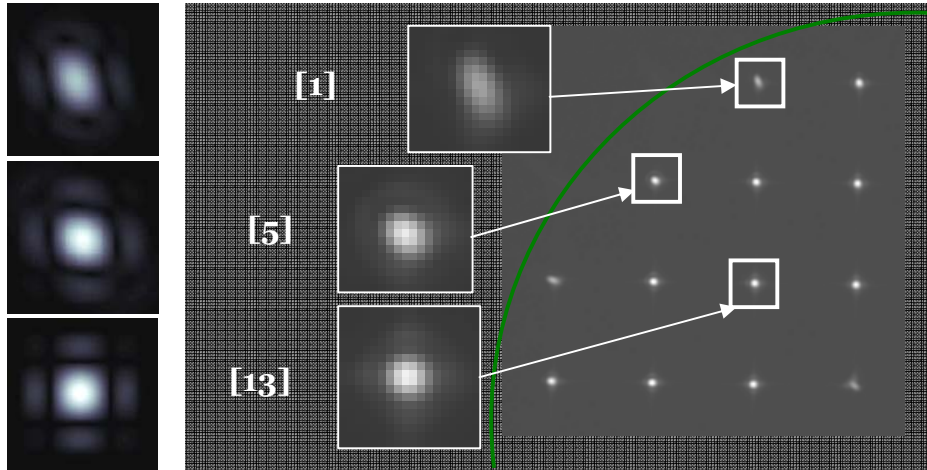


Figure 5.6: Measured spots created by the lenslet array of the MAD SHWFS (right) and simulated ones created by the SHWFS model for the same sub-apertures (left).

5.2.2. Simulations outline

Using the tools described in the previous section, it is possible to simulate the recording of an IM between the SHWFS and the DM conjugated with an altitude of 8.5 km, its inversion, and the application of the CM to correct for measured aberrations. This is what we propose to do in open loop in this section.

Calibration

The process of calibration is described by the Figure 5.2: measured and interpolated IMs are inverted and give respectively the measured and interpolated CMs. The CM links the slopes in x and y directions measured in the useful sub-apertures of the Shack-Hartmann WFS (thus 2×52 values) to the modes applied to the DM (which are the 60 Influence Functions here).

The inversion of the IM is described in the section 2.4.4. In the case of SCAO simulations using 1 DM in altitude, moreover 20 electrodes being outside of the meta-pupil, a lot of modes have to be filtered. In fact, in a direction of the field for which the beam hits one side of the DM, the signal recorded during the actuation of electrodes on the other side is very small, and the corresponding modes have then to be filtered. For the measured IM, we chose to filter the modes with an eigen value higher than 100 times the smallest one. For the interpolated IM, the modes are different, and in order to obtain results not biased by the quality of the filtering, we removed the same number of modes as for the measured IM in the same direction. The number of modes filtered is 25 in average.

A criterion that can be used to evaluate the quality of the interpolated IM before using it in the open loop simulations is the Internal Product (IP) defined as follows between two matrices A and B:

$$\text{IP}(A,B) = \text{trace}(A^T B) \quad (5.1)$$

One can as well define the distance and the angle between two matrices:

$$\text{Dist}(A,B) = \sqrt{\text{IP}(A-B, A-B)} \quad (5.2)$$

$$\text{Cos}(\text{Angle}(A,B)) = \frac{\text{IP}(A,B)}{\sqrt{\text{IP}(A,A)\text{IP}(B,B)}} \quad (5.3)$$

In order to compare the measured and interpolated IMs, we choose to compute the relative distance between them:

$$\text{rDist}(\text{IM}_{\text{meas}}, \text{IM}_{\text{interp}}) = \frac{\text{Dist}(\text{IM}_{\text{meas}}, \text{IM}_{\text{interp}})}{\sqrt{\text{IP}(\text{IM}_{\text{meas}}, \text{IM}_{\text{interp}})}} \quad (5.4)$$

It is logical to think that the larger will be the relative distance, the worst the AO correction. An example of the measured and interpolated IMs is shown on the Figure 5.7. The interpolated one has been computed from a grid of measurement points to the same position as the measured one, as described previously. The interpolation methods are detailed in the section 5.2.3.

On the same Figure is also shown the difference between the two matrices. When we relate the geometry of the DM's electrodes (Figure 5.1) to the way the SH slopes are ordered (Figure 5.4), we notice that the largest errors occur for

5.2 SCAO OPEN LOOP SIMULATIONS

sub-apertures facing the electrode actuated, because it is where the slopes are varying the fastest. It also explains why the errors are very low for the modes over 40 (electrodes outside of the meta-pupil).

The value of rDist gives us a hint of the quality of the interpolated matrix, knowing that for two identical matrices rDist = 0, and for matrices recorded at two totally different positions in the field, rDist can range from 1 to 2.

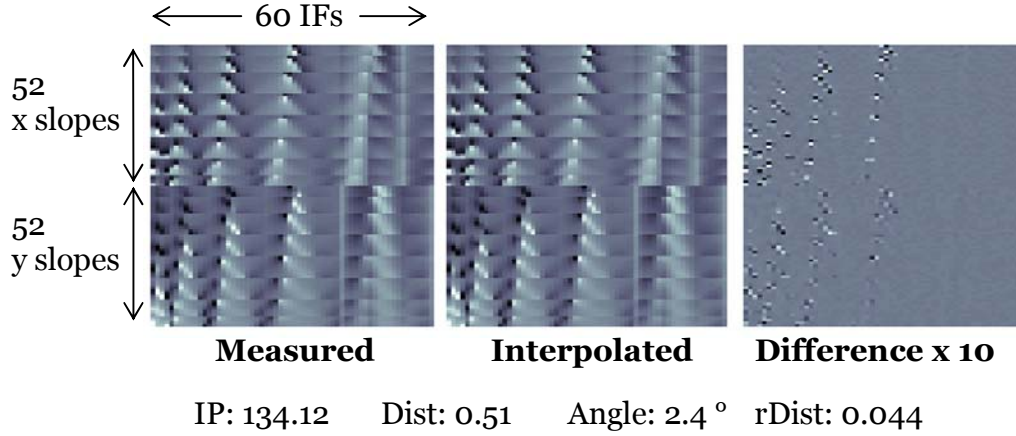


Figure 5.7: Example of measured and interpolated IMs for the same position in the FoV, their difference (magnified 10 times), and the corresponding IP, distance and angle. The grid size used for the interpolation is the one shown on the Figure 5.12, and the method is the number 2, detailed in the section 5.2.3.

SCAO open loop

The AO correction is simulated as follows: several WF maps of aberrations are analyzed by the WFS, and the measured slopes are multiplied by the CM to obtain the correction. This correction is applied to the DM, and its shape is subtracted to the shape of the input WF to get the residual after correction (see the example of the Figure 5.8).

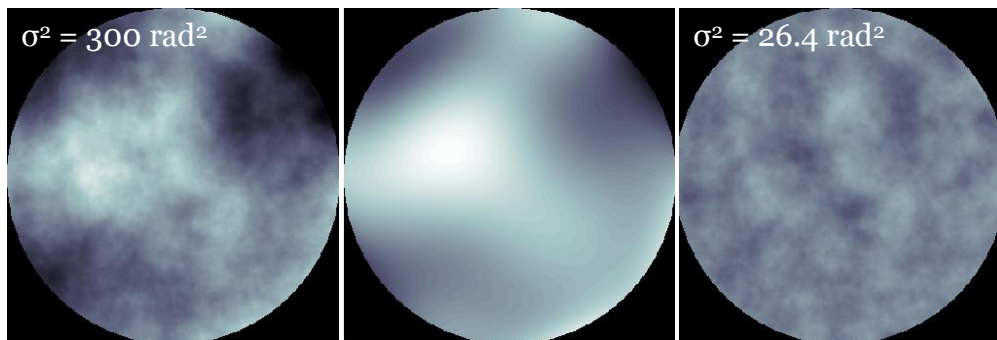


Figure 5.8: Correction of aberrations. Input (left), reconstructed from the WFS measurements (centre) and residual (right) WF.

The input aberrations maps follow the spectrum of a Von Kármán atmosphere with an outer scale of 22m (see section 2.4.2). They are normalized to a given variance that corresponds to the seeing conditions we wish to simulate.

5. INTERACTION MATRIX INTERPOLATION

By combining the equations (3.2) and (3.4) of the section 3.4.3, we obtain the relationship between both:

$$\sigma^2 = f(L_o) \times \left(D \frac{\text{Seeing}}{0.9759\lambda} \right)^{5/3}, \quad (5.5)$$

where D is the telescope diameter, λ the working wavelength, and $f(L_o)$ a scaling factor that depends only on the value of the outer scale; it is equal to 1.029 for an infinite L_o and to 0.207 when $L_o = 22\text{m}$. To give an order of magnitude, a variance of 300 rad^2 corresponds to a Seeing of 1 arcsec.

Estimation of the performance loss.

The reference for the correction (best case) is obtained when the measured CM is used. The criterion to evaluate the loss of performance coming from the use of the interpolated CM is the variance of the residual WF, averaged over a large number of turbulence realizations:

$$\sigma_{\text{meas_IM}}^2 = \frac{1}{N} \sum_{i=1}^N \text{Var}(\text{WFres}_{i,\text{meas_IM}}) \quad (5.6)$$

and

$$\sigma_{\text{interp_IM}}^2 = \frac{1}{N} \sum_{i=1}^N \text{Var}(\text{WFres}_{i,\text{interp_IM}}) \quad (5.7)$$

We use a set of 100 realizations of the turbulence to correct with our AO system simulation in order to have, after averaging, results independent from the realization. The average SR is estimated as follows:

$$\text{SR} \approx e^{-\sigma^2} \quad (5.8)$$

where σ^2 is expressed in radians² at a wavelength of 2200 nm (the imaging wavelength in MAD), and is given by the equations (5.6) and (5.7).

5.2.3. Interpolation methods

Starting from a set of measured IMs, we have to estimate the IM for any direction in the field (Figure 5.2). After experimenting several interpolation techniques, and we came out with two which were giving satisfying results.

Method 1: Weighted average of the IMs of the 3 closest neighbors.

This rather simple method uses only the measured Interaction Matrices (IM_1 , IM_2 and IM_3) of the 3 points of the grid which are the closest from the direction of the interest (at distances d_1 , d_2 , d_3 in arcsec). We use 3 points because of the hexagonal geometry of the grid chosen (Figure 5.12.a) which puts any point of the FoV in a triangle of measured points. The interpolated IM is then:

$$\text{IM}_{\text{interp}} = \frac{1}{\sum_{i=1}^3 \frac{1}{d_i^2}} \times \sum_{i=1}^3 \frac{1}{d_i^2} \text{IM}_i \quad (5.9)$$

Obviously this method is more or less efficient depending on the distance to the measurement points, especially for the sub-apertures facing the actuated electrodes, as we have seen on the Figure 5.7. Its advantage is that it can be easily applied for any point in the FoV.

5.2 SCAO OPEN LOOP SIMULATIONS

Method 2: Cubic interpolation of a full map of Interaction Matrices.

For this method we use all the measured IMs to create, for each of the x and y slopes, a map of values that they take in the FoV for each mode (actuator in this case) pushed, and the IM value in any direction of the FoV is interpolated from this map.

The first step is the interpolate the measured values to a more dense and regular grid of points. This is done by bi-cubic interpolation through the proper function of Matlab. On the Figure 5.9 is shown how a grid of 60 x 60 values (shaded surface) is interpolated from the measurements made on only 53 points of the FoV (black dots).

Then, through a second stage of bi-cubic interpolation, the value of the slope for any direction of the FoV is interpolated from the [60 x 60] grid. The method of the Piecewise Cubic Hermite Interpolating Polynomial is implemented in the Matlab routine. It locally fits the data by cubic Hermite polynomials.

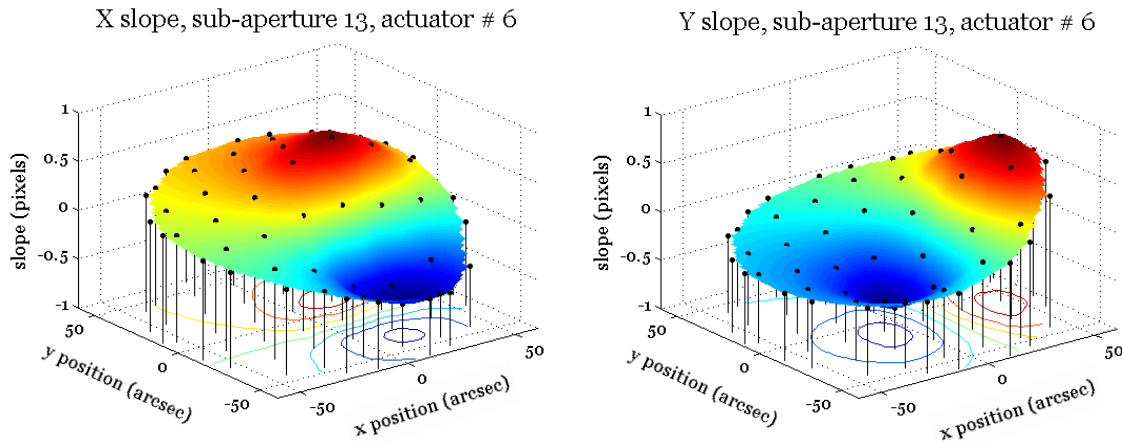


Figure 5.9: Example of interpolated map of the slopes. The dots represent the values measured for all the directions of the grid, and the shaded surface is an interpolation of the measurements to a more dense and regular cartesian grid.

As it takes into account the general evolution of the measurement over the FoV and not only the local measurements, this method of interpolation is better than the other one (see also the Figure 5.13). A drawback of this method is that it requires quite heavier calculations.

Moreover, as it performs a cubic interpolation, it cannot be applied for points which are not surrounded by measurements, i.e. the points at the very border of the FoV. This is illustrated by the Figure 5.10, in which we see the areas at the border of the field where the cubic interpolation fails due to a lack of data outside of the 2 arcmin FoV. In practice, it is not possible to record data outside of the nominal FoV due to the vignetting by the optics in MAD.

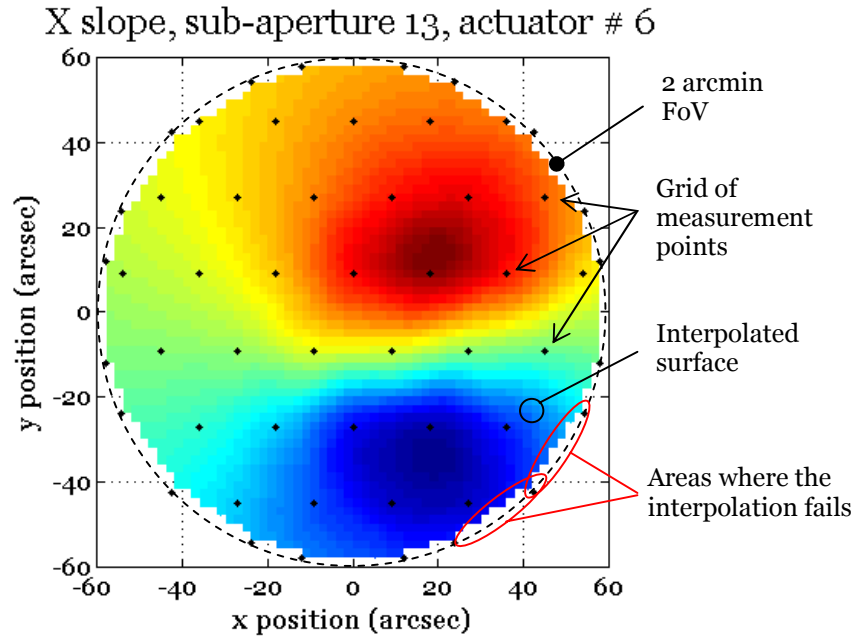


Figure 5.10: 2D view of the X slopes map presented on the Figure 5.9. The limit of the circular 2 arc minutes FoV is also represented.

For the simulations described in the following, we have decided to use this method, more efficient, but to keep as a backup the method 1 for the points in the FoV where the method 2 would fail. This is also a reason why we designed grids of points which are always denser at the border of the FoV: when the cubic interpolation fails and the method 1 has to be used, this density of the grid ensures that the quality of the interpolation doesn't drop.

5.2.4. Size and geometry of the grid

Obviously the number of points of measurements in the grid will affect the quality of the interpolation to any direction. Moreover a clever geometry of that grid can also improve the correction.

After running the simulation for larger and larger pitch sizes (Figure 5.11), we choose an hexagonal geometry for a better filling of the FoV, and placed additional points at the border of the FoV for the reason explained before, and we got to the grid shown in the Figure 5.12 that contains 53 measurement points.

5.2 SCAO OPEN LOOP SIMULATIONS

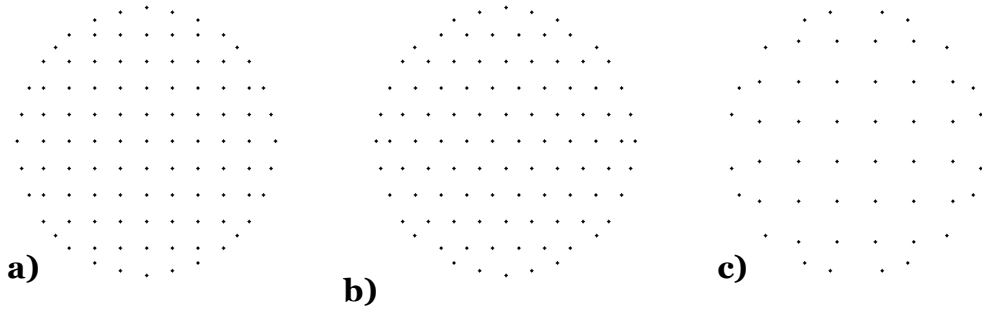


Figure 5.11: Successive samplings of the 2 arcmin FoV used to measure the IMs. a) square geometry, pitch 12", 101 pts. b) hexagonal geometry, pitch 12", 98 pts. c) square geometry, pitch 18", 52 pts.

5.2.5. Simulation results

For a given grid of measurement points, we simulate the SCAO correction of the aberrations maps for a set of 30 GS positions in the FoV. This list of positions is chosen randomly for two reasons:

- To average the effect of the position of the beam footprint with respect to the electrodes of the DM.
- To have a good sample of position of the GS with respect to the grid points (and especially to the closest measurement point).

On the example of the Figure 5.12 we use an hexagonal grid of pitch 18 arcsec (plus some additional points to cover well the 2 arcmin diameter circle), containing in total 53 points for the measurement of the IMs. The position of the 30 evaluations points is also shown.

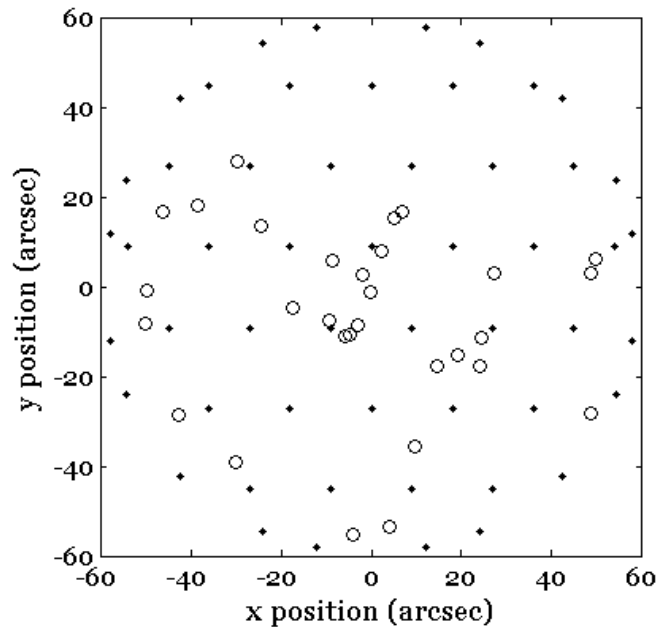


Figure 5.12: Repartition in the FoV of the measurement points grid (dots) and positions of the 30 evaluations points (circles).

The Figure 5.13 shows the computed $rDist$ (equation (5.4)) between the measured and interpolated IMs as a function of the distance of the evaluation point with respect to the closest point of the measured grid, and this for two different methods of interpolations (see section 5.2.3). We notice a general trend of $rDist$ to increase with the distance to the closest measurement point. Computing the relative distance is also a simple way to compare different interpolation techniques without running the full simulation of AO correction. In the case of the Figure 5.13 we see clearly that the method 2 interpolates an IM closer to the measured one than the method 1.

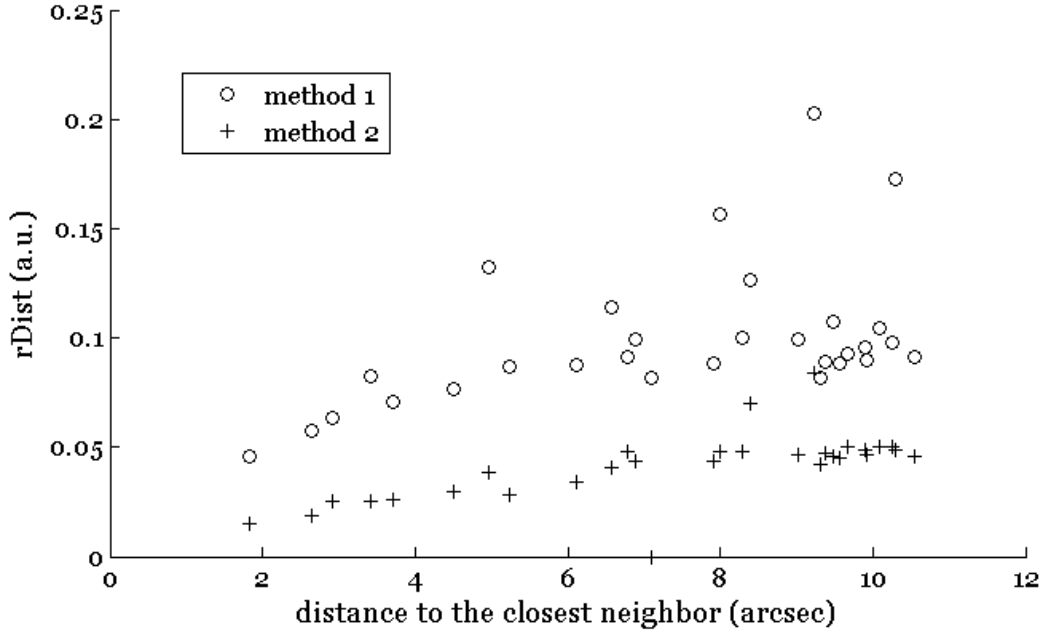


Figure 5.13: Relationship between the distance to the closest measurement point and the relative distance $rDist$ between the measured and interpolated IMs, for the two different interpolation methods described in the section 5.2.3.

The performance of the AO correction (Figure 5.14) is evaluated in terms of Strehl Ratio at a wavelength of 2200 nm, for an input equivalent seeing of 0.8 arcsec. We can see the quite uniform correction brought by the use of a measured IM (around 63 %), and the loss that comes with the use of the interpolation, of 0.2 % of SR in average over the 30 points, with a maximum drop of 1.4 %.

We observe that for some positions the performance with the interpolated matrix is slightly better than with the measured one. This might be a consequence of the modes filtering, that can advantage in some cases the interpolated IM. For instance, let us suppose that a mode $M1$ of radial order n and a mode $M2$ of radial order $n+1$ have almost identical eigen values. In the case of a measured IM, the mode $M1$ can be filtered and the contrary for the interpolated IM. As the modes of radial order n are statistically more important in the input aberrations than the ones of order $n+1$ (see the spectrum of the turbulence on the Figure 2.10), the CM inverted from the interpolated IM will allow correcting more turbulence than the CM inverted from the measured IM.

5.3 MCAO CLOSED LOOP SIMULATIONS

The outcome of the SCAO simulations is that we have found an interpolation method (see 5.2.3) and a grid geometry (see 5.2.4) that allow losing a negligible amount of SR when using the interpolated IM for any position in the FoV.

The grid of 53 points giving excellent results in the SCAO simulations, we decided to proceed with the MCAO simulations (next section) with an even less dense grid of only 33 points (Figure 5.16).

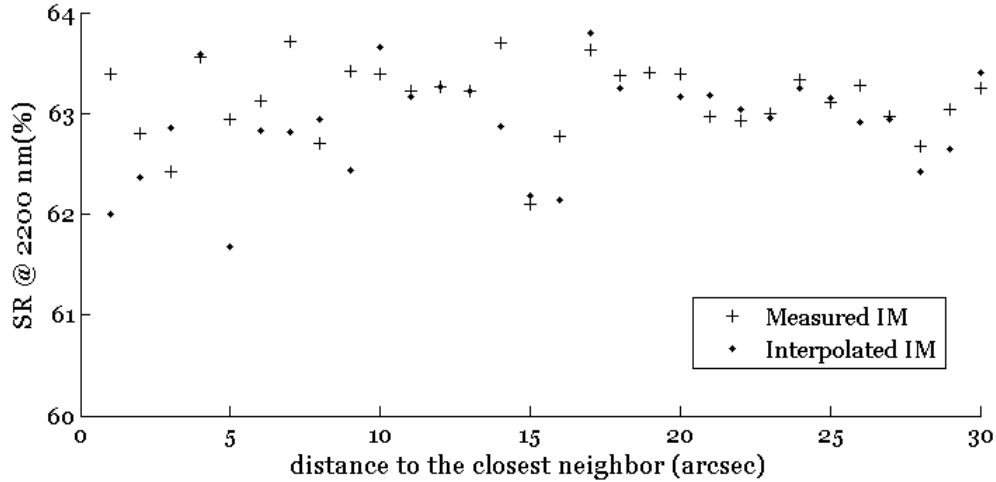


Figure 5.14: Quality of the correction for the 30 points in the FoV, using the measured (crosses) or interpolated (dots) CM.

5.3. MCAO closed loop simulations

The fairly simple open loop SCAO simulations detailed in the previous section give us a good idea of the quality of the interpolation required in order to perform efficient correction of aberrations. This quality implies a proper sampling of the FoV, and a good interpolations method.

But those simulations doesn't tell us the effect of the interpolation on the performances of an MCAO system, where the individual IMs (measured or interpolated) are combined into a meta-IM before the inversion. Will the effect of the interpolation be amplified or averaged? Will the closed loop iterations compensate for the errors, and amplify them until the loop diverges?

To answer those questions, and before the MAD bench was available for MCAO operations, we have tested the interpolation method thanks to closed loop MCAO simulation tool. This tool has been developed by Fernando Quiros-Pacheco in the framework of his PhD thesis at ONERA and ESO [74]. It simulates the MAD system and is used to test new control algorithms [73]. It will be validated by comparing its results to the ones obtained on the MAD bench.

5.3.1. Outline

We have chosen to run the MCAO simulations with asterisms of 3 GS placed at 120° , and at a random radial distance between 40 and 60 arcsec. There are 30 random asterisms in order to have results independent from the asterism. The performance is evaluated for 7 positions on a diameter of the FoV. The parameters of the simulation are:

- Turbulence: 3 layers of turbulence at 0, 6 and 8.5 km of altitude, with a repartition of the variance of respectively 60, 38 and 12 %, and a total seeing of 0.9 arcsec ($r_0 = 11.2$ cm). The time constant τ_0 is of 2.5 ms.
- Deformable Mirrors: model of the MAD DMs (see 2.3.4) using their measured IFs.
- WFS: model of the MAD SHWFS (see 2.3.3): 52 useful sub-apertures with 8×8 pixels per sub-aperture.
- Guide Stars magnitude: 10
- Loop frequency: 400 Hz
- Gain: 0.3
- Number of delay frames: 2
- Reconstruction: TSVD (20 modes filtered)
- Number of loop iterations: 1024
- Performance: estimated by computing the SR of the long-exposure PSF.

5.3.2. Calibration

The first step is to apply the SCAO calibration procedure of the simulation to each direction i of the 33 of the defined grid (shown on the Figure 5.16), in order to get 33 Interaction Matrices $IM_{Alt,i}$ between the altitude DM hit on different portions and one SHWFS (all identical in the simulations), as explained in the section 2.4.4 (equations (2.9) and (2.10)). Also, an Interaction Matrix IM_{Gnd} is recorded between the Ground DM and the WFS. This one is supposed identical for all the directions in the FoV, as the system is simulated aberrations-free.

Then for each star asterism j (including the 3 stars $j1, j2, j3$) among the 30 chosen randomly, the IM and CM are built as follows:

- Interpolated IMs: The grid of IMs is interpolated to the 3 directions of the asterism, giving 3 interpolated IMs between the altitude DM and one SHWFS: $IM_{Alt_j1_interp}$, $IM_{Alt_j2_interp}$ and $IM_{Alt_j3_interp}$.
- Measured IMs: The SCAO calibration procedure of the simulation is applied to the 3 directions of the asterism, giving 3 measured Interaction Matrices between the altitude DM and one SHWFS: $IM_{Alt_j1_meas}$, $IM_{Alt_j2_meas}$ and $IM_{Alt_j3_meas}$.

The “meta-IM” is built from the measured or interpolated IMs by combining them as shown on the equation (5.10):

5.3 MCAO CLOSED LOOP SIMULATIONS

$$\begin{matrix} & 2N_m \\ & \left[\begin{matrix} \text{Meta-IM} \end{matrix} \right] \\ \begin{matrix} 3 \times 2 \times \\ N_{subap} \end{matrix} & \end{matrix} = \begin{bmatrix} \begin{bmatrix} \text{IM}_{\text{Gnd}} \end{bmatrix} & \begin{bmatrix} \text{IM}_{\text{Alt}_{j1}} \end{bmatrix} \\ \begin{bmatrix} \text{IM}_{\text{Gnd}} \end{bmatrix} & \begin{bmatrix} \text{IM}_{\text{Alt}_{j2}} \end{bmatrix} \\ \begin{bmatrix} \text{IM}_{\text{Gnd}} \end{bmatrix} & \begin{bmatrix} \text{IM}_{\text{Alt}_{j3}} \end{bmatrix} \end{bmatrix} \quad (5.10)$$

where N_m is the number of modes applied to each DM (here equal to the number of actuators: 60), and N_{subap} is the number of sub-apertures in each SHWFS (52) which is multiplied by two to include both x and y slopes measurements. The Figure 5.15 shows an example of meta-IM built for the MCAO simulations.

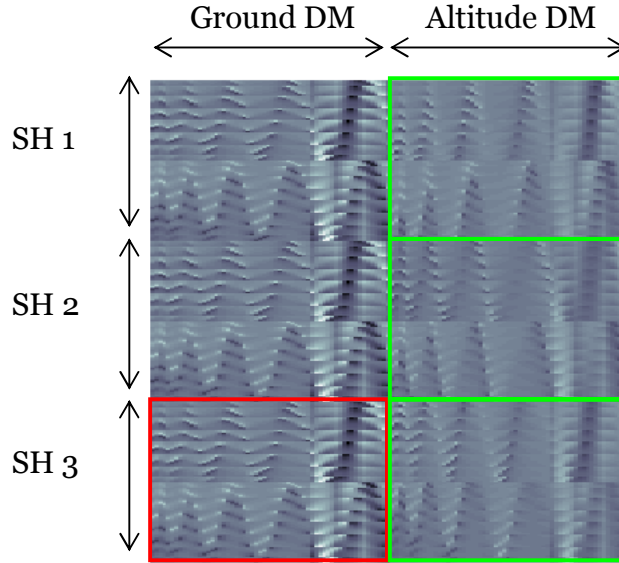


Figure 5.15: Example of meta-IM used in the MCAO closed loop simulations. We see that the 3 Ground DM Interaction Matrices are identical (framed in red) while the Altitude DM's ones are not (in green).

The “meta-CM” is built (from inversion of a measured or interpolated IM) exactly the same way as we used for the SCAO simulations: by generalized inversion (equation (5.12)) of the Truncated SVD decomposition of the meta-IM ((5.11)). The difference lies in the size of the IM, which is now a meta-IM containing the individual IMs between 3 WFS and 2 DMs. The 2 DMs are indeed considered as one, and the columns of the meta-IM are indeed the modes applied

5. INTERACTION MATRIX INTERPOLATION

to the “DM” system. It is the same for the WFS: the rows of the meta-IM are the slopes read by the “SHWFS” system. 20 modes are filtered during the inversion.

$$\text{Meta-IM} = \begin{matrix} 6N_{subap} \\ \left[\begin{array}{c} U \\ \end{array} \right] \\ 6N_{subap} \end{matrix} \times \begin{matrix} 6N_{subap} \\ \left[\begin{array}{c} S \\ \end{array} \right] \\ 2N_m \end{matrix} \times \begin{matrix} \left[\begin{array}{c} V^T \\ \end{array} \right] \\ 2N_m \end{matrix} \quad (5.11)$$

$$\begin{matrix} 2N_m \\ \left[\begin{array}{c} \text{Meta-CM} \\ \end{array} \right] \\ 6N_{subap} \end{matrix} = \text{meta-IM}^\dagger = V \cdot S^\dagger \cdot U^T \quad (5.12)$$

5.3.3. Correction

At each iteration of the MCAO loop, the residual slopes in x and y are measured by the 3 SHWFS simultaneously, and combined to form the aberrations vector:

$$\begin{matrix} 6N_{subap} \\ \left[\begin{array}{c} \text{Ab} \\ \end{array} \right] \end{matrix} = \begin{bmatrix} \left[\begin{array}{c} \text{WFS1} \\ \end{array} \right] \\ \left[\begin{array}{c} \text{WFS2} \\ \end{array} \right] \\ \left[\begin{array}{c} \text{WFS3} \\ \end{array} \right] \end{bmatrix} \quad (5.13)$$

The correction is obtained by multiplication with the meta-CM and gives as a result the list of modes to apply to the 2 DMs:

$$\begin{matrix} 2N_m \\ \left[\begin{array}{c} C \\ \end{array} \right] \end{matrix} = \begin{bmatrix} \left[\begin{array}{c} C_{Gnd} \\ \end{array} \right] \\ \left[\begin{array}{c} C_{Alt} \\ \end{array} \right] \end{bmatrix} = \begin{matrix} \left[\begin{array}{c} \text{Meta-CM} \\ \end{array} \right] \\ 6N_{subap} \end{matrix} \times \begin{matrix} \left[\begin{array}{c} \text{Ab} \\ \end{array} \right] \\ 6N_{subap} \end{matrix} \quad (5.14)$$

5.3 MCAO CLOSED LOOP SIMULATIONS

This correction is combined through the one of the previous loop iteration through a simple integrator.

5.3.4. Results

For each of the 30 asterisms, the MCAO loop is closed with the interpolated and a measured IM (for comparison) and the results are analyzed as shows the Figure 5.16. On this example we can see the triangle formed by the 3 GS. The interpolation of the IM is done in priority with the method 2 (cubic interpolation, see section 5.2.3), and with the method 1 (weighted average) if the other fails, as it is the case for one point of the example.

The profile of SR observed is typical from the MCAO correction with 3 GS and no optimization: the correction is better in the vicinity of the GS. The performance with the interpolate IM follows the same trend, and is degraded by only 0.6 % maximum on the 7 points where the SR is evaluated. This analysis is repeated for the 30 asterisms.

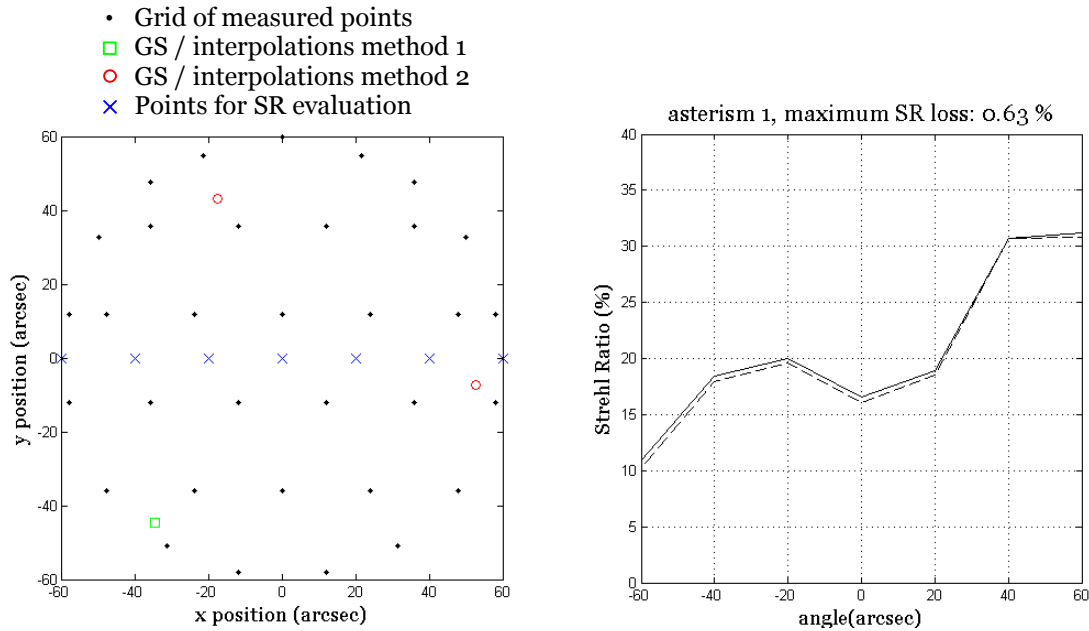


Figure 5.16: Example of performance of the MCAO closed loop in the case of the asterism 1. The IM is interpolated with the method 2 or with the method one if the other fails (section 5.2.3). The SR is evaluated for a line of points crossing the FoV, so is the maximum SR loss.

The SR loss for all of the evaluation points of all the 30 configurations is plot on the Figure 5.17. The average loss of 0.13 % is negligible with respect to the performance itself, between 10 and 35 % depending on the configurations, but it can reach 1 %.

As for the SCAO simulations, we noticed that in some cases the interpolated matrix gives better results than the measured one. This can be explained by the filtering done on the meta-IM during the inversion, and by the fact that noise is introduced in the SHWFS measurements (detector noise and

photon noise coming from a rather bright star of magnitude 10), making the performance not fully reproducible.

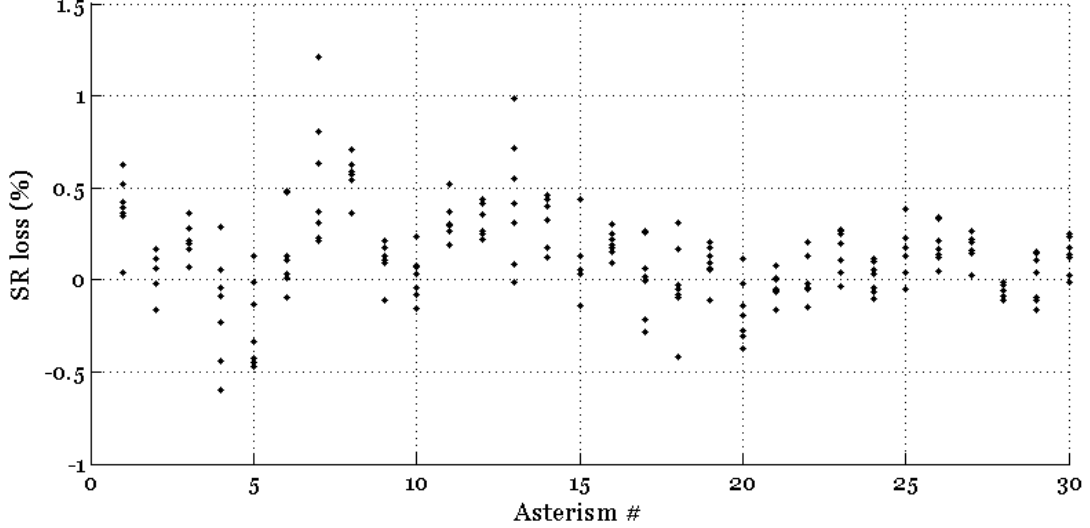


Figure 5.17: Range of SR loss observed among the 7 points where the SR is evaluated, for each of the 30 asterisms simulated. A negative loss means that the SR is better with the interpolated matrix than with the measured one.

5.4. Discussion

A good calibration of the IM is essential to the proper functioning of an AO/MCAO instrument, but it is also important to have an instrument working with a lot of automated function in order to reduce the duration of the calibration. The interpolation of the IM allows saving a lot of time, and the drop of performance can be negligible for an MCAO system as MAD which goal is to reach average performances (30 % in the FoV in K band).

We have seen in this chapter how it is possible, after recording Interaction Matrices for a limited number of points, to interpolate their value to any point in the FoV. The advantage of this method is that it combines calibration measurements made with the instrument and a fast method of interpolation, in order to be able to produce the meta-IM for any stars asterisms. In case of modification of the instrument (or even slight changes due to aging), it is possible to record quickly the IMs for all the points of the grid again, and make the interpolation from this updated grid, which is not possible to do with a fully synthetic IM.

MAD is an instrument suited for testing the interpolation method as its DMs are bimorph ones, thus produce very smooth Influence Functions. In the framework of the development of this instrument, we have made simple matrices comparisons and SCAO simulations to refine the method, and especially to find the best interpolation method and grid geometry. The results of this phase have then been validated thanks to a closed loop MCAO simulation.

By comparing the results of the two simulations, we have noticed that the MCAO one gives much better results. This is explained by the fact that in this case

5.4 DISCUSSION

the altitude DM (the one for which the IMs are interpolated) corrects for only a small fraction of the turbulence (12 % of the variance according to the simulations parameters), and does it with a smaller number of electrodes in the pupil. Also the errors created are corrected by the iterative process of the closed loop.

In the specific case of MAD, the grid of 33 points we have designed is sufficient to interpolate the meta-IM for any stars asterisms without a noticeable loss of performance. Knowing that recording an IM takes less than 1 minute, this would mean that all the required IMs in the FoV (and with each of the SHWFS to keep the information on their differences) can be recorded within 100 minutes. By limiting the FoV accessible by each WFS, this amount of time can be divided by two.

Considering that about 15 points are required on the 2 arcmin circle, it seems useless to try to reduce the total number of GS to less than 30 with the current interpolation techniques. However, developing more clever techniques could be a future work to the one presented here. For instance one could use a model of Influence Functions to enhance the interpolation for the sub-apertures facing the electrodes, as we have seen that they are producing the largest errors.

Once all the IMs recorded, it is then immediate to compute the meta-IM for any star asterism. This technique will be tested on the MAD bench while in the laboratories of ESO and fed by the reproducible turbulence of MAPS. Although the gain of time might not be significant on MAD, it is a promising technique in the case of future AO systems for which the calibration is a time-consuming process, due to a larger number of degrees of freedom (number of actuators and of WFS).

6. Conclusion and perspectives

The objective of this work was to develop new calibration strategies and test tools for MCAO systems. The MCAO Demonstrator (MAD) built by the European Southern Observatory is the first instrument of this kind, thus a perfect support for the application of new MCAO concepts.

In order to perform the laboratory tests of MAD, we have successfully brought from concept to reality a new generation of turbulence and telescope simulator: MAPS. This test tool is based on an all-refractive design and its innovations lie in a large field of view and the use of refractive Phase Screens. Those critical optical elements reproduce the turbulence layers of the Paranal atmosphere, and are quasi-achromatic in the whole wavelength range from 500 to 2500 nm. This last point is of main importance because the WF is sensed in the visible, but the performances are evaluated in the near-IR, and a chromatism of the turbulence produced by the PS would lead to a biased estimation of the performances in the lab. In the framework of this thesis, the Phase Screens have been carefully designed, manufactured, and fully characterized before being used to feed the AO instrument with reproducible and calibrated Wave Front perturbations.

MAPS is being intensively used to characterize and improve the performances of MAD in the laboratory. The same concept of refractive Phase Screens is foreseen for future turbulence generators at ESO in the frame of the test benches APE (Active Phasing Experiment) and HOT (High Orders Test bench), of the AO system for MUSE (the Multi Unit Spectroscopic Explorer), of AO instruments concepts for OWL, and elsewhere (Grantecan ...). Since we have faced the constraints linked to the use of those screens, we now apply the lessons learned as early as the design phase of the following generation of Phase Screens and turbulence generators.

The Non-Common Path Aberrations are limiting the quality of the images obtained on the scientific camera in an AO instrument. The solution we suggested in this thesis is to use the camera itself as a focal plane WFS, by recording two images and estimating the aberrations by Phase Diversity at the level of the detector, i.e. where we wish them to be corrected. In addition, we have proposed the idea of recording a calibration matrix between the camera and the deformable device in order to obtain the correction vector by a simple matrix multiplication. The whole procedure, inspired from the real-time correction of the atmospheric turbulence, is fast and easily applicable to any AO system.

In the specific case of MCAO instruments, we have also shown how a tomographic approach allows reconstructing the aberrations at the level of the optics of the system, and compensate for them thanks to a clever use of the several DMs in the path.

The efficient compensation of the on-axis aberrations by using a calibration matrix has been validated on the MAD bench, increasing the quality of a calibration source image from a Strehl Ratio of 83 % to 93 %. This technique has also proven its applicability to different systems, and is envisaged to be used

for the calibration of the next generation of AO instruments, especially the one aiming at high on-axis performances such as Planet Finder for the VLT for instance. The experimental validation for the FoV compensation of the aberrations will be done as well on MAD in the next future. The experience acquired on this demonstrator will be valuable for a smart implication of those techniques in an early stage of the design of future AO instruments.

The main limitation to a perfect correction of the NCPA remains the stability of the system during the period of time when the calibration matrices are recorded, and its evolution until the moment when the correction is applied. The solution to freeze the turbulence in the bench and the creep of the DMs is to work while the AO loop is closed on calibration sources, and to perform the calibration and the correction by modifying the reference for the closed loop instead of the static voltages of the DM. Although the advantage with respect to the open loop technique has been shown on the BOA bench of ONERA, its usefulness and easiness of implementation is still to be demonstrated for the correction of the field-dependant aberrations on MCAO systems.

Finally, and more specifically to MCAO, we have tested by simulation the possibility to interpolate Interaction Matrices measurements to the whole technical FoV. It is an hybrid solution between recording IMs for any star asterism we observe and using a fully synthetic matrix, and it combines in this sense the advantages of both: staying close to the system and its particularities, but also being flexible and automated for a more efficient use of the instrument. In the case of MAD, the results of the simulations are promising and show that a relatively small number of measurements is enough to interpolate the IMs to the whole FoV. These results will be validated on the MAD bench, and eventually compared to the performances achieved when using a full synthetic matrix, in order to distinguish the effect of the system's imperfections, which were not taken into account in the simulations.

We believe that the efficiency of the interpolation of the Interaction Matrices of MAD can still be enhanced, maybe by enlarging the grid pitch, but especially by working on more clever interpolation algorithms, taking into account the Influence Functions of the DM and the position of the electrodes for instance. The interpolation might become very convenient for future GL/MCAO systems that will accommodate much more actuators and sensors.

In parallel to MAD, ESO is currently designing what is called the AO Facility and that comprises a secondary Deformable Mirror for the VLT, several Laser Guide Stars, and the AO part of the second generation of instruments for the VLT: GALACSI for MUSE and GRAAL for HAWK-I, which are both GLAO systems. Strong of the success of the first generation of AO instruments, the AO Team of ESO is pushing forward the current techniques to achieve the best at all phases of the development: design, manufacturing, assembly, calibration, test and optimization.

In the future, observation time on world class astronomical telescopes will be more and more precious, and the calibration and test tolls will have to be particularly sophisticated to allow the full analysis of an instruments. ESO and many other institutes over Europe are now involved in the Framework Program 6

6. CONCLUSION AND PERSPECTIVES

(FP6) of the European Commission which is funding the research on an Extremely Large Telescope (ELT). Moreover, ESO is exploring for several years concepts for building a 100 meters telescope OWL, and in the USA has just been launched the production of the Thirty Meters Telescope (TMT). All those projects aim at collecting more and more flux from the sky, and their full advantage in terms of resolution can be reached only through Adaptive Optics. Although the detailed roadmap for the instrumentation equipping those giants is not yet defined, the current generation of AO systems will be a baseline to follow, and the scientific community will require from future systems to provide the best achievable images over always larger Fields of View.

7. Bibliography

- [1] Amorim A., Melo A., Alves J., Rebordão J., Lima J., Pinhão J., Bonfait G., Fernandes R., Barros R., Azevedo-Lucas J., Correia L., Carvalho M., Santos J., Marques R., Duarte Santos F., Catarino I., Poncet J., “*The CAMCAO infrared camera*” Ground based instrumentation for astronomy, SPIE Proceedings, [5492-120], June 2004
- [2] Arsenault R., Alonso J., Bonnet H., Brynnel J., Delabre B., Donaldson R., Dupuy C. et al. “*MACAO-VLTI: and Adaptive Optics System for the ESO interferometer*” Proc SPIE 4839, pp. 174-185, 2003
- [3] Babcock H. W. “*The possibility of compensating astronomical seeing*” Pub. Astron. Soc. Pacific, 65:229, 1953
- [4] Bähr J., Brenner K.-H., Sinzinger S., Spick T., Testorf M. “*Index-distributed planar microlenses for three dimensional micro-optics fabricated by silver-sodium ion exchange in BGG 335 substrates*” Appl. Opt. , 33, 5919-5924, 1994
- [5] Beckers J. M. “*Increasing the size of the isoplanatic patch size with multiconjugate adaptive optics*” in ESO conference on Very Large Telescopes and their instrumentation, M.-H. Hulrich, ed., pp. 693, 1988
- [6] Beckers J. M. “*Detailed compensation of atmospheric seeing using multiconjugate adaptive optics*” Proc. SPIE 1114, pp. 215-217, 1989
- [7] Beuzit J.-L., Hubin N., Gendron E., Demailly L., Gigan P., Lacombe F., Chazallet F., Rabaud D., Rousset G. “*Adonis: a user-friendly adaptive optics system for the ESO 3.6-m telescope*” SPIE meeting on Adaptive Optics in Astronomy, Kona, Proc. SPIE 2201, pp. 955-961, M.A. Ealey and F. Merkle Eds, March 17-18 1994
- [8] Blanc A., “*Identification de réponse impulsionnelle et restauration d’images: apports de la diversité de phase*” Thèse de Doctorat, Université Paris XI Orsay, July 2002
- [9] Blanc A., Fusco T., Hartung M., Mugnier L. M., Rousset G. “*Calibration of NAOS and CONICA static aberrations. Application of the phase diversity technique*” Astron. Astrophys., 399:373-383, 2003
- [10] Bonnet H., Stroebele S., Biancat-Marchet F., Brynnel J., Conzelmann R. D., Delabre B. et al. “*Implementation of MACAO for SINFONI at the Cassegrain focus of VLT, in NGS and LGS modes*” Proc SPIE 4839, pp. 329-343, 2003
- [11] Born M., Wolf E. “*Principles of Optics: Electromagnetic Theory of Propagation, Interference, and Diffraction of Light*” 7th ed. Cambridge, England: Cambridge University Press, 1999
- [12] Boyer C., Michau V., Rousset G. “*Adaptive optics: interaction matrix measurements and real-time control algorithms for the Come-on project*”

7. BIBLIOGRAPHY

- Proc. SPIE 1237, pp. 406-421, Amplitude and Intensity Spatial Interferometry, J.B. Breckinridge Ed., 1990
- [13] Butler D., Hippler S., Egner S., Xu W., Bähr J. “*Broadband, Static Wave-Front Generation: Na-Ag Ion-Exchange Phase Screens and Telescope Emulation*” Applied Optics, Vol. 43 Issue 14 Page 2813, May 2004
 - [14] Butler D., Marchetti E., Bähr J., Xu W., Hippler S., Kasper M., Conan R. “*Phase screens for astronomical multi-conjugate adaptive optics: application to MAPS*” SPIE 4830, p. 623, 2002
 - [15] Butler D. “*MAPS conceptual design*” MAD CDR, Doc. No. OWL-TRE-MPI-60000-0039, April 2002
 - [16] Conan R. “*Modélisation des effets de l'échelle externe de cohérence spatiale du front d'onde pour l'observation à Haute Résolution Angulaire en Astronomie*” Ph.D. thesis (Université de Nice-Sophia-Antipolis), 2000
 - [17] Davis C. C., Zhang Y., Plett M. L., Polak-Dingels P., Barbier P., Rush D. W. “*Characterization of a liquid-filled turbulence simulator*” in Artificial Turbulence for Imaging and Wave Propagation, Proc. SPIE Vol. 3432, p. 38-49, edited by John D. Gonglewski; Mikhail A. Vorontsov
 - [18] Dicke R. H. “*Phase-contrast detection of telescope seeing errors and their correction*” Astrophys. J. 198:605-15, 1975
 - [19] Dierickx P., Brunetto E., Comeron F., Gilmozzi R., Gonté F., Koch F., Le Louarn M., Monnet G., Spyromilio J., Surdej I., Verinaud C., Yaitskova N. “*OWL phase A status report*” Ground-based Telescopes, SPIE Proceedings, [5489-23], 2004
 - [20] Egner S. “*Optical Turbulence Estimation and Emulation. Implementation of a maximum-a-posteriori wavefront estimator for the Calar Alto AO system ALFA and laboratory characterization of sodium-silver ion exchange phase screens*” Diploma thesis of the Max Planck Institut for Astronomy, University of Heidelberg, 2003
 - [21] Ellerbroek B. “*First order performance evaluation of adaptive optics system for atmospheric turbulence compensation in extended field-of-view astronomical telescope*” J. Opt. Soc. Am A 11, pp. 783-805, 1994
 - [22] Franza F. “*MAD mechanics final design*” MAD MRR, Doc. No. OWL-TRE-ESO-60000-0084, June 2003
 - [23] Fried D. L. “*Anisoplanatism in adaptive optics*” J. Opt. Soc. Am., 72(1):pp 52-61, January 1982
 - [24] Fried D. L. “*Optical Resolution Through a Randomly Inhomogeneous Medium for Very Long and Very Short Exposures*” J. Opt. Soc. Am., vol. 56, no. 10, pp. 1372-1379, October 1966
 - [25] Fried D.L. “*Statistics of a geometric representation of wavefront distortion*” J. Opt. Soc. Am., vol. 55, no. 11, pp. 1427-1435, November 1965

- [26] Fusco T. "*Correction partielle et anisoplanétisme en Optique Adaptative: traitements a posteriori et Optique Adaptative multiconjuguée*" Thèse de Doctorat, Université de Nice Sophia-Antipolis, October 2000
- [27] Fusco T., Blanc A., Mugnier L. M., Rousset G. "*Development of a Phase Diversity approach to calibrate NAOS and CONICA static aberrations*" ONERA technical report, April 2002
- [28] Fusco T., Conan J.-M., Michau V., Mugnier L. M., Rousset G. "*Phase estimation for large field of view: application to multiconjugate adaptive optics*", Proc. SPIE 3763, 125-133, 1999
- [29] Fusco T., Conan J.-M., Rousset G., Mugnier L. M., Michau V. "*Optimal wavefront reconstruction strategies for multiconjugate adaptive optics*" J. Opt. Soc. Am. A, (10):2527-2538, October 2001
- [30] Gemini Observatory, "*MCAO for Gemini-South Preliminary Design Report*", Doc. No. REV-AO-G0172, 2002
- [31] Gonsalves R. A., "*Phase retrieval and diversity in adaptive optics*" Optical Engineering, 21 (5), pp. 829-832, 1982
- [32] Gonté F. Y. J., Araujo C., Buzzoni B., Delabre B., Derié F., Dierickx P., Dupuy C., Frank C., Guisard S., Karban R., **Kolb J.** et al. "*APE: the Active Phasing Experiment to test new control systems and phasing technologies for a European giant optical telescope*" Optical Engineering and Instrumentation, SPIE Proceedings, [5894-35], 2005
- [33] Hartung M., Blanc A., Fusco T., Lacombe F., Mugnier L. M., Rousset G., Lenzen R. "*Calibration of NAOS and CONICA static aberrations. Experimental results*" Astron. Astrophys., 399:385-394, 2003
- [34] Herriot G., Morris S., Roberts S., Fletcher J.-M., Saddlemeyer L., Singh G., Veran J.-P., Richardson E. "*Innovations in Gemini adaptive optics system design*" Proc. SPIE Vol. 3353, p. 488-499, Adaptive Optical System Technologies, September 1998.
- [35] Hubin N., Le Louarn M., Conzelmann R., Delabre B., Fedrigo E., Stuik R. "*Ground layer AO correction for the VLT MUSE project*" Proc. SPIE, Volume 5490, pp. 846-857, 2004
- [36] Hubin N., Marchetti E., Fedrigo E., Conan R., Ragazzoni R., Diolaiti E., Tordi M., Rousset G., Fusco T., Madec P.-Y., Butler D., Hippler S., Esposito S. "*The ESO MCAO demonstrator MAD: a European collaboration*" Proc. of the ESO Conference 'Beyond Conventional Adaptive Optics', Venice, 7-10 May 2001
- [37] Kelly T.-L., Buscher D., Clark P., Dunlop C., Love G., Myers R., Sharples R., Zadrozny A. "*Dual-conjugate wavefront generation for adaptive optics*" Optics Express Vol. 7, No. 11, November 2000
- [38] **Kolb J.** "*Calibration of the light source for MAPS*" ESO internal memorandum, April 2005

- [39] **Kolb J.** “Calibration of the static aberrations in an MCAO system” Journées Scientifiques de l’ONERA - MCAO, March 2005
- [40] **Kolb J.** “*Characterization of STRAP using a turbulence generator*” Traineeship report, Doc. No. VLT-TRE-ESO-14710-2918, September 2002
- [41] **Kolb J.** “*Correction of the static aberrations of the MAD bench, January ’05*” ESO internal memorandum, April 2005
- [42] **Kolb J.** “*Correction of the static aberrations, Final report on the simulations, May ’04*” ESO internal memorandum, April 2005
- [43] **Kolb J.** “*Integration, alignment and test of MAPS in its flat configuration*” ESO internal memorandum, May 2005
- [44] **Kolb J.** “*MAPS final design*” MAD MRR, Doc. No. OWL-TRE-ESO-60000-0093, June 2003
- [45] **Kolb J.** “*MAPS Phase Screens Proposal Overview*” MAD MRR, Doc. No. OWL-TRE-ESO-60000-0092, June 2003
- [46] **Kolb J.** “*Test report of the Phase screen prototype from SILIOS at IMT Neuchatel*” ESO internal memorandum No. INS-03/26, August 2003
- [47] **Kolb J.** “*Test report of the Phase screen prototype from SILIOS at ESO Garching*” ESO internal memorandum No. INS-03/28, September 2003
- [48] **Kolb J.** “*Test report of the Phase screen prototype from SMOS*” ESO internal memorandum No. INS-03/30, September 2003
- [49] **Kolb J., Gonté F.** “*MAPS Phase Screen prototype Technical Specifications and Statement of Work*” Doc. No. OWL-SPE-ESO-60000-0107, May 2003
- [50] **Kolb J., Marchetti E.,** “*MAPS Phase Screens technical specifications and SOW*” MAD MRR, Doc. No. OWL-SPE-ESO-60000-0070, June 2003
- [51] **Kolb J., Marchetti E., Rousset G., Fusco T.,** “*Calibration of the static aberrations in an MCAO system*”, Advancements in Adaptive Optics, SPIE Proceedings, [5490-109], 2004
- [52] **Kolb J., Marchetti E., Tisserand S., Franza F., Delabre B., Gonté F., Brast R., Jacob S., Reversat F.,** “*MAPS, a turbulence simulator for MCAO*”, Advancements in Adaptive Optics, SPIE Proceedings, [5490-166], 2004
- [53] **Kolb J., Santos J.** “*Test report of the Infrared Test Camera for MAD and SINFONI*” ESO internal memorandum No. TSD-04/003, December 2003
- [54] Kolmogorov A. N. “*The local structure of the turbulence in incompressible viscous fluid for very large Reynolds numbers*” Dokl. Akad. Nauk SSSR, 30:9–13, 1941 (Reprinted in Proc. R. Soc. Lond. A434, 9-13, 1991)
- [55] Labeyrie A. “*Attainment of Diffraction Limited Resolution in Large Telescopes by Fourier analysing speckle patterns in star images*” Astronomy Astrophys, 6:85-87, 1970

- [56] Le Roux B., Conan J.-M., Kulcsár C., Raynaud H.-F., Mugnier L. M., Fusco T. “*Optimal control law for classical and multiconjugate adaptive optics*” J. Opt. Soc. Am. A., 21(7), p. 1261-1276, 2004
- [57] Leal L. “*NACO Phase Diversity Analysis Technical Report*”, Doc. No. VLT-TRE-ESO-11650-3443, Oct 2004
- [58] Löfdahl M. G., Scharmer G. B. “*Wavefront sensing and image restoration from focused and defocused solar images*” Astron. Astrophys., 107, pp. 243–264, 1994
- [59] Love G. “*Wave-front correction and production of Zernike modes with a liquid-crystal spatial light modulator*” Appl. Opt. 36:1517, 1997
- [60] Makidon R., <http://cfao.ucolick.org/Strehl/Makidon/>
- [61] Marchetti E. “*MAD & MAPS electronics requirements*” MAD MRR, Doc. No. OWL-SPE-ESO-60000-0063, January 2003
- [62] Marchetti E., Brast R., Delabre B., Donaldson R., Fedrigo E., Franza F., Hubin N., **Kolb J.**, Le Louarn M., Lizon J.-L., Oberti S., Reiss R., Santos J., Ragazzoni R., Arcidiacono C., Baruffolo A., Diolaiti E., Farinato J., Vernet-Viard E. “*MAD status report*”, Advancements in Adaptive Optics, SPIE Proceedings, [5490-17], 2004
- [63] Marchetti E., Hubin N., “*MAPS Technical specifications*” MAD CDR, Doc. No. OWL-SPE-ESO-60000-0038, April 2002
- [64] Martin F., Conan R., Tokovinin A., Ziad A., Trinquet H., Borgnino J., Agabi A., Sarazin M. “*Optical parameters relevant for High Angular Resolution at Paranal from GSM instrument and surface layer contribution*” Astron. Astrophys. Suppl. Ser. 144, 39-44, May 2000
- [65] Meynadier L. “*Analyse de surface d’onde pour le contrôle actif d’un télescope spatial*” PhD thesis, Université de Nice-Sophia Antipolis, 1997
- [66] Meynadier L., Michau V., Velluet M.-T., Conan J.-M., Mugnier L. M., Rousset G., “*Noise propagation in wave-front sensing with phase diversity*” Appl. Opt., 38 (23), pp. 4967–4979, August 1999
- [67] Neichel B. “*Optimisation expérimentale d’un banc d’Optique Adaptative (BOA)*” Rapport de stage effectué à l’ONERA, July 2005
- [68] Oberti S., Esposito S. “*Calibration strategies overview for large DM AO systems*” Doc. No. VLT-TRE-ESO-11250-3761, September 2005
- [69] Oya S., Takato N., Takami H., Hayano Y., Iye M., Kamata Y., Minowa Y., Kanzawa T., Gaessler W. “*Subaru adaptive optics system after two years of open use*” Proc. SPIE 5490, pp. 409-420, 2004
- [70] Paufigue J., Biereichel P., Donaldson R., Delabre B., Fedrigo E., Franza F., Gigan P., Gojak D., Hubin N. et al. “*MACAO-CRIRES: a step toward high-resolution spectroscopy*” Proc. SPIE, Volume 5490, pp. 216-227, 2004

- [71] Paxman R.G., Schulz T.J., Fienup J.R. “*Joint Estimation of Object and Aberrations Using Phase Diversity*”, J. Opt. Soc. Am. A 7, 1072-85, 1992
- [72] Primot J., Rousset G., Marais T., Fontanella J.-C. “*Deconvolution from wavefront sensing: a new technique for compensating turbulence degraded image*” J. Opt. Soc. Am 7 1598-1608, 1990
- [73] Quiros-Pacheco F., Petit C., Conan J.-M., Fusco T., Marchetti E. “*Control law for the multiconjugate adaptive optics demonstrator (MAD)*” Advancements in Adaptive Optics, SPIE Proceedings, [5490-158], 2004
- [74] Quiros-Pacheco F. “*Reconstruction and Control Laws for Multi-conjugate Adaptive Optics in Astronomy*” PhD thesis. Imperial College London, UK, 2006
- [75] R. J. Noll, “*Zernike polynomials and atmospheric turbulence*” J. Opt. Soc. Am. 66, 207–211, 1976
- [76] Ragazzoni R. “*Adaptive optics for giants telescopes: NGS vs. LGS*” in ESO Proceedings of the Bäckaskog Workshop on Extremely large Telescopes 57, T. Andersen, A. Ardeberg and R. Gilmozzi, eds., pp. 175-180, 2000
- [77] Ragazzoni R. “*Pupil plane wave front sensing with an oscillating prism*” J. of Mod. Opt. 43, pp. 289-293, 1996
- [78] Ragazzoni R., Marchetti E., Rigaut F. “*Modal Tomography for Adaptive Optics*” Astronomy and Astrophysics 342:L53-L56, 1999
- [79] Rhoadarmer T. A., Angel R. “*Low-cost, broadband static phase plate for generating atmospheric-like turbulence*” Applied Optics Vol. 40 No. 18, p. 2946-2955, June 2001
- [80] Rigaut F., Salmon D., Arsenault R., Thomas J., Lai O., Rouan D., Véran J.-P. et al “*Performance of the Canada-France-Hawaii Telescope Adaptive Optics Bonnette*” PASP, 110, 152-164, 1998
- [81] Roberts L. C. Jr., Perrin M., Marchis F., Sivaramakrishnan A., Makidon R., Christou J., Macintosh B., Poyneer L., van Dam M., Troy M. “*Is that really your Strehl ratio?*” Advancements in Adaptive Optics, SPIE Proceedings, [5490-166], 2004 Volume 5490, pp. 504-515 (2004)
- [82] Roddier F. “*Adaptive Optics in Astronomy*” Cambridge U. Press, Cambridge, UK, 1999
- [83] Roddier F. “*The effects of atmospheric turbulence in optical astronomy*” Progress in Optics 19, 282-376, E. Wolf Ed., 1981
- [84] Roddier F.; Anuskiewicz J., Graves J., Northcott M., Roddier C. “*Adaptive Optics at the University of Hawaii I: current performance at the telescope*” Proc. SPIE 2201, 2, 1994, M.A. Ealey and F. Merkle Eds, March 17-18 1994
- [85] Rousset G., Beuzit J.-L., Hubin N., Gendron E., Boyer C., Madec P.-Y., Gigan P., Richard J.C., Vittot M., Gaffard J.P., Rigaut F., Léna P. “*The Come-On-Plus Adaptive Optics System : Results and performance*” ICO

- conference on Active and Adaptive Optics, Garching (Germany), August 2-5 1993
- [86] Rousset G., Fontanella J.-C., Kern P. Y., Gigan P., Rigaut F., Lena P., Boyer C., Jagourel P., Gaffard J.-P., Merkle F. “*First diffraction-limited astronomical images with adaptive optics*” *Astron. and Astrophys.* 230 , L29-L32, 1990
 - [87] Rousset G., Fontanella J.-C., Kern P. Y., Lena P., Gigan P., Rigaut F., Gaffard J.-P., Boyer C., Jagourel P., Merkle F. “*Adaptive optics prototype system for infrared astronomy, I: System description*” *Proc. SPIE* 1237, pp. 336-344, *Amplitude and Intensity Spatial Interferometry*, James B. Breckinridge Ed., 1990
 - [88] Rousset G., Lacombe F., Puget P., Hubin N., Gendron E., Fusco T., Arsenault R., Charton J., Feautrier P., Gigan P., Kern P. Y., Lagrange A.-M., Madec P.-Y., Mouillet D., Rabaud D., Rabou P., Stadler E., Zins G. “*NAOS, the first AO system of the VLT: on-sky performance*” in *Adaptive Optical System Technologies II*. Edited by Wizinowich Peter L., Bonaccini Domenico, vol. 4839 of *Proc. SPIE*, pp. 140-149, February 2003
 - [89] Sarazin M., Roddier F. “*The ESO differential image motion monitor*” *Astron. Astrophys.*, 227:294-300, 1990
 - [90] Sauvage J.-F., Fusco T., Rousset G., Petit C., Blanc A., Beuzit J.-L. “*Fine calibration and pre-compensation of NCPA for high performance AO system*” submitted, 2005
 - [91] Strehl K., *Zf InstrumKde* 22, p. 203, 1902
 - [92] Tallon M., Foy R. “*Adaptive telescope with laser probe - Isoplanatism and cone effect*” *A&A* 235, pp. 549-557, 1990
 - [93] Taylor G.I. “*Statistical theory of turbulence*” *Proc. R. Soc. Lond.*, A164, 476-90, 1938
 - [94] Tisserand S. “*SILIOS Technologies fournit des écrans de phase à l'ESO*” letter published in ‘Photoniques’ 16, December 2004
 - [95] Tokovinin A. “*From Differential Image Motion to Seeing*” *Publications of the Astronomical Society of the Pacific*, 114:1156-1166, October 2002
 - [96] Van Dam M. A., Le Mignant D., Macintosh B. A. “*Performance of the Keck Observatory adaptive optics system*” *Applied Optics* 43, 5458-5467, 2004
 - [97] Vernet E., Arcidiacono C., Baruffolo A., Diolaiti E., Farinato J., Ragazzoni R., Lombini M. “*The Layer-Oriented Wavefront Sensor for the Multiconjugate Adaptive optics Demonstrator*” *Optical Engineering*, accepted for publication, 2005.

8. Appendices

8.1. The shape of the Zernike polynomials

In the Figure 8.1 and Figure 8.2 are represented the first 21 Zernike modes (corresponding to 5 radial orders) as computed over a circular aperture. Details on the Zernike polynomials are given in the section 2.4.1 of this thesis.

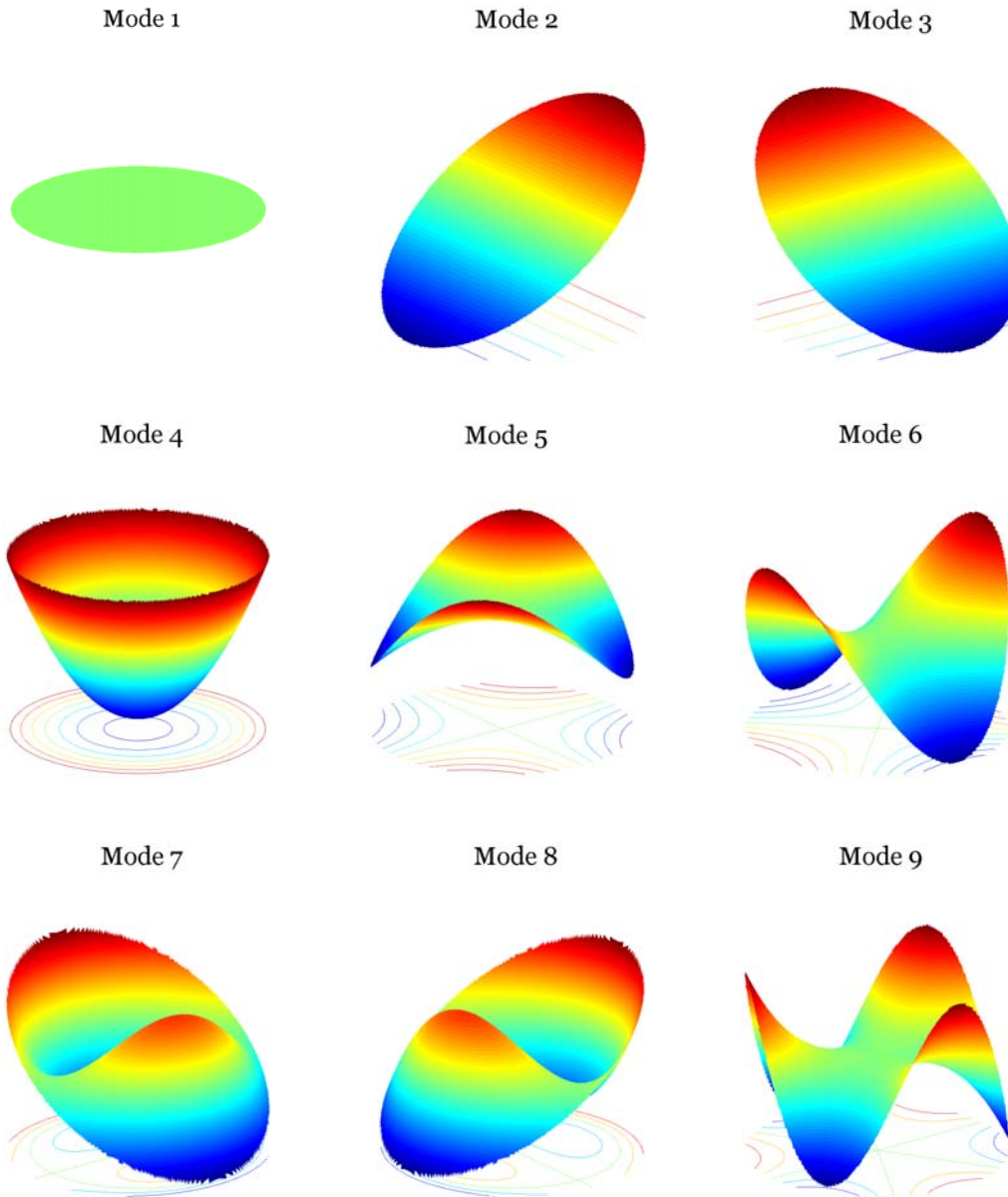


Figure 8.1: Zernike modes 1 to 9.

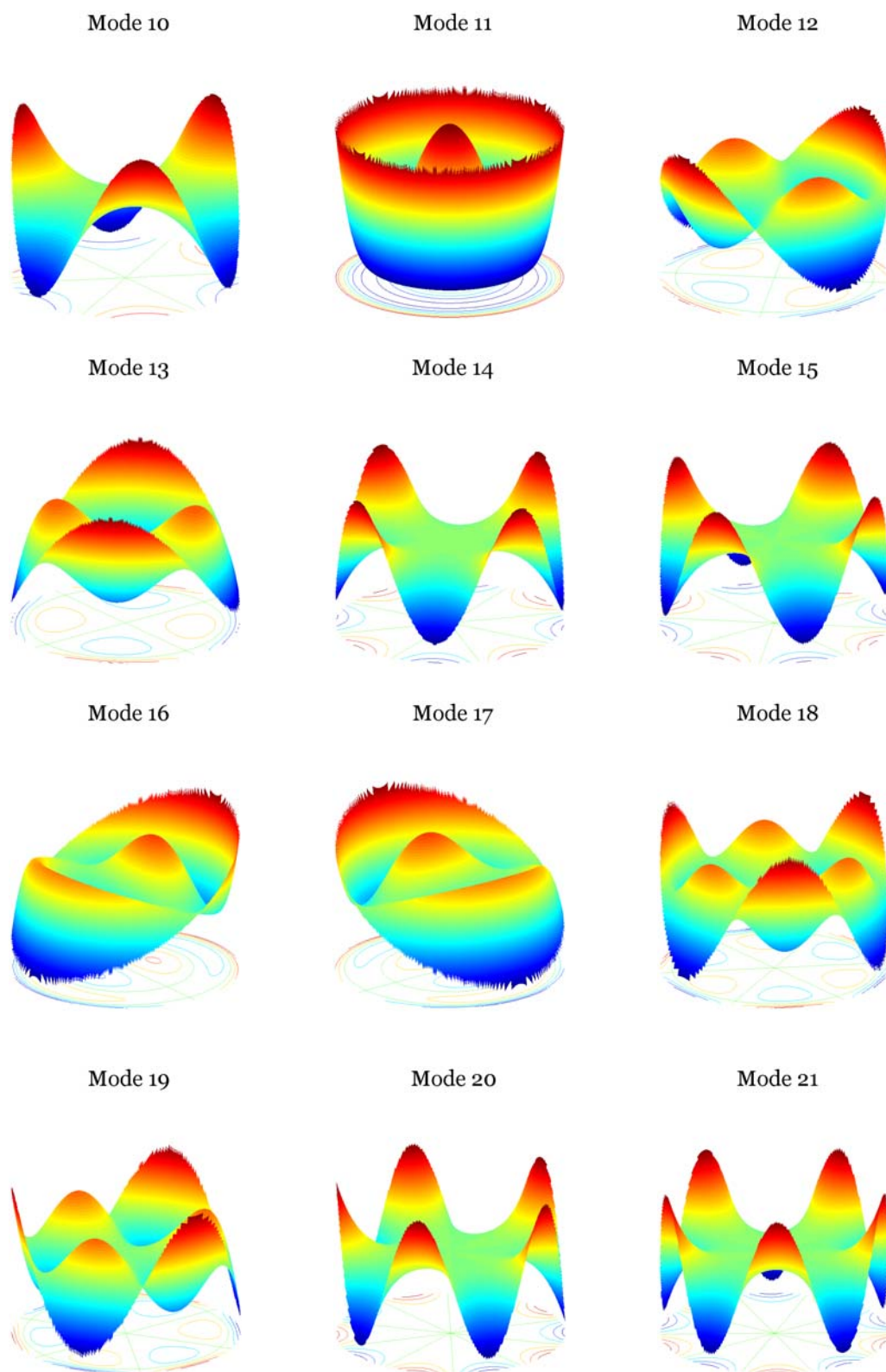


Figure 8.2: Zernike modes 10 to 21.

8.2. SPIE paper “MAPS, a turbulence simulator for MCAO”

This paper [52] has been presented at the SPIE symposium “Advancement in Adaptive optics” that was held in Glasgow (Scotland) from June 21st to 25th 2004 as a poster.

It describes in details the opto-mechanical layout of MAPS and the motor rotation system in complement to the section 3.3.1. Updated information on the Phase Screens manufacturing and testing, as well as all the work performed on MAPS after publication of this paper are detailed in the section 3.

MAPS, a turbulence simulator for MCAO

Johann Kolb ^{*a}, Enrico Marchetti ^a, Stéphane Tisserand ^b, Francis Franza ^a, Bernard Delabre ^a,
Frédéric Gonté ^a, Roland Brast ^a, Sophie Jacob ^b, Fabien Reversat ^b

^a European Southern Observatory, Karl-Schwarzschild-Str. 2, 85748 Garching, Germany;

^b SILIOS Technologies, ZI de Peynier Rousset, rue Gaston Imbert prolongée 13790 Peynier, France

ABSTRACT

The Multi-Atmospheric Phase screens and Stars (MAPS) instrument is a powerful tool that has been developed in the framework of the ESO Multi-conjugate Adaptive optics Demonstrator project (MAD). It allows emulating a 3D evolving Paranal-like atmosphere as well as up to 12 sources in a 2 arc minutes field of view, as seen at a Nasmyth focus of one of the VLT. It will be used to perform advanced laboratory tests on MAD before its shipment to Chile.

In this paper we present the opto-mechanical design of MAPS. This one simulates the characteristics of the VLT focus and achieves a high Strehl Ratio over the whole Field of View in the visible as well as in the infrared. A curved entrance plate crowded with fibers emulates various stars configurations including real sky asterisms.

In order to simulate the atmosphere, three rotating Phase Screens are placed in the beam and conjugated with different altitudes. Those are glass plates dig in their surface in a way that the beam passing through is distorted as it would be by an atmospheric turbulent layer. In this poster we also present the process of research that lead to the choice of a reliable technique to imprint the aberrations into the screens, their properties and expected performance.

Key words: Atmospheric turbulence, turbulence generator, phase screens, MCAO, VLT, ion etching

1. INTRODUCTION AND CONCEPT

MAPS has been recognized as a strategic tool for the laboratory testing of the Multi-conjugate Adaptive optics Demonstrator [9, 11, 13, 16]. The goal of MAPS is to emulate a time evolving three-dimensional atmosphere whose induced aberrations are injected into MAD. The characteristics of the atmospheric turbulence shall be similar to those of the Paranal observatory during typical seeing conditions. Different kinds of turbulence simulators have been under investigation for some years [4, 7, 10], but they all have weak points when it is question of full MCAO turbulence emulation. MAPS creates a 2 arcmin FoV beam as seen at the F/15 Nasmyth focus of one of the VLT Units. The strategy is to use an all refractive solution because of its versatility in changing the atmospheric characteristics without increasing the complexity of the system, as for an all reflective or hybrid solution.

The evolving atmosphere is emulated by some rotating transmitting plates, called Phase Screens (PS). The Optical Path Difference (OPD) of the PS substrate is modified locally in order to produce a phase shift in an electromagnetic wave passing through it. The distribution of the phase shift shall follow a typical distribution given by a Von-Kármán spectrum with a finite outer scale. The PSs are positioned along the optical axis in order to emulate the turbulence at different altitudes with the desired spatial and temporal behaviour.

The concept of MAPS is shown in Fig. 1. The Natural Guide Stars (NGS) are emulated by visible-IR light transmitting fibres. Their positions are changeable to create the desired star configuration. A first group of lenses collimates the light beams from the NGSs and allows the telescope pupil to be created. Different PSs are located in the collimated beams to emulate the atmospheric layers at different altitude. One phase screen is located in the telescope pupil to emulate the ground layer. The PSs have different turbulence power according to the expected vertical C_n^2 distribution. The evolving atmosphere is emulated by rotating the PSs at different speeds according to the wind speed vertical profile. The position of the high altitude PS can be slightly varied in order to modify the atmospheric anisoplanetism and the speeds can be adjusted to reproduce a wide range of atmospheric correlation times. Moreover the PSs are interchangeable in order to emulate a selected range of seeing conditions.

* jkolb@eso.org, phone +49.89.32006331; fax +49.89.3202362; <http://www.eso.org>

A second group of lenses re-images the artificial NGSs whose wavefront quality is degraded by the PSs. The distorted wavefronts are then injected into MAD for MCAO correction and performance evaluation.

Particular care has to be taken when selecting the location of the beam footprints on the different PSs. Because of the rotation, each footprint will experience a differential speed at the edges located along the PS radius. In order to keep this effect as small possible, large PSs have to be considered as well as smaller footprint dimensions. Both conditions are difficult to achieve: large PSs are difficult to manufacture and small footprints require the PSs to be very close to each other, and small pixels size. A reasonable trade-off in the selection of these reduces the differential speed disturbance. The goal achieved is to keep the differential speed smaller than $\pm 50\%$, which is the average variation of the wind speed inside an 8 meter VLT pupil at Paranal.

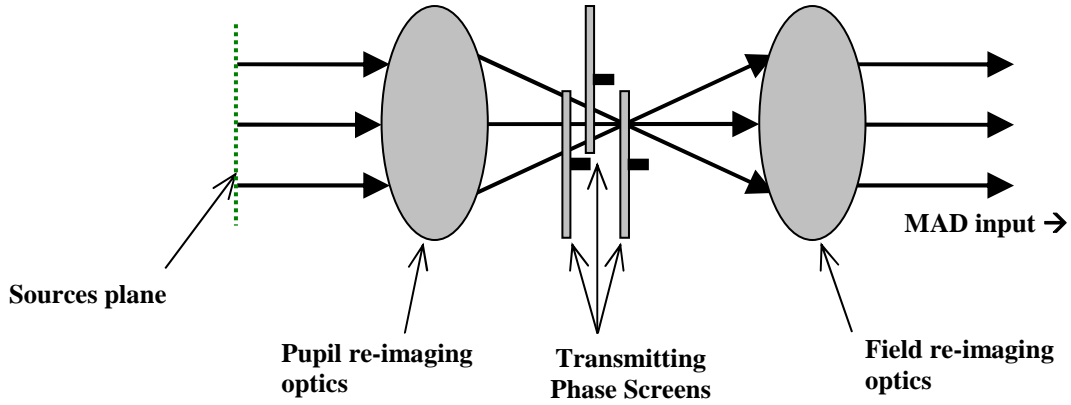


Fig. 1. MAPS concept. The NGS are simulated by optical fibres. A 1:1 imaging system provides to re-image the NGS at the MAD input F/15 focus. The Phase Screens are placed at different altitudes to emulate the turbulent atmospheric layers.

2. OPTICAL DESIGN

The optics of MAPS is constituted of two different groups of lenses (the optical design is shown in Fig. 2):

- The first group provides to collimate the beams from the artificial NGSs placed in a curve field (183 mm radius of curvature), and to create the telescope pupil;
- The second group focuses the disturbed wavefronts of the artificial NGSs on a 2 arcmin focal plane with the VLT F/15 Nasmyth focus characteristics, including the field curvature.

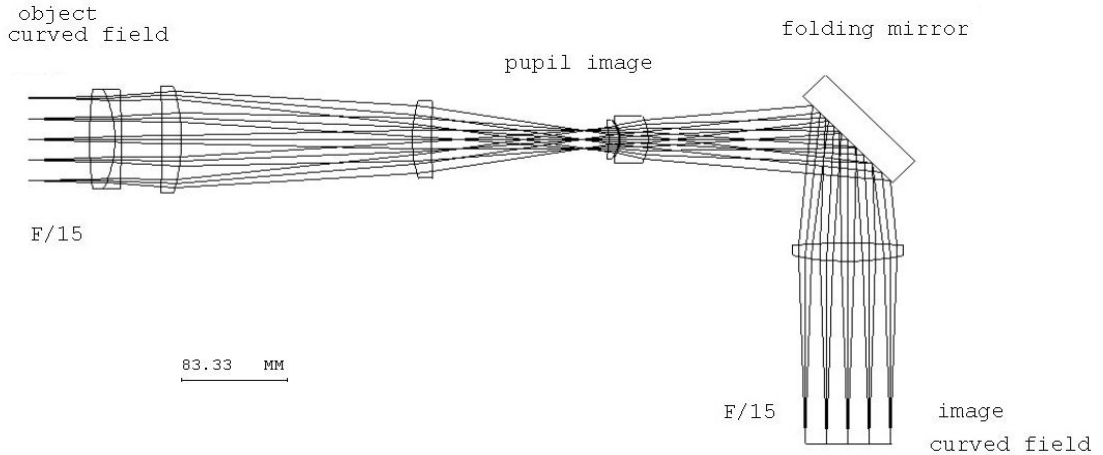


Fig. 2. Optical concept for the MAPS telescope and turbulence simulator. The size of the pupil is 15mm in diameter.

The two groups of optics are manufactured and delivered already mounted in two separate tubes that will then be fixed to the MAPS optical table. As MAPS shall transfer efficiently from 0.5 to 2.5 μm , the choice of the glasses and coatings was done in order to guarantee high transmission up to IR wavelengths.

The purpose of the flat mirror placed in between the second group of lenses is to fold the beam in order to make the turbulence simulator more compact, and to ease its fixation to the MAD bench by reducing the flexure constraints.

The Fig. 3 shows the Strehl Ratio performance of MAPS optics up to 1 arcmin from the FoV centre in the spectral range 0.5-2.5 μm , without PSs. A special care was taken when selecting the optics in order to give preference to an excellent and uniform wavefront quality in the IR range (1 to 2.5 μm) to the prejudice of a good quality in the visible. The Strehl Ratio (SR) in this range is still larger than 55% over the whole FoV, whereas the SR in the IR is fairly constant and never worse than 95%.

In the PS space, 1 mm along the optical axis corresponds to $\sim 280\text{m}$ in the atmosphere. The two optical blocks have been tested and are well in the specifications.

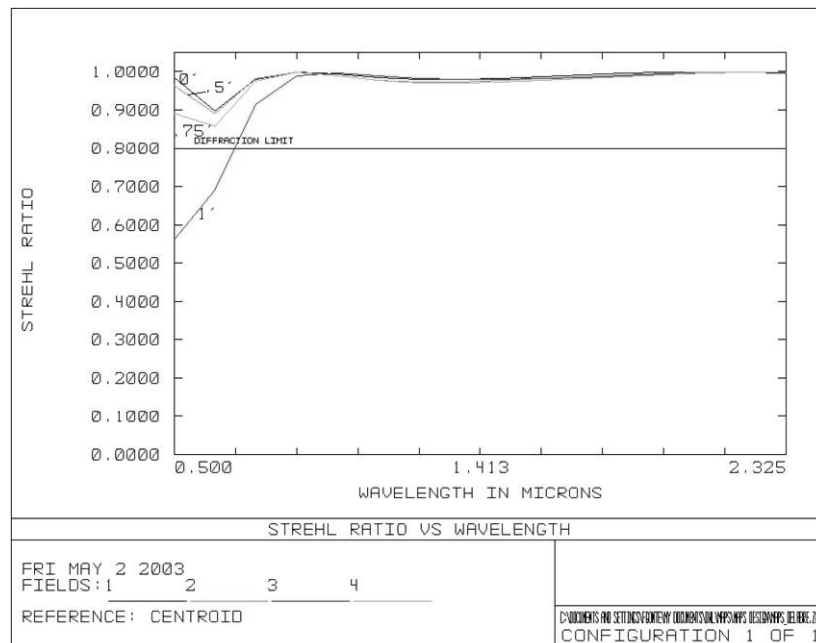


Fig. 3 Strehl Ratio across the FoV of MAPS at different wavelengths (from 500 to 2300 nm).

3. ARTIFICIAL NATURAL GUIDE STARS

MAPS shall simulate up to 12 NGSs for correction and performance evaluation with MAD. The NGS are simulated using single-mode fibres, 9 μm core, transmitting from 0.5 to 2.5 μm . The size of the core is dimensioned to reproduce diffraction limited images of NGSs down to 0.6 μm . The light source is a halogen-tungsten lamp of 150 Watts.

The fibres are distributed in four bunches: one of 12 fibres and three of 8 fibres, so a total of 36 fibres. While the 12 fibres bunch face directly the source, neutral density gelatine filters are placed in front of the 8 fibres bunches in order to dim the light entering. The filters are chosen so that they let respectively 40, 16 and 6.4 % of the light pass through, leading to an attenuation of respectively 1, 2 and 3 magnitudes. Thus MAPS permits to simulate 4 different star magnitudes at the same time (with a maximum of 12 fibres for the brighter magnitude and 8 fibres for the other ones), the magnitude of the brightest star being determined by the dimmer of the source.

The position of the simulated NGS in the field is defined by plugging the fibres on a mask placed in the entrance focal plane of MAPS. The accuracy of positioning of the NGS will be ensured by the use of standard SMA connector for the fibres end, and their female counterpart on the mask. Those connectors are disposed on concentric rings, and each ring is adjusted in depth in order to simulate the telescope field curvature.

The mask is a metallic plate in which are mounted female SMA connectors; the size of those connectors doesn't allow placing two NGS at a closer distance than 18.5 arcsec. The choice of those standards, easy to plug and unplug connectors allows also changing quickly the configuration of the simulated asterism.

In order to simulate NGS asterisms two different solutions are adopted:

- **Flexible configuration:** a grid of 34 pre-defined star positions has been design for a best coverage of the whole FoV (Fig. 4). This grid will be used to check MAD performances in a first time, and compare them to the results of simulations.
- **Real NGS targets:** once the target asterisms to be observed on the sky identified [12], special masks will be manufactured according to the desired geometrical configuration, in order to test the system on real star asterism, and to compare later the performance with on-sky measurements.

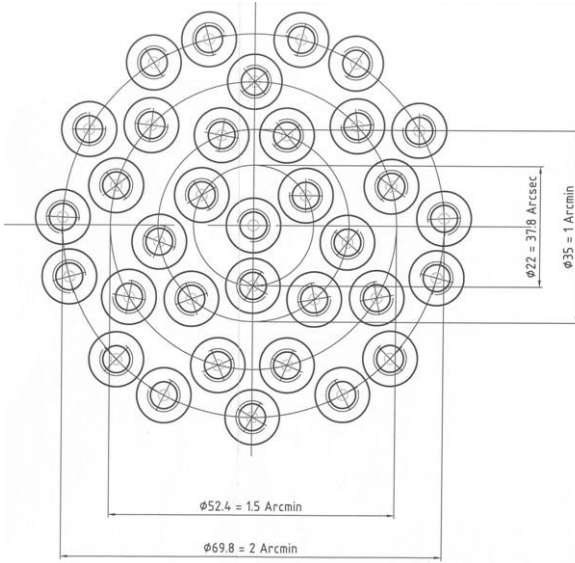


Fig. 4. MAPS entrance plane. Grid of pre-defined positions for plugging the fibers simulating the stars, as designed (left) and during its integration phase (right)

4. PHASE SCREENS

4.1. General Assumptions

MAPS is required to have a set of four phase screens, only 3 of which will be used at any time to simulate two different seeing conditions. The PSs are optical elements capable to transmit the light. They are circular plates (100mm diameter) with a hole at the centre (for fixation of the rotation axis). The PS has encoded on the surface a bi-dimensional aberration with spatial distribution typical of the atmospheric turbulence.

A plane wavefront passing through the PS emerges distorted accordingly to the aberrations encoded on the PS. The aberration is encoded on an annular ring centred on the PS centre, so that the wavefront shift seen through a 15mm pupil centred on the annulus is evolving when the PS is set on rotation. The speed at which this PS is set in rotation gives the value of the wind speed simulated for this altitude.

The mechanical dimensions of a PS are shown in Fig. 5.

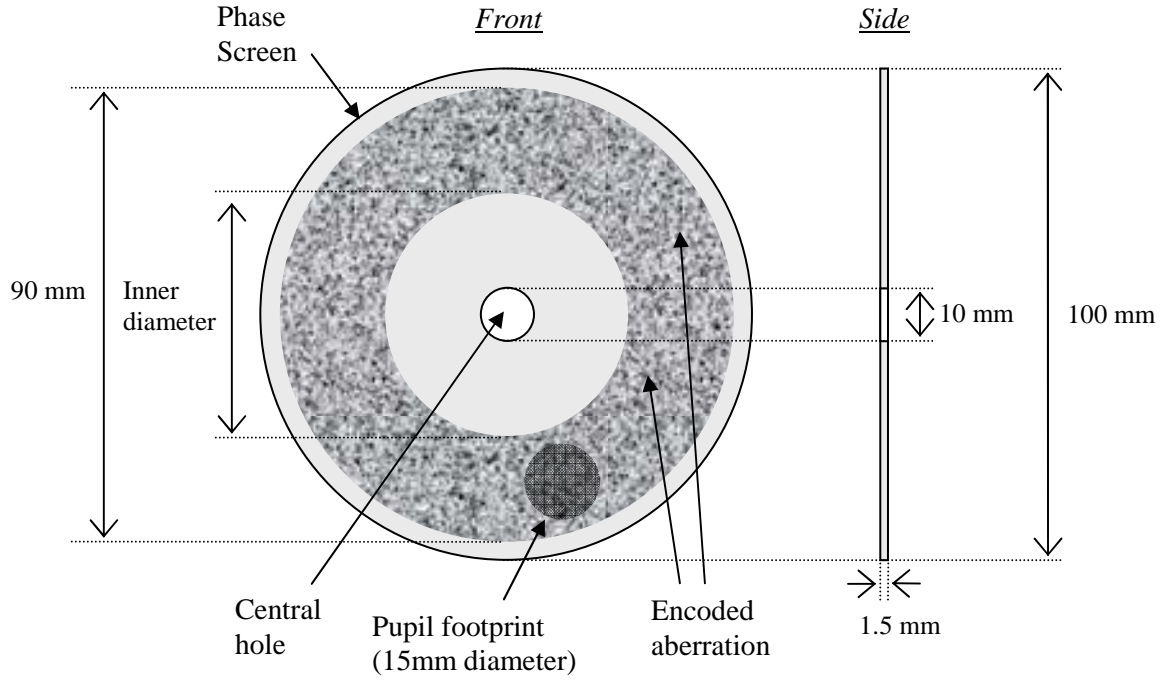


Fig. 5. Dimensions of a Phase Screen. The inner diameter varies depending on the altitude at which the PS is intended to be used.

4.2. Phase maps

The phase screen turbulence data are produced using the invert Fourier transform of a Von Kármán spectrum. Among numerous possible random maps were kept the ones that show the smallest Peak-To-Valley (PTV) phase over their surface, while keeping the global atmospheric properties and particularly the phase variance in the pupil. This property helps for the realization of the PS as a high PTV is always hard to achieve. The size of the phase maps is 900×900 pixels², leading to pixels of 100 microns in the case of a ring of aberration of 90mm in diameter.

A finite outer scale of 22 m is considered [14], and the properties of the atmospheric layers we wish to simulate are summarized in the Table 1. PS-01 to PS-04 label four different phase screens, which combination allows reproducing the aberrations induced by the sky of Paranal in two different conditions. The resulting turbulence parameters at the level of the telescope are shown in the Table 2.

	Median @ ZD=30°				Good @ Zenith		
	Altitude	r_0 (0.5 μ m)	Wind Speed		Altitude	r_0 (0.5 μ m)	Wind Speed
PS-01	0.0 ± 0.2 km	20 ± 1 cm	7 ± 3 m/s	PS-02	0.0 ± 0.2 km	30 ± 2 cm	7 ± 3 m/s
PS-02	6.0 ± 0.2 km	30 ± 1 cm	13 ± 6 m/s	PS-03	6.0 ± 0.2 km	50 ± 2 cm	13 ± 6 m/s
PS-03	8.5 ± 0.2 km	50 ± 1 cm	30 ± 15 m/s	PS-04	8.5 ± 0.2 km	80 ± 2 cm	30 ± 15 m/s

Table 1. Atmospheric parameters for the MAPS phase screens

Parameter (0.5 μ m)	Median	Good
r_0 (cm)	14.4 ± 0.6	22.4 ± 1.2
Seeing (")	0.73 ± 0.03	0.46 ± 0.03
τ_0 (ms)	3.4 ± 0.2	5.5 ± 0.3
θ_0 (arcsec)	2.2 ± 0.1	3.6 ± 0.1

Table 2. Global atmospheric parameters resulting from the use of the Phase Screens defined in the Table 1.

Four phase maps in agreement with those requirements have been found (Fig. 6). Several simulation were performed using those phase maps, such as decomposition on the Zernike polynomials [15], PSF computation, measurement of the variance over one rotation, in order to simulate the aberrations that they will create. Those tests have been carried out for individual PS as well as for theoretical combination of the three PS.

The seeing created by the two different combinations of PSs is given by the FWHM of the integrated PSF at 500 nm wavelength, as shown in Fig. 7. The variance of the projection of the distorted wavefronts on the Zernike polynomials can be compared with the theoretical spectrum given for this r_0 and L_0 . We found a good agreement with the two seeings specified, as well as with the spectra.

Simulated PSFs (in the visible and in K band, static and integrated) are shown in Fig. 9. It is interesting to notice the size of the speckles in both cases, much larger in the IR. The residual speckle pattern in the integrated images comes from the fact that the simulations were done at one single wavelength. As foreseen, the size of the integrated IR PSF is smaller than the visible one.

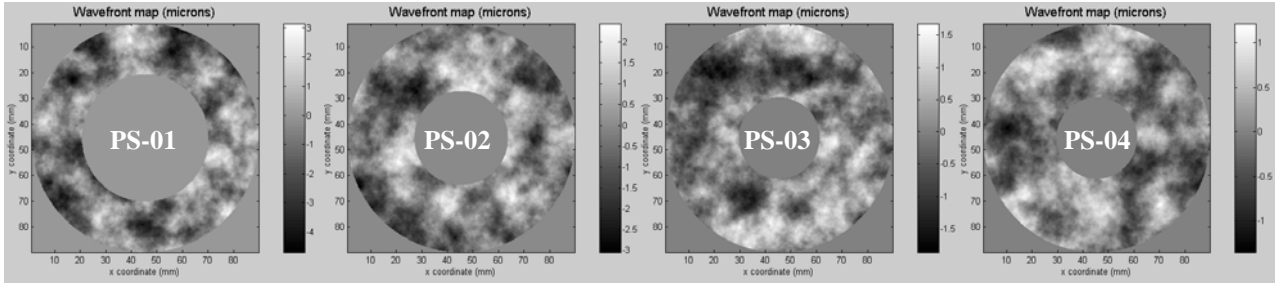


Fig. 6. Phase maps to be imprinted on the 4 phase screens. The width of the imprinted annulus differs, as the footprint of the 2 arcmin meta-pupil increases with the altitude to which the PS is conjugated.

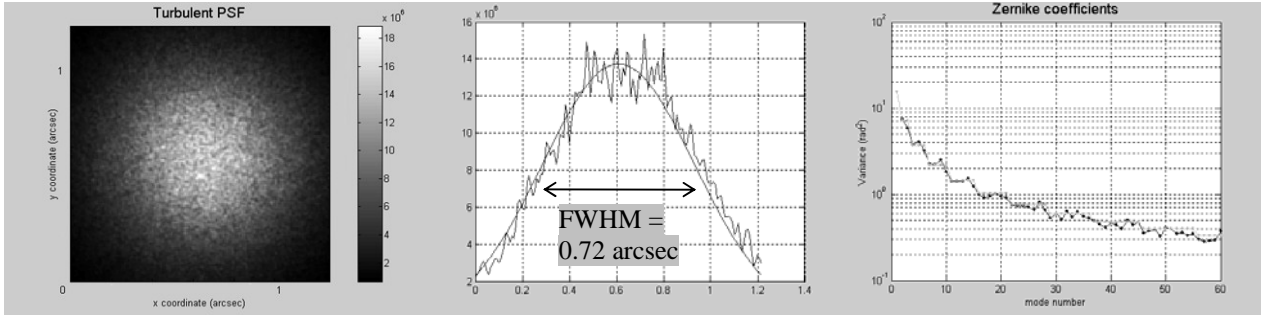


Fig. 7. Simulation result: integrated PSF, PSF profile and variance of the projection on the Zernike polynomials in the case of the combination PS-01/ 02 / 03 (median seeing condition)

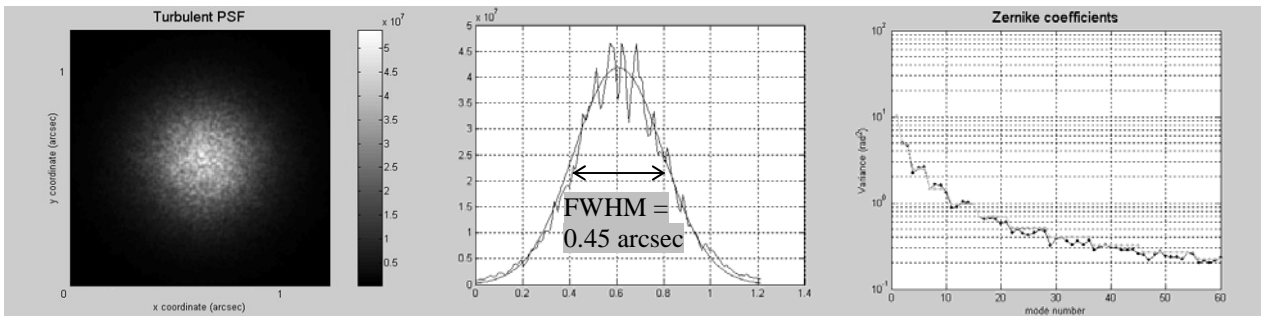


Fig. 8. Simulation result: integrated PSF, PSF profile and variance of the projection on the Zernike polynomials in the case of the combination PS-02/ 03 / 04 (good seeing condition)

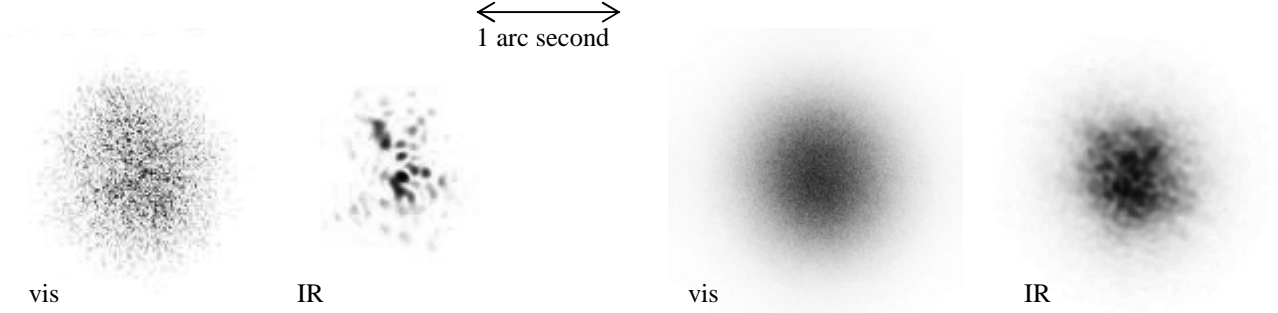


Fig. 9. Simulated visible and IR PSFs, static (left) and integrated over one rotation of the slowest PS (right), resulting from the use of the PS-01, PS-02 and PS-03 in MAPS

4.3. Manufacturing of the phase screens

The methods to produce transmitting PS are numerous [1, 5], and the first method envisaged for the PS of MAPS was an ion-exchange in glass substrate [2, 6]. But after a long process of research and of prototyping, ESO came to an agreement with the company SILIOS Technologies for the manufacturing of several sets of PS satisfying the specifications in terms of mechanical, optical properties and of quality of the aberrations produced. The technique proposed by this company is a wet etching on glass substrate, which description is given below.

SILIOS manufactures the PS in its clean room facilities. 100mm diameter substrates are compatible with off the shelf 4 inches silicon wafer equipments. The basic principle for encoding the 2^N levels of the phase map is to process N individual etching steps which either cumulate or not. The pattern of each individual etching step is defined by a photolithography process (photo-resist deposition, insulation, development). The N patterns are realigned with an accuracy of 0.5 micron (1/200 of a pixel width). The wet etching process is VLSI HF (Very Large Scale Integrated - Hydrogen Fluoride) based. A typical master mask pattern is presented in Fig. 10. 21 master masks were designed (6 for the PS-01, 5 for the PS-02, PS-03 and PS-04). The main issues in the fabrication of the PS are linked to the accuracy of each etching depth and to the uniformity inside the wafer. The technique proposed by SILIOS provides $\pm 0.7\%$ as etching depth accuracy (max etching depth is about 20 microns) and $\pm 0.45\%$ as uniformity inside the wafer.

A series of tests have been performed on a first realization of the PS-01 and they show a product quality within the specifications.

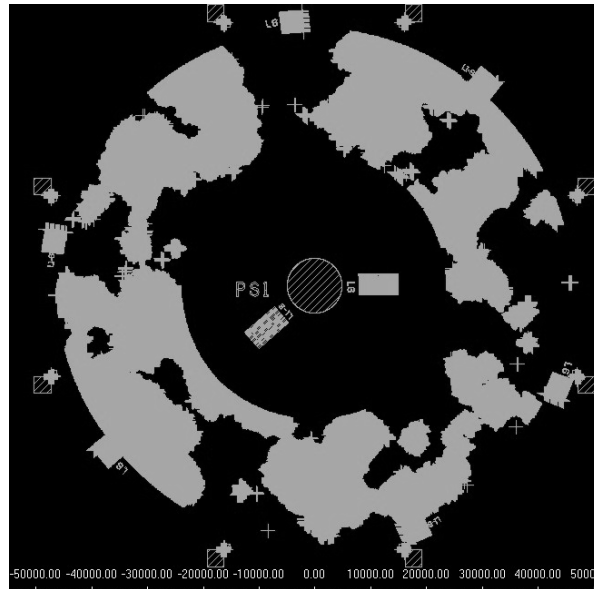


Fig. 10. First mask (out of 6) used to create the PS-01

5. MAPS MECHANICS

MAPS will be located in front of the MAD input and will be used only for laboratory testing. The source for the NGS is located under the bench, far from the MAPS box in order to minimize light contaminations both for MAPS and MAD.

As shown in Fig. 11, the two optical tubes from MAPS are attached to a common plate, itself put at the right height from the bench surface (MAD beam height = 230mm) thanks to some supporting legs standing on the optical table to be screwed on three points to the MAD bench. The fibres support, the optical tube #1 and the whole phase screens system is protected by a removable cover used as a baffle for parasite light. Some apertures are opened in this cover to let the cables and fibres pass through, and of course also the beam.

Due to the size of the motors to rotate the PS, it is not possible to place them directly aligned with the axis of the PS, because of conflicts with the optical tube #1 and with the beam. It was then compulsory to put the motors on the sides and to use a system of belts and ball bearings to fit all the components in the available space. Each PS block is thus constituted of the following parts:

- The motor and the reduction gear
- The belt transmitting the rotation to the PS axis
- The axis on which is fixed the PS. It is attached with a system that allows removing easily the PS plate itself and to exchange it with another, in order to switch between the two possible seeing configurations.

The rotations are possible thanks to ball bearings. All the components of a PS block are interdependent, and mounted on the same structure. This structure is movable along the optical axis for the high altitude PS in order to change the isoplanetic angle simulated, and also to facilitate the operation of exchanging the PSs. A system of elongated holes allows stretching the belt.

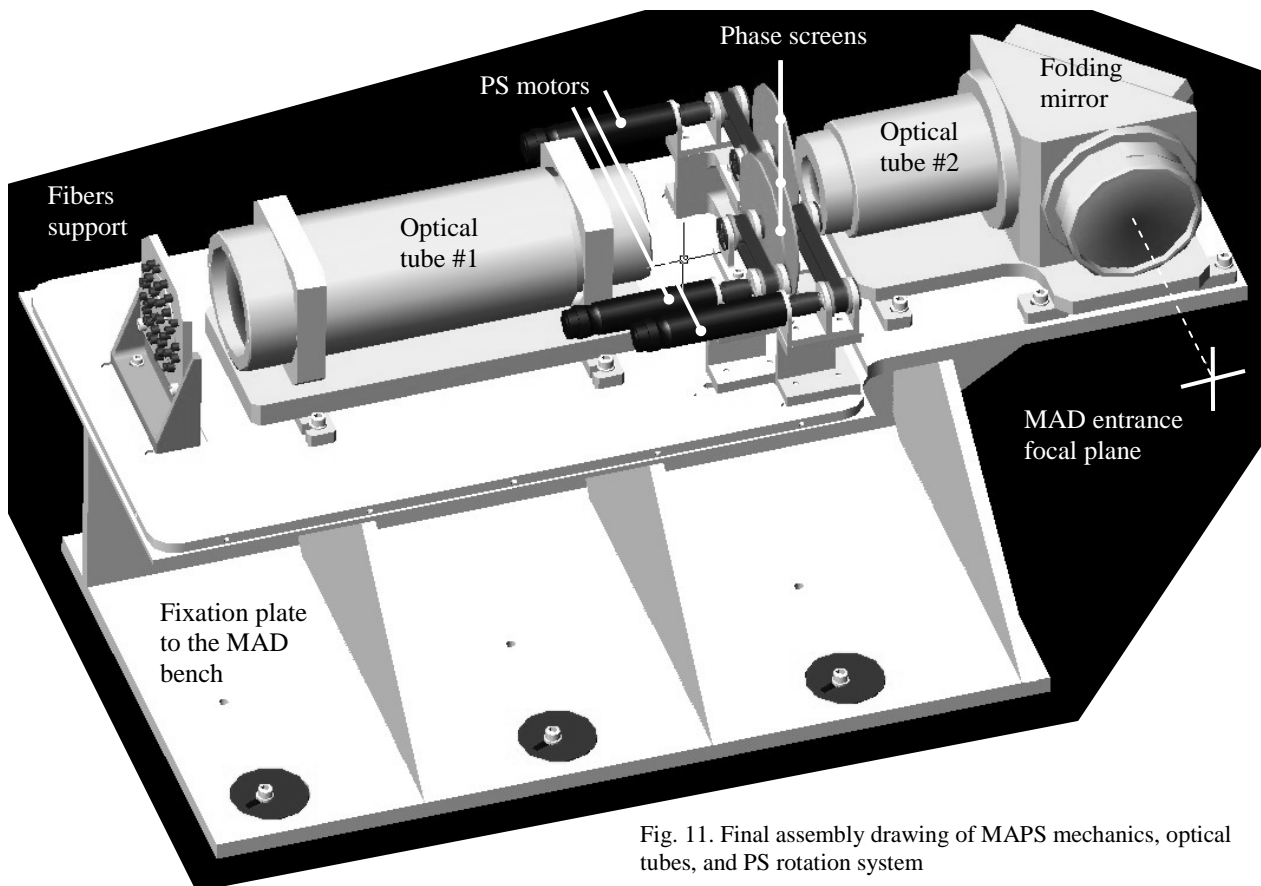


Fig. 11. Final assembly drawing of MAPS mechanics, optical tubes, and PS rotation system

The alignment of the two optical tubes one with respect to the other is done thanks to a guiding tool furnished by the supplier of the optics (Winlight Optics in France). Then the fibers support is placed at the entrance focal plane of the tube #1. The next step consists in finding the pupil position (after placing in the beam some dummy PSs to simulate the additional glass thickness), which is in the output focal plane of the tube #1. The PS rotation blocks being integrated and the PSs mounted in them, they have then to be placed in the beam at the right altitude (a vertical displacement of 200mm is acceptable), and well perpendicular to the beam. MAPS is at this point ready to produce turbulence.

When MAPS is placed at the entrance of MAD, their optical axes have to be aligned, as well as the position of the common focus, which corresponds to 5 degrees of freedom in total.

6. MOTORS CONTROL

The three Faulhaber motors rotating the PS are controlled independently by three boards allowing a great accuracy in the speed of the motion. The boards are housed in the MAPS control box, and the control of the speeds is ensured by three potentiometers (Fig. 12 left). The accuracy is again improved by the fact that we use a gear box 1:134 at the output of the motor so that it runs in its linear range although the speed of the PS themselves is quite slow, comprised between 2 and 30 rounds per minute. Also the motors we use are equipped with a feedback sensor of the effective rotation speed of rotation of the axis. Three rigid cables coming out of the back side of the control box (Fig. 12 right) allow placing the control at a distance of up to 1.5 meter from MAPS, and are relayed inside the covered area by more flexible cables connected to the motors.

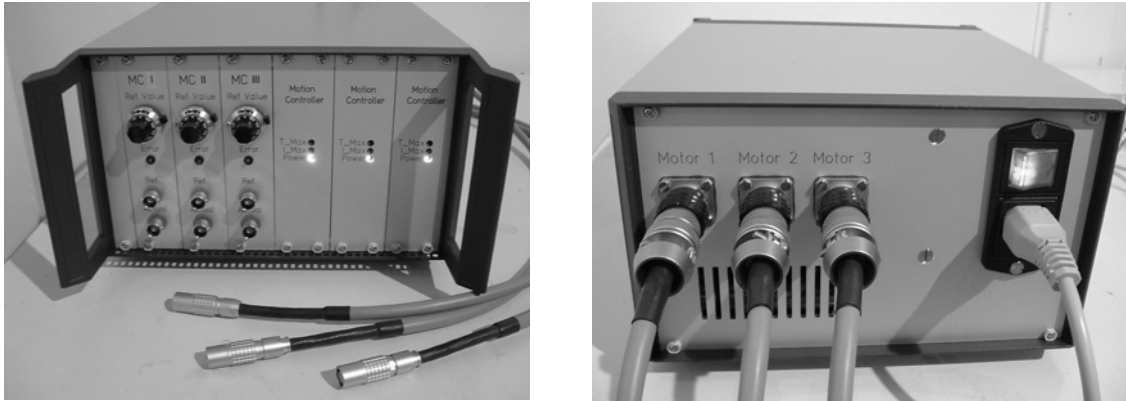


Fig. 12. Front and back side of the PS motors controller box

7. PROJECT STATUS

MAPS is the first full MCAO turbulence simulator ever built, allowing to feed an MCAO instrument as would do a telescope, in terms of wavelength range, FoV and NGS targets. It is compact, easily pluggable to MAD or any other instrument with similar input, as for example ESO's Active Phasing Experiment [8]. The motors and light source controls are totally independent from the instrument. The integration is eased by the fact that the optics blocks are pre-mounted. The turbulence produced is well characterized, reproducible and very similar to the one of the atmosphere, although the number of realizations is limited.

The turbulence simulator is currently integrated and optically aligned in the ESO laboratory (Fig. 13). Only prototype PSs are available for the moment. When the definite ones will be finalized, they will be integrated to the assembly, and the full MAPS system will be tested and the turbulence produced fully characterized.

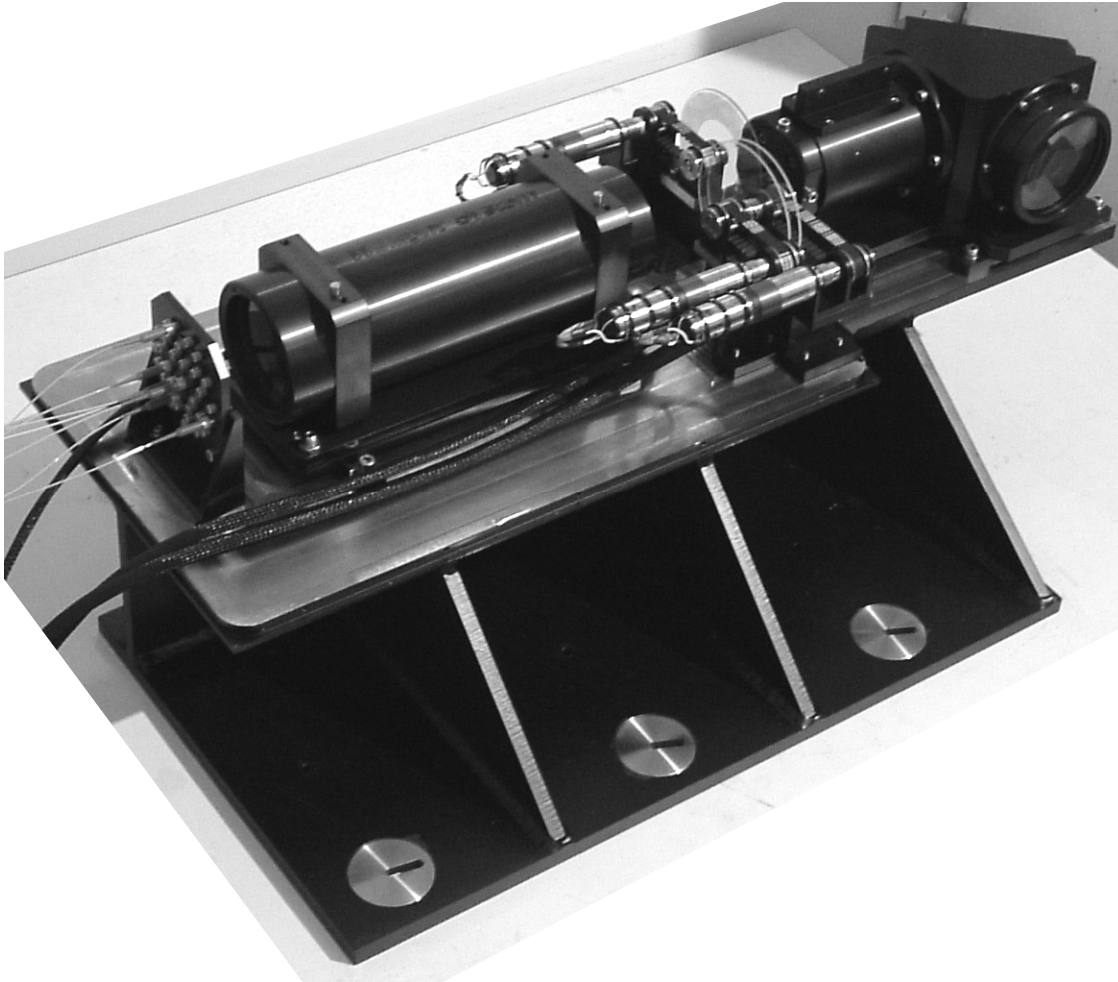


Fig. 13. The turbulence simulator MAPS after its integration and alignment phases

ACKNOWLEDGMENT

This work has been partially funded by the European Research and Training Network *Adaptive Optics for Extremely Large Telescopes* with Contract HPRN-CT-2000-00147.

REFERENCES

1. D. J. Butler, S. Hippler, S. Egner, W. Xu, J. Bähr "Broadband, Static Wave-Front Generation: Na-Ag Ion-Exchange Phase Screens and Telescope Emulation" *Applied Optics*, Vol. 43 Issue 14 Page 2813, May 2004
2. D. J. Butler, E. Marchetti, J. Bähr, Wenli Xu, S. Hippler, M. E. Kasper. R. Conan "Phase screens for astronomical multi-conjugate adaptive optics: application to MAPS" *SPIE* 4830, p. 623
3. R. Conan, "Modélisation des effets de l'échelle externe de cohérence spatiale du front d'onde pour l'observation à Haute Résolution Angulaire en Astronomie", Ph.D. thesis (Université de Nice-Sophia-Antipolis), 2000

4. C. C. Davis, Y. Zhang, M. L. Plett, P. Polak-Dingels, P. Barbier, D. W. Rush "Characterization of a liquid-filled turbulence simulator" in Artificial Turbulence for Imaging and Wave Propagation, Proc. SPIE Vol. 3432, p. 38-49, edited by John D. Gonglewski; Mikhail A. Vorontsov
5. S. M. Ebstein "Pseudo-random phase plates" in High-Resolution Wavefront Control: Methods, Devices, and Applications III edited by J. D. Gonglewski, M. A. Vorontsov, M. T. Gruneisen, S. R. Restaino, A. V. Kudryashov, vol. 4493 of Proc. SPIE, article number [4493-24]
6. S. Egner "Optical turbulence estimation and emulation" Diploma thesis 2003, University of Heidelberg
7. A. Fuchs, J. Vernin, M. Tallon "Laboratory simulation of a trubulent layer - Optical and in situ characterization" Appl. Opt., 35, 1751-1755 (1996)
8. F. Y. J. Gonté, N. Yaitskova, P. Dierickx, A. Courteville, S. Esposito, N. Devaney, K. Dohlen, M. Ferrari, L. Montoya, "APE: a breadboard to evaluate new phasing technologies for a future European giant optical telescope" Advancements in Adaptive Optics, SPIE Proceedings, 5489, article number [5489-144], 2004
9. N. Hubin, E. Marchetti, E. Fedrigo, R. Conan, R. Ragazzoni, E. Diolaiti, M. Tordi, G. Rousset, T. Fusco, P. Y. Madec, D. Butler, S. Hippler, S. Esposito "The ESO MCAO demonstrator MAD: a European collaboration", Proc. of the ESO Conference on 'Beyond Conventional Optics', May 7-10, Venice, 2001
10. G.D. Love, P. Clark, C.N. Dunlop, T.-Kelly, M.Langlois, R. Myers and R. Sharples 'Emulating Multiconjugate Turbulence', Proc. of the ESO Conference on 'Beyond Conventional Optics', May 7-10, Venice, 2001
11. E. Marchetti, R. Brast, B. Delabre, R. Donaldson, E. Fedrigo, F. Franza, N. Hubin, J. Kolb, M. Le Louarn, J. Lizon, S. Oberti, R. Reiss, J. Santos, R. Ragazzoni, C. Arcidiacono, A. Baruffolo, E. Diolaiti, J. Farinato, E. Vernet-Viard, "MAD status report", Advancements in Adaptive Optics, SPIE Proceedings, 5490, article number [5490-17], 2004
12. E. Marchetti, R. Falomo, D. Bello, N. Hubin "A search for star asterisms for natural guide star based MCAO correction in Beyond Conventional Adaptive Optics". Eds. Ragazzoni R., Hubin N. and Esposito S. 1.82 + AFOSC
13. E. Marchetti, N. Hubin, E. Fedrigo, J. Brynnel, B. Delabre, R. Donaldson, F. Franza, R. Conan, M. Le Louarn, C. Cavadore, A. Balestra, D. Baade, J. Lizon, R. Gilmozzi, G. J. Monnet, R. Ragazzoni, C. Arcidiacono, A. Baruffolo, E. Diolaiti, J. Farinato, E. Vernet-Viard, D. J. Butler, S. Hippler, and A. Amorin, "MAD the ESO multi-conjugate adaptive optics demonstrator" in Adaptive Optical System Technologies II. Edited by Wizinowich, Peter L.; Bonaccini, Domenico, vol. 4839 of Proc. SPIE, pp. 317-328, Feb. 2003.
14. F. Martin, R. Conan, A. Tokovinin, A. Ziad, H. Trinquet, J. Borgnino, A. Agabi, M. Sarazin "Optical parameters relevant for High Angular Resolution at Paranal from GSM instrument and surface layer contribution", Astron. Astrophys. Suppl. Ser. 144, 39-44, May 2000
15. R. J. Noll "Zernike polynomials and atmospheric turbulence" JOSA, 66:207 (1976)
16. <http://www.eso.org/projects/aot/mad/>

8.3. SPIE paper “Calibration of the static aberrations in an MCAO system”

This paper [51] has been presented at the SPIE symposium “Advancement in Adaptive optics” that was held in Glasgow (Scotland) from June 21st to 25th 2004 as a poster.

It describes the idea of correction of the field-dependant aberrations by the use of tomography and gives the status of the simulations performed as of June '05.

Updated information on the theory as well as all the work performed on the same topic after publication of this paper are detailed in the section 4.

8. APPENDICES

Calibration of the static aberrations in an MCAO system

Johann Kolb^{*a}, Enrico Marchetti^a, Gérard Rousset^b, Thierry Fusco^b

^a European Southern Observatory, Karl-Schwarzschild-Str. 2, 85748 Garching, Germany;

^b ONERA – DOTA, BP 72 - 29, av. de la Division Leclerc, 92322 Châtillon Cedex, France

ABSTRACT

The ESO Multi-conjugate Adaptive optics Demonstrator (MAD) is a prototype intended to be tested at the VLT Nasmyth focus. With its development raises the problem of calibration of an AO system composed of several correcting devices and wave front sensors. One part of this process is the calibration of the static aberrations of the system, always present in spite of the best efforts made during the design, the manufacturing of the optics and their alignment.

In this paper we present a study to find an optimized way to correct for the static aberrations in the scientific FoV of an MCAO system. Thanks to images from the camera, the WF error in the FoV is computed, the contribution of several altitudes reconstructed, and finally projected on the deformable mirrors in order to compensate for the measured aberrations. This technique, inspired from the calibration of the static aberration of the system NAOS-CONICA, allows bringing the best quality to the scientific instrument fed by an MCAO system, by taking the most of the presence of correcting devices in the optical path.

Key words: Calibration, MCAO, VLT, Phase diversity

1. INTRODUCTION

Since the first developments of adaptive optics, it was clear that trying to get the best beam quality at the level of the Wave Front Sensor (WFS) didn't mean getting the best image at the scientific focus. Indeed the beam doesn't cross the same optics before reaching those two points, and is deformed by the non-common path aberrations, ones that lay in the camera path after the dichroic of the system. The residual is generally not important, but enough to decrease the quality of the images of some percents of Strehl Ratio (SR). That's why the engineers building the instruments have tried to take advantage of the deformable device in the optical path to compensate for those aberrations. This was done by using an empiric method: checking "by eye" the quality of the PSFs at the scientific focus and guessing which modes to apply to the Deformable Mirror (DM) to increase the SR. This was somehow efficient to roughly correct for the low order aberrations.

In the case of the system NAOS-CONICA for the VLT [13], a high SR was required, thus a more accurate technique was set up in order to retrieve the aberrations present at the focus of the IR camera CONICA and to correct them, and this for each combination of dichroics, optics and filter possible. The idea is to use the camera as WFS (thus measuring the aberrations) and to apply static voltages to the DM that minimize the residual aberrations according to a given criterion (not in real time like an AO close loop does). Retrieving the WF from a sole focused image is not possible without indetermination, but for two images separated by a well-known amount of phase variation, a unique solution can be found, thanks to Phase Diversity (ΦD) [11]. This low-cost procedure has the drawback that it requires a complex numerical and iterative processing to restore the unknowns from the images. The easiest aberration to introduce in an optical system is defocus, by shifting the detector for instance. From the focused and defocused images and the parameters of the system (pixel scales of the camera, F ratio, central obstruction...), the ΦD software developed at ONERA [6] retrieves the aberrations present in the optical path from the calibration source to the camera detector.

This procedure has been successfully applied to NACO, achieving great performances in terms of SR on the camera [2, 3, 9]. The conclusions of this work are positive and underline the fact that for future instruments, the implementation of the technique of ΦD should be thought from a very early phase in the design.

* jkolb@eso.org, phone +49.89.32006331; fax +49.89.3202362; <http://www.eso.org>

2. THE MCAO CASE

An upgrade to the procedure used on NACO could have been to record the aberrations in the field of the system and apply a reference shape to the DM that gives a uniform quality in the FoV, instead of an optimized quality at the center. But for this AO system in operation with only one DM in the pupil, the main cause of degradation of the quality in the FoV is anisoplanatism [4], so it is worthless making this effort.

On the contrary, for a Multi-Conjugate Adaptive Optics (MCAO) system which aim is to provide the best uniform performance in the whole FoV, things have to be thought differently. The goal of MCAO is to perform a real-time correction of the aberrations introduced by the atmosphere in a larger FoV than what a normal AO system does. This is possible thanks to the use of several WFS aligned with different Guide Stars (GS) in the FoV and of several correcting devices conjugated with different altitudes of the atmosphere. The difficulty is increased by the large FoV and the complexity of the system, but the presence of several DMs help correcting more efficiently the aberrations in the field.

We can here also consider the camera as WFS that allows taking several WF measurements in the FoV. The optics creating the aberrations can be assimilated as atmospheric layers placed at different altitudes. In order to correct for this, it is then logic to apply a tomographic approach inspired by the atmospheric tomography approach for MCAO real-time correction [5].

The chronologic order of actions required to implement this tomographic correction of the static aberrations is the following:

- Record focused and defocused images at several positions in the FoV. The defocus is obtained either by shifting a focal plane or by displacing a collimator.
- Pre-process the images so that they are suited for the ΦD analysis.
- Run the ΦD algorithm with the images in order to get the estimations of the aberrations.
- Transform the aberrations vectors measured in the N_{GS} directions into the WF at the N_l layers having different altitudes that give the best estimation according to a given criterion.
- Project those vectors on the DMs and apply the correction.

In this paper we focus on the fourth point. We start from simulated images of the PSF at the scientific focus of the MCAO system, we shown briefly how the ΦD algorithm analyses them and gives the resulting aberrations projected on the Zernike polynomial. The following step consists in presenting the algorithm that we developed and that reconstructs the aberrations at the level of the aberrant optics, and projects them on the N_{DM} correcting devices. The simulated performances of this correction are finally presented and discussed.

The tomographic approach for correction of the static aberrations will be tested and implemented on the ESO MCAO Demonstrator [10] coupled with CAMCAO (CAmera for MCAO [1]) when it will be time to finalize its calibration.

3. IMPLEMENTATION OF THE PHASE DIVERSITY

From two images (at least Nyquist-sampled) separated by a well-known amount of phase variation and using a Generalized Maximum Likelihood (GML) approach, the ΦD algorithm minimizes a criterion given by a probability law, after an iterative process. In practice, the result is a list of Zernike coefficients that estimate the best the WF responsible for the measured PSFs.

To test the algorithm, we have submitted it to on-axis simulated images of a WF distorted by a known quantity of aberrations. The list of the input coefficients and of the result of the phase estimation is given in Table 1, for the case of images containing no noise. On this example the ΦD algorithm manages to estimate successfully the aberrations between 4 and 15 with a total error of 6nm rms, over a total WF of about 100nm rms.

The case of noisy images is not studied in this paper, but we can say that the accuracy of the estimation depends on the properties of the images recorded, as the size of the array used and the pixel scale. To this will be added the practical uncertainties on the process of recording of the images: defocusing distance, pixel scale error, pupil shape ...

Zernike number	4	5	6	7	8	9	10	11	12	13	14	15
Input (nm)	60.5	-39.3	58.1	-16.2	-14.1	-2.5	13.7	-24.3	0.5	-3.2	2.8	-2.4
Estimated (nm)	61.2	-39.0	58.7	-16.2	-14.0	-2.5	13.5	-23.0	0.8	-2.8	8.5	-2.4

Table 1. List of coefficients used to simulate the input images for the ΦD algorithm and result of the phase estimation

4. TOMOGRAPHY ALGORITHM TO CORRECT FOR STATIC ABERRATIONS

4.1. Theoretical background

Let us suppose that the aberrations are produced in a discrete number of layers N_t . The expression of the phase measured in the N_{GS} directions is:

$$\Phi_{N_{GS}} = M_{N_{GS}}^{N_t} \varphi + n \quad (1)$$

where φ is the vector of the aberrations in the N_t layers, and n the noise on the measurement. The matrix $M_{\alpha}^{N_t}$ sums the contributions of the wavefronts in N_t altitudes, in the telescope pupil and for a given direction α ; $M_{N_{GS}}^{N_t}$ is the concatenation of the matrices $M_{\alpha}^{N_t}$ for all the directions of interest.

The estimation $\hat{\varphi}$ of φ we seek has the shape:

$$\hat{\varphi} = W \times \Phi_{N_{GS}} \quad (2)$$

where the unknowns are the elements of the reconstruction matrix W .

The criterion to be minimized is the residual phase variance in a FoV of interest $\{\alpha\}_{fov}$:

$$\varepsilon = \left\langle \int_{\{\alpha\}_{fov}} \|M_{\alpha}^{N_{DM}} \hat{\varphi} - M_{\alpha}^{N_t} \varphi\|^2 d\alpha \right\rangle_{\varphi, noise} \quad (3)$$

where $M_{\alpha}^{N_{DM}}$ is defined as $M_{\alpha}^{N_t}$ but for the N_{DM} altitudes.

The minimization of this equation gives [8]:

$$W = P_{N_{DM}, N_t} \times W_{MA} \quad (4)$$

with

$$P_{N_{DM}, N_t} = \left(\int_{\{\alpha\}_{fov}} (M_{\alpha}^{N_{DM}})^T (M_{\alpha}^{N_{DM}}) d\alpha \right)^+ \left(\int_{\{\alpha\}_{fov}} (M_{\alpha}^{N_{DM}})^T (M_{\alpha}^{N_t}) d\alpha \right) \quad (5)$$

and

$$W_{MA} = C_{\varphi} (M_{N_{GS}}^{N_t})^T (M_{N_{GS}}^{N_t} C_{\varphi} (M_{N_{GS}}^{N_t})^T + C_n)^{-1} \quad (6)$$

where C_{φ} and C_n are respectively the aberrations and noise covariance matrices. It is interesting to notice that C_{φ} is computed from statistics on the aberrations in optical systems, and not from the prior knowledge of the atmospheric turbulence like in the classical case. The matrix $M_{N_{GS}}^{N_{DM}}$ is defined the same way as $M_{N_{GS}}^{N_t}$ but for the N_{DM} altitudes of the DMs instead of the N_t altitudes of the layers. $^+$ denotes a generalized inverse.

In the case where the number of layers containing the aberrations N_t is the same as the number of DMs N_{DM} , the projector is equal to identity and then W_{MA} is the reconstruction matrix. In the realistic case where there are $N_t > N_{DM}$ equivalent layers, W_{MA} reconstructs the WF on the N_t layers and the multiplication by the projector P_{N_{DM}, N_t} gives the reconstruction matrix on N_{DM} layers.

From the matrix W , one can then compute $\hat{\varphi}$ as in the equation (2). This gives the estimated correction phase on each DM that ensures a minimal residual phase variance for all the directions of the specified FoV $\{\alpha\}_{fov}$.

In addition to the directions of the GS, we can evaluate the quality of the correction in more directions in the field. The residual seen in those N_a directions of analysis is then:

$$R_a = \Phi_{N_a} - M_{N_a}^{N_{DM}} \hat{\varphi} = \Phi_{N_a} - M_{N_a}^{N_{DM}} W \Phi_{N_{GS}} \quad (7)$$

where $M_{N_a}^{N_{DM}}$ is defined the same way as $M_{N_{GS}}^{N_{DM}}$, but enlarged to the N_a directions of analysis.

R_a is the residual WF seen in the N_a directions of analysis (its calculation requires the knowledge of the aberrations in those directions). From it we can derive the SR (as in the section 6) or the decomposition into Zernike coefficients of the residual.

In this paper we will limit ourselves to the evaluation of the performances in the direction of the GS:

$$R_{GS} = \Phi_{N_{GS}} - M_{N_{GS}}^{N_{DM}} \hat{\varphi} = (1 - M_{N_{GS}}^{N_{DM}} W) \Phi_{N_{GS}} \quad (8)$$

4.2. Practical implementation

The output of the ΦD software is a list of Zernike coefficients, typically from 4 (focus) to 15 for our application. At ESO we have developed a routine in Matlab that computes the reconstruction matrix W .

The first step is to calculate the meta-matrix $M_{N_{GS}}^{N_t}$, which depends only on the position of the calibration stars in the FoV and on the position of the N_t equivalent layers. It has to be calculated only one for a given set of those parameters. The role of this matrix is to sample the Zernike polynomials in the meta-pupils at the N_t altitudes into Zernike polynomials in pupils of the appropriate size. It has been shown [12] that the number of polynomials required for such decomposition is smaller or equal to the number of polynomials used to define the meta-pupil. The analytical expression of the decomposition is demonstrated in [7]. However for the present simulations we use a numerical projection, accurate enough for our need and that shows the same behavior as the theory demonstrated (Fig. 1). We see that from a polynomial of order N over the meta-pupil, it is possible to select any pupil and describe it thanks to a number of polynomials $\leq N$. The whole procedure is repeated for the calculation of $M_{N_{GS}}^{N_{DM}}$.

The second step of the routine is to calculate the reconstruction matrix W described in the equation (4) thanks to the knowledge of the matrices $M_{N_{GS}}^{N_t}$, $M_{N_{GS}}^{N_{DM}}$ and to some priors on the measurements which are included in the aberrations covariance matrix C_ϕ and in the noise covariance matrix C_n . W is determined for a set of positions, altitudes and measurement conditions. Finally by multiplying W to a vector of measurements we get immediately the optimal shape to give to the DMs.

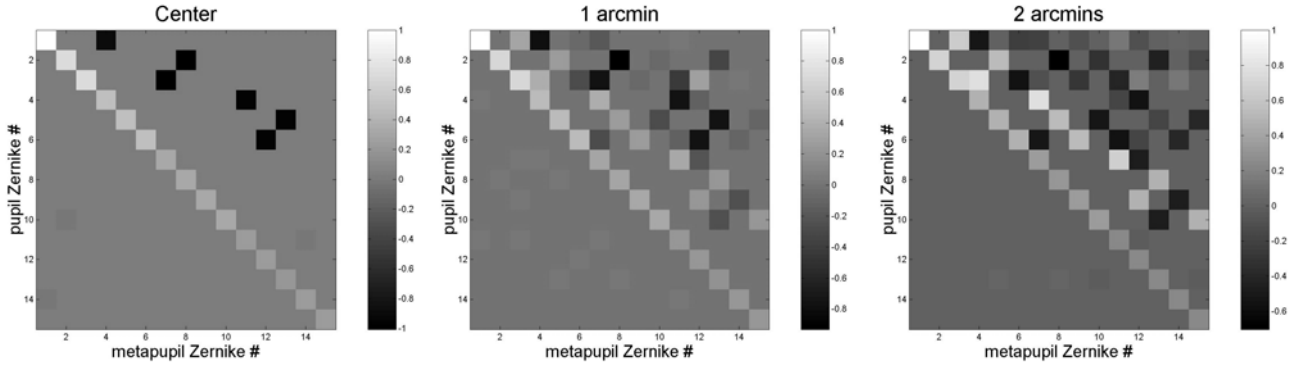


Fig. 1. Result of the projection of Zernike polynomials in a meta-pupil at 6 km altitude in a pupil, placed at the centered of the FoV (left), at 1 arcmin (middle) and 2 arcmins from the center of the FoV (right). The Zernike polynomial of order X in the meta-pupil can always be described by the polynomials of order $\leq X$ in the pupil.

5. FRAMEWORK OF THE SIMULATIONS

For the following simulations, we take the example of the MAD instrument to experiment the tomography algorithm. The optical scheme is shown in Fig. 2, as well as the projected altitudes of the optical element bringing aberrations. We are interested only in the common and IR camera paths for this study. It is interesting to notice that for a perfect system (particularly with the possibility to flatten perfectly the DMs in open loop), the presence of the WFS path is not even required to perform the calibration of static aberrations by ΦD .

When the derotator is active, its optics is rotating in the FoV, thus it is not possible to calibrate it. However the optics is conjugated with high altitudes (small footprints), and are constituted only of flat mirrors, so shouldn't introduce much aberration. All the ΦD images should be recorded on the axis of the IR camera, to disentangle the field-dependant aberrations of the camera from the ones of MAD. The calibration of the aberrations in the field of the camera should be done for the achievement of extreme performances only, but in principle the ΦD approach is able to take care of it too.

The optical elements mainly responsible for the degradation of the beam quality in the IR path are:

- the two collimators situated at equivalent altitudes of 16.2 Km
- the two folding mirrors at 13 and 14 Km
- the IR/visible Dichroic at 7.5 Km
- the residual non-flatness of the two DMs at 0 and 8.5 Km

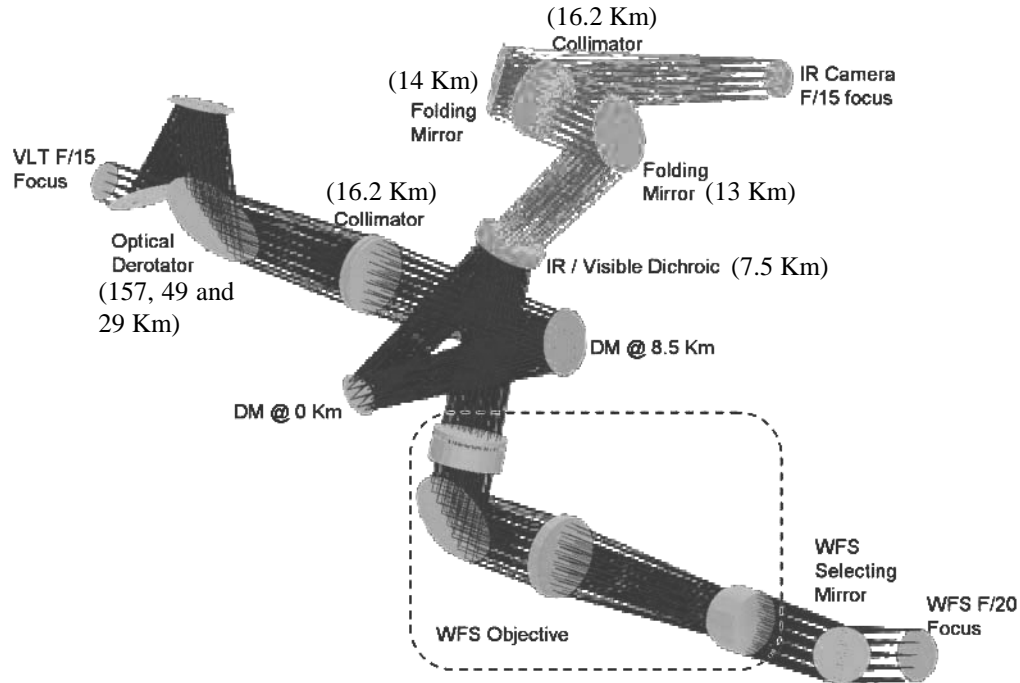


Fig. 2. MAD optical layout and equivalent altitudes of the optics. The optics in the IR camera (not represented) is conjugated with altitudes of 0, 45 and 55 Km and the filters are higher than 100 Km.

Only measurements on the bench once fully integrated and aligned will teach us the amount of aberrations to correct, but we can get an estimation of this value from the data on the separated optical pieces (Table 2) exaggerated to simulate a worst case situation. In a first estimation, we consider that only four elements bring aberrations to the system, and that distortion can be modeled by a simple WF shift when the beam passes through a plane at the position of the optical element.

Thus, in order to simulate the real system, those aberrations were added to the optical design of MAD made by a ray-tracing software. By this way we combine the design aberrations, the chromatic aberrations and the expected optics aberrations.

Optical element	Collimator #1	Mirror IR1	Collimator #2	Mirror IR2
Aberrations added	85 nm rms	65 nm rms	100 nm rms	105 nm rms
Aberrations map				
Useful surface (mm)	130	130	130	170
Beam footprint (mm)	60	60	60	60

Table 2. Aberrations on four optical elements of the common and IR camera path, as implemented in the simulations. The rms value given refers to the aberrations over the whole surface of the optics.

6. RESULTS

6.1. Aberrations measurement

A grid of 13 points has been defined in the FoV, following the geometry shown in Fig. 3. Those points will be the measurement points of the aberrations. But in a first time only the SR was evaluated at those positions in order to check the quality of the PSF in the FoV at the level of the IR focus. The degradation of quality is only due to the static aberrations in the optical path.

The results of the SR measurements (as calculated by the ray-tracing software) are also shown in Fig. 3 for three different wavelengths (J band: 1250 nm, H band: 1600 nm, K band: 2200 nm). In K band the SR is always greater than 90%, except some points at the border of the field where it drops down to 75%. Obviously the shorter is the wavelength, the smaller the SR.

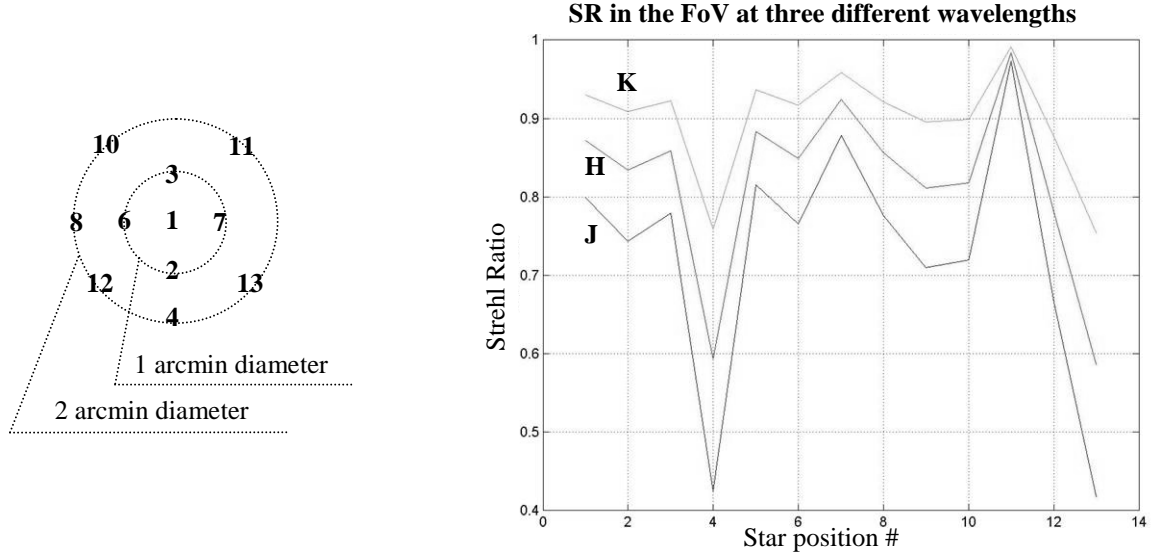


Fig. 3 Repartition of the measurement points in the field and SR associated

6.2. Reconstruction

The WFs calculated by the ray-tracing software Zemax at the stars position are transformed into focused and defocused images (Fig. 4). No noise is added to those images. They are analyzed by the ΦD algorithm that gives a table of Zernike coefficients for each position in the FoV. Those coefficients and the parameters of the system are used as input of our algorithm. As the simulated images contain no noise, the noise covariance matrix C_n is set to identity.

The meaning of the aberrations covariance matrix C_φ is not obvious: in the case of atmospheric tomography, it contains the knowledge we have of the statistical behavior of the turbulence, more exactly the variance of the Zernike coefficients. Using this knowledge leads to a regularization of the solution. In the case of the study of the optical aberrations of a system (which are static), we could fill it with an estimation of the aberrations we expect at the

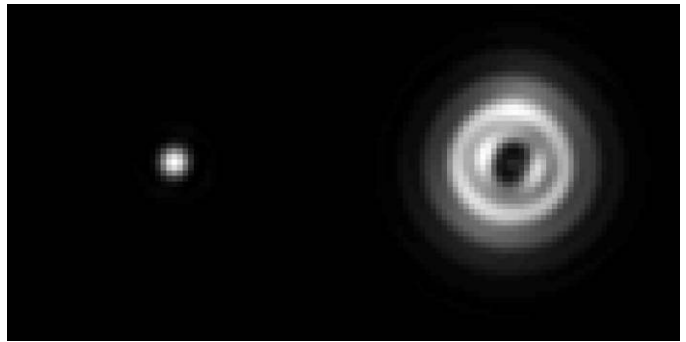


Fig. 4. Examples of simulated focused and defocused images to feed the ΦD algorithm

level of the different optics. Some tests made on simulated images show that the regularization doesn't enhance the results, due to a bad knowledge we have of the aberrations in the system. Thus for the present simulations, the matrix C_ϕ was also set to identity. However in the case of the real system those covariance matrices will play a crucial role for reducing the error brought by the noise of the IR images measured with the camera.

The projection is done on eight layers (at 0, 4, 7.5, 8.5, 13, 14, 16.2 and 30 Km) to take into account the position of the optics and to fill efficiently the equivalent volume occupied by the instrument. The projection is done at the levels of the two DMs (0 and 8.5 Km).

The residual aberrations in the directions of interest are calculated thanks to the equation (8). The correction achieved is plotted in Fig. 5. At the positions of the measurements, the SR in J is ranging from 42 to 97% in the FoV, with an average of 73% (90% in K band). After correction it is restricted to the range 81-96% with an average of 91.5%. It corresponds in K band to an average SR of 97%.

This result proves that the tomographic reconstruction of the aberrations of the optics in the MCAO instrument is efficient, and that the projection on the two DMs brings a great enhancement of the quality of the images in the full scientific FoV.

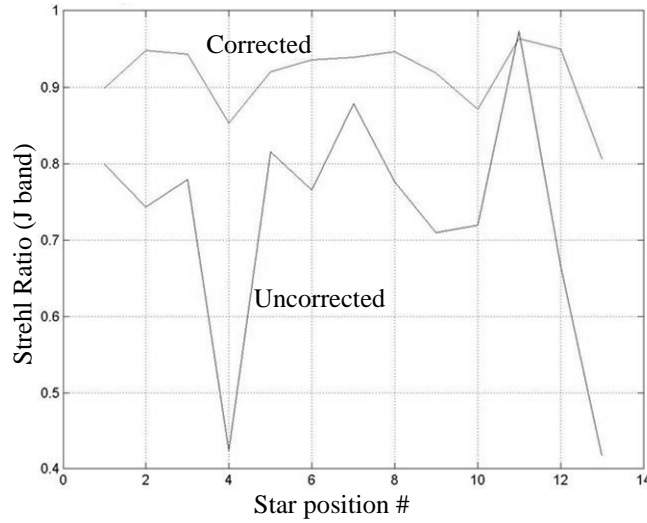


Fig. 5. Result of the correction in the case of the 8 layers tomography projected on 2 DMs. The position of the stars in the FoV is defined in Fig. 3.

6.3. Numerical optimization

Although the minimization of the criterion described previously (equation (3)) leads to the best correction in the field, maybe it would be of an interest to define another one. In the case of the correction of the static aberrations in the FoV, an interesting criterion could rather be the dispersion of the residual variances in the directions of interest. The minimization of this criterion would lead to a solution with the best uniformity of the residual aberrations in the scientific field (or at least in the directions of interest) of the MCAO instrument, even if the average SR is a bit lower than the result obtained in the previous section. A possible expression of this estimator would be:

$$\epsilon' = \left\langle \left(\sum_i a_{\alpha,i}^2 \right)^2 \right\rangle_{\{\alpha\}_{\text{fov}}} \quad (9)$$

where the $a_{\alpha,i}$ are the coefficients of the decomposition on the Zernike polynomials of the residual aberrations R_α in the direction α , and:

$$R_\alpha = \Phi_\alpha - M_\alpha^{N_{\text{DM}}} W \Phi_{N_{\text{GS}}} \quad (10)$$

The drawback of this estimator is that it focuses on the uniformity of the residual variance in the FoV, but doesn't help for increasing its average value. Thus an estimator taking both into account would be:

$$\varepsilon'_G = \int_{\{\alpha\}_{\text{fov}}} \left\| \sum_i a_{\alpha,i}^2 - \text{Goal} \right\|^2 d\alpha \quad (11)$$

The constant “Goal” represents an average variance (that we can also express as a SR) we try to reach in addition to the minimization of the residual variance everywhere in the FoV. More precisely, instead of calculating the variance which is the deviation around the average value, this estimator represents the deviation of the SR around a goal value.

Here again we will limit ourselves to the evaluation of the performances in the direction of the GS:

$$\varepsilon'_G = \sum_{N_{GS}} \left\| \sum_i a_{\alpha,i}^2 - \text{Goal} \right\|^2 \quad (12)$$

The analytical solution to the problem would come from deriving this estimator in order to find its minimum. In a first time we choose to adopt a numerical approach for solving the problem, not optimized but much faster. Thus we considered that a way to make uniform the residuals in the FoV is to put weight on the reference stars. This can be done by filling appropriately the matrix C_n . By default this matrix is set to identity, and its dimension is equal to the number of GS multiplied by the number of Zernike coefficients used for the reconstruction. If we choose to put the same weight on all the coefficients of each GS, the number of parameters to resolve is equal to the number of GS (13 in our example). So we have kept the solution W given by the equation (4), and modified the matrix C_n in it in order to minimize the criterion ε'_G (equation (12)). Thanks to a routine that calculates the minimum of an unconstrained multivariable function, it is possible to numerically find the values of the 13 parameters that minimize ε'_G . The result of this optimization for a Goal of 90% of SR in J band is shown in Fig. 6. The average value of the SR is 89.5 % (pretty close to the goal), and the variation is successfully limited to the range 85-93 %. The use of the new criterion, even if not analytically derived, brings a certain enhancement of the uniformity of the residual aberrations as measured in the directions of the GS.

In Fig. 6 is also shown the shape of the two DMs that brings this correction. We can notice that mainly low order aberrations are present. The amplitude of the correction is of a great importance, as it uses some of the stroke of the DM that then is no more available for the MCAO real-time correction. The two deformable devices in MAD are curvature mirrors, one of 60 mm useful diameter and the other one of 100 mm (fitting respectively the two altitudes of 0 and 8.5Km for a 2 arcmin FoV), both with about 3 microns of stroke. The stroke used to perform the correction is 195 nm for the ground MD and 445 nm for the altitude DM, which is quite a consequent part of the full stroke. If the aberrations in the real system, especially at the edges, turn out to be that greedy in DM stroke, we might have to select carefully the area for the field optimization during the tomographic reconstruction.

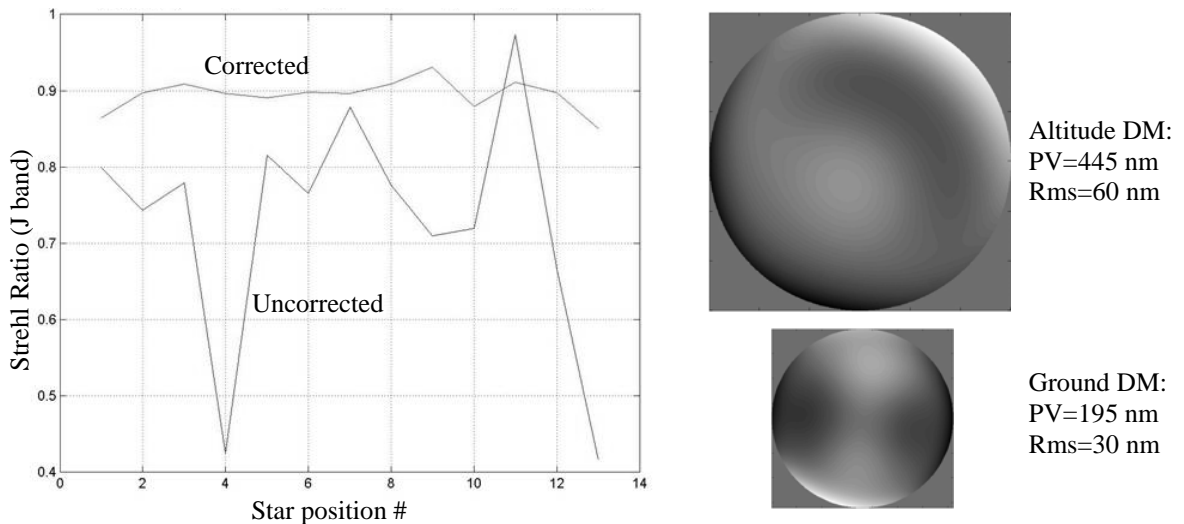


Fig. 6. Result of the correction in the case of the 8 layers tomography projected on 2 DMs, after numerical optimization. The position of the stars in the FoV is defined in Fig. 3.

7. CONCLUSION / FUTURE WORK

It has been demonstrated on the system NAOS-CONICA that it was possible to correct for the optical aberrations in the path of the camera, by the use of the ΦD algorithm to compute the WF from IR images, and by applying the proper shape to the DM. In this paper we have pushed a bit further and demonstrated that it is also possible to correct for the field-dependant static aberrations in an MCAO system, by taking the most of the presence of several correcting devices conjugated with different altitudes. This can be done by using the IR camera as WFS, analyzing its images by the ΦD in order to retrieve the WF, and then by reconstructing tomographically the WF in the layers. On the particular example of a geometry of 13 stars in the FoV of the MAD instrument, and with no noise in the images, we have showed that a very irregular FoV with 73% of SR in average in J band can be enhance to a quasi-flat FoV at 90% of SR.

Some more developments would enhance the reconstruction and/or bring the simulated system closer to the reality. First of all, in order to get an ultimate expression for the reconstruction matrix W , it would be required to derive the estimator defined in the equation (11). A more complete grid of simulated measurement points would allow at the same time optimizing the correction for some areas in the FoV, studying more GS configurations, and estimating the quality of the correction in the whole scientific field. The introduction of noise in the simulated images before their analysis by the ΦD algorithm would give us an idea of the robustness of the algorithms when faced to realistic data. Finally the practical way of recording the images and applying the proper static voltages to the DMs has to be defined accurately; this might introduce some errors in the whole procedure and decrease the quality of the correction.

ACKNOWLEDGMENT

This work has been partially funded by the European Research and Training Network *Adaptive Optics for Extremely Large Telescopes* with Contract HPRN-CT-2000-00147.

REFERENCES

1. A. Amorim, A. Melo, J. Alves, J. Rebordão, J. Lima, J. Pinhão, G. Bonfait, R. Fernandes, R. Barros, J. Azevedo-Lucas, L. Correia, M. Carvalho, J. Santos, R. Marques, F. Duarte Santos, I. Catarino, J. Poncet "The CAMCAO infrared camera", Ground based instrumentation for astronomy, SPIE Proceedings, 5492, article number [5492-120], 2004
2. A. Blanc "Identification de réponse impulsionnelle et restauration d'images : apports de la diversité de phase" Thèse de Doctorat, Université Paris XI Orsay, July 2002
3. A. Blanc, T. Fusco, M. Hartung, L. M. Mugnier, G. Rousset "Calibration of NAOS and CONICA static aberrations. Application of the phase diversity technique" Astron. Astrophys., 399:373-383, 2003
4. D. L. Fried "Anisoplanetism in adaptive optics" J. Opt. Soc. Am., 72(1):pp 52-61, Jan. 1982
5. T. Fusco "Correction partielle et anisoplanétisme en Optique Adaptative: traitements a posteriori et Optique Adaptative multiconjuguée" Thèse de Doctorat, Université de Nice Sophia-Antipolis, October 2000
6. T. Fusco, A. Blanc, L. M. Mugnier, G. Rousset "Development of a Phase Diversity approach to calibrate NAOS and CONICA static aberrations" ONERA technical report
7. T. Fusco, J.-M. Conan, V. Michau, L. M. Mugnier, G. Rousset "Phase estimation for large field of view: application to multiconjugate adaptive optics", Proc. SPIE 3763, 125-133 (1999)
8. T. Fusco, J.-M. Conan, G. Rousset, L. M. Mugnier, V. Michau "Optimal wavefront reconstruction strategies for multiconjugate adaptive optics" J. Opt. Soc. Am. A, (10):2527-2538, October 2001
9. M. Hartung, A. Blanc, T. Fusco, F. Lacombe, L. M. Mugnier, G. Rousset, R. Lenzen "Calibration of NAOS and CONICA static aberrations. Experimental results" Astron. Astrophys., 399:385-394, 2003
10. E. Marchetti, R. Brast, B. Delabre, R. Donaldson, E. Fedrigo, F. Franza, N. Hubin, J. Kolb, M. Le Louarn, J. Lizon, S. Oberti, R. Reiss, J. Santos, R. Ragazzoni, C. Arcidiacono, A. Baruffolo, E. Diolaiti, J. Farinato, E. Vernet-Viard, "MAD status report", Advancements in Adaptive Optics, SPIE Proceedings, 5490, article number [5490-17], 2004

11. R.G. Paxman, T.J. Schulz, J.R. Fienup "*Joint Estimation of Object and Aberrations Using Phase Diversity*", J. Opt. Soc. Am. A 7, 1072-85 (1992)
12. R. Ragazzoni, E. Marchetti, F. Rigaut "*Modal Tomography for Adaptive Optics*" Astronomy and Astrophysics 342:L53-L56 (1999).
13. G. Rousset, F. Lacombe, P. Puget, N. Hubin, E. Gendron, T. Fusco, R. Arsenault, J. Charton, P. Feautrier, P. Gigan, P. Y. Kern, A.-M. Lagrange, P.-Y. Madec, D. Mouillet, D. Rabaud, P. Rabou, E. Stadler, G. Zins "*NAOS, the first AO system of the VLT: on-sky performance*" in Adaptive Optical System Technologies II. Edited by Wizinowich, Peter L.; Bonaccini, Domenico, vol. 4839 of Proc. SPIE, pp. 140-149, Feb. 2003.

8.4. Example test report from SILIOS

This kind of test report was delivered by SILIOS on delivery of each PS for MAPS. It contains measurements made with a surface profiler and shows that on the number of sample positions measured, the PS is in the specifications. The optical properties of the PS have been tested at ESO (section 3.4.6) and the statistical properties of each PS have been tested at the delivery (section 3.4.7).



SILIOS Technologies
ZI Peynier-Rousset
Rue Gaston Imbert polongée
13790 PEYNIER
Tel :+33 4 42 53 89 60
Fax :+33 4 42 53 89 59

General information :

Date : 18th november 2004
Client : E S O
Karl-Schwarzschild strasse 2
D-85748 Garching bei München
Invoice Ref. : 73089/TSD/03/9053/GWI/LET
Object : Manufacture of a phase screen for the MAD Turbulence
Phase Screen Ref : **PS3-F3**

Substrate :

Material : Fused silica – Corning code 7980
Diameter : 100 mm +/- 0.10 mm
Thickness : 1.5 mm +/-0.10 mm
Properties : " http://www.corning.com/semiconductoroptics/products_services/pdf/h0607_hpfs_standard_productsheet.pdf "

Control :

Level	Target depth (angström)	Tolerance (angström)	Measured depth ⁽¹⁾ (angström)	Ecart (angstrom)
Single levels				
L1	2 580	+/- 1 290	2 491	+ 89
L2	5 150	+/- 1 290	5 016	+ 134
L3	10 300	+/- 1 290	10 056	+ 244
L4	20 600	+/- 1 290	20 458	+ 142
L5	41 210	+/- 1 290	41 093	+ 117

⁽¹⁾ Etching depths are measured with a profilometer (DEKTAK 3ST). The profilometer is calibrated with 3 standards. The measurement precision is better than +/-5 nm. Measurements are made inside 4 test gratings located outside the encoded aberration area.

8.5. The Infrared cameras of MAD

As introduced in the sections 2.3 and 4.4, MAD will use successively two IR cameras: the ITC belonging to the integration group of ESO (Figure 8.3), and CAMCAO built by a Portuguese consortium for the purpose of wide-field imaging (Figure 8.4).

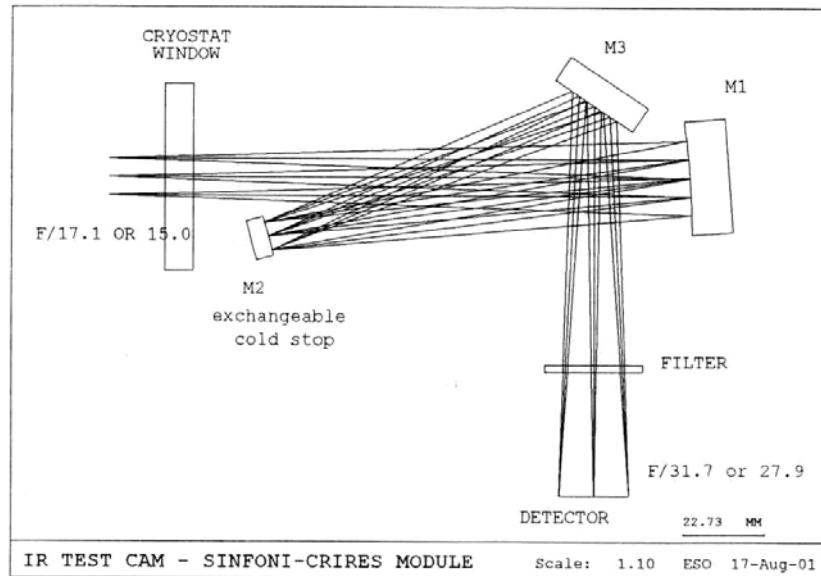


Figure 8.3: Optical design of the Infrared Test Camera (ITC).

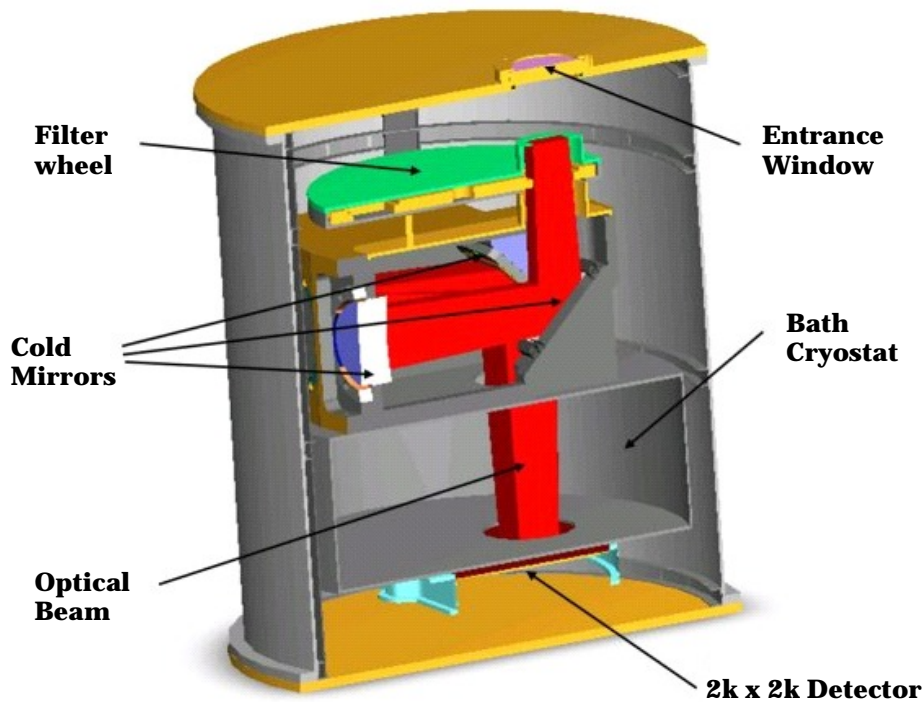


Figure 8.4: Opto-mechanical design of the Camera for MCAO (CAMCAO).

